

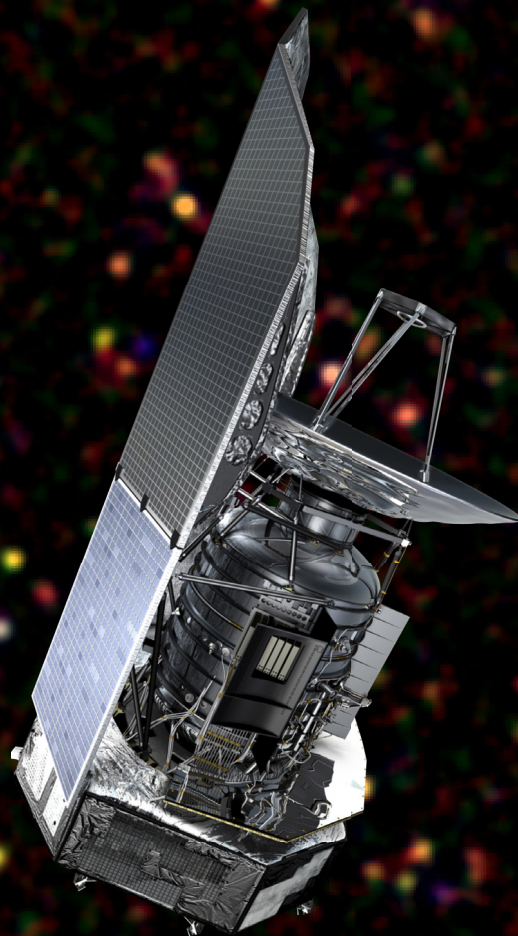


MAX-PLANCK-GESELLSCHAFT

Max-Planck-Institut für  
extraterrestrische Physik  
Garching



Report  
2007 - 2009



**Front Cover:**

Surveys of the extragalactic sky with Herschel resolve the cosmic infrared background into its constituting sources. The image shows galaxies from the COSMOS field, combining Herschel/PACS observations at 100 and 160 micrometer with Spitzer 24 micrometer data. The galaxies appear in different colors according to their redshift and the temperature of their interstellar dust, which is heated by stars and in some cases by active galactic nuclei.

**Back cover:**

Important instruments for MPE scientists to pursue their research in multiwavelength astronomy and in fundamental physics.



# Report 2007-2009

MPE Report 297

## Imprint

Responsible for contents: R. Genzel  
Editors and Layout: W. Collmar, E. Collmar, H. Hämmerle and J. Zanker-Smith  
Print: MPE Printshop (R. Hauner)

Text and Figure Contributions: C. Ahlig, M. Ajello, S. Berta, H. Boehringer, M. Brusa, W. Bunk, V. Burwitz, W. Collmar, L. Couedel, N. Drory, R. Diehl, P. Erwin, K. Dodds-Eden, R. Fassbender, N. Foerster Schreiber, R. Genzel, O. Gerhard, S. Gillessen, J. Greiner, F. Haberl, G. Haerendel, R. Heidemann, S. Khochfar, B. Klecker, S. Komossa, D. Lutz, V. Nosenko, N. Nowak, G. Paschmann, W. Pietsch, R. Saglia, A. Sanchez, S. Savaglio, M. Scholer, M. Schwabe, L. Strueder, R. Suetterlin, L. Tacconi, K. Tarantik, M. Thiel, M. Thoma, H. Thomas, E. van Dishoeck, D. Wilman

Further Support: R. Mayr-Ihbe, H. Steinle

1. Edition June 2010

# Table of Contents

<b>PREFACE</b>	5
<b>1 RESEARCH AREAS AND INSTITUTE STRUCTURE</b>	9
<b>2 SCIENTIFIC RESULTS</b>	
2.1 Large-Scale Structure and Cosmology	13
2.2 Galaxies and Galaxy Evolution	23
2.3 Massive Black Holes and Active Galactic Nuclei	38
2.4 Stellar Evolution and the ISM	56
2.5 Physics of the Solar System	65
2.6 Complex Plasmas	77
<b>3 EXPERIMENTS AND PROJECTS</b>	
3.1 Infrared/Submillimeter Astronomy	94
3.2 Optical and Interpretative Astronomy	102
3.3 High-Energy Astrophysics and MPI HLL	105
Projects in High-Energy Astronomy	105
The MPI Semiconductor Laboratory	110
3.4 Space Physics of the Near-Earth Environment	113
3.5 Complex Plasmas	118
3.6 Technology Transfer	122
<b>4 THE INSTITUTE</b>	
4.1 Technical Services	126
4.2 General Services	128
4.3 Vocational Training and Education	129
4.4 Public Outreach	130
4.5 Social Events	132



## PREFACE

This report summarizes the scientific, experimental and project activities at the Max-Planck Institute for Extra-terrestrial Physics (MPE) during the period 2007-2009, and including the first few months of 2010. Following an introduction of the Institute in chapter 1, the second chapter summarizes the scientific research in six main research areas and across the Institute's science groups. In each chapter, we start with an introduction and explain how the research at MPE fits into the overall research activities worldwide. This summary is then followed by a few selected highlights of our work during the last 3 years. Naturally, this structure cannot capture all of the many individual research projects and results at the MPE. For this purpose, we refer the readers to the 'Poster Booklet' that gives extended Abstracts of the individual activities. For clarity we have left out references in the text of Chapter 2, and we refer to the Poster Booklet for more details. In the case of the work on solar system 'Space Plasmas' at the MPE (section 2.5), this research is coming to an end in the near future, thus completing a superbly successful endeavor over the last forty years. On this occasion, we have decided to provide here a 'closing report' encompassing more than the last three years, and giving the readers an overall account of the accomplishments of MPE research in this field.

Chapter 3 covers the experiments, instrumental developments and projects, this time ordered by research groups. The final chapter summarizes the activities of our central technical and administrative groups, as well as our teaching and public outreach.

The last three years have been quite successful. On the project side, we saw the flawless launch of ESA's far-infrared space telescope HERSCHEL (together with PLANCK), followed by commissioning and first light science of the PACS instrument built at MPE. Outstanding science results on a wide range of science topics are now emerging every day, thus crowning a development that started at MPE about twenty-three years ago. Another milestone was the launch of the FERMI  $\gamma$ -ray satellite (again with significant MPE contributions), a third the continuing series of successful complex-plasma experiments on the International Space Station (PK3-plus, PK4). On the ground, we saw the start of regular science observations with laser guide star adaptive optics at the ESO-VLT with the PARSEC laser system, the beginning of science with the GROND  $\gamma$ -ray burst follow-up experiment and the commissioning and first science with the LUCIFER near-infrared camera/spectrometer on the LBT. MPE has entered the PanSTARRS1 collaboration for the next series of precision studies of the nature of dark energy and the first scientific results have been emerging this year.

We have also made good progress in preparing the next series of future experiments and projects. eROSITA is now an approved DLR-project and the road is clear for a launch in 2012/2013. The formal technical agreement on the German-Russian collaboration was signed last summer by RosCosmos and DLR. The technical developments of detectors and telescopes for eROSITA are proceeding well. The GRAVITY experiment for the ESO-VLT interferometer, the KMOS multi-integral field unit for the VLT, the HETDEX multi-fiber spectrograph on the HET, the ARGOS wide-field adaptive optics system for the LBT, and the MICADO study of an astrometric camera for the E-ELT all have successfully gone through major project milestones. The merger between the ESA and NASA studies in the next generation X-ray mission has led to the IXO project, in which MPE hopes to be engaged in the future. MPE is also part of the ongoing ESA feasibility study of EUCLID, a mission to explore the cosmic evolution of the fundamental cosmological parameters as well as of galaxies.

On the science side we have seen spectacular new results with SINFONI on the Galactic Center, on nearby massive black holes and on distant galaxy dynamics. HERSCHEL/PACS is delivering new insights on cosmic star formation, in the Milky Way, in nearby external galaxies and in very luminous distant galaxies. The IRAM Plateau de Bure interferometer has given exciting glimpses on the amount and properties of cold gas in forming massive galaxies at high redshift. GROND is discovering the most distant  $\gamma$ -ray bursters seen to date. Our studies of the hot gas, stellar light and stellar dynamics in the intra-cluster medium have given important new insights on the structure and dynamical processes in massive galaxy clusters. Our work on the cosmic evolution of galaxy clusters, as well as the angular distribution of galaxies has yielded new constraints on the nature of dark energy.

We are continuing to learn ever more about the properties of accreting massive black holes, their interaction with their host galaxies and beyond, with each other as a result of galaxy mergers, and their cosmic evolution. Our work with FERMI, INTEGRAL and XMM has delivered new insights into the properties and evolution of magnetars, pulsars, neutron stars, stellar black holes and evolved binaries, as well as the ejection by massive stars of radioactive material into the interstellar medium of the Milky Way. Our studies of complex plasmas under microgravity have uncovered a remarkable range of new phenomena, including bubbles and droplets, lane formation in penetrating streams and phonon/soliton excitations. We have also been able to gain important new insights into the microphysics of the melting of plasma-crystals.

I am grateful to all my colleagues at the MPE for their inputs and help, which was essential for preparing this tri-annual report.

A handwritten signature in black ink, appearing to read 'Reinhard Genzel', written in a cursive style.

Professor Reinhard Genzel  
Managing Director

# 1 Research Areas and Institute Structure





# 1 RESEARCH AREAS AND INSTITUTE STRUCTURE

Our research at the Max-Planck-Institut für extraterrestrische Physik (MPE), located on the University and Research Campus in Garching (Fig. 1), addresses topics of astrophysics and plasma physics. We combine experiments and instrumental development with observations, data analysis and theoretical work. The main themes of our work during the period 2007 to 2009 were:

- Large-Scale Structure and Cosmology
- Galaxies and Galaxy Evolution
- Massive Black Holes and Active Galaxies
- Stellar Evolution and Interstellar Medium
- Physics of Complex Plasmas
- Physics of the Solar System.

Our experimental work during the last three years focused on astronomy with a number of projects, spanning more than twelve decades of the electromagnetic spectrum from millimeter/submillimeter, infrared to optical, X- and Gamma-ray bands. For the high energies we used satellites and space probes to avoid the atmospheric absorption of the radiation. In the infrared and optical bands we also used ground-based or airborne telescopes. Our investigations are complemented by laboratory experiments. In particular the research field of "Complex Plasmas" carried out laboratory activities at MPE as well as under microgravity conditions on parabolic flights and aboard the International Space Station. Research groups at MPE also conducted analytical, numerical and observation-related interpretational research and addressed topics that cover all experimental research areas. The teaming up and strong interaction of theoreticians, observers and experimentalists is a hallmark of our research style.

Our scientific activities are organised into four major research fields, each of which is supervised by one of the directors: (1) Infrared- and Submillimeter Astronomy, (2) Optical and Interpretative Astronomy, (3) High-Energy Astrophysics and (4) Theory and Complex Plasmas. A small group carried out research in space plasma physics. This research branch of MPE came to an end with the ending of 2009. Within these main areas, research is organized in integrated project groups, which include scientists, postdocs, students and technical staff from the Institute's central division. Currently there are about forty independent project teams. Given our leadership in the development of ambitious space- and ground-based instruments, experiments and telescopes, our technical and engineering branches played a key role, working in close liaison with individual research groups. We also were engaged

in the development of large software projects and in the analysis of large amounts of primary data. Key facilities of the Institute outside of Garching are the X-ray test facility (PANTER) located in Neuried near München (Fig. 2) and the Max-Planck-Institute Semiconductor Laboratory (MPI-HLL) on the Siemens campus in München-Neuperlach (Fig. 3), a collaborative enterprise between MPE and the Max-Planck-Institut für Physik in München. In addition to several technical central groups in mechanical and electronic engineering and their associated workshops mentioned above, our administration and technical services team supported our Institute, as well as the neighbouring Max-Planck-Institut für Astrophysik.

Know-how transfer from our research into applications is particularly important in two research areas at MPE. The theory division transfers know-how in the area of "analysis of complex systems" into applications in medicine, engineering and pharmacology, and new results in plasma



*Fig. 1: The MPE building on the science campus in Garching. The building is connected to the Max-Planck-Institute for Astrophysics (MPA).*

research triggered the opening of the new field "plasma medicine". The semiconductor laboratory manufactured X-ray detectors that are applied in other research institutes and in industry.

Our major experimental projects were mostly developed in close cooperation with industry, both locally in the Munich area as well as all over Europe and world-wide. Our success record in experimental astrophysics and space research demonstrates the efficiency of such cooperations, primarily with space industry and electronics companies. The challenging technological requirements of our experiments also often led to technology transfer to industry.

In addition to the institutional support by the Max-Planck-Gesellschaft, the most important element of our funding of personnel and projects, our research was also supported by government institutions such as the Federal Ministry



*Fig. 2: An aerial photograph of the MPE Panter X-ray test facility in Neuried. The X-ray source and the telescope chamber are separated by a 130m vacuum pipe system.*

for Education and Research (BMBF) and the German Center for Aeronautics and Space Research (DLR), international organisations such as the European Space Agency (ESA) and European Southern Observatory (ESO) as well as the European Community, with additional financial contributions from the German Science Foundation (DFG), the Humboldt Society and the Dr. Johannes Heidenhain-Foundation.

Our institute is strongly engaged in university education: MPE researchers taught at several universities and supervised student research (Diplo-

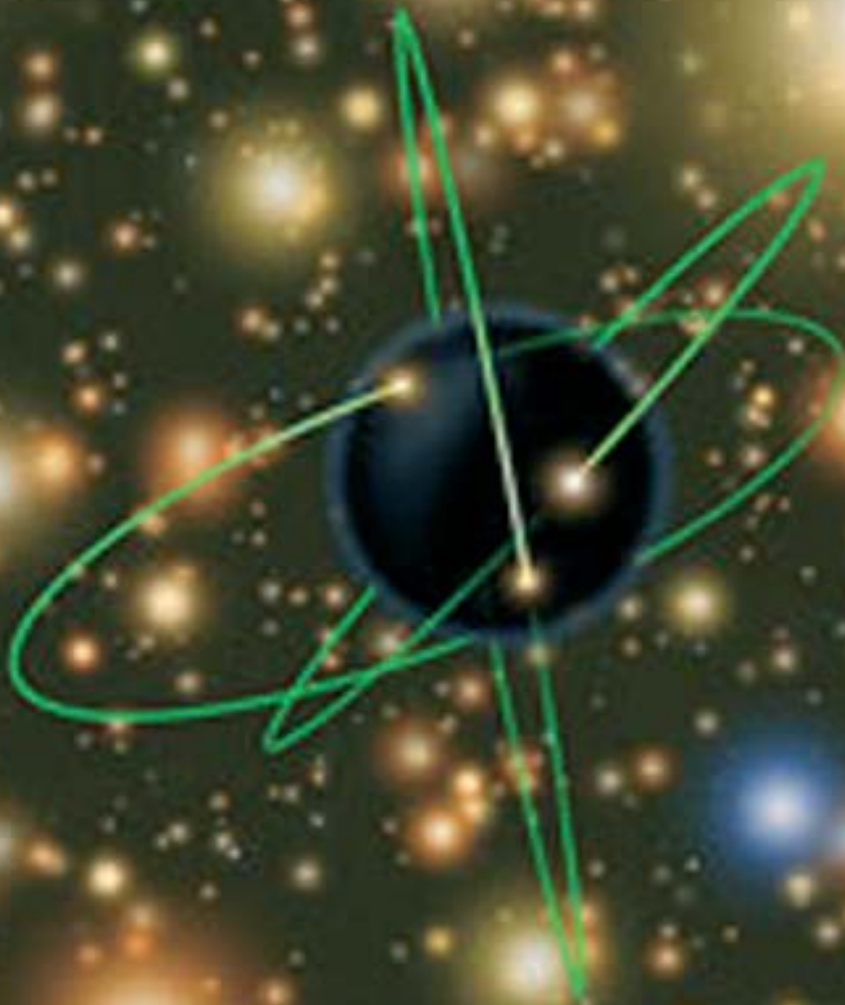
ma, Ph.D.), mainly at both Munich universities, but also at other German universities, and as far away as the University of California (Berkeley). Seminars, workshops and conferences were held by the Institute in our own and adjacent research fields, often in cooperation with the universities. Our very successful "International Max-Planck Research School on Astrophysics" at the Ludwig-Maximilians-Universität München continued to attract young motivated people to astrophysical research.

During the report period MPE increased its efforts and professionalism in public outreach by creating a new post together with MPA, the first position, in the history of the Institute, dedicated to PR. One of the main aims is to supply information, like Press releases and other scientific PR material, not only to the specialist press but also to a wider audience.



*Fig. 3: The MPI Halbleiterlabor (semiconductor laboratory) on the Siemens campus in München-Neuperlach.*

## 2 Scientific Results





## 2.1 LARGE-SCALE STRUCTURE AND COSMOLOGY

Our strong interest in the study of the large-scale structure of the Universe is based on two objectives: On the one hand, all objects that we observe in the sky today were formed in the environment of the cosmic large-scale structure. Our goal therefore is to understand the properties of the observed population of galaxies and galaxy clusters from first principles and the initial conditions provided by the large scale structure. On the other hand, by observing the large scale structure itself and comparing these results with model predictions we can characterize the cosmological model describing our Universe as a whole. The following highlight article gives an ideal example of this second objective, where clusters of galaxies, the largest well defined objects in the Universe, are used to probe the initial conditions in the early Universe.

To study the large-scale structure and the population of galaxy clusters we need deep and wide-field surveys providing statistically complete catalogues of galaxies and galaxy clusters. The research groups of our institute are therefore involved in a number of such surveys in the optical, X-ray and infrared wavebands. From the PanSTARRS, SDSS-BOSS, VIPERS, HEDTEX, KIDS, and Dark Energy Survey in the optical we hope to gain new insight into the statistics of the large-scale galaxy distribution with a particular emphasis on detecting the signature of so-called baryonic acoustic oscillations (BAOs). We are also of preparing the next generation X-ray all-sky survey with the eROSITA Mission. Described below is an important study for which an unprecedented sample of distant, X-ray luminous galaxy clusters is assembled through a search in XMM-Newton archival data. A dedicated XMM-Newton sky survey together with the South Pole Telescope project allows the simultaneous detection of galaxy clusters in X-rays and at millimetre wavelengths. The wavelength coverage is even more detailed in the COSMOS survey, which is by far the most comprehensive deep survey ever undertaken. To probe the large-scale structure at high redshift, the COSMOS field is observed by all major observing facilities, including the Hubble Space Telescope, and covers a large enough volume to show a representative sample of distant galaxy groups and poor clusters. For our studies of the large-scale structure in the nearby Universe, we continue to increase the catalogue of galaxy clusters identified in the ROSAT all-sky survey.

The use of galaxy clusters as cosmological probes requires a good understanding of their properties. We therefore study the structure and composition of representative samples of galaxy clusters at several wavelengths. XMM-Newton and Chandra data allow us to probe the cluster structure by means of the X-ray luminous intracluster medium (ICM). With optical observations we can understand the cluster dynamics and the galaxy population, as well as getting a mass measurement through a gravitational lensing analysis. Below we describe our progress in understanding galaxy clusters as a self-similar family of large cosmic structures. The properties of the ICM vary most in the cluster centre, where in some clusters with so-called cool cores plasma cooling can lead to the feeding of a central Black

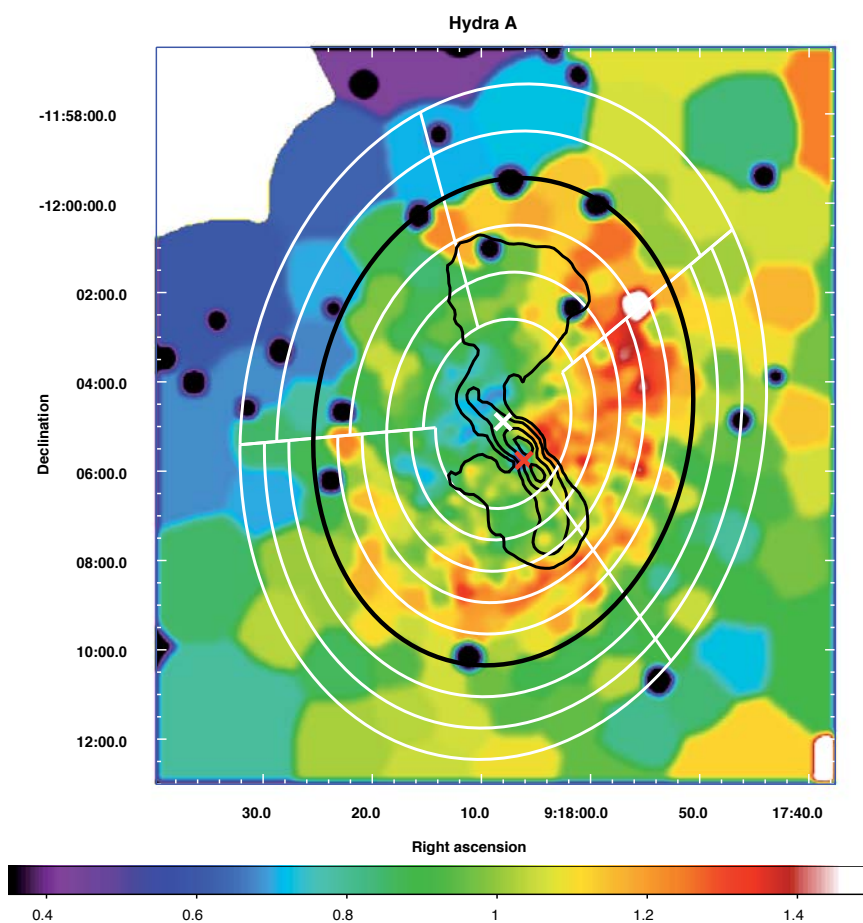


*Fig. 1: Pressure map of the intracluster medium in the Hydra A cluster of galaxies produced from a deep XMM-Newton observation. The pressure enhancement detected in the map (red areas) traces an explosion shock approximated by the black ellipse. The explosion energy is estimated to be about  $10^{42}$  MegaWatt hours. The irregular, thin black line in the centre shows the radio emission.*

Hole, which then injects some of the energy released back into the ICM with spectacular interaction effects. Fig. 1 shows a particularly powerful AGN explosion in the Hydra A cluster, which we have diagnosed in detail using XMM-Newton observations.

## Modeling non-linearities in the large scale galaxy correlation function

Oscillations in the baryon-photon fluid in the very early universe imprint characteristic signatures on the power spectrum and correlation function of matter fluctuations, which are called baryonic acoustic oscillations (BAO). Measuring these features using galaxy surveys allows us to determine important cosmological parameters, in particular, the equation of state of the Dark Energy. The accuracy required to achieve competitive constraints demands an extremely good understanding of how the BAO change due to the non-linear evolution of density fluctuations by the distortions introduced when redshifts are used as distance indicators in the presence of peculiar velocities and by differences in the galaxy and matter density fluctuation (bias). We developed a model for the full shape of the correlation function that accurately takes into account these systematic effects and provides an unbiased measurement of the Dark Energy equation of state.

Over the past few years, a wealth of high precision observations, mainly in the form of measurements of the cosmic microwave background (CMB) and the large scale structure (LSS) of the galaxy distribution, have revolutionised our view of the Universe. We seem to live in a Universe more complex than originally suspected, whose energy content is dominated by a Dark Energy component that is responsible for the acceleration of the universal cosmic expansion. Understanding the nature of Dark Energy is one of the most important outstanding problems in physics as its mere existence has far reaching implications concerning our current understanding of the fundamental laws of nature.

This situation has led to an ambitious observational programme to accurately determine the properties of this component. The MPE contributes substantially to this effort. In particular, the MPE has a leading role in several ground breaking galaxy surveys such as Pan-STARRS, BOSS and HETDEX, as well as galaxy cluster surveys

such as eROSITA. These surveys will map the positions of millions of galaxies and thousands of galaxy clusters allowing us to measure the large scale clustering pattern of the Universe with unprecedented precision. Using this information we will be able to obtain new constraints not only on Dark Energy, but also on other important physical parameters such as neutrino masses or the curvature of the Universe, and to probe inflationary physics, the last great epoch to be uncovered following the Big Bang.

The power spectrum of galaxy clustering and its Fourier transform, the two-point correlation function, are the preferred tools for analysing the large scale structure of the Universe. To link observations with theoretical models simplifying assumptions were made: on large scales, the shape of the galaxy power spectrum was expected to closely follow the prediction made with linear perturbation theory for the Dark Matter distribution. However, as improved measurements and more refined models became available, it became clear that this simple picture is no longer sufficient to accurately describe the data.

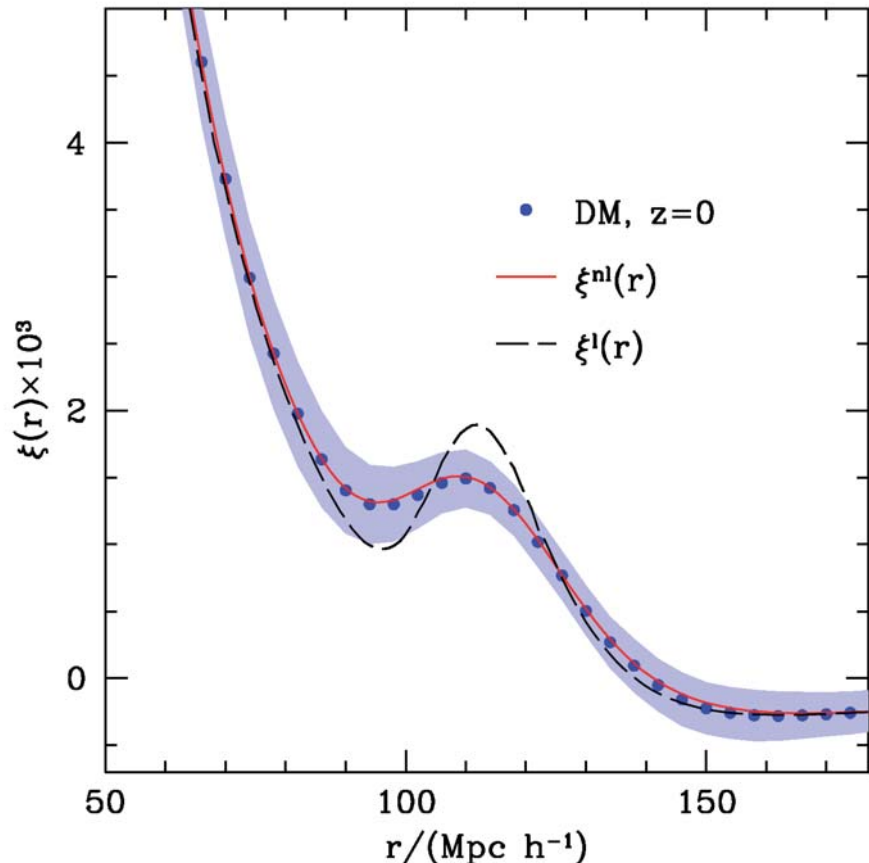


Fig. 1: Mean correlation function of the dark matter distribution at redshift  $z=0$  measured from the L-BASICC II ensemble of simulations (points). The shaded region represents the variance of the different realizations. The shape of the acoustic peak significantly deviates from the predictions of linear theory (long dashed line). These deviations are accurately described by our model (shown by the solid red line).

In principle, if the simple models described the form of the observed power spectrum, then the power spectra measured from different galaxy samples should give the same cosmological parameters. However, if we compare the constraints on cosmological parameters obtained from the galaxy power spectra measured from two different surveys (the two-degree Field Galaxy Redshift Survey 2dFGRS and the Sloan Digital Sky Survey (SDSS), which use different selection criteria for the galaxies, we found a fundamental difference. SDSS is dominated by more strongly clustered red galaxies, which have a stronger scale dependent bias. Similar scale dependent effects have been seen in the power spectrum of dark matter haloes and galaxies modelled in simulations. The tension between SDSS and 2dFGRS shows that the LSS is more complicated than was generally thought. Although the scale considered is very large, there are still scale dependent effects such as galaxy bias and redshift space distortions, which cause deviations from linear theory. The quality of the forthcoming surveys demands that these effects must be incorporated into the models so that we can extract the maximum amount of information from the new observations.

As a consequence of these difficulties, recent analyses have not attempted to model the overall shape of the power spectrum. Instead, attention has shifted to the BAO pattern, a series of quasi-harmonic oscillations imprinted on the power spectrum. The scale of these oscillations is related to the sound horizon at recombination. As the size of the sound horizon can be inferred from CMB observations, the scale inferred from the BAO can be used as a standard ruler to measure the distance-redshift relation. Using a simple geometrical relation, the distance to a given galaxy sample can be measured from the apparent size of the BAO ruler which has been inferred from their clustering pattern. This test can provide tight constraints on parameters such as the curvature of the Universe or the equation of state for the Dark Energy, as these parameters determine the angular diameter distance to a given redshift.

By inferring the acoustic scale from the positions of the BAO nodes, this can be isolated from a measurement of the power spectrum as a whole, ignoring information from its amplitude and broadband shape, which can be affected by scale dependent distortions. However, this approach has the disadvantage of sacrificing useful information contained in the shape of the power spectrum. Using

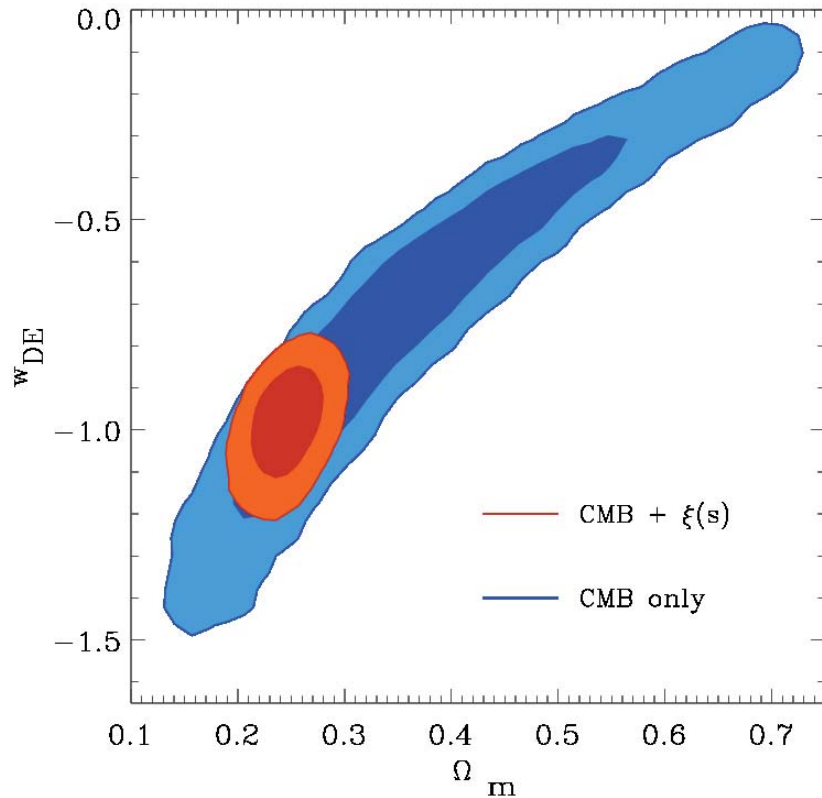


Fig. 2: Constraints on Dark Matter and Dark Energy: This plot shows the two-dimensional marginalized constraints in the  $\Omega_m$ - $w_{DE}$  plane (assuming a time-independent  $w_{DE}$ ). The contours show the 68 and 95 per cent confident levels obtained using CMB data alone (blue) and CMB plus LRG  $\xi(s)$  (orange). The inclusion of the LRG correlation function in the analysis breaks the degeneracy present in the CMB only, providing tight constraints on both of these parameters.

this method, recent studies found a significant discrepancy compared to constraints inferred from supernovae type Ia (SN) data. This could point to a possible problem in the modelling of the BAO data or challenge the standard  $\Lambda$ CDM cosmological mode.

To clarify these discrepancies we analysed an ensemble of large volume N-body simulations to investigate the BAO signature in the two-point correlation function, where the BAO appear as a broad peak at large scales. The massive computational volume allowed us to explore in detail how the shape of the correlation function is distorted by the non-linear growth of perturbations, redshift space distortions and bias. We found that the correlation function is less affected by these scale-dependent effects than the power spectrum. A simple model, based on Renormalized Perturbation Theory, can correctly account for these effects with the necessary accuracy for the next generation of galaxy surveys and thus give an unbiased measurement of the Dark Energy equation of state. With this model, we can use information from the large-scale shape of the correlation function together with the form of the BAO peak to provide robust constraints on cosmological parameters. Therefore, this approach provides a better constraint on the Dark Energy equation-of-state (about 50% smaller errors) than the more conservative method using the power spectrum (which requires long-wavelength shape information to be discarded).

In Fig. 1 we show the correlation function of the dark matter distribution measured from the ensemble of simulations (points) and its correspondent variance (shaded region). The shape of the acoustic peak shows strong deviations from the predictions of linear theory (dashed line). Non-linear evolution damps the acoustic peak and shifts its position towards smaller scales. These effects are accurately described by our model (solid line).

Recently, we applied this new model to the correlation function measured of the luminous red galaxies (LRG) sample from the SDSS Data Release 6. We combined the LRG information with the latest measurements of CMB and supernovae data to perform a comprehensive study of the constraints on cosmological parameters obtained from different combinations of data sets and for different parameter spaces. Fig. 2 shows the 68 and 95 per cent confident levels for the matter content and equation of state for the Dark Energy obtained using CMB data alone (blue) and information from the CMB plus the LRG correlation function (orange). There is a strong degeneracy between these parameters if only CMB data are used which leads to poor one-dimensional marginalized constraints. The inclusion of the LRG correlation function breaks this degeneracy, leading to a dramatic improvement of the constraints on these parameters. In this case we get a matter content of  $\Omega_m = 0.245 \pm 0.020$  and a value for the Dark Energy parameter of  $w_{DE} = p_{DE}/\rho_{DE} = -0.996 \pm 0.095$ , which is in complete agreement with a cosmological constant (i.e.,  $w_{DE} = -1$ ). Using a larger galaxy sample and accurate modelling of the BAO allowed us to show that the LRG clustering and the latest supernovae data give constraints on cosmological parameters, which are in remarkably good agreement, thus resolving the tension reported in previous studies. Combining all datasets we obtain constraints on the Dark Energy equation of state consistent with a cosmological constant at the 5% level. If we combine the LRG correlation function with the measurement of the radial BAO peak from Gaztañaga et al. (2009), for the first time we can constrain the Dark Energy equation of state at the 15% level by only using information contained in the LSS. This provides further confirmation of the Dark Energy scenario, independent of CMB or SN observations.

Our model is an ideal tool for analysing the LSS in future surveys as it provides an accurate description of clustering for the level expected in datasets with volumes up to two orders of magnitude larger than current ones. We can, for example, predict the constraints on cosmological parameters that will be obtained from the Baryonic Oscillations Spectroscopic Survey (BOSS) by applying this model to the correlation function of its up to one million luminous red galaxies up to a redshift of 0.7. By combining this information with data available from the Planck satellite in the next couple of years, it will be possible to constrain the Dark Energy equation of state at the 2.5% level, providing a radical improvement on current constraints. Besides the analysis of individual catalogues, the simultaneous access to different datasets will provide excellent opportunities. The characteristics of BOSS and HETDEX make them complementary, their combination will span a larger redshift range than any other set available. The application of our model to this combined information will allow to simultaneously measure the Dark Energy equation of state to 3% accuracy and the curvature of the Universe to the 0.0015 accuracy level, something impossible for any individual LSS dataset combined with CMB data. Nevertheless, in order to achieve robust constraints on the values of cosmological parameters such as the Dark Energy equation of state and its possible evolution with time, we need to pursue as many approaches as possible to allow for comparisons between the results obtained with different techniques and datasets.



A.G. Sanchez

## Galaxy Clusters in the First Half of Cosmic Time

The latest generation of X-ray surveys helps us to shed new light on the population of galaxies in clusters and groups at lookback times of 7-10 Gyr, when the universe was less than half its current age. These observations provide a unique opportunity to trace the assembly and evolution of the most massive structures in the Universe and their different components, i.e. Dark Matter, hot Intracluster Medium (ICM), and cluster galaxies.

Detailed cluster studies so far exist only for relatively small redshifts. We are interested in extending these with a sizable sample of objects over a wide mass range into the first half of cosmic time ( $z > 0.8$ ) up to the highest redshifts currently accessible. Cluster studies at these redshifts could directly probe the mass assembly of the largest Dark Matter halos, the thermodynamic and metal enrichment history of the ICM, and the galaxy transformation and evolution processes in the densest environments. Furthermore, the number density evolution of massive galaxy clusters is one of the most promising observational techniques to constrain the properties of the Dark Energy through its influence on the structure growth rate and the evolution of co-moving volume elements. Such a cosmological test requires a precise knowledge on the mass-observable relations at these redshifts, i.e. a calibration of the evolution of the different cluster scaling relations. The study of these relations is of particular importance while preparing for the upcoming next generation all-sky cluster survey with eROSITA.

With the currently available instruments, there are two main routes to identify new high redshift galaxy clusters and groups in X-rays: either deep, designated multi-wavelength surveys over relatively small contiguous fields with an area of a few square degrees on the sky, or serendipitous surveys over larger areas from the XMM-Newton archives with the need for extensive optical and infrared follow-up observations. To securely identify galaxy clusters as gravitationally bound objects and to characterize their physical properties, X-ray observations are crucial. While XMM-Newton with its large effective collecting area has been the leading workhorse for discovering the most distant systems ( $z > 1$ ) over the last few years, detailed follow-up observations with the Chandra observatory have led to important new insights into the structure of some of these young systems.

Whereas galaxy groups and low mass clusters can now be observed up to high redshifts with surveys such as COSMOS (2 deg<sup>2</sup>) or the Subaru-XMM Deep Field (1.3 deg<sup>2</sup>; see Fig. 1), the detection of distant clusters at the high-mass end ( $M > 2 \cdot 10^{14} M_{\text{sun}}$ ), which are very rare, requires much larger survey volumes. Analysing more than 50 square degrees of deep X-ray survey area from the XMM archive, the XMM-Newton Distant Cluster Project (XDCP) has been successful in increasing the number of distant massive systems identified out to  $z \sim 1.5$ .

Currently, 20 clusters have been spectroscopically confirmed with  $z > 0.8$  within the XDCP survey, which constitute the largest available distant cluster sample. With our ongoing spectroscopic confirmation campaign we aim at tripling this number over the next few years. Fig. 2 shows a selection of our confirmed  $z > 1$  systems, which were initially selected as extended X-ray sources (contours). The follow-up observations in optical and near-infrared bands were used to identify cluster galaxies (background images) and optical spectroscopy allowed to determine accurate redshifts, which are indicated in the top right corners (3 redshifts come from other surveys).

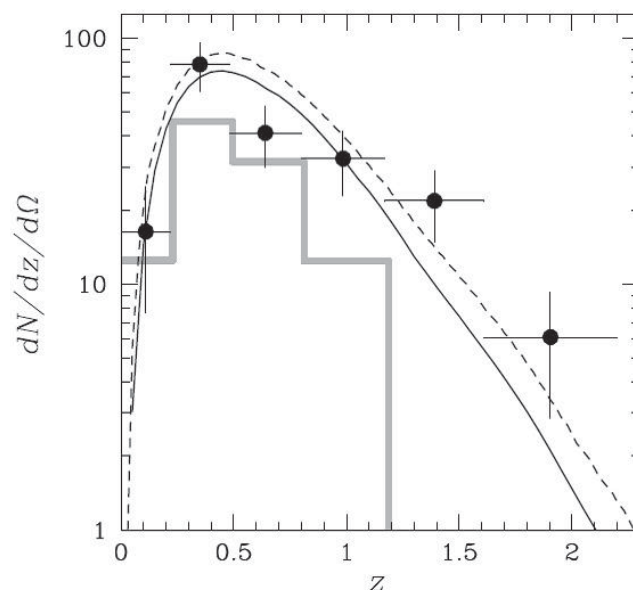


Fig. 1: Observed differential redshift distribution of the 57 identified groups and low-mass clusters in the 1.3 deg<sup>2</sup> Subaru-XMM Deep Field survey. The grey histogram shows spectroscopically confirmed systems, whereas the solid and dashed lines indicate two model predictions in good agreement with the observations.

Many of our newly discovered clusters are very rewarding astrophysical laboratories, which triggered extensive multi-wavelength follow-up campaigns for in-depth studies of their properties. These efforts can be roughly divided into four categories: (i) studies of the ICM structure and the evolution of scaling relations up to the highest accessible redshifts ( $z > 1.3$ ), (ii) detailed investigations of the galaxy populations in distant clusters, (iii) the extension of strong and weak gravitational lensing methods to higher redshifts, (iv) the compilation of the first well-defined sample of massive clusters at  $z > 0.8$  for cosmological studies.

In the following, three XDCP clusters are highlighted as examples of particularly interesting astrophysical studies:

(1) Extensive multi-wavelength studies of the first confirmed cluster in our survey, XMMU J2235-2557 at  $z = 1.39$  (Fig. 2, top centre), revealed remarkable properties for this system. With a robust total mass measurement from X-rays and weak lensing of  $(6-7) \times 10^{14} M_{\text{sun}}$ , XMMU J2235-

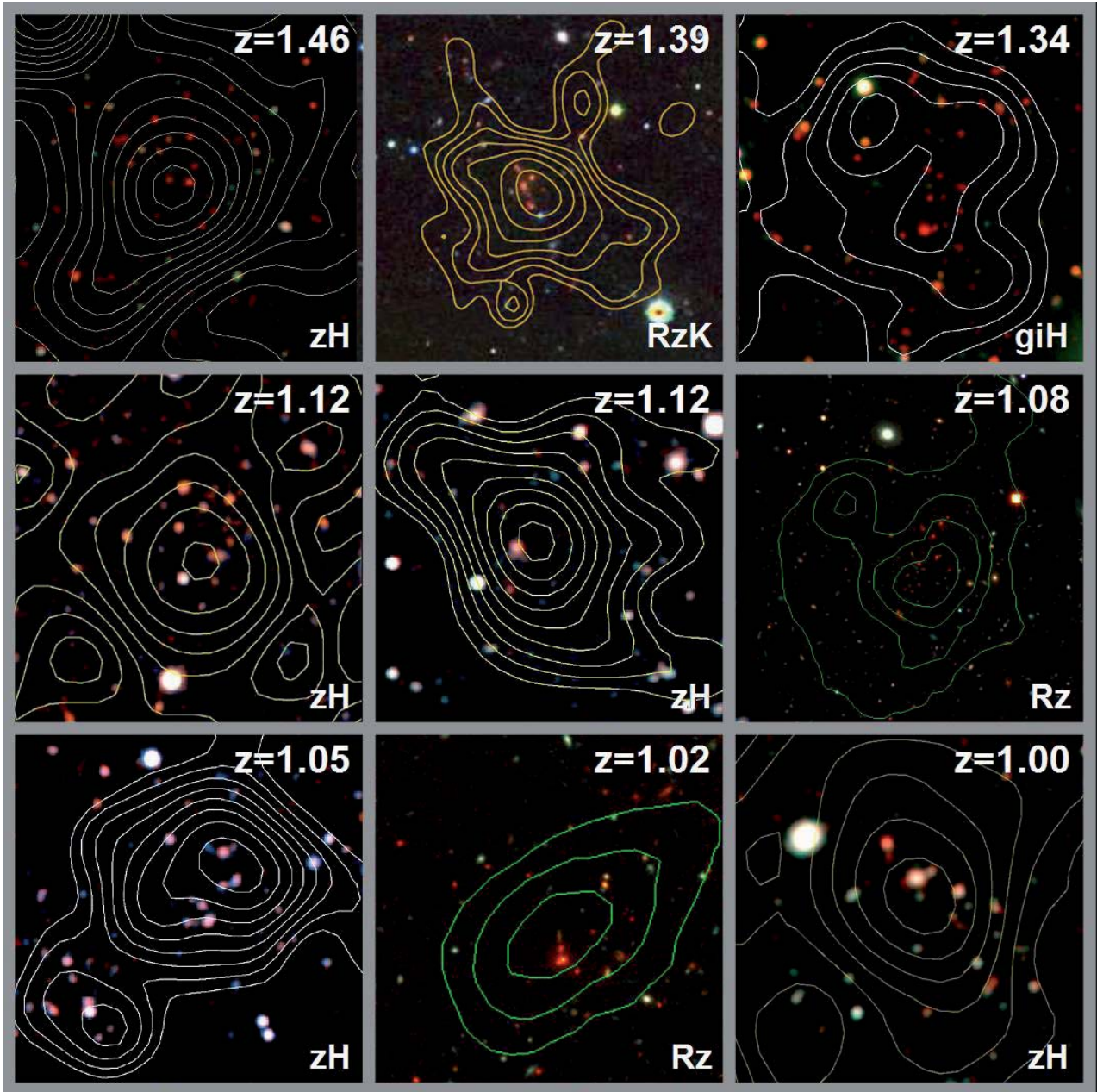
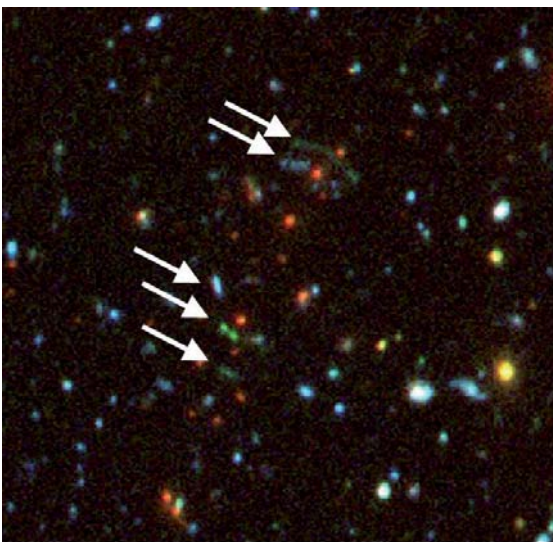


Fig. 2: Selection of spectroscopically confirmed XDCP galaxy clusters at  $z > 1$ . The images have a side length of approximately 1.5 arcmin. X-ray contours are overlaid on multi-band images, with the cluster redshift indicated in the upper right corner and the used optical/near-infrared bands shown in the lower right.



2557 is currently the most massive object known at  $z > 1$ . Within the concordance cosmological model, we expect only one such cluster in more than 1000 square degrees. The ICM of the cluster has a temperature of about 8 keV and already shows indications of significant metal enrichment. The galaxies in the cluster core are very old in terms of their stellar populations and show no signs of ongoing star formation. The brightest cluster galaxy seems to be already similarly developed as its local counterparts.

Fig. 3: True-colour image of the central core region (1 arcmin) of the cluster XMMU J1007+1258 at  $z = 1.08$ . Several distorted background galaxies due to the strong gravitational lensing effect are indicated by white arrows.

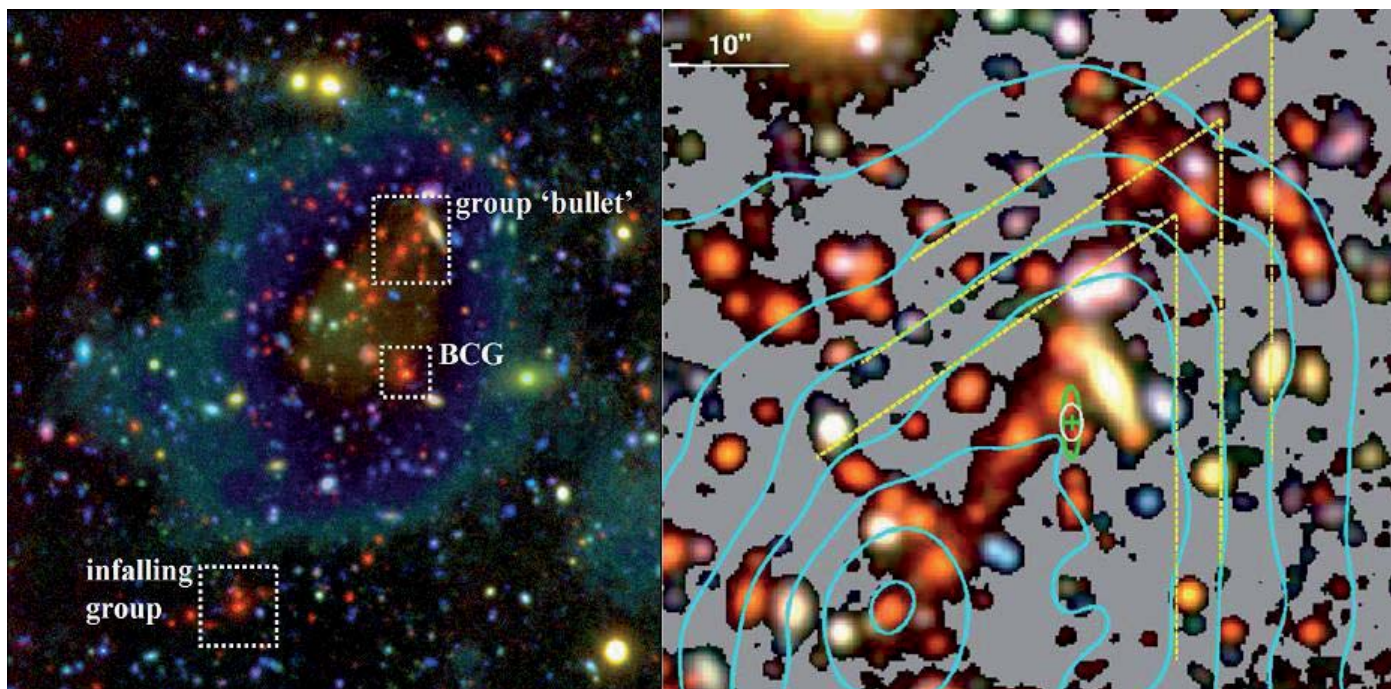


Fig. 4: Multi-wavelength view on the massive galaxy cluster XMMU J1230+1339 at  $z=0.98$ . Left: 3x3 arcmin true-colour image of the cluster overlaid with the semi-transparent X-ray emission of the ICM. Several groups and the brightest cluster galaxy are highlighted. Right: Detailed 1x1 arcmin view of the dynamically active region to the upper right of the cluster centre, where an infalling group ('bullet') passing close to the core has been identified as the cause of the observed conical shape of the X-ray contours (cyan). This passage is also responsible for the tidal stripping features in some of the galaxies. The black background was remapped to a lighter grey in order to enhance low surface brightness features.

(2) The recently discovered cluster XMMU J1007+1258 at  $z=1.08$  (Fig. 2, middle right) is another rare object, as it exhibits various strong gravitational lensing features close to its core as shown in Fig. 3. These arcs and multiple images of background galaxies hold information about the mass distribution of the lensing cluster in its central region and extend the accessible redshift regime for strong lensing studies.

(3) The cluster XMMU J1230+1339 at  $z=0.98$ , displayed in Fig. 4, contains a remarkably rich galaxy population of several hundred members. This system allows the study of astrophysical processes on many different scales, from its connection to large-scale structure filaments, to infalling groups on the cluster outskirts, and to the intense dynamical activity close to the cluster core (Fig. 4, right). Due to the high mass of the system ( $\sim 5 \cdot 10^{14} M_{\text{sun}}$ ), we were able to perform a (ground-based) weak lensing study and to measure a significant Sunyaev-Zeldovich effect signal in order to obtain a full physical characterization of the system.



R. Fassbender, H. Böhringer and A. Finoguenov  
with R. Suhada, G. Pratt, D. Pierini, G. Chon, M. Lerchster, A. Nastasi, M. Mühlegger

## Structure of Galaxy Clusters and Scaling Relations

When using galaxy clusters for cosmological studies, we need to understand the cluster structure and its statistics. This is also important if we want to use galaxy clusters as laboratories to investigate composition of matter in the universe, the evolution of the galaxy population in clusters, the thermal and chemical history of the gaseous intracluster medium (ICM), and the energy release of the central Active Galactic Nuclei (AGN) into the ICM held by the cluster's gravitational potential. Therefore we are conducting a research programme to systematically study the structure of clusters and their ICM with statistically representative samples of galaxy clusters drawn from our ROSAT all-sky survey cluster catalogues and from dedicated deeper X-ray surveys.

Galaxy clusters form when overdense regions of matter in the cosmic large-scale structure collapse due to gravitation. The virial end product of the collapse depends for a given mass to a small extent on the shape of the overdense region and on the density of the Universe when the collapse occurs. As we can expect that statistically similar shapes of overdensities are found at different mass scales, we expect clusters to have a self-similar appear-

To compare different clusters terms of their radial profiles, we make use of the trivial scaling relation that the radius is proportional to the cube root of the cluster mass to bring clusters of different mass on the same radial scale. Using this scaling we can compare the radial temperature and density distribution of the ICM in clusters of different sizes as shown in Fig. 1. For both temperature and density, the profiles show a surprisingly tight agreement, except for the central region. The inner temperature profile is either increasing with radius or approximately flat and the outer profile has a remarkably homogeneous gentle decrease. The density profiles show a similar homogeneous behaviour in the outer parts. The large diversity in the inner region originates from the so-called cool cores in some clusters where the ICM can cool significantly and where we also expect extra energy input from a central AGN.

The vast amount of data produced by surveys with MPE participation (e.g. KIDS, PanSTARRS and HETDEX) will thus enable us to derive further constraints on Dark Matter and Dark Energy, that is one of the biggest mysteries in physics today.

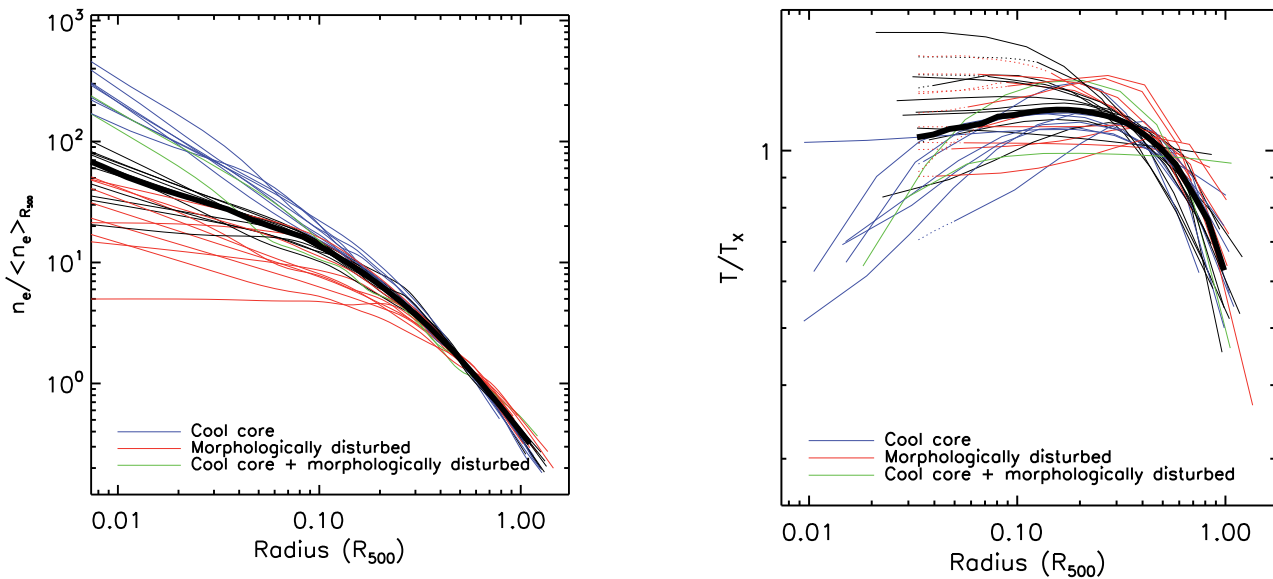


Fig. 1: Density (left) and temperature (right) profiles of 31 REXCESS clusters observed with XMM-Newton. The profiles have been scaled by the fiducial radius  $R_{500}$  (where the mean cluster density is 500 times the critical cosmic density) and by the density at  $R_{500}$  and global temperature, respectively. The profiles show a high degree of self-similarity, particularly in the outer regions.

ance as a function of mass with some scatter around the mean properties. This self-similarity allows us to predict the global cluster parameters (within some scatter) if we know some characteristic observables. The important global cluster properties should therefore be connected by so called scaling relations. For our application the most important scaling relation is that between a few simple observables and the cluster mass.

If we assume that the ICM is in hydrostatic equilibrium in the gravitational potential of the cluster, we can combine the ICM density and temperature profiles to determine the total mass profile of the galaxy cluster. For regular clusters we find a good agreement of the shapes with those predicted from simulations (e.g. Navarro-Frenk-White-profiles). There is also a good correlation between the X-ray luminosity and the estimated cluster mass, and the relation becomes especially tight when the central region is excluded from the luminosity measurements as shown in Fig. 2 for the REXCESS sample.

In a simple scenario of hierarchical structure formation we expect a self-similar picture where the matter density in clusters is independent of cluster mass. However, agreement in the outer ICM density profiles in Fig 1 (left; in the inner parts of the profiles the effect of the central AGN energy output causes to much variations) has only been

far. To determine if this could explain the missing baryon problem, we used detailed information from the COSMOS survey, i.e. optical/NIR observations of galaxies in galaxy groups and clusters, complemented by information from the literature for more massive clusters. Our results on the baryon budget of the groups and clusters are summarized

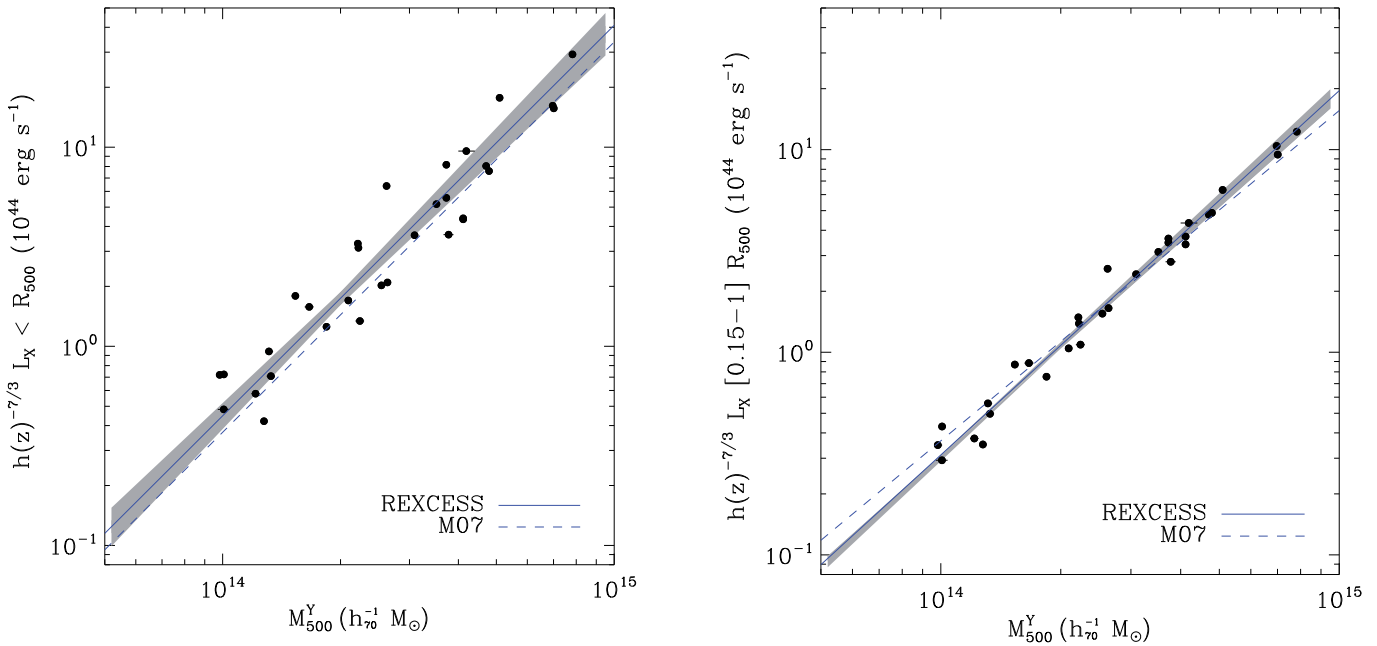


Fig. 2: Scaling relation of X-ray luminosity and cluster mass for the REXCESS cluster sample, for cluster luminosities out to the fiducial radius,  $R_{500}$  (left), and for the same region with centres excluded (right).

achieved by using a particular scaling, which implies a decreasing ICM mass fraction with decreasing cluster mass. If all clusters begin their formation with the same cosmic mass density ratio of dark to baryonic matter, small mass systems seem to lose part of their ICM, most probably to additional heating by galactic winds and energy input from the AGN. Also, more baryonic matter is locked up in stars in the galaxies, which has not been accounted for so

in Fig. 3. While we find a higher fraction of baryons in stars and gas in smaller galaxy systems, this cannot account fully for the baryon deficit in groups and poor clusters. A detailed modelling of the feedback from the central AGN in groups including radio information on AGN activity leads us to the conclusion that AGN feedback is the most likely cause of the baryon deficit in groups.

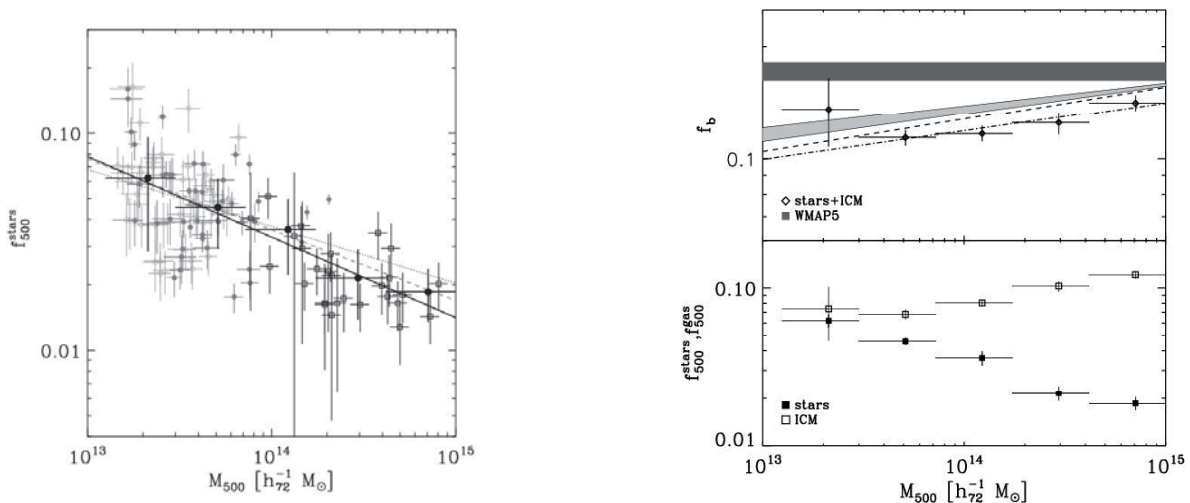


Fig. 3: Stellar mass fraction observed in the COSMOS galaxy groups and clusters as a function of the total mass (left). Mass fraction of baryons found in stars and gas (ICM) in the COSMOS groups and other cluster samples including REXCESS (bottom right) as a function of mass compared to the cosmic baryon mass density fraction (top right). Especially for lower mass systems, there is a significant deficit in the baryonic mass fraction in galaxy systems compared to the cosmic value for which AGN feedback is made responsible.

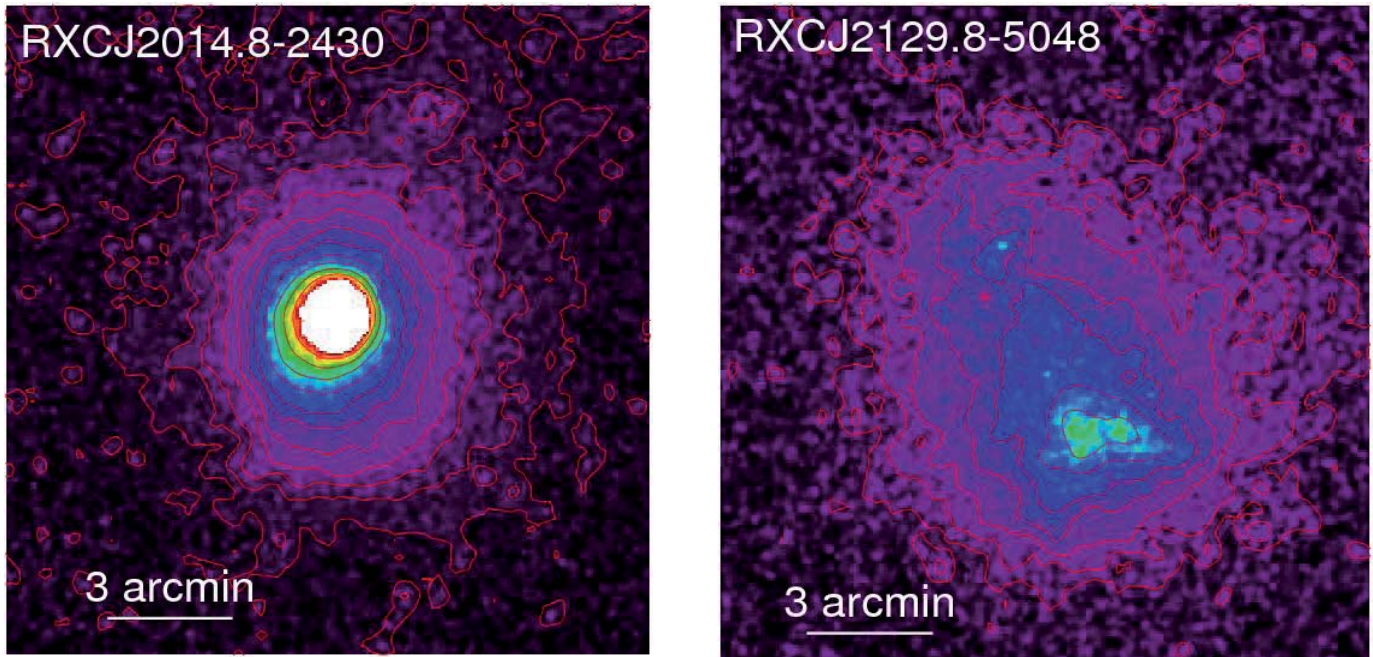


Fig. 4: XMM-Newton images of clusters from the REXCESS sample. On the left, a very regular object with a cool core is shown, on the right, a cluster with obvious substructure and no cool core.

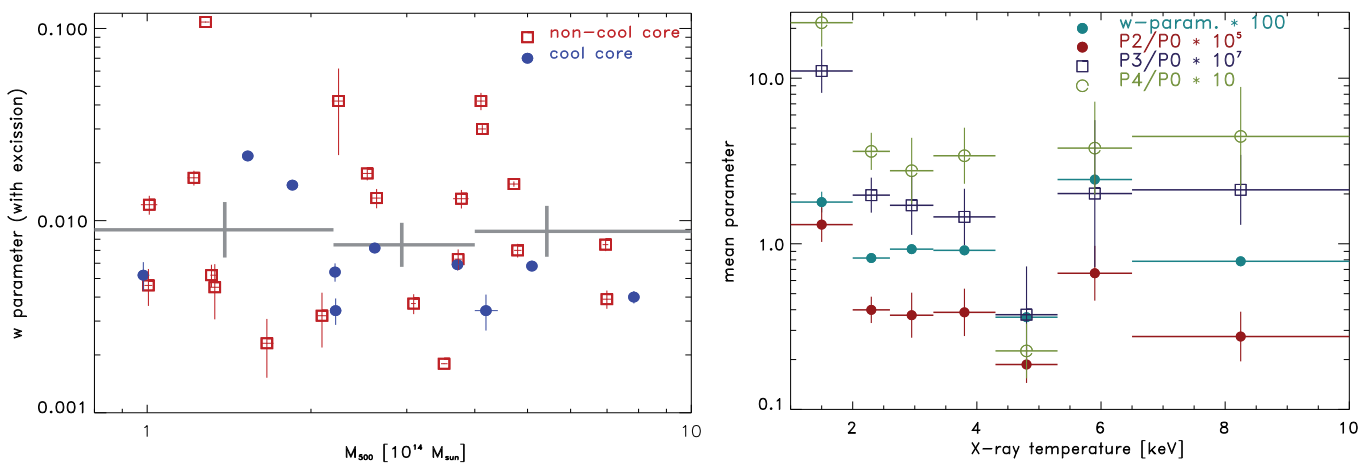


Fig. 5: Isophotal centre shift parameter  $w$  used to characterize substructure in the REXCESS clusters (left) and a similar statistic of other substructure measures (centre shift and power ratios) as a function of cluster mass in simulations (right). Please note that in the right diagram  $w$  is multiplied by 100. No significant trend with cluster mass is observed (excluding the lowest bin in the right panel).

To better understand how various properties in scaling relations depend on the dynamical structure of the galaxy clusters, we characterise the observable substructure in clusters as deviations from azimuthal symmetry in the cluster images. In particular, we use power ratios and isophotal centre shifts of X-ray images to study the importance of substructure in the REXCESS sample. Fig. 4 shows examples of a very relaxed cluster and a cluster with strong features of substructure from our sample. Disturbed clusters, for instance, have on average lower X-ray luminosities than more regular ones. A lack of substructure is well correlated with the occurrence of cool cores, which is expected from the general picture that cool cores need quiet clusters to develop. A surprising and important new result, however, is the fact that the occurrence of substructure seems independent of cluster mass (Fig. 5), as we would have expected more merger signatures

in massive clusters due to the bottom-up structure formation scenario. Comparing the observational results with a simulated set of galaxy clusters we find that the observed clusters are more regular. We traced this back to the fact that the simulations did not yet feature AGN feedback from the central AGN. This means that too many cool cores develop early on, which lead to substructure when the galaxy clusters merge in their later evolution.



H. Böhringer, G. Pratt, S. Giodini

## 2.2 GALAXIES AND GALAXY EVOLUTION

Our understanding of the formation and evolution of galaxies has improved dramatically over the past decade. This is largely due to the multitude of observations carried out at large ground-based telescopes and space-based facilities from the X-ray, ultraviolet, optical, infrared, to radio wavelengths. We now have a robust outline of the global evolution of galaxies since as early as 1 – 2 billion years after the Big Bang right up to the present epoch. However, we have yet to understand how exactly galaxies assembled their mass and evolved with time. The major limitation is our incomplete knowledge of the relevant mechanisms that control the phase, angular momentum, cooling, and dynamics of the baryonic, or ordinary, matter. Scientists at MPE are filling in many gaps in this knowledge through deep galaxy surveys at many wavelengths, through spatially resolved studies of galaxies at both low and high redshift, and through detailed galaxy simulations.

Deep optical and near infrared photometric surveys provide a census of the galaxy population at various redshifts. The rest frame red and infrared colours provide us with a good measure of the total stellar mass of galaxies and allow us to construct galaxy mass functions for different look-back times. These data combined with stellar population synthesis modelling tell us how the galaxy mass function evolved with time. The surprising result is that at redshifts of about one, the more massive galaxies have essentially been in place with the same abundance as at present. It is mostly the low luminosity galaxies that formed late, and these consequently still show active star formation today. We probe the star formation rates and histories with rest-frame optical spectroscopy and using their properties in the mid-infrared to millimetre bands using the Herschel satellite and the IRAM mm-telescopes. Detailed observations provide indications of the galaxies' internal dynamics.

This chapter focuses on six selected highlight results on galaxy formation and evolution, which illustrate the broad scope of observational and theoretical research that has been undertaken at MPE in this important astrophysical field from 2007-2009. The first article presents results from complementary programmes using high resolution imaging spectroscopy in the NIR and in the millimetre, showing in detail how galaxies assemble and form stars from redshifts 1-3. A first glimpse of the power of the Herschel/PACS instrument is given in the second article, which introduces the preliminary results from the Guaranteed Time deep

extragalactic surveys (PACS Evolutionary Probe, PEP). The PEP surveys resolve more than half of the cosmic infrared background into individually well detected sources, and will shed light on the importance of dusty, obscured star formation in the star formation history of the Universe. The high-resolution hydrodynamic simulations described in the third article by the members of the new Theoretical Modelling of Cosmic Structures (TMOX) group at MPE show how cold flows of gas along cosmic filaments is the main mode of galaxy growth at high redshift. Looking from a more "local" perspective, the authors from the MPE OPINAS group provide in the fourth article a comprehensive discussion of the dominant physical processes driving the morphological and mass evolution of galaxies from  $z=1$  to the present day Universe. The fifth section describes how scientists obtain valuable information on the environmental effects on galaxy evolution by studying the kinematics of stars, which make up the intra-cluster light in the cores of several low and intermediate redshift clusters. The chapter closes with a description of how members of the high-energy group study the properties of distant galaxies that host the most energetic phenomena in the Universe: Gamma-ray bursts (GRBs).

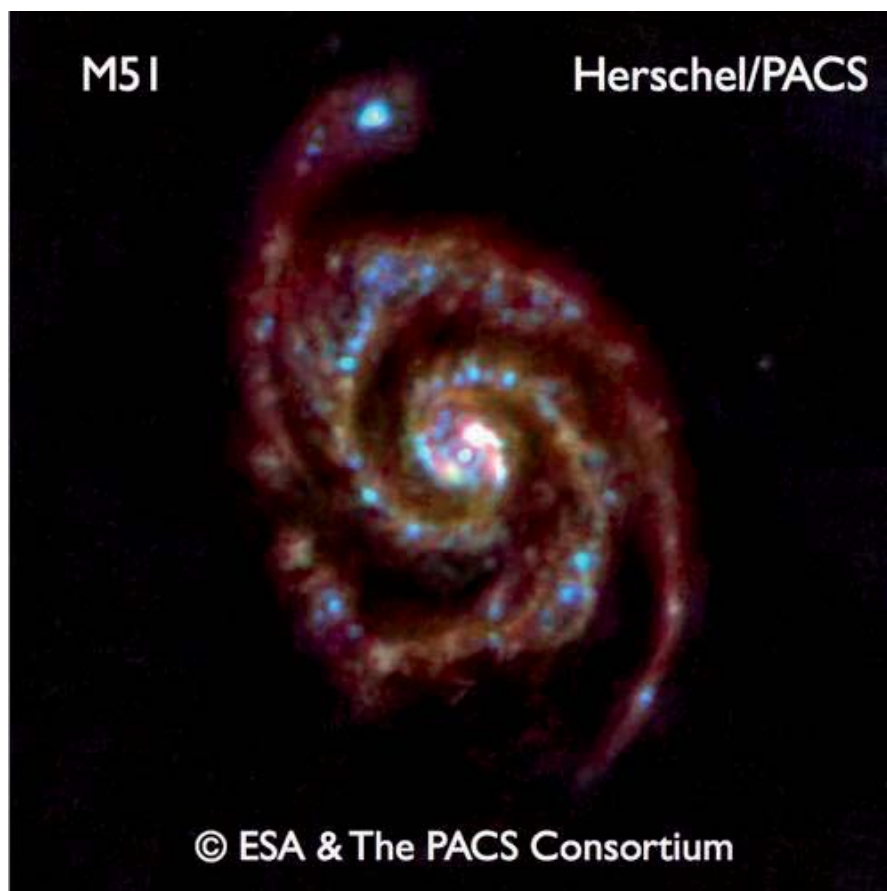


Fig. 1: Far-infrared colour image of the "Whirlpool Galaxy" M51 by Herschel/PACS in three bands. The image shows dust between and around stars, and so provides information on the star formation rate in M51.

## Witnessing the growth of galaxies at early cosmic epochs

We describe the results from two major observational programmes that investigate the physics of galaxy mass assembly at redshifts 1-3. In our VLT SINFONI SINS survey, we investigate the dynamics and evolution in more than 100 redshift $\sim$ 2 star forming galaxies (SFGs). Our IRAM Large Program is a complementary study that embarks on taking the molecular gas census in two samples of SFGs at redshifts 1 and 2.

For some time, the star formation and stellar mass growth of massive galaxies at early cosmic epochs has been widely attributed to violent major mergers. Motivated by a number of recent and quite unexpected observational findings, the picture is now changing towards one, in which smoother yet efficient modes of gas accretion fuelling intense star formation play an important, if not dominant, role at  $z>1$ . Spatially-resolved SINFONI observations from our group have revealed large rotating disks at  $z\sim 2$  with high star formation rates (SFR $\sim 100 M_{\odot}/\text{yr}$ ) but without any sign of ongoing merging. In parallel, multi-wavelength galaxy surveys by Daddi, Elbaz, Noeske and collaborators have shown that the SFR correlates tightly with stellar mass  $M^*$  (with small scatter  $\sim 0.3$  dex in logarithmic units), and that the overall relation of SFR to stellar mass steadily declines from  $z\sim 2.5$  to  $z\sim 0$ . The majority of SFGs thus

appear to be continuously fed by gas that promotes and maintains star formation, rather than occasionally bursting as a result of a (major) merger.

This empirical evidence matches remarkably well the recent state-of-the-art cosmological simulations, which indicate that massive galaxies acquire a large fraction of their baryonic mass via steady, narrow cold flows or streams that penetrate effectively through the shock-heated media of massive dark matter halos. These cold streams of smoothly flowing material, along with clumps that trigger minor merger events, can sustain elevated star formation activity over much longer timescales than major mergers. Under these conditions, the angular momentum is largely preserved as matter is accreted, early (thick) disks can survive and be replenished, and internal dynamical processes can drive the secular evolution of disks and the formation of bulges/spheroids at high redshift. The shift from a “major merger-dominated” to a “cold flow/stream-fed galaxies” picture has been largely supported by key evidence from our SINS survey of high-redshift galaxy dynamics. Our parallel survey of the cold gas in “normal” high-redshift SFGs is now providing further compelling evidence and reveals directly the substantial gas reservoirs replenished by this cold flow accretion and fuelling the intense star formation activity.

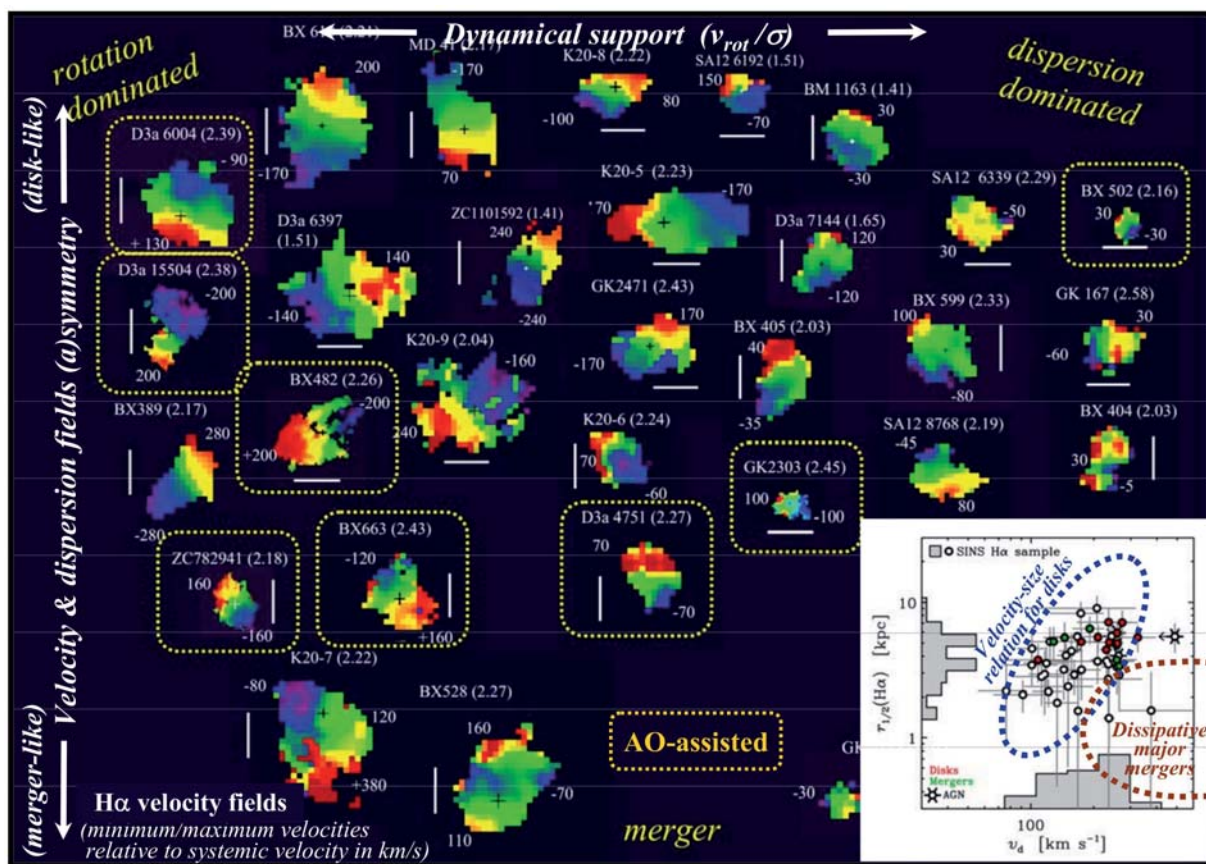


Fig. 1: Overview of the H $\alpha$  velocity fields of 30 of the now more than 100 massive  $z\sim 2$  SFGs observed with SINFONI as part of our SINS survey. The kinematics and velocity-size relation (inset) reveal a significant fraction of rotating disks, which could steadily replenish their gas through smooth “cold flows” and/or rapid series of minor mergers, and subsequently undergo efficient secular evolution leading to the rapid build-up of a central bulge.

## SINS: Dynamics and star formation of 100 massive galaxies at $z \sim 2$

SINS is the first and largest survey with a full two-dimensional mapping of gas (H $\alpha$ ) kinematics and distribution in  $z \sim 2$  SFGs. Carried out with the near-IR integral field spectrograph SINFONI at ESO's VLT, SINS formed a major component of the MPE IR/submm group SINFONI Guaranteed Time Observations, and is continuing through several normal and large follow-up SINFONI programmes. It is further complemented with deep high-resolution near-IR imaging programmes with the HST and the adaptive optics-assisted VLT/NACO camera. SINS has now surveyed the star formation and kinematics of more than 100 galaxies at redshifts from 1.5 to 2.5, covering two orders of magnitude in stellar masses ( $M_* \sim 3 \times 10^9 - 3 \times 10^{11} M_\odot$ ) and a wide range of star formation rates ( $\text{SFR} \sim 10 - 800 M_\odot/\text{yr}$ ). The ionized gas distribution and kinematics are spatially-resolved on scales of 1–2 kpc for the current subset of 20 sources studied with adaptive optics (AO) assisted SINFONI observations, and to typically 4–5 kpc for the seeing-limited data. One of the initial major – and surprising – outcomes of SINS was the significant number of large rotating disks already in place at  $z \sim 2$ . The full sample now confirms this key result. About one third of the galaxies are rotation-dominated yet turbulent disks, one third are more compact dispersion-dominated objects, and one third are clear mergers (see Fig. 1). The data imply comparable current and past-averaged star formation rates, high gas mass fractions of  $\sim 30\%$  and baryonic mass fractions of  $\sim 60\% - 80\%$  within the central  $\sim 10$  kpc of the galaxies. The specific angular momenta of the disks are comparable to those of present-day late-type galaxies, and suggest little loss of angular momentum upon collapse of the baryons from the dark matter halos. These early disks are clearly more turbulent and gas-rich than their present-day counterparts, often showing luminous massive ( $\sim 3 \times 10^7 - 3 \times 10^9 M_\odot$ ), kpc-sized “clumps”.

While major mergers undoubtedly take place at high redshifts, the new findings from SINS reveal that other mechanisms must also play an important role in driving the mass assembly and star formation in early stages of galaxy evolution. The properties of the SINS galaxies suggest their gas reservoirs are constantly replenished, fuelling intense star formation over a substantial part of their stellar lifetimes and  $\sim 10$  dynamical timescales, in agreement with the cold-flow accretion picture. This accretion heats the gas in early disks through the release of gravitational energy without destroying the highly ordered motions. As a result of the large turbulence in the disks, dynamical friction and viscous processes proceed on timescales of less than 1 Gyr – at least an order of magnitude faster than in present-day disks. Early secular evolution drives gas and stars into the central regions and can build exponential disks and massive bulges on short timescales. A characteristic of this evolutionary scenario is the presence of massive self-gravitating clumps from the fragmentation of the turbulent, gas-rich unstable disks that migrate inwards and rapidly coalesce to form a young bulge. Among our SINS disks with deep,

high-resolution H $\alpha$  and continuum data, we find compelling support from both dynamics and morphologies, with central inner bulge/disk components whose mass fraction relative to the total dynamical mass appears to scale with the galaxies' stellar evolutionary stage.

## IRAM/PdBI Large Program: Direct detection of the molecular gas in normal high-redshift SFGs

We need observations of molecular gas in individual galaxies at high redshift to understand how galaxies have turned their gas into stars and how they have evolved as the Universe has aged. A direct assessment of this important component is essential to gauge any galaxy formation model. We are undertaking a first systematic survey of CO emission of a moderately sized sample of “typical” massive star forming galaxies (SFGs) at redshifts larger than one with the IRAM Plateau de Bure Interferometer (PdBI). We focussed our observations on two samples of SFGs spanning similar ranges in stellar mass and star formation rates: one at  $z \sim 1.2$  and the other at  $z \sim 2.3$ . We are measuring the gas properties and dynamics of 15–20 galaxies in each redshift range through CO J=3–2 observations. We are also following up the brightest targets with high spatial resolution to measure the first CO rotation curves of these sources.

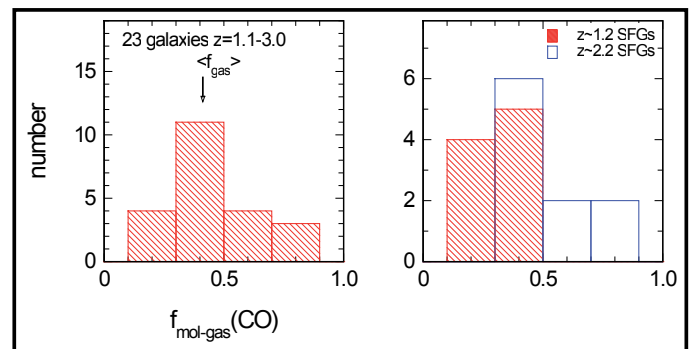
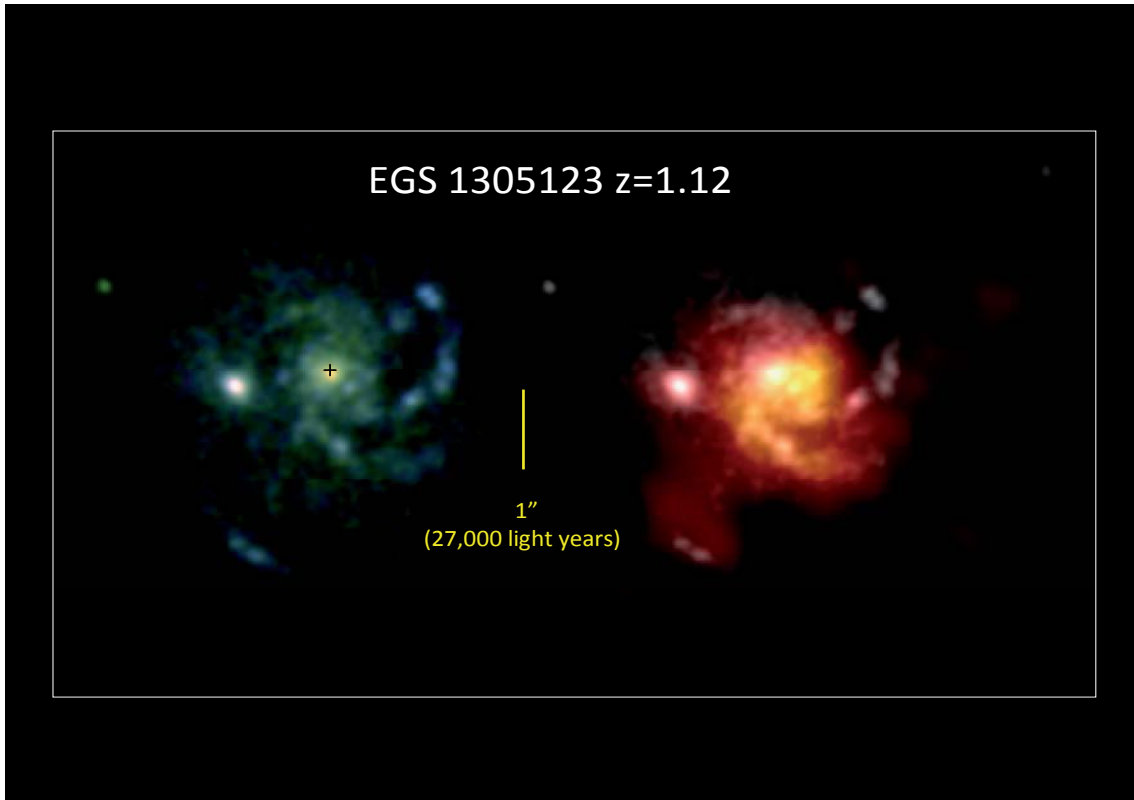


Fig. 2: High gas fractions in normal SFGs. Left: The distribution of molecular gas fractions for 23 SFGs at  $z=1-3$  with good stellar mass estimates from our survey and from the literature. Right: Comparison of the distribution of molecular gas fractions for  $z=1.2$  (red) and  $z=2.2$  (blue) SFGs. We define  $f_{\text{mol-gas}}$  as  $M_{\text{gas}}/M_*+M_{\text{gas}}$ .

Thus far we have detected CO in about 20 out of 25 SFGs. The data reveal that these galaxies are very gas rich, and that the star formation efficiency is not strongly dependent on cosmic epoch. The average fraction of cold gas relative to the total galaxy baryonic mass at  $z=2.3$  and  $z=1.2$  is  $\sim 44\%$  and  $34\%$ , respectively, which is three to ten times higher than in local spiral galaxies (see Fig. 2). A slow decrease from  $z \approx 2$  and  $z \approx 1$  likely requires semi-continuous replenishment of fresh gas to the galaxies. Our survey provides direct empirical evidence for the theoretical scenarios outlined above, showing that high-redshift SFGs are much more gas rich than galaxies at  $z \sim 0$ , which explains many of their observed properties. We highlight one of the cases, EGS1305123 ( $z=1.12$ ), where we obtained spatially resolved maps (see Fig. 3). The data clearly resolve the cold molecular gas distribution in a non-merging high-redshift SFG, enabling a



*Fig. 3: Spatially resolved optical and millimetre images of a typical massive galaxy at redshift  $z=1.12$ , EGS 1305123. Left: A Hubble Space Telescope V- and I-band optical image, taken as part of the AEGIS survey of distant galaxies. Right: An overlay of the CO 3-2 emission observed with the PdBI (FWHM  $0.6'' \times 0.7''$ ; red/yellow colours) superposed on the HST image (grey). These observations clearly show that the molecular line emission and the optical light from massive stars trace a massive, rotating disk with a diameter of  $\sim 60,000$  light years. This disk is similar in size and structure as seen in  $z \sim 0$  disk galaxies, such as the Milky Way. However, the mass of cold gas is in this disk about an order of magnitude larger than in typical  $z \sim 0$  disk galaxies. This explains why high-redshift galaxies can form continuously at about ten times the rate of typical  $z \sim 0$  galaxies.*

detailed investigation of the cold gas kinematics. In the optical images EGS 1305123 is a nearly face-on (inclination  $\sim 27^\circ$ ), large ( $R_{1/2} \sim 9$  kpc) spiral disk with a number of large star forming clusters. The clumpy CO emission extends over the entire galaxy disk but is somewhat more concentrated ( $R(\text{CO}) \sim 6$  kpc) than the rest-frame B-band stellar distribution, with a strong concentration of gas near the nucleus and innermost spiral arms.

Our observations are a first major step towards a more complete mapping of the gas supply as a function of cosmic epoch, galaxy mass and environment. Extensive observations of larger samples and of the more common, lower mass galaxies should soon become possible with further upgrades of the present millimetre facilities and, in particular, with the Atacama Large Millimetre Array (ALMA) in the Chilean Andes.



N. Förster Schreiber and L. Tacconi

## Herschel uncovers dusty high-redshift star formation

In our PACS Evolutionary Probe (PEP) project we use the sensitivity and spatial resolution of Herschel, the largest infrared space observatory launched to date, for deep far-infrared surveys of galaxy evolution in a number of well characterized cosmological multi-wavelength fields. Already the first Science Demonstration observations of the GOODS-N field resolve more than half of the cosmic infrared background into individually well detected sources, and provide unique measurements of star formation rates and spectral energy distributions of high-redshift galaxy populations.

Already during the design and development of our 60-200 $\mu\text{m}$  far-infrared camera/spectrometer PACS for ESA's Herschel space observatory it was obvious that one of the most promising scientific applications of this instrument would be deep cosmological far-infrared surveys, which would provide a missing key component of multi-wavelength studies of galaxy evolution. For that reason, the MPE infrared group has invested the major part of its guaranteed Herschel observing time into such a programme, in collaboration with other PACS consortium institutes in France, Italy, Spain and the Herschel Science Centre. We probe four different tiers in a "wedding cake" survey scheme: from the wide (2 square degrees) COSMOS field, which is observed close to the 160 $\mu\text{m}$  confusion limit, through medium depth areas, such as the Lockman Hole and Groth Strip, all the way down to the 100 $\mu\text{m}$  confusion limit in the pencil-beam, very deep observations in the GOODS-S field – and even beyond by exploiting lensing in some nearby galaxy clusters.

After checkout and instrument calibration, our programme started during the Science Demonstration period in October 2009 with 30h observations of the GOODS-N field and 13h of the lensing cluster Abell 2218. This was followed by an exciting and feverish period of rapid data analysis, leading to the first science results in late November. Since then, increasingly larger parts of our observing programme are being executed and analysed, step by step completing the different fields scheduled for PEP.

With the favourable diffraction limit of the large Herschel mirror, blending of sources is much less of a limitation than with previous smaller infrared space telescopes. For the first time, this permits to resolve a large fraction of the cosmic far-infrared background (CIB) peak into individually well detected galaxies, that can be identified and studied in detail. The GOODS-N data with  $3\sigma$  limits of about 3mJy at 100 $\mu\text{m}$  and 5.7mJy at 160 $\mu\text{m}$  already resolve ~45% and 52% of the CIB respectively. This will improve with deeper observations that are already taken in GOODS-S and with analysis of the cluster data with additional amplification by gravitational lensing.

All PEP fields benefit from an extensive multi-wavelength coverage: our PACS sources can be identified with galaxies of already quite well known properties. Hence we can now split the CIB into the contribution of different classes of galaxies, different time intervals in the history of the universe, and so on. From the science demonstration data and their identification with GOODS-N galaxies, most of the 100 $\mu\text{m}$  and 160 $\mu\text{m}$  CIB arises at redshift  $z < 1$ , with red sources peaking at higher redshift than blue ones. Luminous IR galaxies ( $10^{11} \leq L < 10^{12} L_{\odot}$ , LIRGs) provide 80-90% of the CIB resolved at  $0.5 < z < 1.0$ , while ultra-luminous ones ( $L \geq 10^{12} L_{\odot}$ , ULIRGs) dominate at higher redshift (60-70% at  $1.0 < z < 2.0$  and 100% above).

Much of the energy radiated by the newly formed stars in a galaxy is absorbed by dust and re-radiated at far-infrared wavelengths. The far-infrared is thus an important wavelength range for a "calorimetric" determination of the energy output by young stars and therefore one of the key properties of a galaxy: its star formation rate. Before the advent of Herschel, sensitivity limits severely limited the application of this diagnostic to high redshift galaxies, and astronomers were typically forced to use an extrapolation from the mid-infrared, making the assumption that the spectral energy distributions of galaxies of given luminosity are the same locally and at high redshift. With Herschel we can finally replace this extrapolation by true, direct far-infrared measurements.

Massive optically/near-infrared selected galaxies at redshifts around 2 are at the focus of many current studies of galaxy evolution, including our near-in-

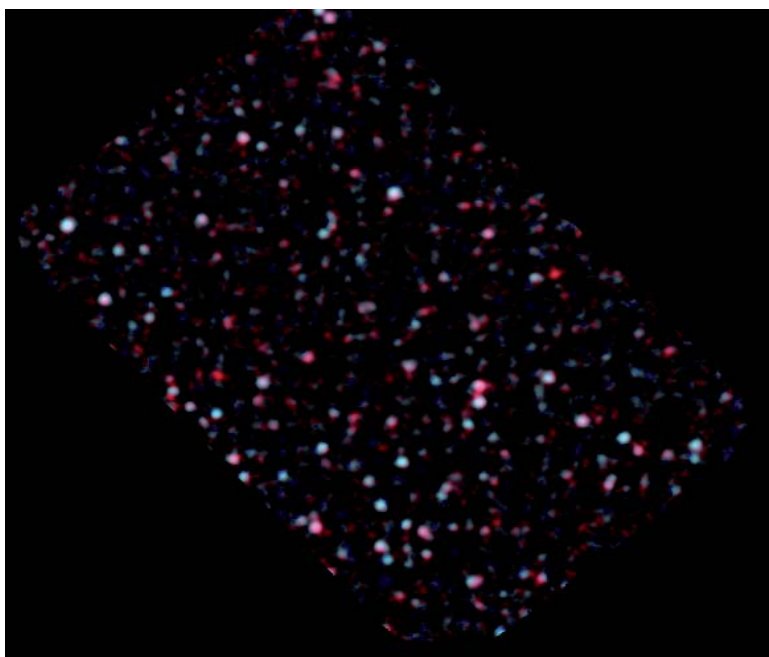


Fig. 1: Combined Herschel-PACS images of the GOODS-N field in the constellation of Ursa Major at far-infrared wavelengths of 100 and 160 $\mu\text{m}$ . Galaxies at high redshift (i.e. larger cosmological distance) or with colder dust are displayed in red, while nearby galaxies appear in blue.

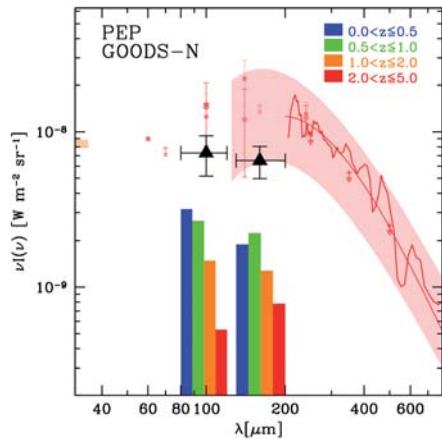


Fig. 2: In the 1990s, observations with NASA's COBE spacecraft detected the cosmic infrared background (pink), which carries a similar amount of energy as the total optical/near-infrared light of distant galaxies. Already the first deep Herschel observations resolve roughly half of this background into individually well detected sources (total energy output indicated by black triangles). It is now possible to study their properties and determine, for example, the contribution of different redshift ranges to the cosmic infrared background.

ers. Again, extrapolation from the mid-infrared was somewhat uncertain while our far-infrared results agree well with previous extrapolations from the radio that assumed applicability of the radio-far infrared correlation. PEP is assembling a complete view of the spectral energy distributions of these (ultra)luminous infrared galaxies, and allowing careful determinations of their dust temperatures. These are both key steps towards a true FIR luminosity selection and for a detailed understanding of the selection effects in pre-Herschel methods to locate high-redshift, IR-luminous galaxies. For example, we find evidence of strong dust temperature differences between submillimeter galaxies and optically faint radio galaxies.

The updated star formation measures have implications for the next level of studies, for example concerning the influence that the environment of a galaxy has on the star formation activity. Our Herschel-based results support a reversal of the star formation-density relation from local to  $z \sim 1$  galaxies, which has already been suggested on the basis of Spitzer mid-infrared data. They also provide evidence for a  $z \sim 1$  specific star formation rate-density relation that was elusive from the mid-infrared data.

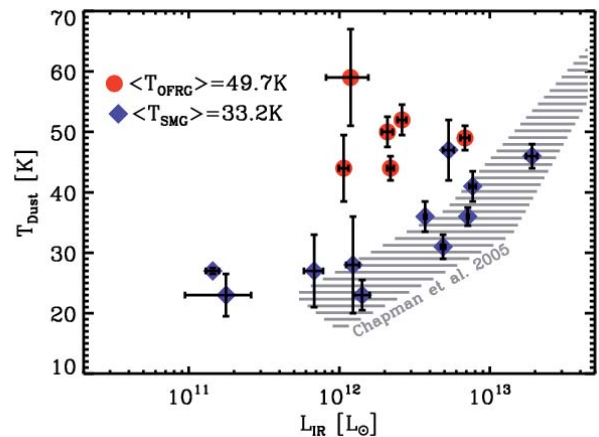
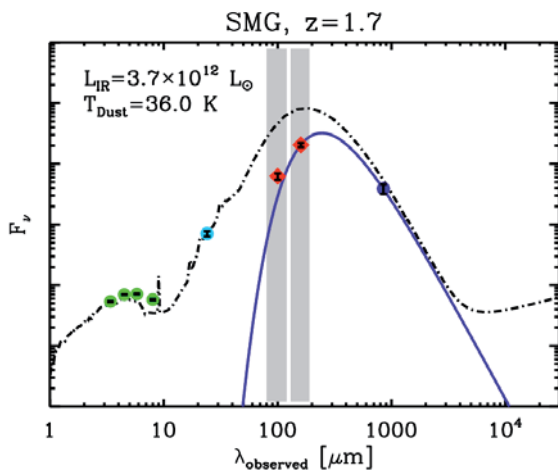


Fig. 3: For high redshift galaxies such as submm galaxies (SMGs), we sample with our PACS-detections the peak of the spectral energy distribution (left). This is essential to determine the total luminosities and star formation rates of the galaxies and to measure the dust temperatures, which are indicating conditions in their interstellar medium. While previous extrapolations based on the radio-far-infrared correlation are supported for the SMGs, extrapolation from the short wavelength side can be off as in the example shown here. On the way to an unbiased "calorimetric" measure of the far-infrared emission of high-redshift galaxies, we see a picture emerging with respect to the selection effects induced by previous methods to obtain populations such as SMGs or optically faint radio galaxies (OFRGs), as can be seen in the right panel.

frared based SINS programme highlighted in the previous article. For these galaxies, we find the true far-infrared fluxes to be lower than the ones extrapolated from the mid-infrared using standard SED templates (by Chary & Elbaz), requiring a downward revision of their star formation rates by a factor of about 4. These new lower star formation rates fit well into the picture of secular evolution, possibly driven by cold inflows from the cosmic web that has emerged for these objects from our SINS dynamical studies.

On the other hand, the Herschel data support huge  $\sim 1000 M_{\odot} \text{yr}^{-1}$  star formation rates for submillimeter galaxies, which can likely be reached only via violent galaxy merg-



S. Berta and D. Lutz  
with B. Magnelli, R. Nordon, P. Popesso, A. Saintonge  
and L. Shao

## Cold accretion driven galaxy formation in the high-redshift Universe

High-resolution hydrodynamic simulations of galaxy formation in a cosmological context reveal that the main mode of galaxy growth at high redshifts is by cold flows of gas along cosmic filaments. While this is a feature clearly seen in simulations (see Fig. 1), observational confirmation of cold streams of gas feeding galaxies remains elusive. However, the wealth of recent observational data on galaxy properties at  $z \geq 2$  allows detailed comparisons to the output from simulations and models as well as an in-depth analysis with respect to the effects that cold flows have on them. To this end the Theoretical Modelling of Cosmic Structures group (TMOX) at MPE is undertaking simulation projects and modelling efforts.

Hydrodynamical effects, such as Kelvin-Helmholtz instabilities, present during the accretion of cold flows onto galaxies need careful numerical treatment as well as high spatial and mass resolution. This, in effect, limits self-consistent simulations of galaxies within a cosmological context to one individual object. The semi-analytic modelling (SAM) technique is a useful tool to overcome such limitations and to analyse and model the global properties of large statistical samples of galaxies, based on simplified recipes for the baryonic processes involved. Traditionally cold flows were implemented based on the cooling time of hot gas within a Dark Matter halo. This approach, however, neglects cold flows that penetrate through diffuse hot halo gas, in particular at high redshifts. We have successfully implemented a prescription of such cold accretion into a SAM and compared the results in detail to fully numerical hydro simulations to show that the accretion rates match each other.

The infall velocities of cold accretion flows are generally several times the sound speed in the surrounding gaseous medium, which means that the flows reach the galaxy in about one halo dynamical time once they enter the virial radius. At impact onto the interstellar medium (ISM) of the central galaxy, the kinetic energy of the accretion flow is converted via several possible mechanisms. In part, it will be radiated away in shocks or contribute to the rotation of a gaseous disk in the host galaxy. Another important way to deposit the accretion energy is by driving turbulence within the ISM.

Recent observations conducted as part of the SINS survey show that gas velocity dispersions in  $z \sim 2$  galaxies are a few times larger than in local disk galaxies. Lensed galaxies at even higher redshift confirm this trend. Several different possibilities as to the origin of these high velocity dispersions have been suggested, of which we investigate the conversion of accretion energy into turbulence. Using the modified SAM and adopting an equilibrium between the change in energy

due to accretion, the dissipation in the ISM, and the contributions from supernovae, we are able to estimate the fraction of accretion energy needed to drive turbulence at the level observed in high-redshift galaxies. Approximately 20% of the accretion energy is sufficient to recover the trend seen in the observations (see Fig. 2). This agrees well with the fraction of dense clumps in cold flows seen in hydro simulations. These clumps are able to survive the impact and “stir up” the ISM, driving turbulence.

Interestingly, a constant conversion efficiency of accretion energy to turbulence is able to recover the overall trend of the importance of turbulence with respect to ordered rotational motion as a function of the latter. Our results are the first to recover this trend over a wide range of mass scales within a self-consistent cosmological background, which is a direct consequence of the importance of cold accretion flows as a function of host dark halo mass. Low mass Dark Matter halos show only cold accretion, while gas in massive halos is primarily in the hot gaseous component that does not contribute to the cold accretion flows feeding the galaxy.

Within the standard structure formation paradigm cold accretion flows of several  $100 M_{\odot} \text{ yr}^{-1}$  dominate the accretion rates of gas onto galaxies at high redshifts, and thus the fuel for star formation. For a Schmidt-Kennicutt star formation law with constant efficiency, predictions are that the star formation rate is proportional to the gas accretion rates. At early times these are approximately equal to the growth rates of the Dark Matter host times the universal baryon fraction, since most of the baryons are not yet shock heated to high temperatures or locked up in stars.

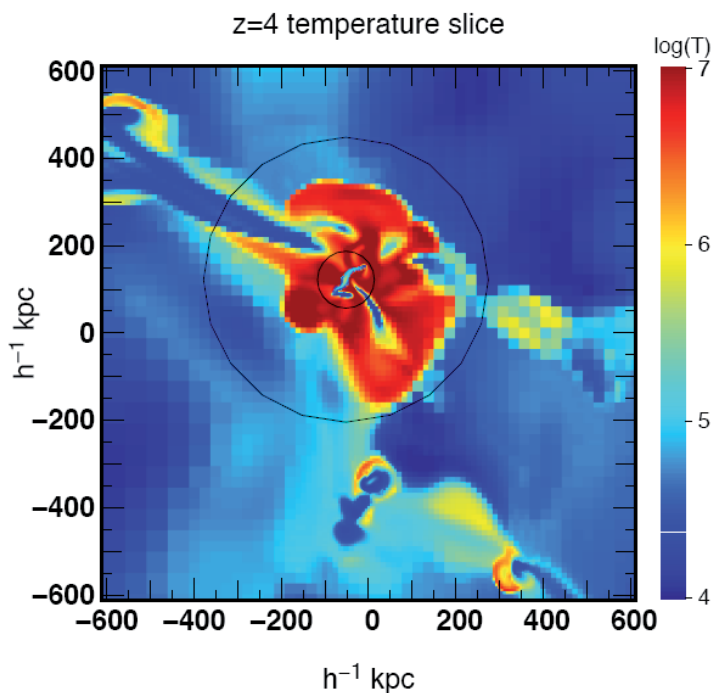


Fig. 1: Cold accretion flow in a cosmological simulation.

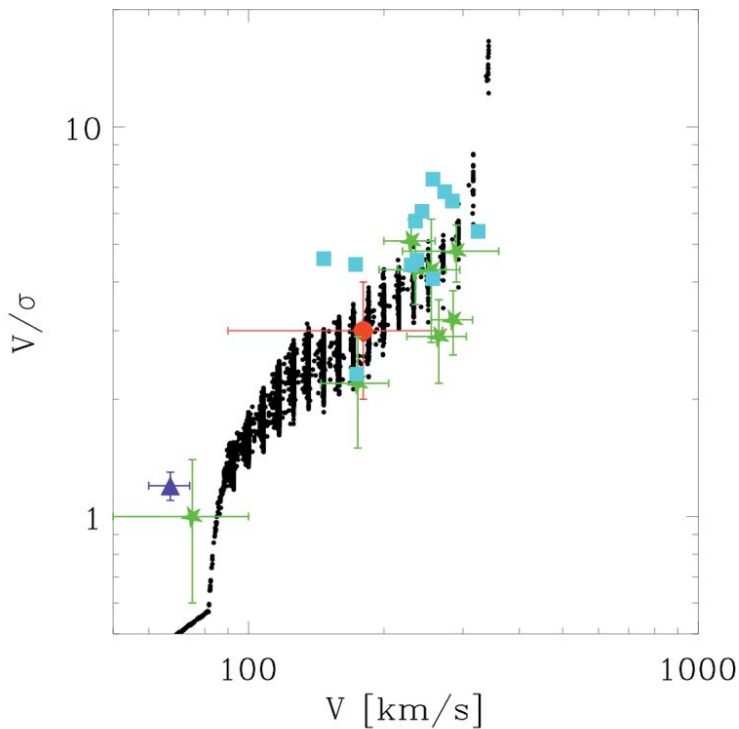


Fig. 2: Ratio of ordered motion to velocity dispersion as a function of maximum rotational velocity in the SAM simulation (black dots) and various observations (coloured symbols).

Within our SAM we are able to recover the high-redshift galaxy mass function, and such features as the steeper faint-end slope of the luminosity function as a function of redshift. A detailed investigation of the galaxy mass function in our SAM reveals that galaxies at high redshifts live in halos that are less massive than their same mass counterparts at low redshifts. This is mainly due to the short timescale over which halos grow at high redshifts. In general we find that Dark Matter halos in our N-body simulations grow on the order of their dynamical time at a given redshift. As dynamical times become shorter in the high-redshift universe accretion rates become larger and so do star formation rates. Our results suggest a possible observational estimate of cold accretion rates and a test of this early phase of galaxy formation: accurate measurements of the luminosity function at high redshift are able to provide a good statistical match between galaxies and their host halo masses. In addition, star formation rates can be used as a proxy for the cold accretion rates onto these halos.

In an attempt to investigate the effect of other physical processes such as supernovae feedback or star formation prescriptions we have been analysing a large suite of  $\sim 50$  fully cosmological N-body+SPH (smoothed-particle hydrodynamics) simulations that include variations in their models governing the unresolved sub-grid physics. This set of simulations is unique as it provides the first systematic study of this kind. The simulations show that in general the same mode of cold accretion flows is the dominant source of fuel for star formation at high redshifts. In addition, the resolved gas kinematics in the simulations

show velocity dispersions in very good agreement with the observed ones at  $z=2$ , independent of the sub-grid model. This supports the notion that the observed high velocity dispersions are not dominated by energy injections from sources such as supernova explosions, but are regulated mostly by gravitational processes converting potential energy into turbulence.

The first generation of stars in the Universe are formed from gas with a metallicity close to the primordial value. The cold accretion flows in our simulations are mainly primordial in their chemical composition making them ideal agents for continued Population III star formation. We find that the ISM at early epochs is mostly enriched by the ejecta from stars that do not escape the galaxy. While the early onset of star formation is governed by cold flows, the enrichment in the star formation regions within the simulation is quickly dominated by the first generation of stars. Generally one generation of stars is sufficient to boost the metallicity in star forming regions to switch to Population II star formation. Subsequent continued inflow of primordial gas by cold flows is able to dilute the overall average metallicity of the ISM, but not significantly enough within the dense star forming regions, which are fed from gas that cools down efficiently via metal lines. Thus missing observational signatures of Population III stars in galaxies is no proof for missing cold flows.



S. Khochfar

## Morphological and Mass Evolution of Galaxies

In our galaxy studies, we find that a fraction of S0 galaxies in groups is similar to that in rich clusters but significantly enhanced with respect to the lower density field. Bright elliptical galaxies exist preferentially in group cores, but with a similar global abundance in all environments. This implies that ellipticals form early in regions of frequent mergers (i.e. halo cores) and lenticulars form later through accumulated minor mergers, which results in the observed environmental distribution, while disks are retained as the bulge grows. Using the COSMOS data, we also investigate the stellar mass function of galaxies to unprecedented depth, reaching  $\sim 1.5$  orders of magnitude lower masses than before. We find that the faint end slope of both blue and red galaxies steepens significantly. We also find that single Schechter functions do not adequately describe the mass function of either blue or red galaxies. The blue galaxy mass function shows a bump that is associated with the assembly history of Dark Matter halos and is most likely linked to the distinction between central and satellite galaxies.

The formation and evolution of galaxies appear to follow a remarkably homogeneous path. Despite a wide variety of merger histories for galaxies and their haloes and the complexity of the hydro-dynamical physics driving the baryonic evolution of galaxies, the resultant populations nonetheless obey tight and well defined scaling laws, such as the fundamental plane and the Tully-Fisher relation. To understand the dominant physical processes driving galaxy evolution it is useful to isolate distinct populations (such as passive or satellite galaxies), and try to reconstruct the events or processes that shape their properties. In this article we describe two applications of this concept: the first section describes the division of galaxies by morphology, focussing on the environment to assess how and where late-type galaxies are transformed into early-types; the second section describes the stellar mass function of galaxies which, owing to the survey depth and subsequent low mass limit, requires a bimodal fit of bright and faint galaxies for both passive and star-forming populations up to  $z \sim 1$ . In both cases we discuss physical processes that might explain these distinct populations and their evolution.

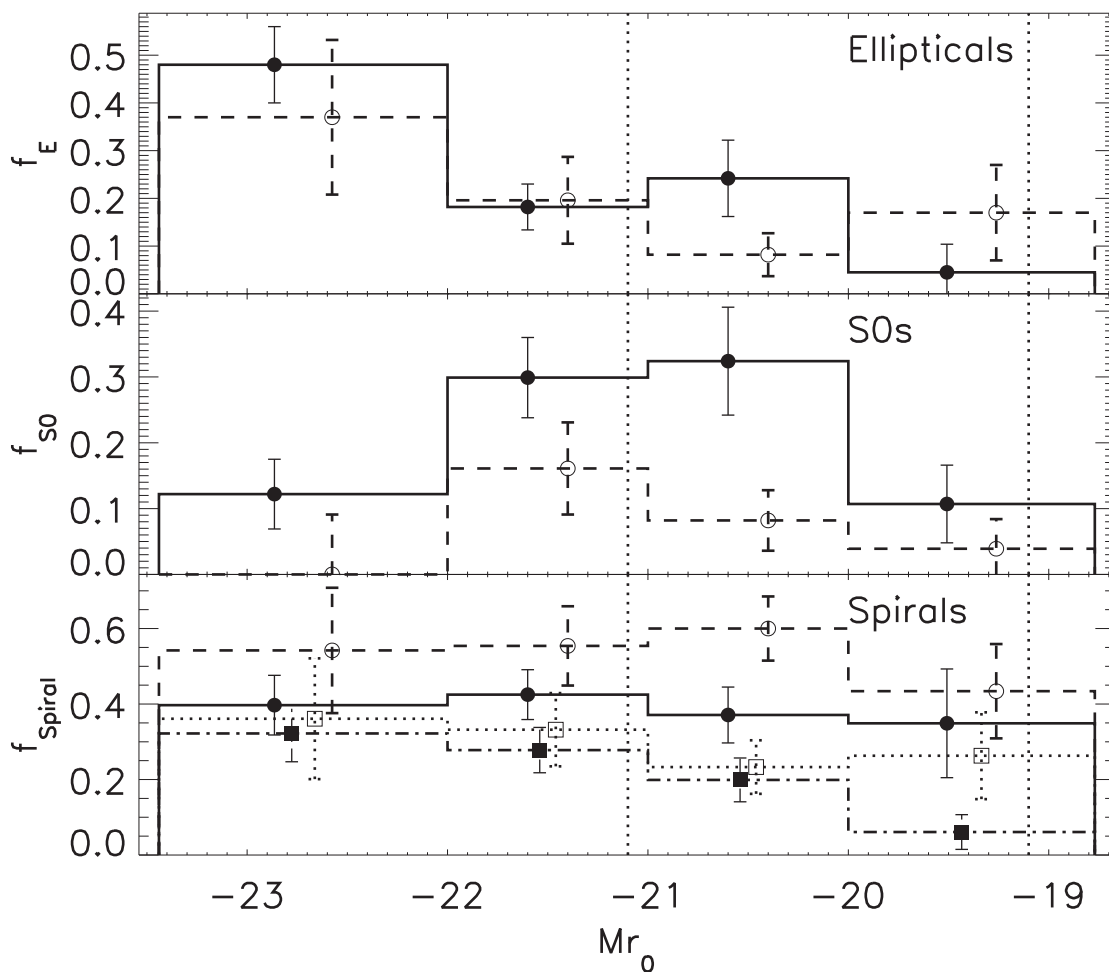


Fig. 1: The morphological composition of group (solid lines and circles) and field (dashed lines and empty circles) galaxies with  $0.3 < z < 0.55$  as a function of rest-frame  $r$ -band luminosity. The sample is complete to  $M = -21.1$  at  $z = 0.55$  and  $M = -19.1$  at  $z = 0.3$  (vertical dotted lines). The fraction of early type spirals (eSp, Sa-Sbc) is also indicated (squares and dotted/dash-dotted lines). Errors on fractions are computed using the Jackknife method and points are offset in luminosity for clarity.

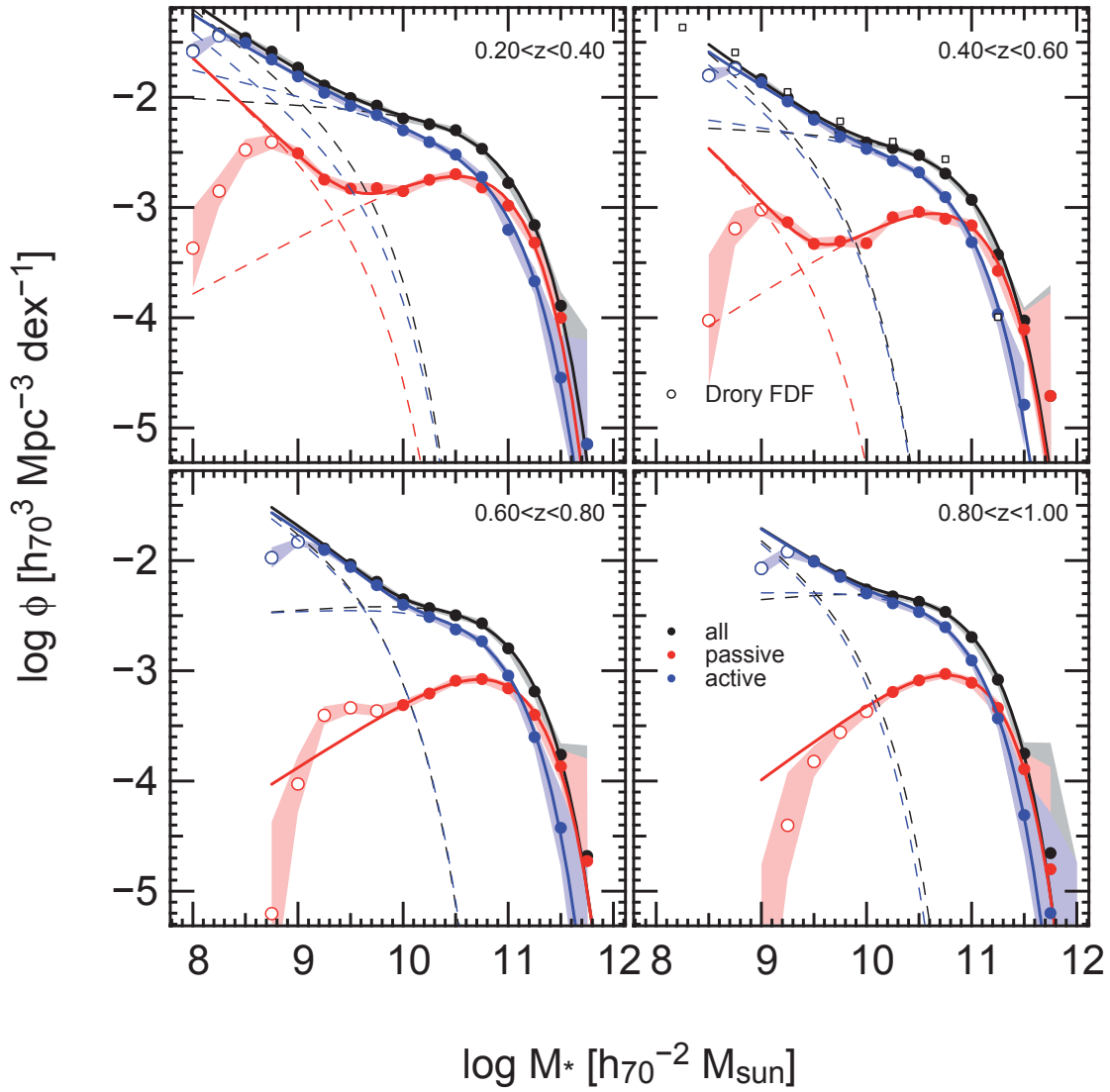


Fig. 2: The stellar mass function of galaxies in four redshift bins in the interval  $0.2 < z < 1.0$ . The mass function of passive galaxies is marked in red, that of star-forming galaxies in blue, and that of all galaxies in black. Data points below the mass completeness limits are denoted by coloured open symbols. The uncertainty in the mass function due to Poissonian errors in the counts as well as the uncertainty propagated through photometric redshifts is shown as shaded regions. Data from the FORS Deep Field are shown as small black open squares at  $z=0.5$  for comparison. The solid lines show double Schechter function fits to the data. The thin dashed lines show the individual bright and faint components of the double Schechter functions.

The decline in the volume-averaged star formation rate of the Universe since  $z \sim 1$  by at least an order of magnitude can be partially related to the increasing fraction of (particularly high mass) galaxies for which gas accretion has declined to almost zero and for which cold gas supplies are exhausted. We examine changes in the galaxy structure (morphology) and the environment in which such passively evolving galaxies are found – as a function of redshift and galaxy mass or luminosity – to find clues to the relevant physical processes.

Since  $z \sim 0.5$  the fraction of disk galaxies lacking spiral arms (lenticular/S0 galaxies) in massive galaxy clusters has increased by a factor  $\sim 5$  relative to the elliptical or total fraction. However cluster galaxies only account for  $\sim 5$ –10% of the global budget, and may have experienced pre-processing prior to their accretion onto the cluster. Indeed, the fraction of star forming galaxies is a strong function of local density both inside and outside of clusters and the morphology-3D density relation is ubiquitous at  $z \sim 0$ .

To examine how galaxy morphologies are mapped onto lower mass haloes at higher redshift, we obtained HST-ACS F775W-band imaging of 26 spectroscopically selected groups at  $0.3 < z < 0.55$ . We visually classified 179 group galaxies and 111 serendipitous field galaxies in the same redshift range, and obtained consistent results for two independent classifiers. A field galaxy is defined as one outside any spectroscopically identified group. While in the absence of complete spectroscopy this does not mean isolated, field galaxies do on average belong to lower mass haloes.

The fraction of elliptical, S0 and spiral galaxies in group and field environments are computed in bins of r-band luminosity (see Fig. 1). Although the overall elliptical fraction in groups is much higher than in the field, it is immediately apparent that there is no significant difference at fixed luminosity. However, the bright ( $M_r < -21$ ) ellipticals are almost twice as common in the inner  $0.3 h_{75}^{-1}$  Mpc of groups than at larger radii. Random re-sampling of the (luminos-

ity-matched) population demonstrates this excess in the group cores is statistically highly significant (confidence >99.999%). Ellipticals are more likely to be formed in the centre of their halo, consistent with expectations: satellite galaxies migrate inwards via dynamical friction and merge with the central galaxy to form a bright elliptical.

The situation is very different for S0 galaxies. The fraction in groups is significantly higher than in the field (confidence >99.999% from luminosity-matched re-sampling), indicating that the environment plays a role in their formation. However, we find with 97% confidence a lower fraction in the inner  $0.3h_{75}^{-1}$  Mpc of groups than at larger radii. Also the S0 fraction integrated down to  $M_V=-21.5$  is comparable to that in  $z\sim 0.4$  clusters found by Fasano and collaborators, and to the one in X-ray selected groups. These results all suggest that the process of gas exhaustion in spirals does not require a particularly high density environment, occurring in low mass group outskirts or progenitor halos (sub-groups/pairs). This seems to rule out a leading role for direct interactions between galaxies and the intra-group medium which should be enhanced in group and cluster cores.

The lower fraction of field S0s is made up for by spirals – however, there is little environmental dependence in the fraction of Sa-Sbc spirals (squares in Fig. 1). The difference is mainly made up by later type spirals (Sc+). The process of turning a Sc+ galaxy or even an intermediate earlier type spiral into an S0 requires significant structural evolution. Bulge growth due to intense star formation is unlikely to provide a solution, since we observe similar numbers of  $24\mu\text{m}$ -bright galaxies in our group and field samples. Therefore the best solution might be a realignment of stellar orbits via minor mergers in small group and subgroup halos with the low gas fractions in the local Universe, inhibiting the retention of cold gas disks during any merger as proposed by Hopkins and collaborators.

More than half of the galaxies in local spectroscopic surveys are assigned to groups. Therefore, understanding the physical mechanisms underlying these trends is vital to our understanding of galaxy evolution and the global decline of star formation in the Universe.

The general view is that galaxy formation and evolution is driven primarily by two processes: the successive merging of their parent dark matter halos, which causes the accretion of material and ultimately mergers between galaxies; and the feedback-regulated conversion of gas into stars within galactic disks with a potential rearrangement of the disk material by dynamical processes (secular evolution). Both processes contribute to the growth of stellar mass in galaxies with time. The stellar mass function of galaxies and its evolution with time is therefore fundamental to the understanding of galaxy formation.

We present a new analysis of stellar mass functions in the COSMOS field at  $z\leq 1$  to fainter limits than have previously been probed. The increase in dynamic range reveals fea-

tures in the shape of the stellar mass function that deviate from a single Schechter function. Neither the total nor the red (passive) or blue (star-forming) galaxy stellar mass functions can be well fit with a single Schechter function once the mass completeness limit of the sample probes below  $\sim 3\times 10^9 M_\odot$ . We observe a dip or plateau at masses of  $\sim 10^{10} M_\odot$  (just below the traditional  $M^*$ ) and an upturn towards a steep faint-end slope (of  $\alpha\sim -1.7$ ) at lower mass at all redshifts below  $z=1$ . This bimodal nature of the mass function is not solely a result of the blue/red dichotomy. Indeed, the blue galaxy mass function is by itself bimodal at  $z\sim 1$ . This suggests a new dichotomy in galaxy formation that predates the appearance of the red sequence or the transformation of blue galaxies into red ones.

We propose two interpretations for this bimodal distribution. If the gas fraction increases towards lower mass, galaxies with a baryonic mass (stars+gas) of  $M_{\text{baryon}}\sim 10^{10} M_\odot$  would shift to lower stellar masses, creating the observed dip. This would indicate a change in star formation efficiency, which could perhaps be linked to supernovae feedback becoming much more efficient below  $\sim 10^{10} M_\odot$ . Therefore, we investigate whether the dip is present in the baryonic mass function and find that with current observations of the average gas fraction as a function of stellar mass the dip is lessened, but not filled in. Another mechanism seems necessary.

Alternatively, the dip could be created by an enhancement of the galaxy assembly rate at  $\sim 10^{11} M_\odot$ , a phenomenon that naturally arises if the baryon fraction peaks at halo masses of  $M_{\text{halo}}\sim 10^{12} M_\odot$ . In this scenario, galaxies occupying the bump around  $M^*$  would be identified as central galaxies, and the second, fainter component of the mass function (having a steep faint-end slope) as satellite galaxies.

The low-mass end of the blue and total mass functions exhibit a steeper slope than has been detected in previous work and may approach the halo mass function value of  $-2$ . While the dip is apparent in the total mass function at all redshifts, it appears to shift from the blue to the red population, which is likely a result of transforming high-mass blue galaxies into red ones. At the same time, we detect a drastic upturn in the number of low-mass red galaxies. Their increase with time seems to reflect a decrease in the number of blue systems, so we tentatively associate them with satellite dwarf (spheroidal) galaxies that have undergone quenching due to environmental processes.



D. Wilman and N. Drory

## Intracluster Light and Galaxy Disruption in Clusters

Diffuse intra-cluster light (ICL) has been observed in nearby and intermediate redshift clusters and is becoming an important probe of galaxy evolution. The ICL probes on the order of 10% of the total stellar mass in the cluster, but in the cores of some dense and rich clusters such as Coma, the local ICL fraction can be as high as 50%. Most of the ICL is believed to come from stars that are tidally dissolved from galaxies. Much of this happens at low surface brightness so that observational studies of these processes have been difficult. With planetary nebulae as tracers, we have been able to study the kinematics of the diffuse light in the cores of several nearby clusters. These data show that merger and disruption processes are ubiquitous in transforming galaxies in cluster cores.

A vivid illustration of the diffuse light in galaxy halos and the intracluster space is shown in Fig. 1. Whereas on typical sky images the large Virgo galaxies M87, M86 and M84 appear well-separated, in this deep image they are of the size of the full moon and appear to touch or even overlap. In addition, a multitude of small-scale structures and streamers is visible as well as a faint diffuse component between the galaxies. Virgo is a young, unrelaxed galaxy cluster, and so the fraction of ICL in the cluster is still small. By contrast, in the much richer, denser, and more dynamically evolved Coma cluster a much larger fraction of light is seen as diffuse ICL: Fig. 2 shows the elongated diffuse light contours from the photographic work of Thuan & Kormendy.

To understand the dynamical processes in these environments requires kinematic data. Integrated light absorption line spectroscopy is very difficult if not impossible for these old stellar populations with low surface brightness. The only tracers that currently allow us to measure the motions of the diffuse stellar component are planetary nebulae (PNe). These dying stars emit  $\sim 10\%$  of their luminosity in a single emission line,  $[\text{OIII}]\lambda 5007\text{\AA}$ , which can be used both to detect the PN and to measure its redshift. Unfortunately, the PN phase of a dying star is brief, and so PNe are rare: only about one is seen for every few  $10^8$  stars. In the Coma cluster at 100 Mpc distance, PNe are also exceedingly faint. On an 8m telescope, at this distance the flux from the brightest PNe corresponds to only  $\sim 2$  photons reaching the detector per minute. We therefore developed a special multi-slit, blind search technique to find these faint sources and at the same time measure their velocities.

In the core of the Virgo cluster, we obtained spectra of a few dozen PNe in the outermost halo of M87 and in the region between M87 and M86. Combining the distribution of the star velocities with a dynamical model, we could show that the halo of M87 is truncated at a radius of  $\sim 40$  arcmin ( $\sim 150$  kpc); further out no PNe are found at or around the systemic velocity of M87. At larger radii, between M87 and M86, the velocity distribution is very irregular, with a fraction of stars belonging kinematically to M86. The two

galaxies may thus be falling towards each other and we could be observing them just before their first close pass. The new data support the view that the core of the low-density Virgo cluster is not yet virialized, and that the main action is still to come.

The situation is much different in the richest and most compact nearby cluster, the Coma cluster. With our multi-slit imaging technique we were able to measure the line-of-sight velocities of 37 intracluster PNe in the Bernstein field (the red circle in Fig. 2), about 150 kpc south of the main cD galaxy NGC 4874. Surprisingly, the main component of the line-of-sight velocity distribution is  $\sim 700$  km/s off this galaxy's radial velocity and thus cannot be bound to NGC 4874. Rather, it is close to the radial velocity of the other giant elliptical galaxy, NGC 4889. More recent work has shown that this "inversion" of velocities is typical for on-going mergers between giant elliptical galaxies. During the interaction with each other and with the Dark Matter core of the cluster, they leave a broad fan of low-density halo material on their orbits. The elongated distribution of the ICL in Fig. 2 comes from stars, which in this interaction were stripped from the halos of the two cD galaxies and from the cores of the two merging sub-clusters around them.

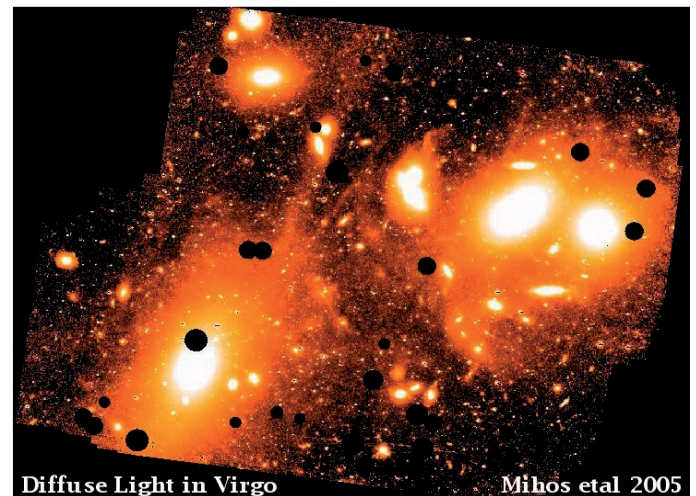


Fig. 1: Deep image of the core of the Virgo cluster, obtained with the Case-Western Schmidt telescope by C. Mihos and colleagues.

From new long-slit data we were also able to show that the stellar population of the outer halo of NGC 4889 (at a radius of  $\sim 60$  kpc) has sub-solar metallicity and a near-solar abundance ratio, i.e. an extended star formation history. This is in contrast to the inner half of the galaxy, whose chemical structure is consistent with a rapid dissipative merger collapse at early times. The outer halo of NGC 4889 may have been accreted later in the form of smaller galaxies. Now this light is stripped again from the galaxy and incorporated into the ICL.

Our third target cluster, Hydra I, is known (from the X-ray morphology) as a quiescent and dynamically relaxed galaxy cluster. Yet our recent work on the line-of-sight velocity distribution of the PNe corresponding to the ICL in the central 100 kpc around the giant bright cluster galaxy NGC 3311 has shown a multi-peaked structure. Two of the peaks apparently correspond to diffuse light of star that were stripped from small groups of galaxies falling through the cluster centre. A closer look at the photometry shows an excess of light in the halo of NGC 3311, amounting to  $\sim 3 \times 10^9 L_{\odot}$ , as well as a number of small galaxies (see Fig. 3). A deep spectrum shows that the excess is at a relative velocity of 1000 km/s with respect to NGC 3311, just like the half dozen small galaxies on top of it. The same spectrum covers one of these galaxies and shows that this is a former dwarf or spiral galaxy that must be in the final stages of dissolution: it now has a luminosity of only  $\sim 10^8 L_{\odot}$  but an effective radius of  $\sim 3$  kpc. At such a large relative velocity, the light from the disrupted galaxies will not be bound to NGC 3311, but will spread out in the inner cluster as ICL.

The remarkable conclusion from this work is that none of these clusters is quiescent when looked at in detail and at low surface brightness. Signatures of merging and disruption are common, and as predicted by simulations, much of the light from the disrupted galaxies contributes to the build-up of the ICL. The simulations also predict that a major fraction of the ICL comes from the halos of giant galaxies which later merge with the central cD galaxy, but beyond cluster radii of 250 kpc stripping processes on other galaxies dominate. The halos of the giant ellipticals are predicted to build up by accretion of smaller objects in their earlier group environments. In the final interactions in the cluster potential, evidently much of this earlier accretion is undone. The galaxy population in clusters must have gone through a lot of transformation since they formed, not only in terms of their stellar populations, but also in terms of their structure and even stellar mass function.



O. Gerhard

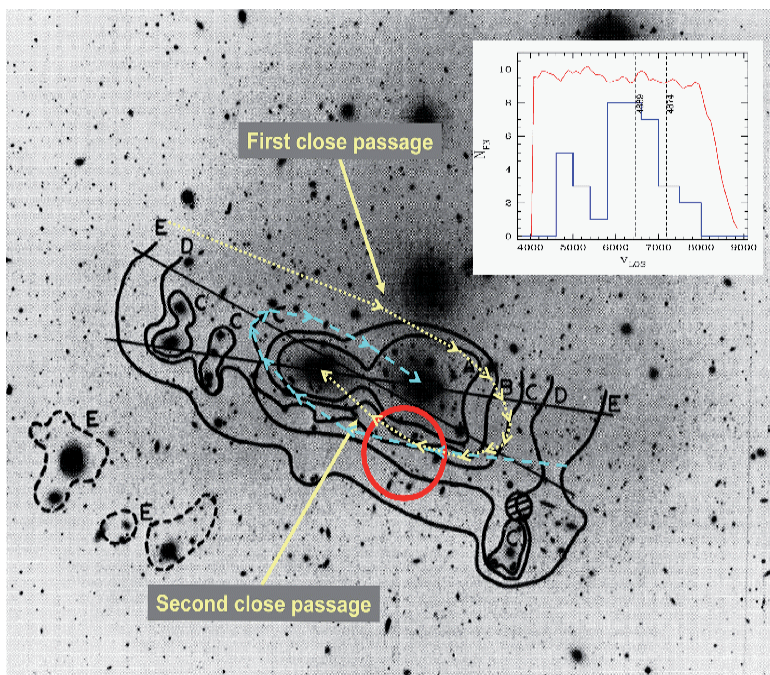


Fig. 2: Image of the core of the Coma cluster with the isodensity contours of the diffuse ICL drawn in black. The Bernstein field highlighted in red is located 5' south of NGC 4874, the second giant elliptical galaxy NGC 4889 is 7' east (to the left). The bright object north of NGC 4874 is a star. From their line-of-sight velocity distribution (inset), most of the stars in the Bernstein field are not bound to NGC 4874, but are trailing NGC 4889 after having been tidally dissolved from its halo by the on-going interaction with NGC 4874. The likely orbits of NGC 4889 and NGC 4874 up to their present positions are sketched in yellow and blue.

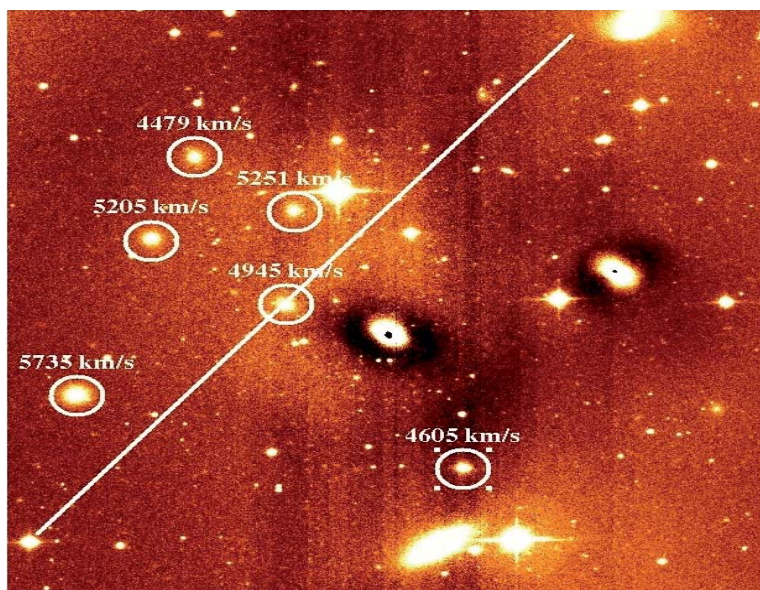


Fig. 3: Photometric excess in the Hydra cluster core after subtracting a model of the bright cluster galaxy NGC 3311 and the background galaxy NGC 3309. Circled in white are several small galaxies on top of the cluster. Also shown is the slit used to measure the mean velocity of the excess and of one of the galaxies.

## Gamma-Ray Burst Host Galaxies and the Cosmic Chemical Evolution

Gamma-Ray Bursts (GRBs) are the most energetic explosions in the universe, associated with supernovae, neutron stars, and black holes. Even though they are among the most investigated astronomical objects of the last two decades, there are still major controversies about their origin. Today the scientific community recognises their importance also as cosmological probes and invests in dedicated projects and telescopes, both on the ground and in space.

GRB events are so luminous that they can shine through the most remote and highly obscured corners of galaxies, both nearby and in the distant universe. These regions are normally hard to reach even with the most sophisticated instruments. Thanks to new technologies and the bright GRB emission, it has been possible to explore many diverse and hidden phenomena. Today there are more than 200 GRBs with known redshift. The most distant one, GRB 090423 at  $z=8.2$ , is also the most distant astronomical object with confirmed spectroscopic redshift ever discovered (see Fig. 1).

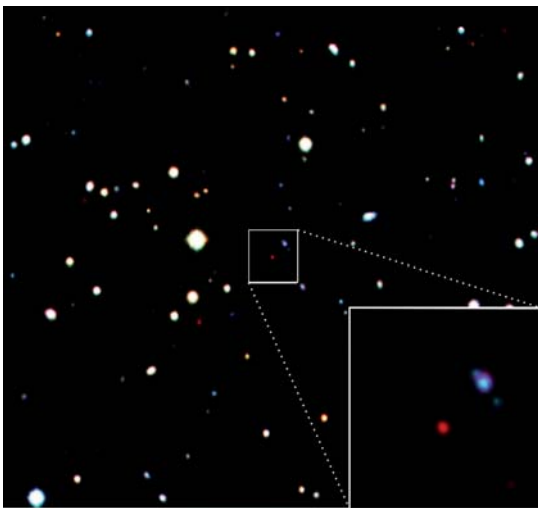


Fig. 1: The red object in this image taken with GROND is a the GRB 090423 at  $z=8.2$ , the most distant astronomical object ever discovered.

Studying GRB host galaxies can help to elucidate how galaxies formed and evolved from a few hundred million years after the Big Bang to today. Small galaxies are particularly important, because they are likely the most common type of galaxy in the universe, especially in the past (since galaxies become larger with time and not smaller). Even with the largest observational facilities faint galaxies are hard to find, because they require very long integration times to detect them and measure their redshift. GRBs are detected with gamma-ray instruments regardless of the host galaxy brightness. The detection and redshifts of their faint hosts come almost for free from observations of the generally bright X-ray and optical afterglow. Although it is often thought that GRB hosts are peculiar galaxies, it has also been suggested that they represent the total galaxy population.

With the growing optical and infrared data obtained after gamma-ray detections, our group has created a public database that collects observational results on galaxies hosting GRB events. The goal of the GRB Host Studies (or GHostS) is to unveil whether these galaxies are different from the general galaxy population, and to determine whether we can use them to understand galaxy formation under extreme conditions. The galaxy parameters investigated with GHostS are the chemical enrichment (metallicity), the star formation rate, the stellar mass, the age of the stellar component and the dust properties. GHostS includes information on 78 GRB hosts, almost 40% of all GRBs with known redshift. Since going public in 2006, GHostS has been used by astronomers for a total of 10 refereed papers.

In our complete investigation of 44 GRB hosts, many of which are at  $z < 2$ , we found that the stellar mass is generally low. The mean stellar mass is similar to the stellar mass of the Large Magellanic Cloud ( $M \approx 10^{9.3} M_{\odot}$ ), with a large dispersion of 0.8 dex. Observational limitations prevent us to fully explore this parameter at larger distances. The star formation rate in GRB hosts is generally high, with a median value of  $2.5 M_{\odot} \text{ yr}^{-1}$ . We found that half of the GRB host galaxies even have high enough star formation rates to be classified as starburst galaxies (see Fig. 2). Starburst galaxies are easily found in the nearby universe because they are small and very bright. Their masses are tens of times lower than the mass of the Milky Way, but their star formation rate is several times higher. The fact that most GRB hosts are forming stars makes us think that to produce a GRB star formation is a more stringent requirement than low metallicity, as traditionally thought.

This idea is supported by the large dispersion of metallicities found in GRB host galaxies over a large redshift interval (see Fig. 3). At  $z < 1$ , we derive the metallicities of the ionized gas using emission lines from the galaxy integrated light. Measurements in 18 GRB hosts are on average 1/6 of the solar value. At  $z > 2$ , absorption lines detected in GRB afterglow spectra that are associated with the damped Lyman- $\alpha$  system – DLA – in the host give metallicities for the cold interstellar medium. The mean metallicity in 18 GRB-DLAs is about 1/10 of the solar value.

If we consider the total sample with  $0 < z < 6.3$ , not only is there no evidence of an evolution with time in a huge redshift interval, but we also find a high dispersion with a factor of about six. This large dispersion indicates that the galaxy population hosting GRBs at high redshifts is different from the one at low redshifts. It might also support the idea that the metallicity of the host galaxy is not the physical quantity triggering the GRB event, as often proposed.

Most popular theories explaining the physics of the majority of GRB events (long-duration GRBs) predict that the GRB progenitor is a supermassive star with nearly primordial chemical enrichment. In this respect, we find

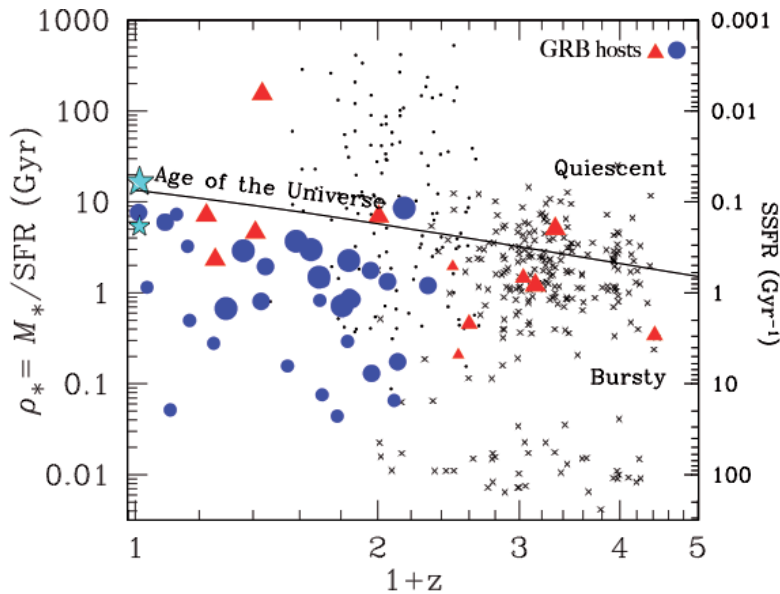


Fig. 2: Growth timescale  $\rho^* = M^*/SFR$  (left y-axis) or its inverse, the specific star-formation rate  $SSFR = SFR/M^*$  (right y-axis) as a function of redshift. Filled circles and triangles are GRB hosts with SFRs measured from emission lines and UV luminosities, respectively. Small, medium, and large symbols are hosts with  $M^* \leq 10^{9.0} M_\odot$ ,  $10^{9.0} M^* < M^* \leq 10^{9.7} M_\odot$ , and  $M^* > 10^{9.7} M_\odot$ , respectively. The curve shows the age of the universe as a function of redshift, and indicates the transition from bursty to quiescent mode for galaxies. Dots and crosses show the comparison with field galaxies at  $0.5 < z < 1.7$  and Lyman break galaxies at  $1.3 < z < 3$ , respectively. The big and small stars at zero redshift represent the growth timescale for the Milky Way and the Large Magellanic Cloud, respectively.

the two extreme values derived in the afterglow spectra of GRB 090323 (at  $z=3.57$ ) and GRB 090926 (at  $z=2.11$ ) remarkable (see also Fig. 3). The former has two close-pair DLA systems (with a velocity separation of about 660

km/s) with more than solar metallicity ( $\log(Z/Z_\odot) = +0.35$  and  $+0.75$ ). These are the highest metallicities ever found in galaxies at high redshift. The DLA in the other, GRB 090926, on the other hand has a metallicity of less than 1/100 of the solar value, one of the lowest metallicities ever measured at  $z > 2$ . We have shown that GRB host galaxies are fundamental probes of the cosmic chemical evolution. The main goal now is to increase the relatively small sample.

Among other new interesting discoveries made with GRBs, we report strong absorption of the afterglow light, which is due to the presence of dust in the interstellar medium of some host galaxies. The UV bump has only recently been detected in several GRB hosts – a feature observed in the past mainly in local galaxies such as the Milky Way and the Large Magellanic Cloud. Observations from MPE's multi-band optical-near-infrared imager GROND led to the first detection in GRB 070802 at  $z=2.45$ .

GRBs are extremely useful for understanding the primordial universe. Satellites and ground-based telescopes have discovered and spectroscopically confirmed seven GRBs at redshifts  $z > 5$ , and three at redshift  $z > 6$ , including the record-holder GRB 090423 at  $z=8.26$ . That corresponds to 3.5% and 1.5% of the total GRB population with a measured spectroscopic redshift, respectively. Probably the numbers would be higher if we were able to observe all GRB afterglows early on. For comparison, the fraction of quasars at  $z > 5$  and  $z > 6$  is 0.05% and 0.01%, respectively. In a total population of 105 quasars, only eight have a redshift larger than 6. All recent striking results of GRBs have demonstrated that these extremely energetic sources open a new view on the primordial universe at  $z > 8$ .



S. Savaglio

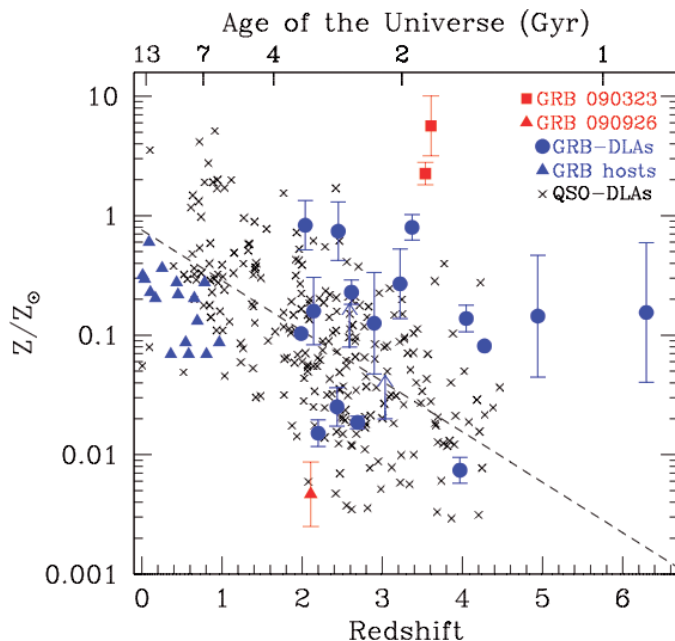


Fig. 3: Metallicities as a function of redshift. Values measured in the neutral gas of GRB 090323 ( $[Zn/H]=+0.35 \pm 0.09$  and  $[S/H]=+0.75 \pm 0.25$ ) and GRB 090926 ( $[Si/H]=-2.33 \pm 0.27$ ) are indicated as red squares and triangle, respectively. The metallicities of other GRB-DLAs and QSO-DLAs are plotted as blue dots and black crosses, respectively. The blue triangles at  $z < 1$  are metallicities derived from the hot gas in GRB host galaxies. The long-dashed line is the linear correlation for the QSO-DLA sample.

## 2.3 MASSIVE BLACK HOLES AND ACTIVE GALACTIC NUCLEI

Observations of active galactic nuclei (AGN) are of wide astrophysical interest. The amount and efficiency of the energy release within the immediate neighbourhood of black holes is a consequence of some of the most extreme physical processes observed to date. The most probable explanation for the huge amount of energy output and for other observational parameters, such as characteristic optical emission lines and the presence of strong radio emission and jets is given by the transformation of potential energy into radiation by accretion of matter onto a supermassive central Black Hole. The velocities of the accreting matter reach values of about one third of the velocity of light, deduced by relativistically broadened line profiles centred at about 6.4 keV. The emission from the matter around the black hole may vary on very short time scales of only a few hundred seconds. The corresponding changes in luminosity reach values of about  $10^{10}$  solar luminosities. All this is further suggestive for the presence of supermassive black holes at the cores of AGN.

Energy production processes and radiation mechanisms for the innermost regions of AGN are an important research field in X-ray astronomy. Other astrophysically important aspects include the detection and study of binary black holes, expected to produce strong gravitational wave emission during their final coalescence, and the search for recoiling black holes as a consequence of anisotropic emission of gravitational waves during coalescence. At larger distances from the black hole, the optical, UV and infrared emission from photoionized gas can be studied. Imprinted absorption and emission lines give information on the chemical composition of the gas and of infall and outflow velocities.

Apart from the study of the physical processes in nearby AGN, statistical studies of large samples of AGN out to high redshift provide important constraints on the evolution of galaxies and black holes. The  $\log N - \log S$  distribution of AGN and resulting luminosity functions allow us to study the density and luminosity evolution of AGN in dependence of redshift.

While supermassive black holes in AGN are actively accreting matter from their environment, the majority of galaxies hosts non-accreting or only mildly accreting black holes at their centres. The best such case is the black hole at the centre of our own Galaxy, which has been traced by measuring the stellar kinematics

in its immediate environment. While the motion of individual stars can only be resolved at the centre of our own Galaxy, the average bulge stellar kinematics in nearby galaxies can also be used to estimate black hole masses, applying known scaling relations between black hole mass and bulge stellar velocity dispersion. Another way to trace non-active black holes is by tidal disruption events of stars in the vicinity of black holes, producing luminous flares of electromagnetic radiation.

The following selected highlight contributions on 'Massive Black Holes and Active Galactic Nuclei' describe important results obtained in the last 3 years, based on multi-wavelength observations with ground- and space-based observatories, and based on theoretical studies.

They describe (1) precision measurements of the vicinity of the black hole in our Galactic Center, (2) simulations of star formation near Galactic Centers, (3) measurements of black hole masses in nearby non-active galaxies, (4) observational evidence for, and implications of, the presence of recoiling black holes, (5) probing star formation in high- $z$  AGN hosts with Herschel, (6) statistical properties of nearby and distant AGN in the COSMOS survey, and (7) Swift results on AGN and the cosmic background.

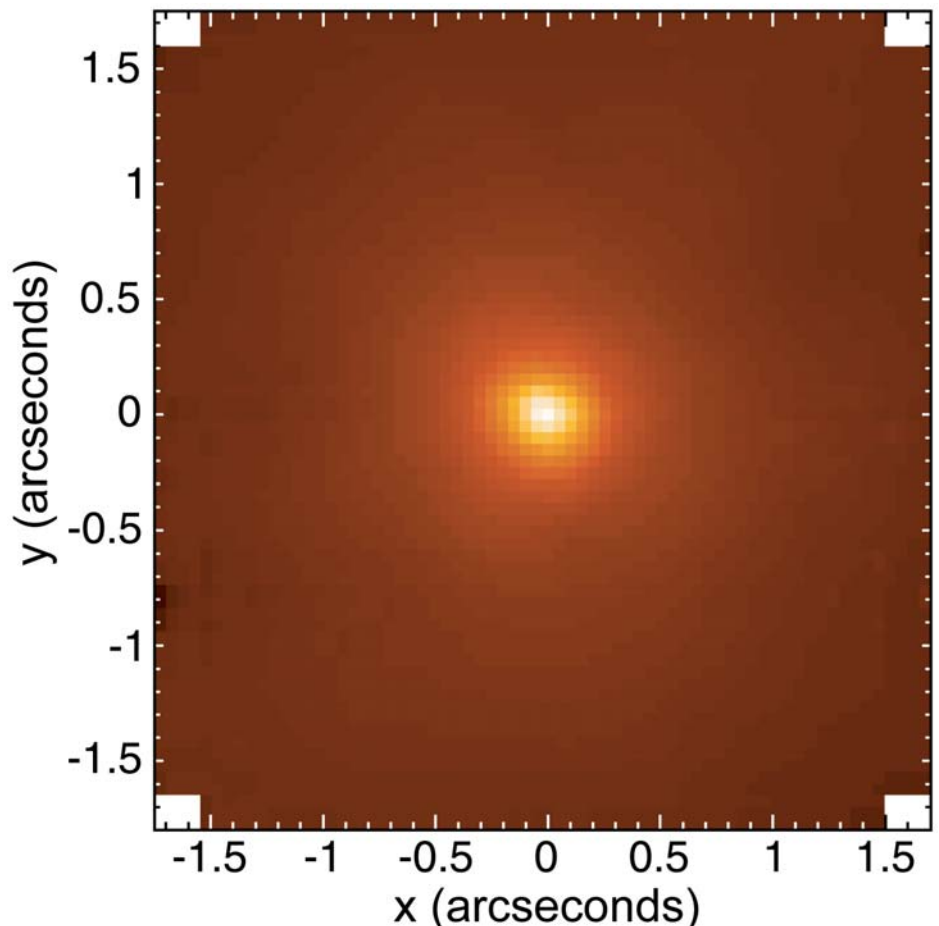


Fig. 1: The central region of the nearby galaxy NGC 3368 observed with MPE's SINFONI at the ESO VLT. A massive black hole of seven million solar masses could be deduced from the data.

## Precision measurements in the Galactic Center

The Galactic Center (GC) is a uniquely accessible laboratory for exploring a broad range of scientific questions related to the interaction of a massive black hole (MBH) with its environment. We highlight two central aspects: The stellar orbits and the flares from the MBH. Stellar orbits show that the gravitational potential, to a scale of a few light hours, is dominated by a concentrated mass associated with the compact radio source Sgr A\*, which must be a MBH, beyond any reasonable doubt. Once per day Sgr A\* exhibits infrared flares during which its flux increases by a factor 10–50. Flares are probably due to synchrotron emission of transiently heated electrons in the innermost accretion zone.

The vicinity of the GC allows us to study in great detail physical processes which also play a role in the nuclei of other galaxies, such as nuclear star formation, dynamical processes (relaxation or mass segregation), and the radiatively inefficient accretion flow onto the MBH. Observationally, the use of adaptive optics assisted imaging (Fig. 1) and integral field spectroscopy in the near-infrared wavelength regime (1 $\mu$ m to 5 $\mu$ m) at an 8m-class telescope is state of the art. The current generation of instruments has been available for a few years now, and as a result the GC science is characterized rather by impressive precision measurements than by the discovery of qualitatively new phenomena. Some recent results are:

- A dense stellar cusp surrounds the MBH in the central light month containing a large concentration of young B stars. This 'paradox of youth' is currently poorly understood.
- A population of O/WR stars in the central 0.5 pc resides in two warped disks. They may have formed in a starburst in gaseous accretion disks with a top-heavy initial mass function.
- Detailed atmosphere modeling for the young stars in the GC shows that the O/WR stars have an age of about 6 Myr, while the cusp stars are ordinary B-dwarfs.
- A large number of stellar motions are determined throughout the cluster and the associated dynamic modelling shows that the old population is a relaxed system, co-rotating with the Galaxy.

In the following, we highlight the two most important results: the more and more precisely determined stellar orbits and the SED modelling of rich multi-wavelength data of simultaneous NIR- and X-ray flares.

### The rewards of monitoring stellar orbits

The central arcsecond hosts a population of ~100 so called S-stars with magnitudes between  $m_K=14$  and 18. The astrometric precision for the bright stars has improved recently from a few mas to 200–300  $\mu$ as. Radial velocities can be measured with a precision of ~15km/s for the brightest early-type stars and for many late-type stars, limited by the accuracy of the wavelength calibration.

The brightest S-star, S2, has completed a full revolution around Sgr A\* since the beginning of the monitoring in 1992. Its orbital period is 15.9 years, the semi-major axis of the orbit is 125 mas. S2 allows for a geometric determination of  $R_0$ , the distance to the GC. The currently best such estimate is  $R_0 = 8.28 \pm 0.15(\text{stat}) \pm 0.29(\text{sys})$  kpc. The accuracy is limited by systematic uncertainties. The corresponding value for the central mass is  $M = 4.30 \pm 0.15(\text{stat}) \pm 0.20(\text{sys}) \times 10^6 M_\odot$ . For a fixed value of  $R_0$ , the mass error is  $0.06 \times 10^6 M_\odot$  only, corresponding to a precision of 1.5%. At most ~5% of the mass of the MBH can reside in some extended configuration at radii between the peri- and the apocenter distance of the S2 orbit. A comparison of the MPE results with that published by our colleagues at UCLA shows an apparent mismatch at first glance (Fig. 2). However, allowing for an offset in position and velocity between the two coordinate systems suffices to bring the measurements into agreement.

In total, we have determined ~30 stellar orbits. The distribution of orbital planes reveals two dynamically distinct populations. Six orbits at  $r \sim 1''$  share a common plane. This explicitly confirms the existence of the clockwise stellar disk that was previously defined only in a statistical sense. Closer to the center ( $r < 1''$ ), the distribution of orbital planes is consistent with being randomly oriented orbits.

The distribution of eccentricities of the non-disk stars is slightly hotter than a thermal ( $n(e) \sim e$ ) distribution:  $n(e) \sim e^{2.8 \pm 0.8}$ . This can be explained in a scenario including the Hills mechanism. Massive perturbers (e.g. molecular clouds) scatter field binaries into near loss-cone orbits. The three-body interaction with the MBH breaks the binary, leaving one member as an S-star and ejecting the other

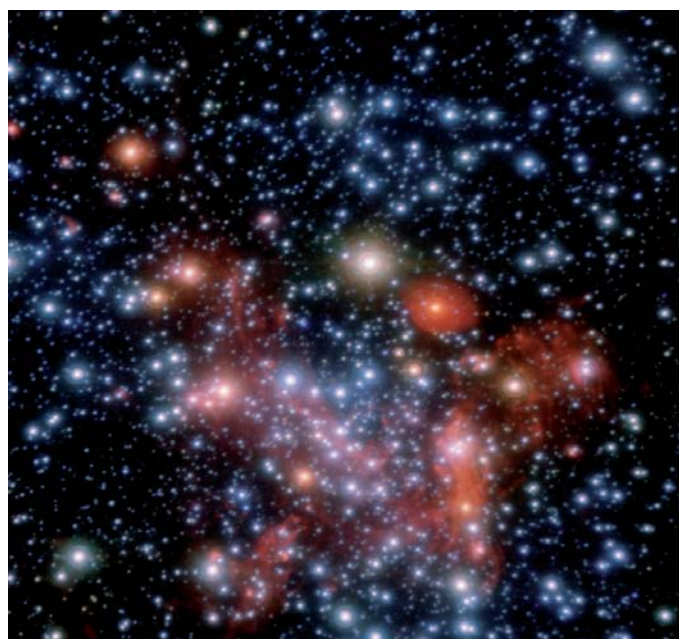


Fig. 1: HKL color composite of the Galactic Center from the adaptive optics imager NACO.

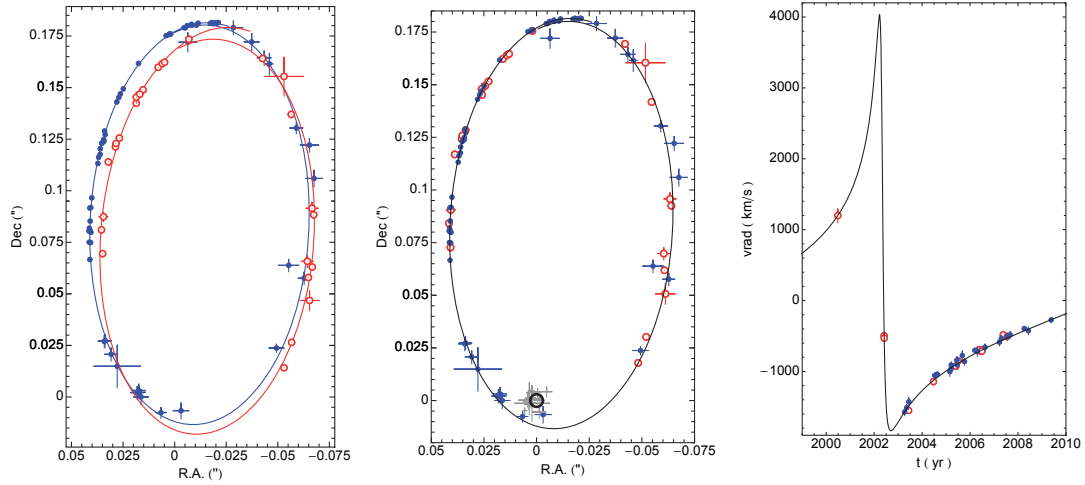


Fig. 2: The star S2 orbits around Sgr A\* in a 15.9 years. Left: The two data sets from the MPE group (blue, filled symbols) and our colleagues at UCLA (red, open symbols) show a mismatch larger than the measurement precision. Middle: A small offset in position and velocity between the two coordinate systems suffices to bring the data into perfect agreement. The black circle shows the position of the fitted mass, the grey crosses the location of various NIR flares. Right: The radial velocity of S2 as a function of time.

star as a hypervelocity star. This would however yield a very hot eccentricity distribution (typical  $e \sim 0.98$ ). Hence, an additional relaxation mechanism such as resonant relaxation needs to be invoked. Whether this rather complicated scenario indeed solves the riddle of the young S-stars, is yet open. However the eccentricity distribution is clearly the key.

### Even closer to the black hole: flares from Sgr A\*

Since 2003 we have been monitoring the NIR emission from Sgr A\*. We have compiled an extensive dataset, which sheds light on the nature of the NIR variability. Fig. 3 shows the light curve and flux distribution of all good quality Ks-band observations between 2004 and 2009. Apart from a stellar background offset, there are evidently two components to the variability of Sgr A\*: a continuously variable, lognormal component that dominates at fluxes  $< 11$  mJy, and a tail that extends to 40 mJy, which corresponds to flare “events”. X-ray binaries and

some AGN also show two components to the variability: in Cygnus X-1 for example, the prototype of a “low-state” X-ray binary, the variability follows a lognormal distribution, but there are also rare high-flux events.

Targeted multiwavelength observations of flares provide further important insights into the emission mechanism and require co-ordinated campaigns. The spectral energy distribution (SED) constrains the magnetic field strength, density and energies of the relativistic electrons in the emission region. A large worldwide campaign took place in April 2007 and involved telescopes from the radio to the X-ray regime (APEX/LABOCA, VLA, SMA, VLT/NACO+VISIR, HST/NICMOS, XMM-Newton, INTEGRAL). We observed a particularly strong flare at both NIR and X-ray wavelengths (Fig. 4). Mid-infrared measurements constrained the slope ( $\beta$ ) of the SED in the infrared, showing that the NIR flare was blue in terms of energy ( $\beta_{\text{NIR}} > 0$  where  $v_{L_V} \sim v^\beta$ ), while the X-ray flare was observed to be red ( $\beta_X < 0$ ).

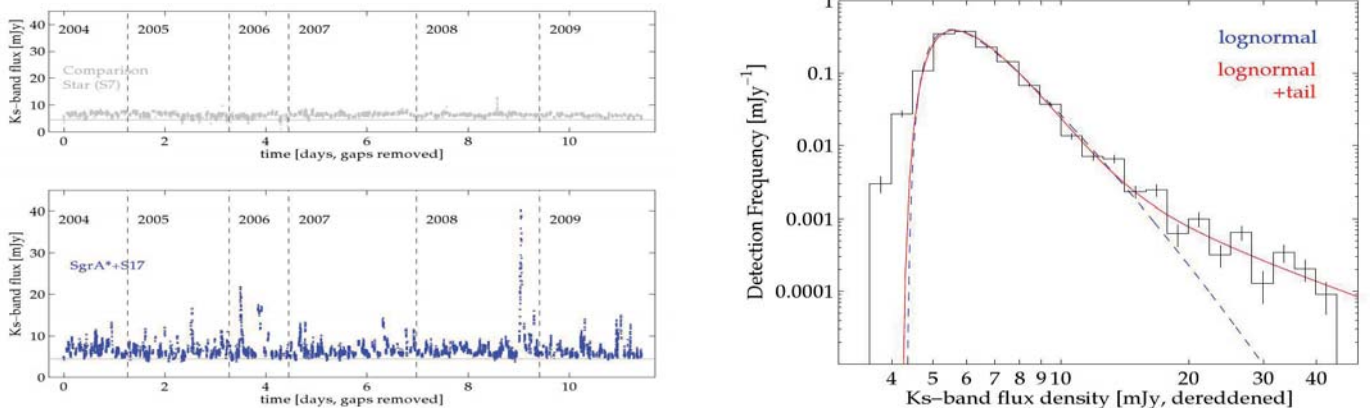


Fig. 3: Left: Lightcurve of Sgr A\* from 2004 to 2009, omitting large sampling gaps. Right: The flux distribution.

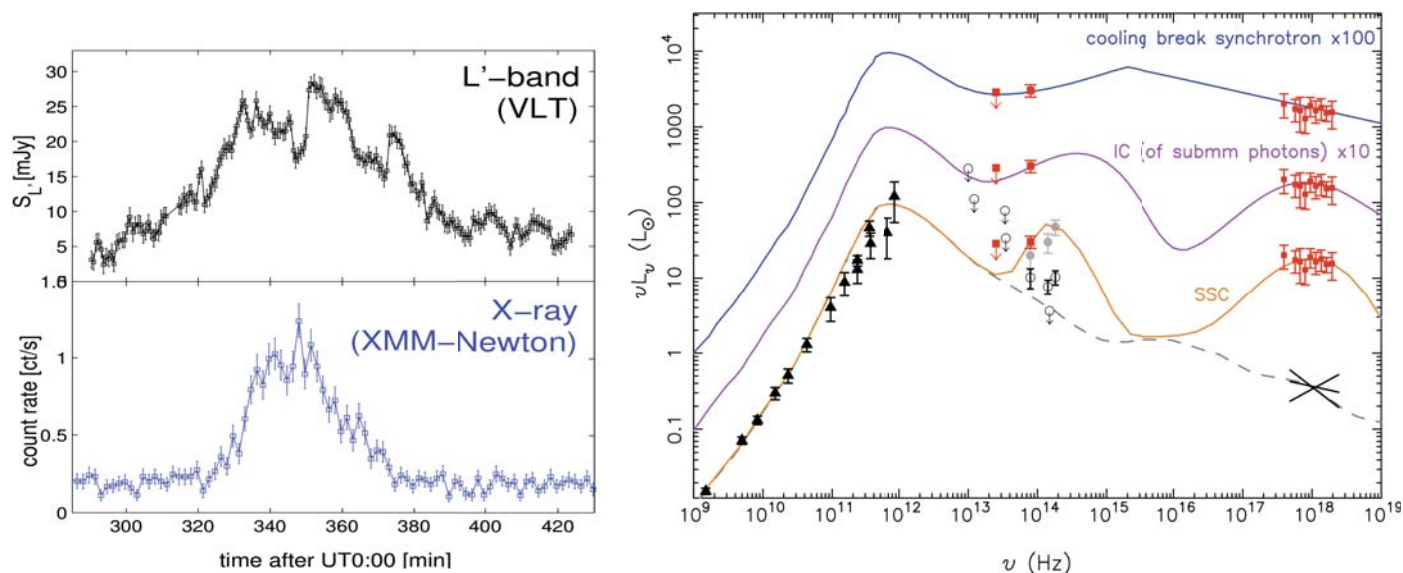


Fig. 4: Left: Simultaneous NIR and X-ray lightcurves of Sgr A\* obtained in April 2007. Right: Various models compared to the observed SED (offset from one another for clarity).

This has surprising implications for the previously favored emission models where the X-ray flare is produced via inverse Compton scattering. For example, if the X-ray emission is due to scattered submm photons (IC model in Fig. 4), an unrealistically small ( $<0.3$  Schwarzschild radii) seed photon region would follow, in contradiction to VLBI measurements of the submm source size of  $\approx 4 R_s$ . Alternatively, if the X-ray emission is due to scattered NIR photons (synchrotron self-Compton model, SSC in Fig. 4), unrealistically high magnetic fields and electron densities are needed. Instead, a pure synchrotron model with a spectral break due to synchrotron cooling allows parameters more natural to the inner regions of the accretion flow.

In this case the X-ray flare is also synchrotron radiation; differences in substructure and duration of the light curves may be explained by magnetic field fluctuations and an overall decrease in magnetic field during the flare such as it would occur in a magnetic reconnection event.



K. Dodds-Eden and S. Gillessen

## Simulating Star formation near the Galactic Centre Black Hole

We try to theoretically understand the formation of the discs of stars near the Galactic Centre in our Milky Way, as observed by the infrared group at the MPE. For this we simulate the infall of molecular clouds onto the central black hole using the smoothed particle hydrodynamics (SPH) code GADGET2. During the encounter, the clouds engulf the black hole in part, leading to gas streaming around the black hole with opposite angular momentum. This gas collides and settles into an eccentric accretion disc around the black hole which eventually becomes unstable and fragments into the observed stellar disc. We find gaseous disc masses of typically  $10^4$  solar masses, sizes of around 1 pc and eccentricities of around 0.4 which already compare well with the observed stellar disc. In the future, we will apply this mechanism also to other galaxies such as M31 for where observations show an eccentric disc of stars in the centre. Furthermore the infall of multiple clouds would provide a simple explanation of the origin of the second observed disc (the existence of this second disc is however contested) in our Milky Way which is rotating contrarywise to the first one.

Observations reveal an interesting feature in our Galactic Centre (GC): two sub-parsec-scale rings of young stars near the radio source Sgr A\* which cannot be explained by normal means of star formation due to the hostility of the environment (see previous article). Tidal forces would disrupt typical molecular clouds in the vicinity of the central black hole, preventing their condensation into stars. However there are about 100 young and massive stars distributed in a warped clockwise rotating disc and a second inclined counter-clockwise rotating disc. The outer edge of the system measures at about 0.5 pc and the inner edge at about 0.04 pc. The mean eccentricity of the clockwise rotating system is measured to be 0.36.

An alternative and more plausible formation scenario postulates that the stellar rings formed by fragmentation of self-gravitating, eccentric accretion discs. Previous studies concentrated mainly on the fragmentation of an already existing accretion disc. The question how these discs formed in the first place has been discussed only recently. The models assume that the accretion discs are built up by the rapid deposit of gas around the central black hole through the infall and tidal disruption of a gas cloud. However, here the problem arises that a gas

cloud that most likely formed far from the GC where tidal forces are inefficient, must be placed on an orbit with a close passage around the black hole. Furthermore, the cloud should not be disrupted by internal star formation processes before encountering the black hole.

In our work we use the model proposed by M. Wardle and F. Yusef-Zadeh (2008) in which the infalling cloud covers the black hole in parts during its passage. This process efficiently redistributes angular momentum and dissipates kinetic energy through the collision downstream of material with opposite angular momentum streaming around the black hole from both sides, finally resulting in a compact accretion disc. These processes are studied in great detail using high-resolution numerical simulations performed with the N-body Smoothed Particle Hydrodynamics (SPH) Code Gadget2.

The black hole is included as a static potential of a point mass of  $3.5 \times 10^6$  solar masses placed at the origin of the coordinate system. Initially we adopt an isothermal equation of state with a typical GC cloud temperature of 50 K. In the future we plan to use a more realistic equation

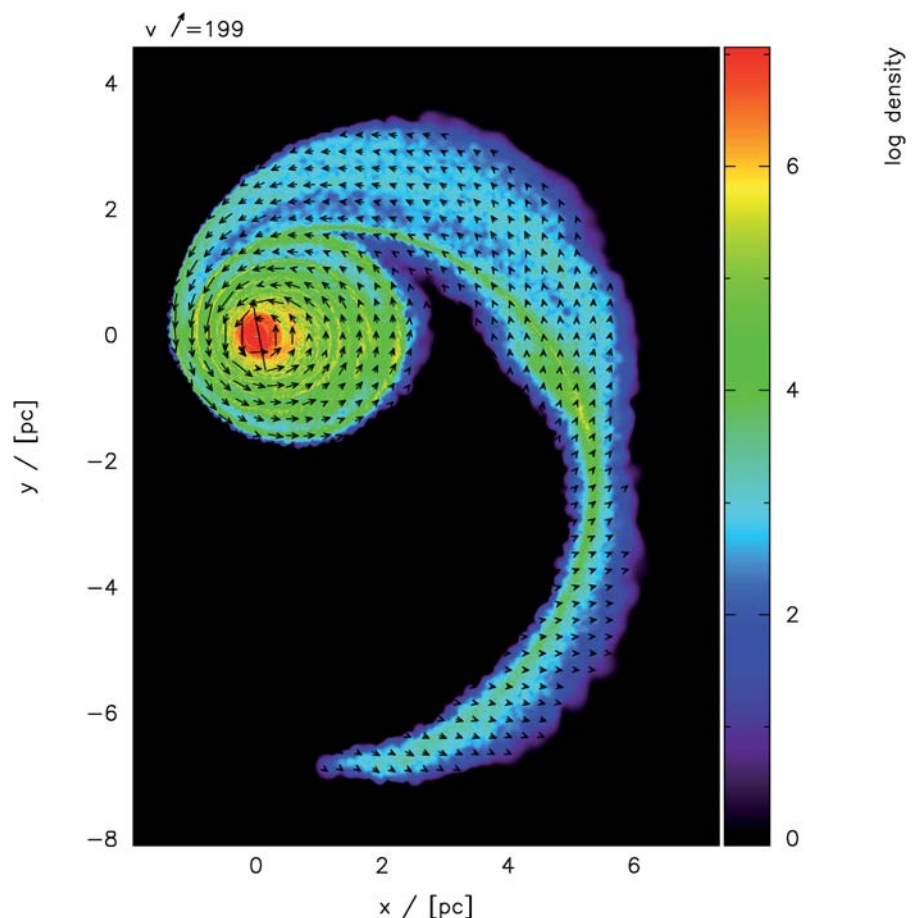


Fig. 1: Density of our standard model cloud in the  $xy$ -plane ( $z=0$ ) at the end of our simulation run.

of state together with a cooling prescription. We start with a spherical and homogeneous cloud of radius 3.5 pc typical for the GC. The  $H_2$  gas density is  $10^4 \text{ cm}^{-3}$ , leading to a cloud mass of  $8.81 \times 10^4$  solar masses.

In order for the simulations not to become too time-consuming as a result of very small particle time steps in the vicinity of the black hole we define an accretion radius of 0.02 pc within which all SPH particles are considered to be accreted by the black hole.

The centre of mass of the cloud is placed at a distance of 5 pc from the origin/black hole on the x-axis (the direction of motion) and an offset  $b$ , which can vary from 0.5 to 2.5 pc, on the y-axis. We have chosen this relatively small distance in order to prevent the cloud from collapsing before it reaches the black hole. The initial cloud velocity in x-direction is a typical value (30 km/s to 80 km/s) taken from observations of the GC molecular clouds. All simulations were usually run for an evolutionary time of 0.25 Myrs which corresponds roughly to a time when all parts of the cloud have crossed the black hole.

The amount of accreted gas is mainly determined by the cloud's impact parameter relative to its radius. After the cloud passed the black hole, the inner gas disc has already relaxed to an approximate equilibrium state. The instability of such pressure stabilized discs can be assessed with the help of the so-called Toomre parameter. We compare the Toomre unstable region of our (gaseous) discs to the observed (stellar) discs. We find that the initial cloud velocity determines the resulting stellar mass of the disc (the higher the velocity, the lower the disc mass). Our standard model (Cloud velocity of 50 km/s and  $b = 1.5$  pc) shows a disc eccentricity of order 0.4, an outer radius of 1.35 pc and a disc mass of  $0.7 \times 10^4$  solar masses. This is in good agreement with the observations. Fig. 1 shows the density in the xy-plane at  $z=0$  pc for our standard model at the end of the simulation.

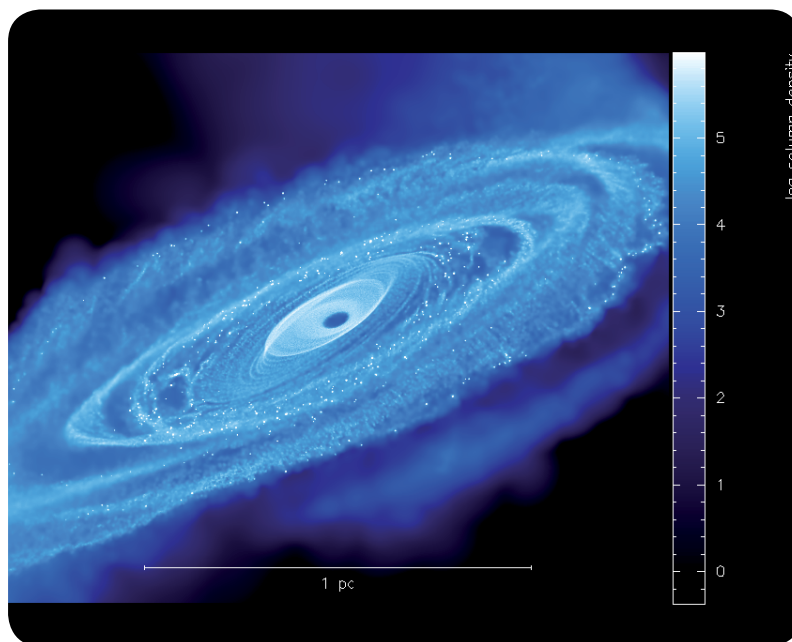


Fig. 2: The model of our primary shows a substantial warp due to the infall of a second cloud.

To further refine our model, we included the potential of the cluster of old stars near the GC (see previous article). This leads to precession of the eccentric orbits on time scales which, compared with the infall time, are short. The resulting gaseous disc fragments a lot faster than it would without including the cluster potential but to the same initial conditions.

Furthermore, since observations show two discs in the GC, we study the infall of a second cloud within a short time after formation of the first unstable gaseous disc. The infall of the second cloud leads to a substantial warp in the primary gaseous disc (see Fig. 2), which is also observed in one of the stellar discs.

Currently the work focuses on including a more realistic equation of state and a cooling prescription, together with a star formation prescription in order to be able to directly compare stellar orbits from the simulations to the observed stellar orbits.



C. Alig, A. Burkert, M. Hirschmann, P. Johansson, M. Krause and M. Schartmann

## The SINFONI Search for Supermassive Black Holes (S<sup>3</sup>BH)

All massive galaxies appear to host supermassive black holes (SMBHs) in their nuclei, with strong correlations between SMBH mass and host-galaxy properties (e.g. central velocity dispersion or bulge luminosity/mass). Because of the paucity of reliably measured masses in both low- and high-mass regimes however, key questions remain unanswered: Are the relations simple power laws for all SMBH masses, or do they deviate at the high-mass (or low-mass) end? Do the same relations hold for “pseudo-bulges” and merger remnants? To answer these questions, we have created a program to significantly increase the number of SMBH measurements. To date, we have observed 33 nearby galaxies with the SINFONI near-IR integral field unit on the VLT, using adaptive optics, using 2D stellar kinematics to dynamically measure their SMBH masses. Once fully analysed, our data will almost double the number of galaxies with reliable SMBH detections. Presently, the basic data reduction is complete, with kinematic results in hand for over half the galaxies; dynamical modelling of 5 galaxies (published or submitted) already shows significant deviations from the  $M_{\bullet}$ - $L_{\text{bulge}}$  relation.

**Background:** In the past fifteen years, we have learned that essentially all massive galaxies in the local universe harbour supermassive black holes (SMBHs, with masses  $M_{\bullet}$  of  $\sim 10^6$ – $10^9$  solar masses) in their centres; these are

thought to be “dead” active nuclei. The SMBH masses correlate with global properties of their host galaxies, including the central velocity dispersion  $\sigma$  (the mean random motions of stars in the central region of the galaxy, outside the direct gravitational influence of the SMBH) and the total stellar luminosity (or stellar mass) of the host galaxy’s bulge ( $L_{\text{bulge}}$ ; elliptical galaxies are considered “pure bulges”). This is surprising, given that SMBHs are only  $\sim 0.5\%$  of the host galaxy mass and directly influence a tiny fraction only of its volume and stars. The implication is that the processes which drove galaxy growth and the those which drove black hole growth were intimately linked. Indeed, one of the most popular models argues that the feedback from gas accretion into a SMBH acts to shut off both its own fuelling and star formation at large within a galaxy.

There are several important, unresolved problems with the SMBH–host galaxy relations. They can be used to estimate the local SMBH mass function which can be compared to the black hole density needed to explain Active Galactic Nuclei (AGN). If AGN activity is the dominant mechanism for SMBH growth, then the AGN luminosity function can be integrated over time to yield a comparable estimate for the local SMBH mass function. But the result is ambiguous: it appears that the local SMBH–host galaxy relations may underpredict the expected number of SMBHs at the very high-mass end. Related to this are

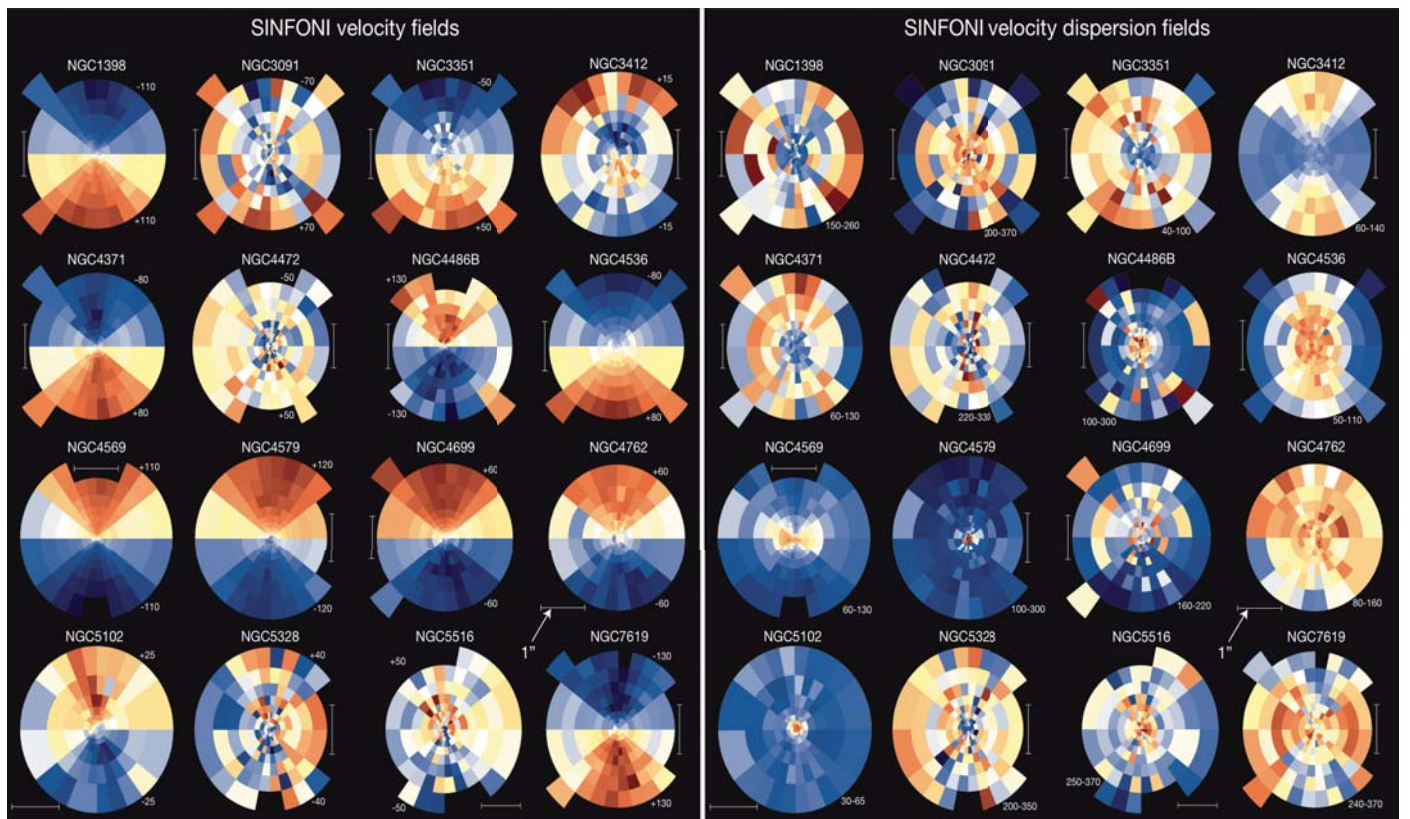


Fig. 1: 2-dimensional maps of stellar velocity fields (left) and velocity dispersion fields (right) derived from SINFONI data for 16 of the 33 galaxies in our SMBH sample. Blue and red represent approaching and receding velocities (left) or low and high values of the dispersion (right).

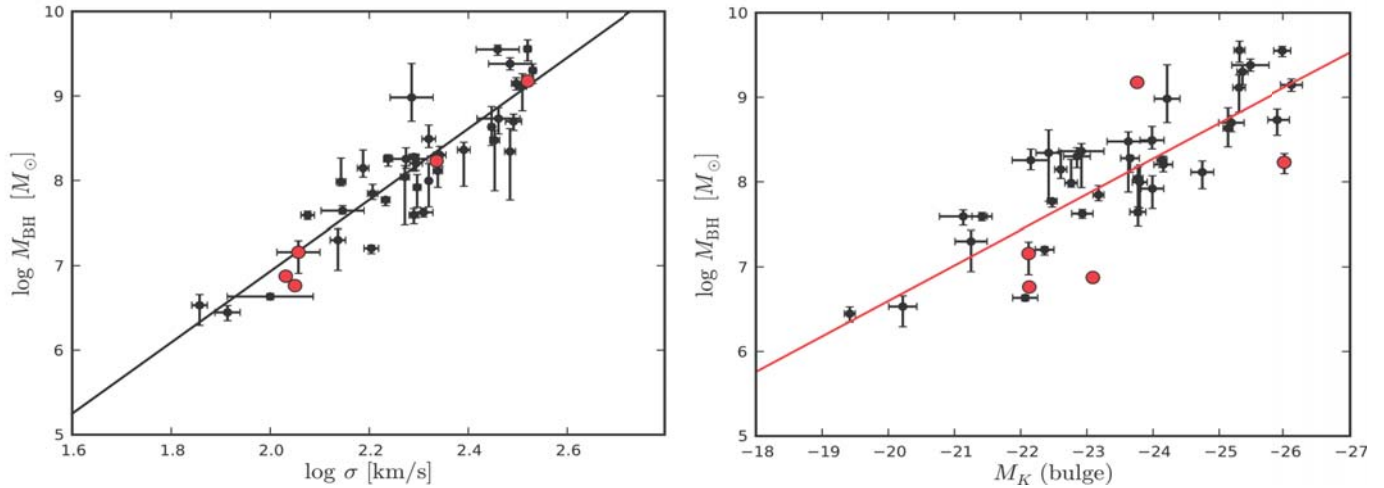


Fig. 2: Correlations between SMBH mass and host galaxy properties (horizontal axis). Left: SMBH mass versus velocity dispersion; right: SMBH mass versus bulge luminosity. Only galaxies with well-determined distances are plotted; diagonal lines are linear fits. Our published measurements are in red; while all five galaxies agree with the  $M_{\bullet}$ - $\sigma$  relation, several deviate prominently from the  $M_{\bullet}$ - $L_{\text{bulge}}$  relation.

the two questions whether the local relations are simple power laws, as has been assumed so far, and which relation is the strongest and most appropriate to use.

Additional mysteries lurk at the low-mass end. The simplest models for SMBH and bulge growth suggest that black holes and bulges grow primarily via major mergers, with rapid gas accretion into the black hole and rapid build-up of a kinematically hot spheroid (a “classical bulge”). But evidence now suggests that many “bulges” in spiral galaxies are actually “pseudobulges”: disk-like structures that grow via slow, internal processes (“secular evolution”). We do not know if SMBHs in such galaxies follow the same relations—and if they even should. There are also galaxies with both pseudobulges and classical bulges: which “bulge” does the SMBH correlate with then? Finally, if mergers are the main mechanisms for SMBH and bulge growth, we might expect to find deviations from the SMBH–host galaxy relation in merger remnants, where one or both growth processes are not yet finished.

One of the main reasons these problems remain unresolved is the relative paucity of SMBH measurements at both the high-mass and (especially) the low-mass end of the relations. To address these issues, we have undertaken a program to significantly increase the number of directly measured SMBH masses, with a particular focus on the questions outlined above. We have defined a target sample encompassing several areas: lower-mass galaxies with pseudobulges; corresponding lower-mass galaxies with classical bulges; galaxies containing both pseudobulges and classical bulges; high-mass galaxies (with velocity dispersions  $> 300$  km/s); and recent merger remnants. Our goal is to directly measure the SMBH mass using stellar kinematics from K-band spectroscopy with the highest possible spatial resolution. Near-IR spectroscopy helps avoid the effects of strong dust absorption present in the optical and allows the use of adaptive op-

tics (AO), which corrects for the effects of atmospheric turbulence, thereby allowing a ground-based telescope to deliver nearly diffraction-limited performance. High spatial resolution is necessary for resolving the SMBH’s “sphere of influence” (the region where its effects on stellar kinematics dominates over that of the surrounding stellar potential). Our primary instrument is the near-IR integral-field spectrograph SINFONI, mounted on the VLT.

### Results of the S<sup>3</sup>BH SINFONI Supermassive Black Hole survey:

Between 2005 and mid-2009 we invested 22 GTO nights at the VLT, observing a total of 33 galaxies with SINFONI, using natural guide star mode (with galaxy centres as adaptive-optics references) or the laser guide star PARSEC (for galaxies with faint centres). Around one third of the observed galaxies have a pseudobulge, one third are high- $\sigma$  bulges ( $\sigma > 300$  km/s), and the remainder consist of low- $\sigma$  galaxies or merger remnants. We achieved excellent spatial resolution (AO-corrected FWHM of 0.08–0.16”), resolving the estimated sphere of influence of the SMBHs. To reduce the raw data to calibrated data cubes, we created a pipeline combining the best elements of the MPE SPRED and ESO pipelines; over 90% of the observations have been reduced, and we expect the remainder to be finished by March 2010.

To determine the mass of the central black hole ( $M_{\bullet}$ ), we use stellar dynamical modelling, as the most direct signature of a black hole in inactive galaxies comes from the motions of the stars in its vicinity. This method requires measurements of the stellar motions in the galaxy as well as the knowledge of the gravitational potential generated by the stars. The kinematics of the stars is measured by fitting the spectra in the reduced SINFONI data cubes using a maximum penalized likelihood (MPL) technique. Fig. 1 shows as an example of the velocity fields for a number of our galaxies; stellar kinematics has been determined

for over half the observed galaxies. To determine the mass contributed by the stellar component in a galaxy, it is necessary to analyse the light profiles derived from e.g. high-resolution Hubble Space Telescope or SINFONI imaging and - for the outer regions — ground-based images. Many galaxies consist of several components (e.g., bulge and disc) with different stellar populations and thus different mass-to-light ratios. In these cases it is necessary to derive separate light profiles for each such component. The three-dimensional density distribution of the stars in each component then can be obtained by deprojecting the surface brightness profile.

For the dynamical modelling we use an axisymmetric code based on the Schwarzschild orbit superposition technique. The modelling procedure comprises the following steps: First, the gravitational potential of the galaxy is calculated from the stellar luminosity density and a trial mass-to-light-ratio  $M/L$ , along with a SMBH with trial mass  $M_{\bullet}$ . Then, an orbit library is generated for this potential and a weighted orbit superposition is constructed such that the observational constraints are matched. Finally, everything is repeated for other potentials until the appropriate parameter space in  $M_{\bullet}$  and  $M/L$  is sampled. The best-fitting values for  $M_{\bullet}$  and  $M/L$  then follow from a  $\chi^2$  analysis.

Schwarzschild modelling has been completed for five galaxies, with published or submitted papers describing the results; work on all other objects is in progress. We always make use of the full velocity field from our SINFONI data and model each of the four quadrants independently. This lets us assess the possible effects of deviations from axisymmetry. Below, we summarise the most recent results and compare them with the predictions of the  $M_{\bullet}-\sigma$  and the  $M_{\bullet}-L_{\text{bulge}}$  relations; see Fig. 2, where we plot the first four galaxies, plus NGC 4486A:

**NGC 1316 (Fornax A):** a massive radio galaxy in the outskirts of the Fornax galaxy cluster, which underwent a major merger about 3 Gyrs ago. The SMBH mass of  $(1.3 \pm 0.4) \times 10^8 M_{\odot}$  (is consistent with the  $M_{\bullet}-\sigma$  relation, but off from the  $M_{\bullet}-L_{\text{bulge}}$  relation).

**NGC 3368:** A double-barred spiral with a pseudobulge and a small classical bulge. The SMBH mass of  $(7.5 \pm 1.5) \times 10^6 M_{\text{sun}}$  agrees well with the  $M_{\bullet}-\sigma$  relation, but the  $M_{\bullet}-L_{\text{bulge}}$  relation predicts  $M_{\bullet}$  several times larger when the total (pseudo+classical) bulge mass is used. The mass of the classical bulge component alone seems to be a much better indicator of  $M_{\bullet}$ .

**NGC 3489:** a barred S0 galaxy, similar to NGC3368, with both a pseudobulge and an inner classical bulge. Its SMBH mass of  $(6.00 + 0.56 - 0.54)_{\text{stat}} \pm 0.64_{\text{sys}} \times 10^6 M_{\odot}$  agrees with the  $M_{\bullet}-\sigma$  relation, but with the  $M_{\bullet}-L_{\text{bulge}}$  relation only if the pseudobulge component is ignored.

**NGC 1332:** a high-mass S0 galaxy with a velocity dispersion of 328 km/s. The central SMBH has a mass of  $(1.5 \pm 0.2) \times 10^9 M_{\text{sun}}$ , consistent with the  $M_{\bullet}-\sigma$  relation but about an order of magnitude higher than expected from the  $M_{\bullet}-L_{\text{bulge}}$  relation.

**NGC 5102:** the galaxy with the smallest velocity dispersion ( $\sim 50$  km/s) in our sample. It is an S0 galaxy with a young star cluster in the centre. The first set of dynamical models indicate a SMBH mass of  $\sim 3 \times 10^5 M_{\odot}$ , in agreement with the  $M_{\bullet}-\sigma$  relation.

From the results obtained so far, it appears that the  $M_{\bullet}-L_{\text{bulge}}$  relation is not as good a predictor for  $M_{\bullet}$  as the  $M_{\bullet}-\sigma$  relation. Galaxies with pseudobulges, merger remnants with relatively young stellar populations, and high- $\sigma$  galaxies seem to deviate from the  $M_{\bullet}-L_{\text{bulge}}$  relation. After finishing the analysis of the remaining galaxies, our sample will be large enough to provide answers to all the questions posed above concerning the validity of the SMBH-bulge relations.



P. Erwin and N. Nowak

## Signatures and Implications of Recoiling Black Holes

Recent numerical relativity simulations predict that coalescing supermassive black holes (SMBHs) can receive kick velocities up to several 1000 km/s due to anisotropic emission of gravitational waves, leading to long-lived oscillations of the SMBHs in galaxy cores, and even SMBH ejections from their host galaxies. The presence of these kicks has a wide range of astrophysical implications which only now start being explored, including consequences for black hole and galaxy growth at the epoch of structure formation, modes of feedback, unified models of Active Galactic Nuclei (AGN), and the number of obscured AGN. SMBH recoil oscillations beyond the torus scale can be on the order of a quasar life time, thus potentially affecting a large fraction of the quasar population. We have searched for recoiling black holes in observations and presented the first candidate, and we have explored observational signatures of recoiling black holes, which will guide future searches.

A natural place to search for SMBHs is at the centers of galaxies, where they presumably are born and spend most of their lives. But it has become increasingly clear that a SMBH can be violently separated from its birthplace as a result of linear momentum imparted by gravitational waves during strong-field interactions with another SMBH. As a result, the newly formed single SMBH recoils when two SMBHs coalesce. Configurations of coalescing black holes can lead to recoil velocities up to 3800 km/s for maximally spinning equal-mass black hole binaries with anti-aligned spins in the orbital plane. Since escape velocities from the centers of even the largest galaxies are  $<2000$  km/s, it follows that the kicks can in principle remove SMBHs completely from their host galaxies. While such extreme events may be relatively rare, recoils large enough to displace SMBHs at least temporarily from galaxy cores - to distances of several hundred to a few thousand parsecs - may be much more common.

Upon recoil, the most tightly bound gas will remain bound to the recoiling black hole, and therefore high-velocity kicks imply the existence of interstellar and intergalactic quasars. Identifying recoiling SMBHs through observations is of great interest and several key electromagnetic signatures of kicks have been predicted in the last few years. After the kick, matter remains bound to the recoiling SMBH within a region which is of the order of the size of the broad line region (BLR) of AGN which will therefore typically remain bound to the SMBH while the bulk of the host galaxy's narrow-line region will remain behind. Recoiling SMBHs will therefore appear as AGN which have their broad emission lines kinematically shifted by up to 3800 km/s with respect to their narrow lines. Predicted in 2007 by Bonning and collaborators, the emission-line signatures of such a recoiling BH were found by us in 2008 in the Sloan Digital Sky Survey archive. The quasar SDSSJ0927+2943 shows the characteristic optical

signatures of a recoiling SMBH: Its broad emission lines are shifted by 2650 km/s with respect to its narrow emission lines, the broad lines are symmetric, and the narrow emission lines lack an ionization stratification as expected if the accreting SMBH is no longer at the center of the system. SDSSJ0927+2943 also shows a second system of narrow emission lines with unusual properties when compared with other known quasars. The origin of these lines is still being explored. Its unique properties make SDSSJ0927+2943 an excellent candidate for a recoiling SMBH.

We have also predicted a number of observational signatures of recoiling SMBHs, which will be searched for in future observations. While others have predicted "accretion-related" flares in gas-rich mergers, we have focused on SMBH recoil in gas-free systems. Even in the absence of an accretion disk, ejected SMBHs will always carry a retinue of bound stars. These stars are subject to tidal disruption, leading to powerful X-ray flares of quasar-like luminosity when the debris of the disrupted star is accreted by the black hole. The flare would appear off-nuclear or even intergalactic. We determined disruption rates for the bound, and the unbound, stellar populations, under recoil conditions. In the resonant relaxation regime, we find that the rates are of order  $10^{-6}$  yr $^{-1}$  for a typical galaxy; smaller than, but comparable to, rates for non-recoiling SMBHs. Future X-ray all-sky surveys, especially the one planned with eROSITA, will play a key role in detecting such events. Another signature related to the stars bound to the recoiling SMBH is episodic X-ray emission from accretion due to stellar mass loss. Mass loss provides a reservoir of gas, and therefore also optical emission lines from gas at the recoil velocity even in the initial absence of a gaseous accretion disk. Other consequences include the presence of intergalactic planetary nebulae and supernovae, produced after the ejected SMBH has left its host galaxy.

While the "tidal recoil flares" are very luminous and could be detected out to very large distances, the compact system of bound stars itself will be detectable in the nearby universe, and would resemble a globular cluster in total luminosity, but with a much greater velocity dispersion due to the large binding mass. We have explored the properties of these "hypercompact stellar systems" (HCSS) in great detail, and related the structural properties (size, mass, and density profile) of HCSSs to the properties of their host galaxies and to the amplitude of the kick. Since the kick velocity is encoded in the velocity dispersion of the bound stars, future detection of large samples of HCSSs would therefore allow us to determine empirically the kick distribution, and therefore the merger history of galaxies in clusters. Nearby clusters of galaxies are best suited to search for and identify HCSSs, and  $\sim 100$  of them should be detectable within 2 Mpc of the center of the Virgo cluster.



Fig. 1: Artist's view of a recoiling black hole, ejected from its host galaxy. The most tightly bound stars remain bound to the black hole.

A recoiling SMBH with a bound gas disk that passes through the dense molecular torus in the core of an AGN might cause local shocks leading to temporary electromagnetic radiation. Further, during the long-lived “Phase II” recoil oscillations, when the SMBH oscillation amplitude is on the torus scale, the SMBH might efficiently accrete from the dense molecular gas at each turning point, causing repeated flares of radiation. Such flares would locally destroy the dust, while photoionization of the dense surrounding gas would produce a strong emission-line response. Such a signal would not only help in identifying kicks but could also be used as a new probe of the properties of the torus itself.

There are potentially far-reaching consequences of SMBH recoil for unified models of AGN. Spatial oscillations of the SMBHs about the cores of their host galaxies imply that the SMBHs spend a significant fraction of time off-nucleus, at scales beyond that of the molecular obscuring torus. An intrinsically obscured quasar of type 2 with its BLR hidden by the torus will therefore appear as unabsorbed, type 1 quasar during the recoil oscillations, when moving beyond the torus scale. Assuming reasonable distributions of recoil velocities, we have computed the off-core timescale of (intrinsically type-2) quasars. We found that roughly 50% of all major mergers result in a SMBH being displaced beyond the torus for a time of  $10^{7.5}$  yr or more. This is an interesting number, because it is comparable to quasar activity time scales. Since major mergers (i.e., quasars)

are most strongly affected by gravitational wave recoil, our results imply a deficiency of luminous type 2 quasars in comparison to low-luminosity Seyfert 2 galaxies, as is in fact observed. Recoil oscillations may therefore naturally explain the long-standing puzzle, why few absorbed type 2 quasars exist at high luminosities. It would be these which are affected by the recoil oscillations, and therefore appear as type 1 rather than type 2 for a significant fraction of their lifetime.

Recoil oscillations also have a number of other observable consequences related to AGN. For instance, they will affect the X-ray background and its modeling since a fraction of sources will be unobscured at any given time. In particular, small amplitude oscillations of the order the torus size will affect the ratio of Compton-thin to Compton-thick sources, and could lead to measurable variability in the absorption and extinction of AGN spectra once the recoiling SMBH passes the individual clouds making up the torus



S. Komossa

## Probing star formation in high-z AGN hosts with Herschel

The rest frame far-infrared is a unique wavelength range to characterize star formation in the host galaxies of high redshift active galactic nuclei (AGN). Herschel Space Observatory results, obtained in our PACS Evolutionary Probe (PEP) project, explore this emission near its peak and with unique sensitivity. Star formation can thus be studied in large samples of hosts for AGN with different properties and redshifts. Our first results suggest that, for luminous AGN, star formation is linked to the AGN activity but for other AGN rather decoupled and, similar to the AGN activity in non-active massive galaxies, at same redshift.

Recent progress suggests that the co-evolution of active galactic nuclei (AGN) and their hosts may be a central factor in shaping galaxy evolution. One of the imminent tasks is to quantify star formation rates in the hosts of high redshift AGN. Since many AGN shine extremely bright, especially at short wavelengths between the ultraviolet and mid-infrared and since they can also excite bright emission lines, it has been difficult to use the same star formation indicators traditionally applied to other non-active high redshift galaxies. The rest frame far-infrared continuum is a region where the brightness contrast between star

formation in the host galaxy and the AGN is particularly favourable, but instrumental limitations have precluded its widespread determination for high-z AGN up to now.

Our studies at other infrared/submillimeter wavelengths further support this approach. By using Spitzer Space Telescope mid-infrared spectroscopy we have detected PAH emission features from host star formation in low and high redshift quasars (see Fig.1). This implies that the far-infrared is indeed dominated by the host galaxy in all but the most extreme such objects. These mid-infrared spectroscopic studies, while very powerful, are time consuming and still limited to small samples. On the other hand, current submillimeter surveys cover large AGN samples, in particular the survey of the ECDFS field which a consortium, including our group, has obtained at the APEX telescope. This survey has given first results on the evolution of AGN host star formation, but faces limitations because it is necessary to extrapolate from the submillimeter to the far-infrared SED peak and to average over large numbers of objects to get sufficient sensitivity.

This has changed with the launch of the Herschel Space Observatory in May 2009 and the start of our `PACS Evo-

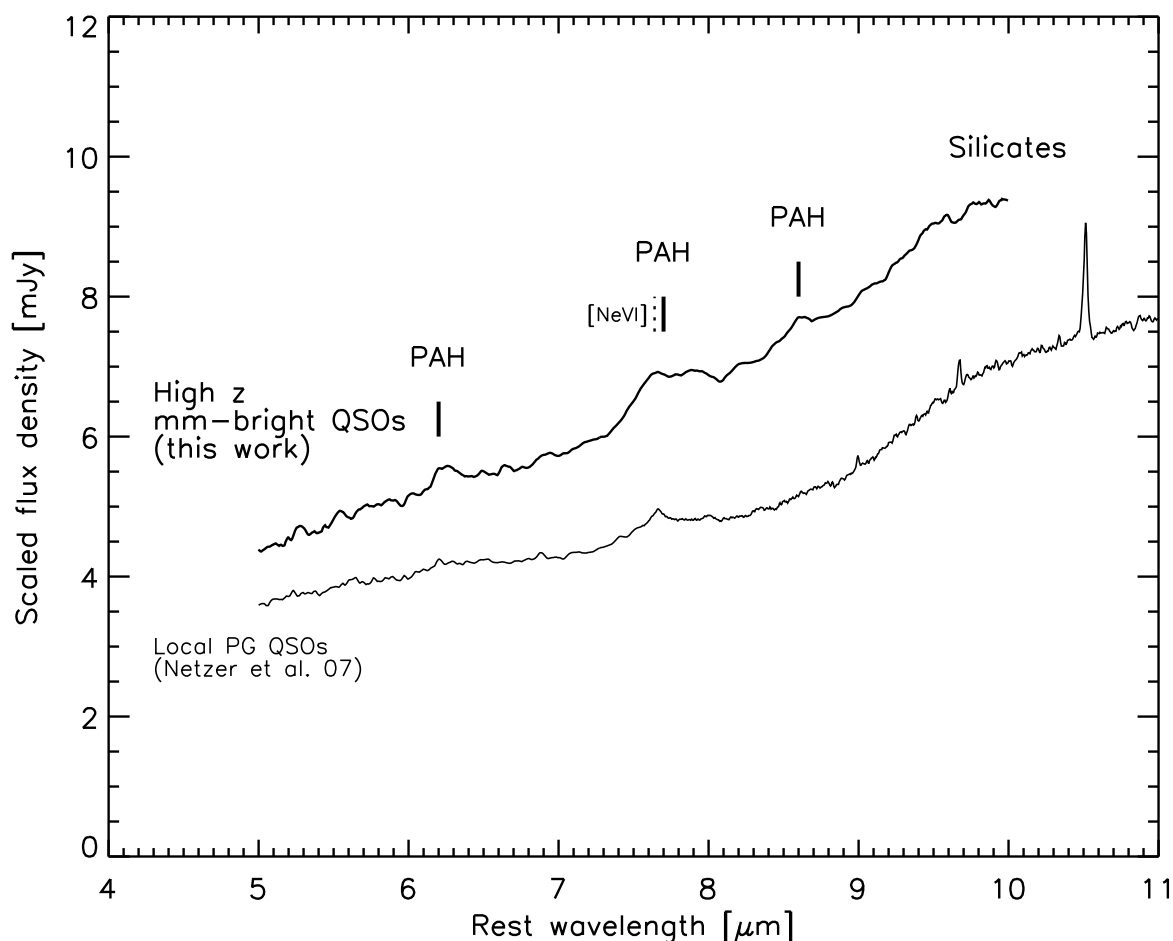


Fig. 1: Using mid-infrared spectroscopy with the Spitzer Space Telescope, we have detected the 'PAH feature' star formation tracers from the hosts of low and high-z quasars. Our results support the quality of the rest frame far-infrared emission as an indicator of star formation in AGN hosts.

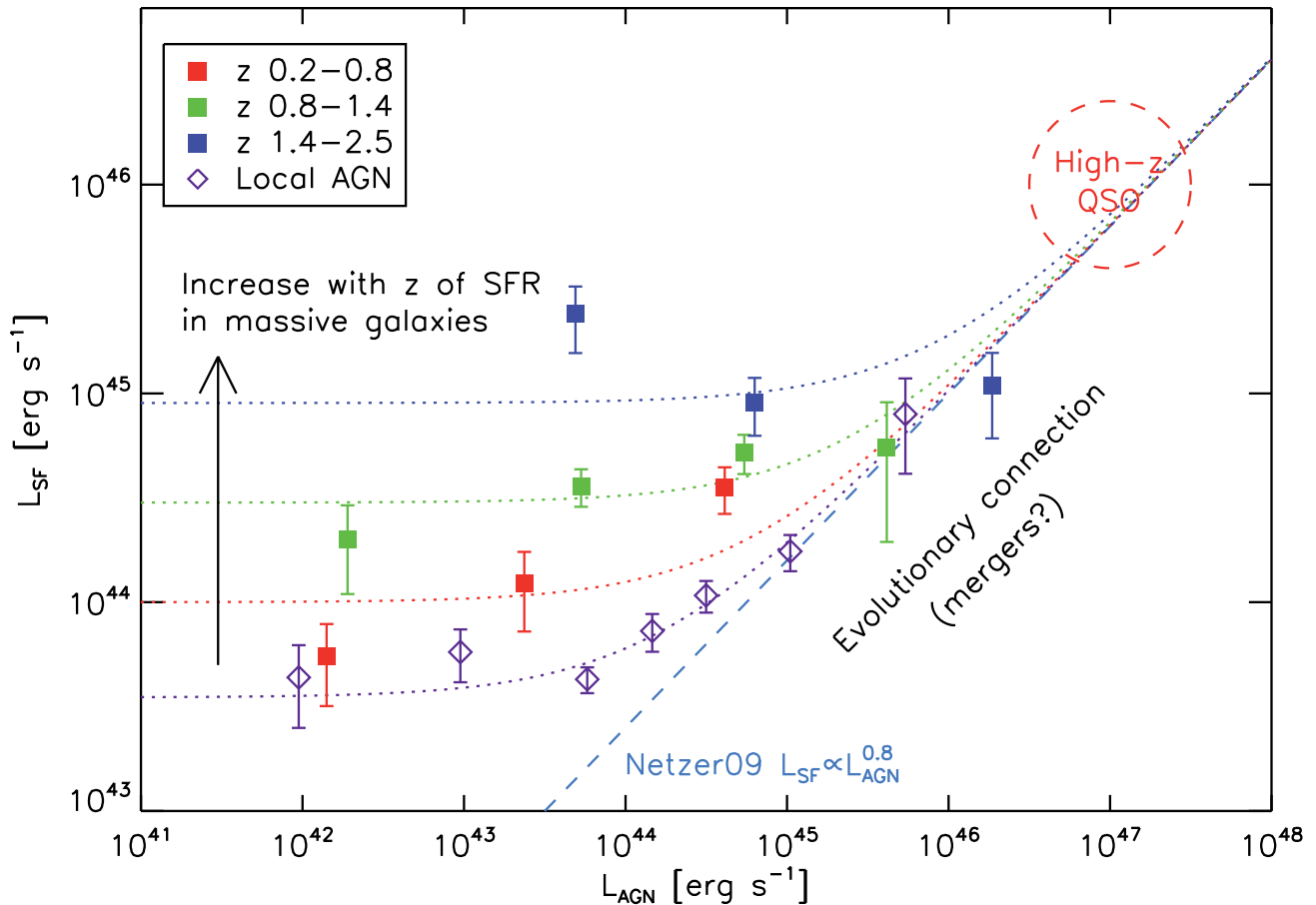


Fig. 2: Star forming (=far-infrared) luminosity vs. AGN luminosity for the GOODS-N AGN and a local reference sample of extremely hard X-ray selected Swift/BAT i.e. AGN. The dotted coloured lines indicate schematically how the observations are explained by the combination of a diagonal 'evolutionary connection' trend with a general increase of host star formation with redshift in hosts of moderate luminosity AGN, similar to that for the general galaxy population.

lutionary Probe' survey program (see also section 2.2): Starting with observations of the GOODS-N field we can now directly probe the rest-frame far-infrared SED peak and have sufficient sensitivity to individually detect 20% of X-ray selected bona fide AGN from the deepest X-ray data in the overlapping "Chandra deep field" exposed for 2 Msec by Chandra. We can now break the AGN samples into small groups, according to parameters like redshift, AGN luminosity or other quantities, and avoid degeneracies that are present by averaging over larger samples. For the redshift and AGN luminosity range sampled by the GOODS-N data, the dominant effect is an increase of the star host formation rate with redshift, while at redshifts above  $z=1$  both, AGN luminosity and obscuration, seem to play a less important role. In conjunction with properties of local and luminous high- $z$  AGN, we interpret our results as reflecting the interplay between two paths of AGN/host co-evolution. A correlation of AGN luminosity and host star formation is traced locally over a wide range of luminosities and also extends to luminous AGN at high  $z$ . This correlation reflects an evolutionary connection, probably via galaxy merging. For lower AGN luminosities, star forma-

tion is similar to that in non-active massive galaxies and shows little dependence on AGN luminosity. The level of this secular star formation increasingly dominates over the correlation at increasing redshift.

Upcoming Herschel observations will further enhance sensitivity, sample size, and the covered AGN luminosity range. This will permit a more detailed comparison of AGN hosts with inactive galaxies, as well as a better characterisation of the most luminous AGN where evolutionary effects may play a stronger role.



D. Lutz with L. Shao, R. Nordon

## AGN in the COSMOS Survey: The Population of $z>3$ Black Holes and the Evolution of Black Hole-Galaxy Scaling Relations at $1<z<2$

We highlight here two recent results on the properties of Active Galactic Nuclei (AGN) detected in the COSMOS survey. First, we present a study of a large, complete sample of X-ray selected AGN for  $z>3$ . It shows for the first time, evidence of a rapid decline in the number density of un-obscured and moderately obscured X-ray AGN at high redshift, a behaviour analogous to that of more luminous SDSS quasars. Second, we discuss new constraints on the evolution of the scaling relations between SMBH and host galaxies as derived from a sample of 89 broad-line AGN, selected spectroscopically from the zCOSMOS survey between 1 and 2.2. Clear deviations are observed from the local relation both in its absolute normalization and, possibly, its scatter. This provides important tests for wide families of AGN feedback models.

### Introduction

Several seminal discoveries in the past decade revealed tight links and feedback loops between super-massive black holes (SMBH) growth, nuclear activity and galaxy evolution, supporting the notion that AGN not only are witnesses of the process of galaxy formation and/or assembly, but most likely among the leading actors. The discovery of SMBH in the center of most nearby bulge dominated galaxies, and the steep and tight correlations between their masses and galaxy bulge properties constituted the first piece of evidence in favor of such a connection between galaxy evolution and central SMBH growth. Such a growth is now known to be due to radiatively efficient accretion over cosmological times, taking place dur-

ing “active” phases. The characterization of the bulk of the AGN population, made possible by extensive programs of optical and NIR follow-up observations of X-ray selected sources, has allowed astronomers to put the evolution of accretion luminosity over a significant fraction of cosmic time on solid grounds. The evolution of the AGN luminosity function (LF) turns out to be luminosity dependent, with lower luminosity AGNs peaking at a lower redshift than luminous QSOs. This “anti-hierarchical” behavior observed in AGN and inferred for the SMBH growth is similar to that observed for star formation, and is usually referred to as “cosmic downsizing”. This is one of the greatest achievements in observational cosmology obtained by Chandra and XMM-Newton surveys, lending a second, independent support to the idea that the formation and evolution of SMBHs and their host galaxies are closely related.

Many open issues however remain. If AGN are indeed such a fundamental ingredient of the structure formation process, a full understanding of galaxy evolution requires a SMBH census through cosmic time as complete as possible. Hard X-ray surveys could so far constrain the luminosity function up to relatively low redshift ( $z\sim 2-3$ ). The question then remains of the exact form of the high-redshift evolution of AGN, and of their possible role in a crucial epoch of galaxy formation. On the other hand, the local scaling relations between black holes and host galaxies have proved themselves unable to uniquely determine the physical nature of the SMBH-galaxy coupling. A large number of feedback models have been proposed which can reasonably well reproduce them, but make different predictions for their redshift evolution.

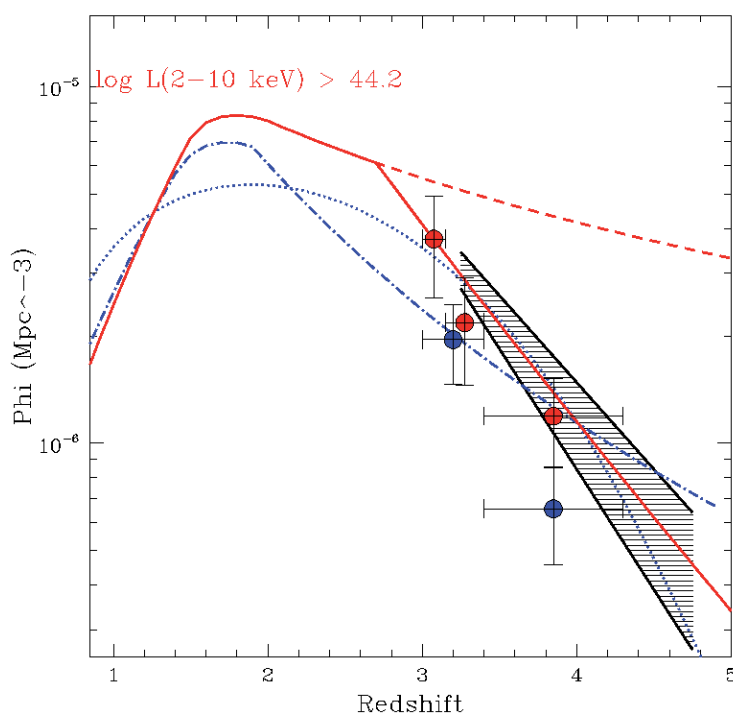


Fig. 1: The comoving space density in three different redshift bins for the  $z>3$  XMM-COSMOS sample. Red symbols (with associated errors) refer to the full sample (34 objects) and have been corrected for incompleteness against obscured sources. The red curve corresponds to the X-ray selected AGN space density computed for the same luminosity limit from a X-ray Background model. At  $z>2.7$  we plot two curves: with (solid) or without (dashed) exponential decline in the LF. The dot-dashed and dotted lines correspond to two extrapolations of LF. Thus should be compared to the blue symbols, which refer to the  $i<24$  sample (28 objects) and are corrected only for volume incompleteness. The black shaded area represents the shape derived from brighter optical quasars surveys, rescaled up by a factor of  $\sim 80$  for an easier comparison with the X-ray data.

## The COSMOS, XMM-COSMOS and zCOSMOS Surveys

The Cosmic Evolutionary Survey (COSMOS) is the largest HST survey ever undertaken, imaging an equatorial of  $2\text{deg}^2$  field with single-orbit I-band exposures to a point source depth of IAB=28 mag. Extensive multi-wavelength ground- and space-based observations collected, spanning from X-ray, UV, optical/IR, mid-infrared, mm/submm to the radio band, with very high sensitivity in imaging and spectroscopy. The aim of COSMOS is to thoroughly map the morphology of galaxies as a function of local environment (density) and epoch, from the high redshift ( $z>3$ ) to the nearby ( $z<0.5$ ) Universe.

The XMM-Newton wide-field survey in the COSMOS field (XMM-COSMOS) covered the entire area of the HST/ACS COSMOS for a total of  $\sim 1.55$  Ms during AO3, AO4 and AO6 cycles of XMM observations. XMM-COSMOS provides a uniquely large sample of point-like X-ray sources ( $>1800$ , mostly AGN), detected on a large, contiguous area, with complete ultraviolet to mid-infrared (including Spitzer data) and radio coverage, and extensive spectroscopic follow-up. The excellent multi-band photometry available in this area allows a robust photometric redshift estimate for the faint sources not reachable by optical spectroscopy, thus allowing a virtually complete sample of X-ray AGN for which a full characterization of the physical properties is possible. Thus far MPE played the leading

role in the survey, as well in the data reduction, as well as in analysis and exploitation. The zCOSMOS survey is the spectroscopy follow-up of the COSMOS field. Its bright sample consists, at the time of writing, of 10,644 medium resolution spectra, observed with the VIMOS multi-object spectrograph on ESO-VLT, in the COSMOS field, selected only on the basis of their IAB magnitude (IAB $<22.5$ ). MPE scientists have taken up an important part in the data-reduction and scientific exploitation of the AGN component of the zCOSMOS survey.

### XMM-COSMOS: unambiguous signs of a fast decline in the number of bright AGN at high-z

The  $z>3$  QSO sample drawn from the XMM-COSMOS survey allowed, for the first time, to firmly address the issue of the evolution of high redshift hard X-ray selected AGN. This homogeneous and sizable sample of X-ray sources is much less biased against mildly obscured AGN and has an almost complete redshift information. The results indicate that the comoving space density of X-ray luminous ( $L_x \geq 10^{44}$  erg/s) QSOs at  $z \sim 3$  is  $(3.7 \pm 1.2) \times 10^{-6} \text{ Mpc}^{-3}$  and declines exponentially (by an e-folding per unit redshift) in the  $z \sim 3.0-4.5$  range (Fig. 1).

Such a high-redshift cut-off is similar to that of luminous ( $M_1 < -27.6$ ), optically bright, unobscured QSOs, which is well established by SDSS observations. Therefore, it appears that the evolution of mildly obscured (Compton thin)

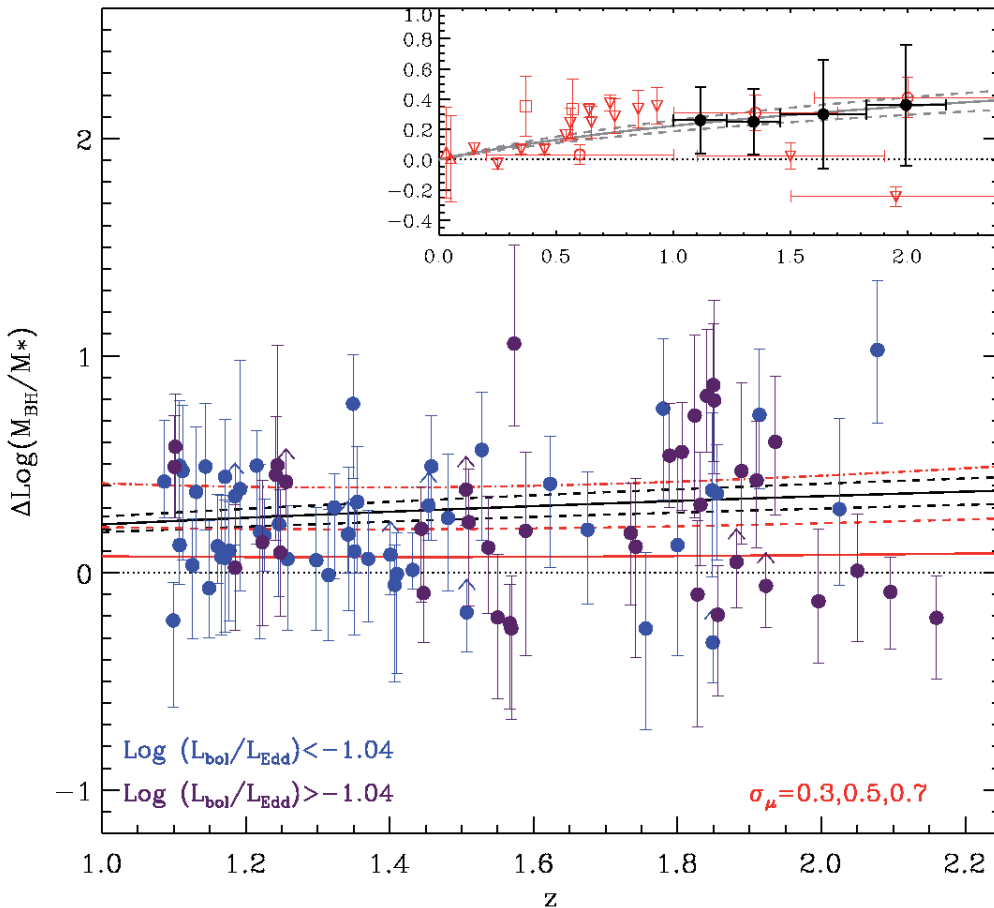


Fig. 2: Redshift evolution of the offset measured for zCOSMOS type 1 AGN from the local  $M_{\text{BH}}-M^*$  relation. Black lines show the best fit assuming an evolution of the form  $\Delta\text{Log}(M_{\text{BH}}/M^*)$ : of  $(z)=(0.68 \pm 0.12) \text{Log}(1+z)$ . Red lines show the bias due to the intrinsic scatter in the scaling relations, expected even if they are universal. The solid line is for an intrinsic scatter of 0.3 dex, similar to the locally observed value; dashed of 0.5 dex and dot-dashed of 0.7 dex. The inset, shows a comparison of our data (black circles) for data from the literature.

AGN follows that of unobscured, optically luminous QSOs, provided that the shape of the high-redshift decline holds also for luminosities about an order of magnitude lower than those probed by SDSS.

The observed decline in the comoving space density of X-ray selected QSOs, at least for luminosities larger than  $\sim 10^{44}$  erg/s, has a significant impact on the predictions of QSOs number counts expected for future large area X-ray surveys, in particular for the MPE-led eROSITA (extended ROentgen Survey with an Imaging Telescope). eROSITA will fly on the SRG (Spectrum Röntgen Gamma) mission, which will be launched at the end of 2012. eROSITA will survey the entire extragalactic sky, down to a limiting flux of  $\sim 10^{-14}$  erg/s/cm<sup>2</sup> in the 0.5-2 keV band, providing an estimate of  $\sim 25000$  QSOs for  $z > 3$  and 2100 for  $z > 4$ . An area of  $\sim 400$  deg<sup>2</sup> will be covered in a deeper survey with a limiting magnitude of  $4 \times 10^{-15}$  erg/cm<sup>2</sup>/s and additional  $\sim 2500$  QSOs for  $z > 3$  and about 200 for  $z > 4$ .

### Evolution of scaling relations between $1 < z < 2$ in zCOSMOS unobscured AGN

Within the zCOSMOS collaboration we have pioneered a new method to unveil the intrinsic physical properties of AGN hosts, using the unprecedented multi-wavelength

coverage of the COSMOS field. We were able to measure rest frame K-band luminosities and total stellar masses,  $M^*$ , of the hosts of 89 broad-line (un-obscured) AGN in the redshift range  $1 < z < 2.2$ , the largest high redshift sample so far for which reliable black hole and galaxy masses are available. We found that, as compared to the local value, the average black hole to host galaxy mass ratio appears to evolve positively with redshift, with a best fit evolution of the form  $(1+z)^{0.68}$  (see Fig. 2). A thorough analysis of observational biases, induced by intrinsic scatter in the scaling relations, reinforces the conclusion that an evolution of the  $M_{\text{BH}}-M^*$  relation must ensue for actively growing black holes at early times: either its overall normalization, or its intrinsic scatter (or both) appear to increase with redshift.

All models, relying on very rapid (“explosive”) AGN feedback to halt star formation in the host galaxies, have difficulties in reproducing these observations. The situation changes if we assume that black holes and spheroids obey a universal relation, whereby  $M_{\text{BH}} \sim M^* \sigma^2$ . In this case, dissipation effects occurring in gas-richer environments (at higher redshift) may deepen the potential well around the black hole, allowing it to grow above the local relation, to a degree marginally consistent with our results. Further constraints will be possible by thorough theoretical modeling of our data, especially of the observed scatter.



M. Brusa, A. Merloni, G. Hasinger, A. Bongiorno and N. Cappelluti

## Results from the Swift all-sky Survey

The all-sky survey at hard X-rays performed by the Burst Alert Telescope (BAT) on board the Swift Mission has significantly changed our knowledge of the X-ray sky. At MPE we have been (and are currently still) processing all the data of the BAT all-sky survey. We apply a maximum likelihood algorithm (originally developed for COMPTEL data analysis) which allows us to minimize systematic noise inherent in the canonical way of co-adding coded-mask images (Ajello et al. 2008). The main result arising from this study (Ajello et al. 2008) is a clear lack of strongly absorbed AGN. These sources were expected to constitute a relevant fraction (20-30%) of the total AGN population (in the BAT energy band). Our study rejects the hypothesis that Compton-thick AGN comprise  $>20\%$  of the total population at  $>2\sigma$ . BAT resolves only 1.5% of the Cosmic X-ray background (CXB) into AGN, nevertheless its unbiased sample (with respect to absorption) can be used to test AGN unification schemes. Indeed, Seyfert 1 and 2 show different spectral slopes in the BAT survey. This seems to be due to a different cut-off energy which in turn might arise from a different energy of the electron population in the corona.

The CXB spectrum peaks around 30 keV. However, its spectral shape and normalization were poorly known in the 15-150 keV band because of the difficulties connected with its measurement. The uncertainty on its normalization translates into a similar uncertainty about the density of Compton-thick AGN. Using the Earth occultation technique a new measurement of the X-ray background with Swift/BAT has been made. This measurement turns out to be the most accurate one so far and reveals that the normalization of the CXB spectrum is  $\sim 8\%$  larger than previously measured (Ajello et al. 2008, and left panel of

Fig. 1). This translates into a constraint for the density of Compton-thick AGN in the Universe. As a side product of this analysis we also derived the 15–150 keV spectrum of the Earth albedo emission. This albedo spectrum, also the most accurate so far obtained, is crucial to estimate the orbital photon background for the next generation hard X-ray missions. Both these measurements are anticipated to be a reference for many years to come.

Using data from BAT, we have performed the very first thorough study of a sample of 10 galaxy clusters above 10 keV. We aimed at determining the level of energy locked in non-thermal cosmic rays. This is very important as clusters are often used as cosmological probes, but their mass is simply estimated from hydrostatical equilibrium. This estimate would not be correct if the energy deposited in cosmic rays is relevant. Contrary to previous claims, we detected no inverse Compton emission from non-thermal electrons (at the current sensitivity). This allowed us to place a sensitive lower limit on the intra-cluster magnetic field. We also showed that the non-thermal emission, present in some clusters, is due to the central AGN (Ajello et al. 2009, and right panel of Fig. 1).

We also used the BAT sample to study the clustering of AGN in the local Universe for the first time (Cappelluti et al., submitted to ApJ). The real space-projected auto-correlation function displays a significant signal on projected scales below 200 Mpc/h with a typical correlation length of  $7.35 \pm 1.50$  Mpc/h. Moreover, we found  $\sim 3\sigma$  evidence of a luminosity-dependent clustering of AGN, since we detected a larger correlation length of luminous AGN than of low luminosity sources. We find that the typical host of the BAT AGN has a dark matter halo mass of  $\log(\text{mass}) < 13-13.5 M_{\odot}$ , showing that local ( $z < 1$ ) AGN environments are red, massive early-type galaxies in low massive groups.

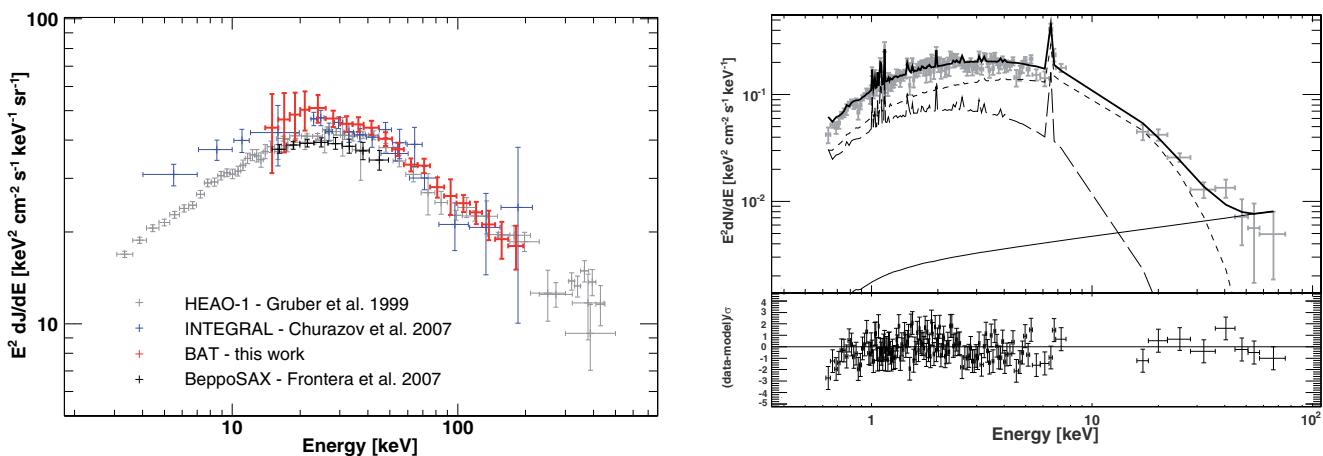


Fig. 1: (Left) Spectrum of the Cosmic X-ray Background as derived from Swift/BAT data compared with recent measurements. (Right) Combined XMM-Newton and Swift/BAT spectrum of the Perseus cluster of galaxies. The solid line is a power-law like emission produced by the Active Galaxy NGC 1275.

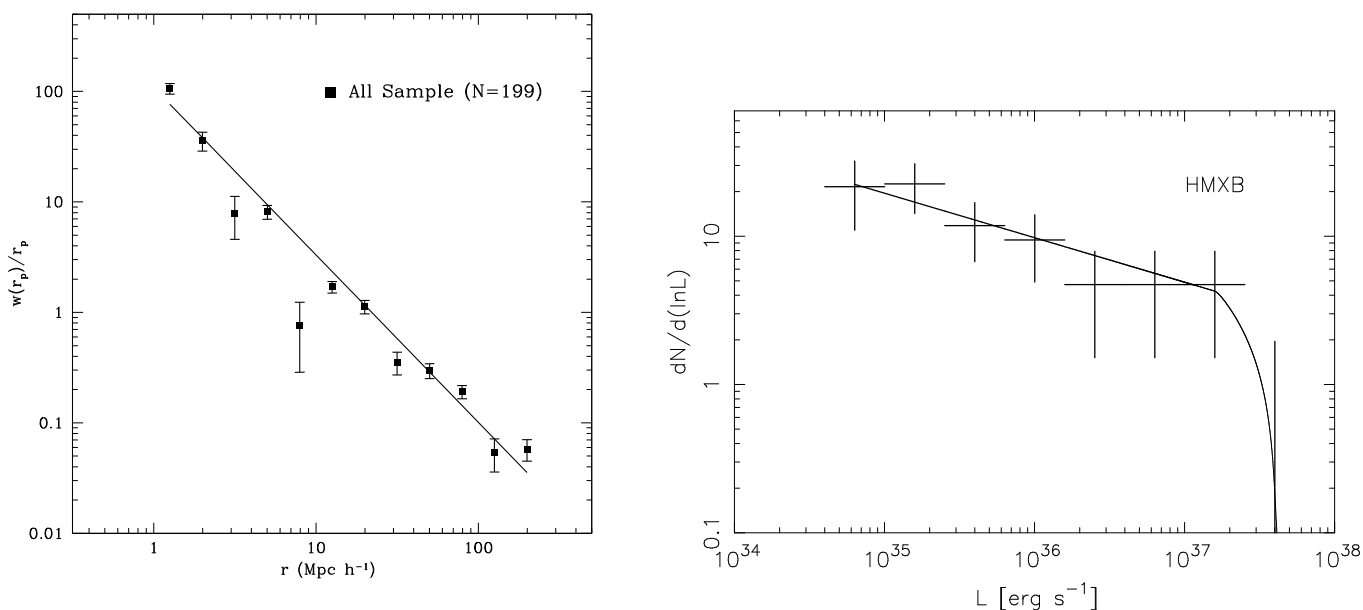


Fig. 2: (Left) Auto-correlation function of 199 AGN found in the BAT survey. The power-law behavior shows that AGN tend to cluster together built clusters/to cluster. (Right) Luminosity function of HMXBs as derived in the 15-55 keV band using BAT.

Using two years of BAT data we performed a study of the populations of X-ray sources in the Milky Way concentrating in particular on the properties of the X-ray binaries (Voss et al. submitted to ApJ). For the low-mass X-ray binaries (LMXBs) and the high-mass X-ray binaries (HMXBs) we derive the luminosity functions to a limiting luminosity of  $L_x \sim 7 \times 10^{34} \text{ erg s}^{-1}$ . Our results confirm the previously indicated flattening of the LMXB luminosity function below a luminosity of  $L_x < 10^{37} \text{ erg s}^{-1}$ . The luminosity function of the HMXBs is found to be significantly flatter in the 15-55 keV band than in the 2-10 keV band. From the luminosity functions we estimate the ratios of the hard X-ray luminosity from HMXBs to the star-formation rate, and the LMXB luminosity to the stellar mass. We use these to estimate the X-ray emissivity in the local Universe from X-ray binaries and show that it constitutes only a small fraction of the hard X-ray background.

White dwarf masses in cataclysmic variables are difficult to determine accurately, but are fundamental for understanding binary system parameters, as well as binary evolution. We investigated the X-ray spectral properties of a sample of Intermediate Polars (IP) detected above 15 keV by Swift/BAT to derive the masses of their accreting white dwarfs (Brunschweiler et al. 2009). We were able to produce mass estimates for 22 out of 29 confirmed IPs. Comparison with the one IP from which the mass is accurately determined through eclipse mapping shows perfect agreement, demonstrating that the method is not too simplistic. For GK Per, we were able for the first time to detect spectral changes due to the changes in the accretion rate, as predicted by theory since 2 decades. The Swift/BAT detector with its combination of sensitivity and all-sky coverage provides an ideal tool to determine accurate white dwarf masses for all IPs, also those which are being identified with presently operating missions (already 7 new systems since our publication).



M. Ajello and J. Greiner

## 2.4 STELLAR EVOLUTION AND THE INTERSTELLAR MEDIUM

Stars are created from dense cores in molecular clouds. Depending on their mass, they evolve more or less rapidly through mainsequence and giant phases, until they end either as compact remnant stars and/or in violent explosions. MPE interests are the studies of stars in a few specific phases: Early-on near formation (IR emission from protostellar disks and circumstellar matter), the late compact remnants (optical, X-ray, and  $\gamma$ -ray emission from pulsating neutron stars, X-ray emission from binary mass accretion and from novae), and through their explosions (X-ray and  $\gamma$ -ray emission from  $\gamma$ -ray bursts, from supernova remnants and from nucleosynthesis). The interstellar medium is the host of stars, its state and dynamics determine how stars are created eventually. Stellar outputs, their wind and explosion energies and their ejecta, shape this state and dynamics. MPE's special access to the processes in the interstellar medium is through molecular lines near newly forming stars and through radioactive ejecta and cosmic-ray initiated radiation processes.

Lessons from specific objects are transferred to populations of sources or entire galaxies. This connects these specific studies on nearby, more easily accessible objects to models of stellar and galaxy evolution, used to interpret data from distant-universe observations when those objects cannot be resolved. In this 2009 report, we cover the full range of science issues and wavelength regions, and highlight first results from the Herschel mission on circumstellar chemistry, on the high-energy aspects of interstellar medium in our Galaxy, on novae in M31, and on Gamma-Ray Bursts.

Beyond these separately presented results, MPE scientists have learned other new aspects of stellar evolution and the ISM: SN1987's X-ray brightening came as a surprise and will probe the pre-supernova star's wind history.  $^{44}\text{Ti}$  radioactivity constrains Cas A inner ejecta to still being faster than  $500 \text{ km s}^{-1}$  on average, 350 years after the explosion. A bright X-ray nova showed remarkable variations of its accretion disk. Magnetar flares were seen at optical and  $\gamma$ -ray energies. This stimulates and challenges our models for magnetized neutron stars. Newly discovered gamma-ray pulsars take us closer to a standard model for pulsar magnetospheres and their radiation beams from radio through optical to  $\gamma$ -rays. Gamma-ray burst pulse arrival simultaneously across different wavelength regions constrains models for quantum gravity. New sources, embedded in interstellar clouds, are being discovered by INTEGRAL, among them a surprising new class of high-mass X-ray binaries. The role of starlight interacting with cosmic-ray electrons has been underestimated, diffuse  $\gamma$ -ray emission can now be modelled more realistically (see Fig.1).

In the coming years, we will see the late-mission phases of XMM-Newton and INTEGRAL, where the discoveries they made will receive consolidation and refinements. New missions, Herschel and FERMI, are creating more excitement. MPE will continue its multi-bandview on all aspects of stellar-evolution and the interstellar medium.

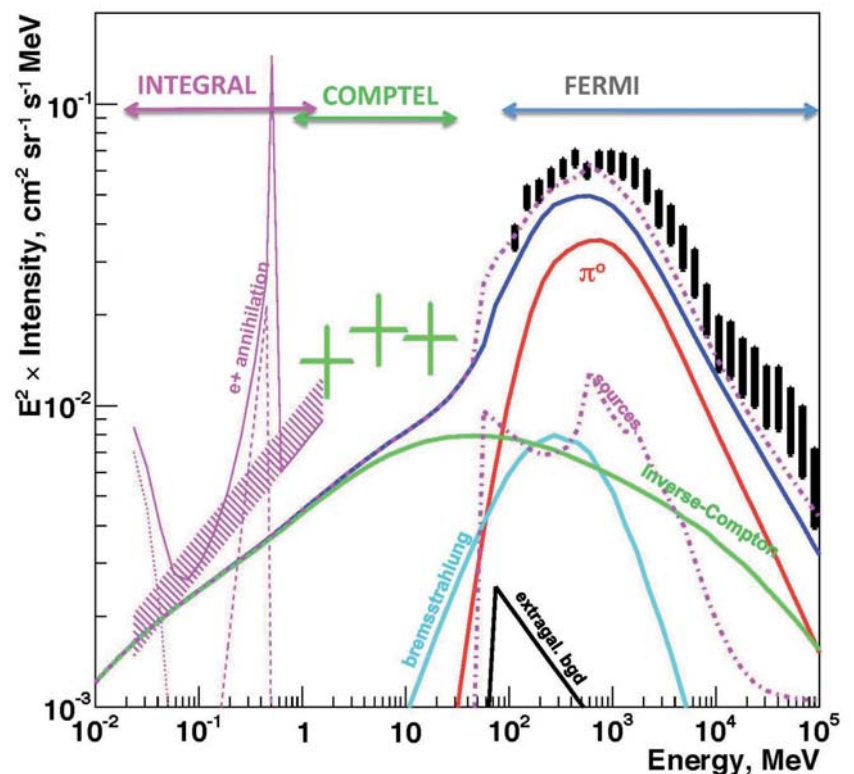


Fig. 1: Broad-band spectrum of the Galactic Ridge over 7 decades of energy, from recent INTEGRAL and FERMI measurements. The radiation process components as estimated from GALPROP code (see second article for details) are shown.

## Studies of Star Formation and the ISM in the Herschel Era

Warm dense gas in the interstellar medium (ISM) and star-forming regions in our Milky Way as well as in other galaxies is best probed at sub-millimetre and far-infrared wavelengths. Due to its unprecedented capabilities (high sensitivity, high spatial and spectral resolution, large far-infrared wavelength range) the Herschel Space Observatory will revolutionize the study of these regions. We are carrying out various guaranteed time programmes on this subject. Herschel, launched in May 2009, has already delivered spectacular first results from these programmes.

A key molecule for the study of star- and planet-forming regions is  $\text{H}_2\text{O}$ . Water is one of the most abundant and important molecules in such regions, not in the least because of its direct association with the biology of living organisms on Earth. Although only a trace species in general clouds, water becomes the third most abundant molecule in the warm regions created by the presence of newly-formed stars. With PACS we have now detected water in three young stellar objects observed during the Herschel Science Demonstration Phase. These are from a sample of almost 90 young stellar objects that will be observed as part of the Water In Star-forming regions with Herschel (WISH) key programme. WISH will investigate the physical and chemical structure of star forming regions by focussing on the distribution of water and its related species in regions in which new stars are forming. This process takes place deep inside dark clouds and cannot be studied at optical wavelengths.

Young stars produce powerful jets during their birth, in a process which is not yet fully understood. In the first PACS observations of L1157 (a low mass young stellar object comparable to our Sun when it was a toddler), the water distribution in the environment of this young protostar clearly traces regions along the jets where shocks deposit energy into the cloud surrounding the protostar. Fig. 1 shows the first water map of such a region and beautifully illustrates the power of PACS to 'light up' the interaction of the young star with its surroundings.

Strong water lines were also detected in NGC 7129 (an intermediate mass young stellar object), along with other related trace lines (OH, CO and [OI]). These new observations (Fig. 2) challenge the current models describing the environment of this object. As young stars heat up their surroundings, water molecules frozen on the icy grains evaporate back into the gas phase, just like ice on a comet in our own Solar System sublimates when heated by the Sun. Thus, the embryonic stars themselves are expected to exhibit copious signatures of steam. PACS has detected numerous fingerprints of gaseous water toward a forming star that is slightly more luminous than our own young Sun (Fig. 2). The cloud, seen by PACS, contains enough water to fill at least a million oceans!

As an example of extragalactic studies of the ISM with Herschel we show here (Fig. 3) results for Messier 82 (M82), a prototype nearby starburst galaxy, about 12 million light years away in the constellation of Ursa Major. The obser-

ervations are part of the PACS Guaranteed Time Programme SHINING (Survey with Herschel of the ISM in Nearby Infrared Galaxies). The aim of this programme is to study star formation and activity in infrared bright galaxies (starbursts, active galactic nuclei, (ultra-)luminous infrared galaxies, low metallicity galaxies, and interacting galaxies) at local and intermediate redshifts. M82 is part of an interacting group of galaxies, including the large spiral M81 from which material is being stripped by the gravitational interaction with M82. M82 is famous for its spectacular bi-polar outflow or "superwind", gas and dust driven outwards by stellar winds and supernovae in the galaxy's central regions, where stars are produced at a very high rate. The physical conditions in the interstellar medium of such a galaxy vary strongly across the different environments. PACS provides for the first time the necessary sensitivity and imaging capability with sufficient spatial resolution in the far infrared to study these variations in detail. Spectral images from two important tracers of the ISM in the far infrared are shown in Fig.

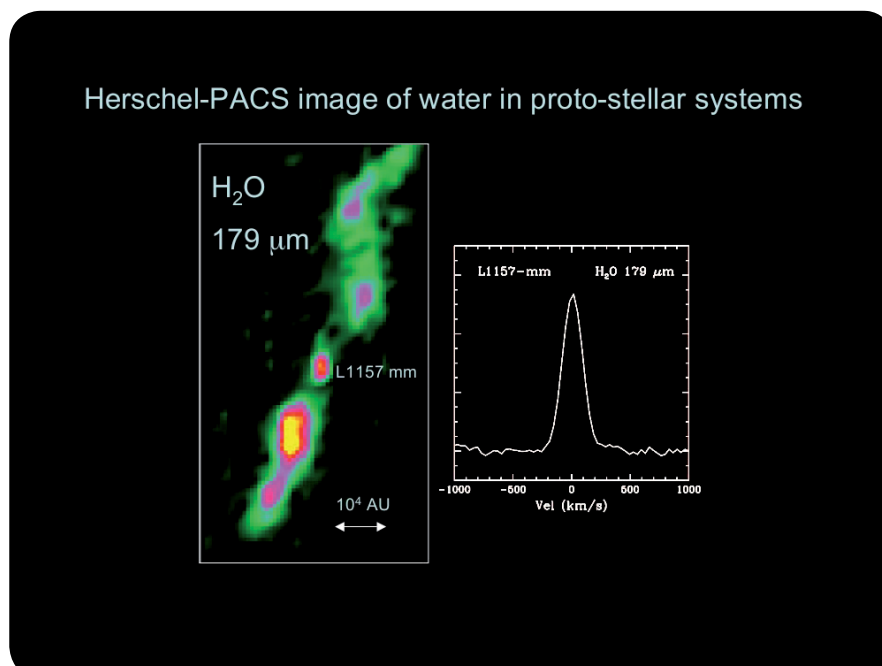


Fig. 1: The water molecule is a particularly sensitive probe of where a young star deposits energy into its surroundings. Its signatures are strongly detected and imaged by PACS along the two-sided outflow lobes of an analogue of the young Sun, L 1157. The water emission shows up most strongly in "hot spots" due to strong shocks symmetrically displaced from the young star. The extent of the outflow is about  $3'$ , corresponding to 0.35 parsec at the distance of L1157 (or 70000 AU).

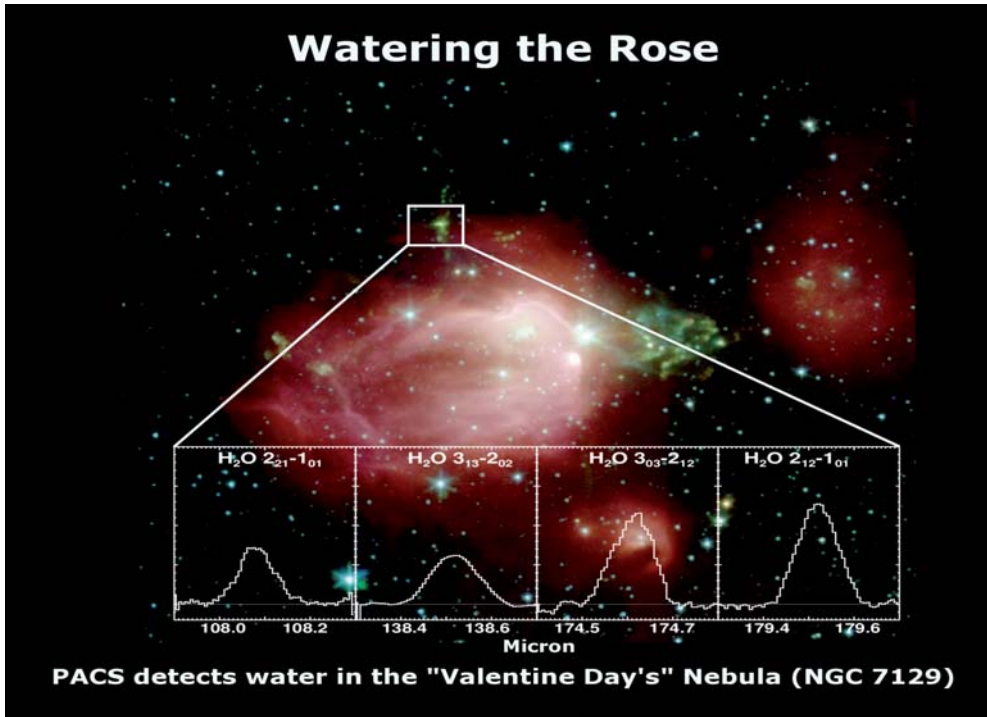
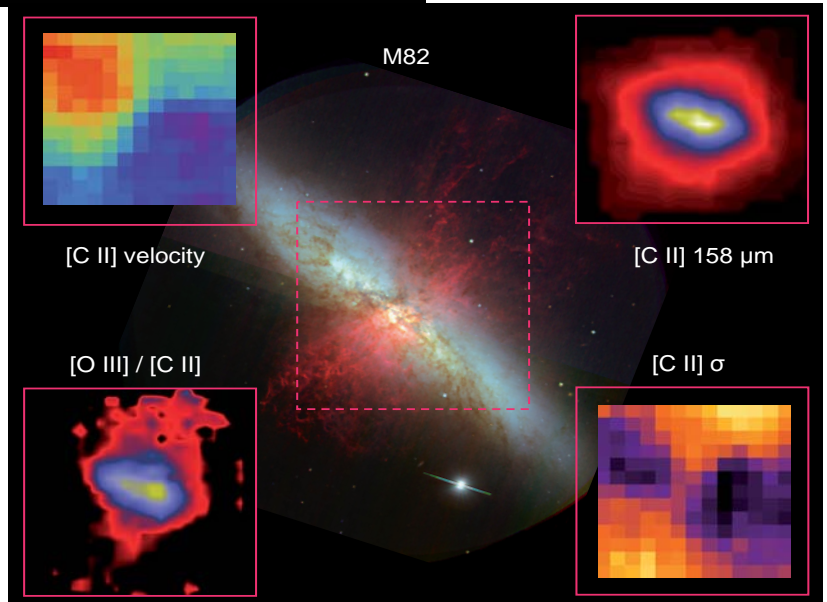


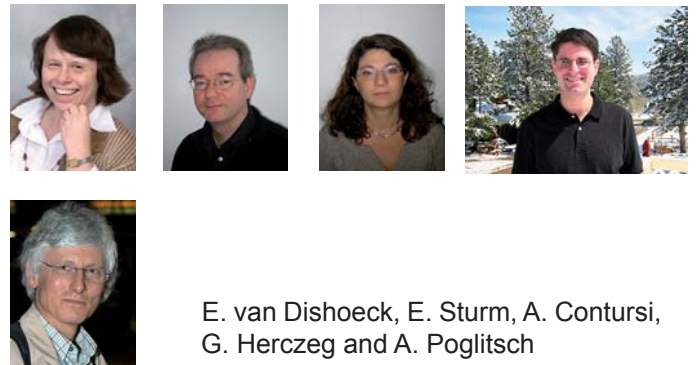
Fig. 2: PACS spectra of various strong fingerprints of water toward the embryonic star NGC 7129. The background image is the 'Valentine day' ('Rose') nebula - a stellar nursery resembling a pink rosebud - observed by the Spitzer Space Telescope (NASA/Caltech).

Fig. 3: Hubble Space Telescope image of the starburst galaxy M82 (NASA/ESA/STScI/AURA/The Hubble Heritage Team) with the pink box outlining the area mapped by the PACS spectrometer. Insets: top right: (colour-coded) intensity map in the light of a spectral line of carbon ([C II]); bottom right: the velocity dispersion of that line, showing increased turbulence in the super wind; bottom left: the ratio of an oxygen line over the carbon line; the variation of this ratio reflects the different physical conditions across this galaxy; top left: the peak velocity of the [C II] line, showing the typical distribution of a rotating disk.



3: line emission from doubly ionized oxygen ([O III]) and from singly ionized carbon ([C II]). The ratio [O III]/[C II] of these two lines, a diagnostic of ionized gas vs. neutral gas drops rapidly going outwards from the galaxy centre along the disk. In contrast to this the ratio drops less when going outward in the super-wind direction.

These are only the very first examples from our Herschel programmes on the study of the ISM in the Milky Way and in nearby galaxies. Many hundreds of hours of observations for a large number of different objects are still to come and will undoubtedly improve drastically our knowledge in this research area.

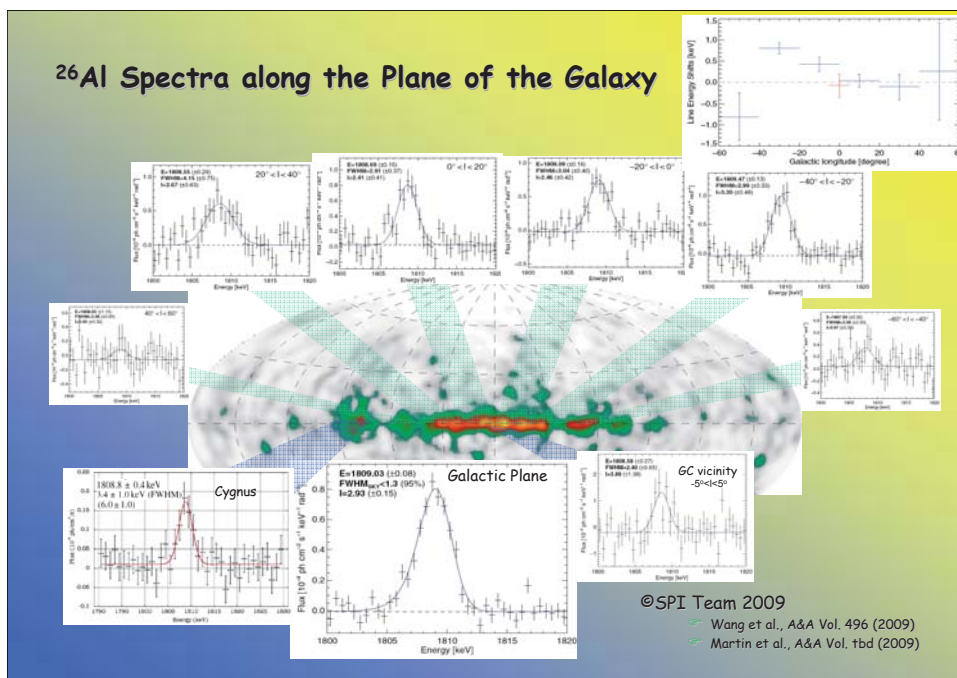


E. van Dishoeck, E. Sturm, A. Contursi, G. Herczeg and A. Poglitsch

# Studying our Galaxy's Interstellar Medium with High-Energy Photons

Gamma-rays at 10 keV to 100 GeV result from cosmic-ray interactions in the interstellar medium, from nuclear processes following radioactive decays and annihilation of positrons. At MPE, SWIFT, INTEGRAL and Fermi  $\gamma$ -ray data are used to study the origin of cosmic rays and their propagation in the interstellar medium, and the associated role of massive star. Such stars determine the state and morphology of the interstellar medium through their various outputs (radiation, wind and explosion energies, and ejecta). Cosmic-ray acceleration is also assumed to take place in massive-star regions. Such stars, presumably formed from interstellar-cloud filaments, swept up by interstellar turbulence; but exactly how such "feedback" happens is still not understood, yet is one of the most important processes to shape the evolution of galactic disks.

ridge of the Galaxy, is now possible for spatially confined regions as exposure (hence signal strength) increases. Different regions of massive stars along the plane of the Galaxy can be separated (Fig. 1). For the Cygnus complex of massive stars, which includes one of the Galaxy's most-massive clusters Cyg OB2, initial hints for Doppler broadening and a small shift are not confirmed. Line centroid and width are compatible with bulk motion below 50 km/s and turbulent velocities less than 100 km/s. The measured  $\gamma$ -ray intensity falls on the high side of model predictions, and points to inadequacy of massive-star nucleosynthesis models, in particular for the Wolf-Rayet wind ejections, which dominate  $^{26}\text{Al}$  in this region. The nearby Sco-Cen region was now identified as an individual and distinct source of  $^{26}\text{Al}$ . Stellar subgroups of Sco-Cen have been considered one of the best cases for "triggered star formation".



The spatial distribution of  $^{26}\text{Al}$  can enlighten the massive-star activity over the past several Myr, and contribute to put this conjecture on firmer ground.

Massive-star activity from this region at 110-150 pc distance is held responsible for shaping the morphology of the ISM in the solar vicinity, and for creating the "Local Bubble". The discovery of radioactive  $^{60}\text{Fe}$  nuclei in a sample of crust material from the Pacific Ocean is dated to a nearby event  $\sim 3$  Myr in the past, and attributed to one of the Sco-Cen stars exploding as a supernova.  $^{60}\text{Fe}$   $\gamma$ -rays are also expected from radioactive supernova ejecta. The radioactive lifetime of  $^{60}\text{Fe}$  has been re-measured and found considerably larger than thought before (3.8 versus 2.2 Myr). With SPI, the diffuse glow of the

Fig. 1: INTEGRAL measurements of  $^{26}\text{Al}$   $\gamma$ -ray spectra for regions along the plane of the Galaxy, superimposed onto the all-sky  $^{26}\text{Al}$  image obtained with COMPTEL.

Nucleosynthesis in cores and explosions of massive stars produces new elements and isotopes; among them some are radioactive.  $^{44}\text{Ti}$ ,  $^{26}\text{Al}$  and  $^{60}\text{Fe}$  isotopes emit characteristic  $\gamma$ -rays, that have been measured with  $\gamma$ -ray telescopes. Radioactive  $\beta^+$  decay also produces characteristic  $\gamma$ -rays at 511 keV energy from  $e^+$  annihilation. New measurements have been obtained with INTEGRAL's SPI Spectrometer, where MPE is a PI institute.

Long-lived radioactivities ( $^{26}\text{Al}$ :  $\tau \sim 1.0$  Myr,  $^{60}\text{Fe}$ :  $\tau \sim 3.8$  Myr) trace ejecta flow and dispersion in the ISM on their characteristic decay time scales, which are comparable to the lifetimes of massive stars. The SPI spectrometer is able to measure interstellar velocities down to the 100 km/s range by the shape of these radioactivity  $\gamma$ -ray lines. This measurement, obtained from the first year of INTEGRAL data only for a sufficiently strong integrated signal for the inner

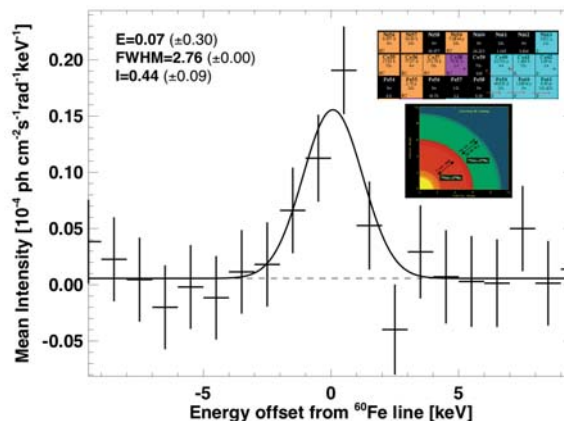


Fig. 2:  $^{60}\text{Fe}$   $\gamma$ -rays have been measured from the Galactic ridge.  $^{60}\text{Fe}$  originates in neutron-capture reactions in massive-star-shell-burning, and is ejected only in the final supernova explosion.

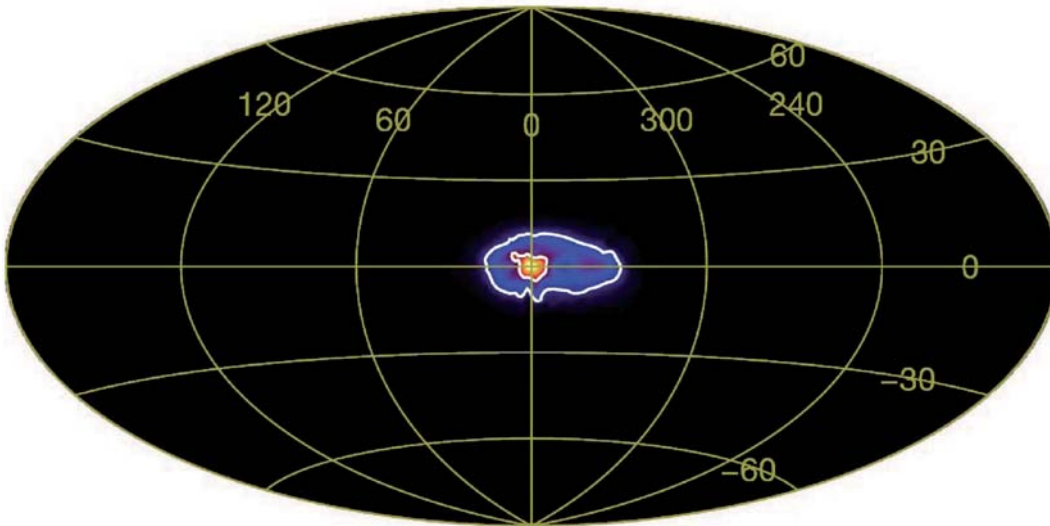


Fig. 3: INTEGRAL map of annihilation emission from the Galaxy. The bulge brightness exceeds the disk brightness by at least a factor 3, candidate positron sources (as e.g. shown in Fig. 1) can explain this only if positron transport can occur over large distances.

Galaxy in  $^{60}\text{Fe}$   $\gamma$ -rays was measured for the first time (Fig. 2). This signal is weaker than expected from massive-star/supernova nucleosynthesis models, which also have been used to predict  $^{26}\text{Al}$   $\gamma$ -rays. The  $\gamma$ -ray intensity ratio  $^{60}\text{Fe}/^{26}\text{Al}$  provides a key constraint to such models.

Positrons will be ejected from  $^{26}\text{Al}$  and  $^{44}\text{Ti}$  decays into interstellar space, and also from  $^{56}\text{Co}$  decay following abundant  $^{56}\text{Ni}$  production in supernovae. SPI has mapped annihilation  $\gamma$ -rays from the Galaxy. Surprisingly, we find the annihilation emission morphology to be significantly different from what is expected from the variety of nucleosynthesis-produced positrons: These sources would all release a substantial amount of positrons along the disk of the Galaxy. In contrast, the Galaxy's bulge is by far the brightest source of annihilation  $\gamma$ -rays (Fig. 3). Cosmic-ray electrons and positrons have been measured directly with space instruments PAMELA and FERMI, and reported a surprising excess of high-energy positrons over a general powerlaw spectrum typical for cosmic rays. It is an interesting puzzle to trace the origins and trajectories of positrons in interstellar space. The GALPROP code for cosmic-ray related high-energy processes in the Galaxy, developed by an international team under the leadership of MPE, has been adopted in a wide community as a mod-

el standard for tracing the effects of cosmic ray / ISM interactions and  $\gamma$ -ray production. This code will play an important role in these positron-source studies. It has been adopted as a model standard in the FERMI team for interstellar  $\gamma$ -ray production. New Galactic-plane survey results are now available from INTEGRAL and FERMI, throughout the keV to GeV-range. GALPROP is our tool to deepen our understanding of these radiation processes in the interstellar medium.



R. Diehl, A. Strong and G. Weidenspointner with M. Lang, P. Martin, H. Ohlendorf, E. Orlando, W. Wang

## Gamma-Ray Bursts – The Phenomenon and a Tool

The understanding of gamma-ray bursts (GRBs) has largely increased over the last 3 years, primarily due the combination of successful continuation of the NASA Swift mission and ground-based follow-up observations, and the launch of NASA's Fermi satellite in June 2008. At the same time, the application of GRBs as probes of the early Universe has made significant progress. While the use of GRBs for studying the properties of their host galaxies is discussed in the section 2.2 on galaxy evolution, we want to describe here the recent contributions of MPE's GRB group to the study of the prompt and afterglow emission properties.

The physics of the prompt emission in GRBs is still widely discussed. While there is general agreement on a non-thermal origin, and mathematically the spectra are well fit by the empirical Band function (two smoothly joined power laws) or a cut-off power law, two problems still plague theoreticians: first, the slope of the low-energy power law of the Band function does not obey the synchrotron limit. Second, the higher the photon energy that is measured, the higher is the required Lorentz factor to avoid the compactness problem, i.e. the pair creation threshold in the dense photon field. Observations with the GBM (where MPE is co-PI institute) and LAT instruments on Fermi, which together span 7 orders of magnitudes in photon energy, were expected to solve these issues. However, the problem may have become worse with the discovery of the long-duration GRB 090902B: it was one of the brightest GRBs observed by the LAT, which detected several hundred photons above 100 MeV during the prompt phase.

Time-resolved spectral analysis revealed a significant power-law component underlying the canonical Band component and dominating the emission below  $\sim 50$  keV and above 100 MeV (Fig. 1). The Band component underwent substantial spectral evolution over the duration of the burst, while the photon index of the power-law component remained constant for most of the prompt phase, and then hardened significantly toward the end. Not only is the origin of this separate power law component difficult to explain, but, more generally, this implies much larger energies emitted in the GeV band. The highest energy photon (33 GeV) is measured from this burst (in fact from any GRB so far). At a redshift of 1.82 it implies a minimum Lorentz

factor of  $>1500$  (assuming a synchrotron origin). This can be relaxed by assuming the synchrotron self-Compton scenario, which therefore seems more likely.

Besides GRB 090902B, several more LAT-detected events are among the most energetic (equivalent isotropic energy emitted) bursts ever observed. Observations of the afterglows of some of these bursts with GROND have allowed us to measure the jet opening angles, and thus to go even one step further: it turns out that also the true, beaming-corrected energy release is very high. In fact, for several of these bursts this energy is approaching the maximum rotational energy of a proto-neutron star, indicating that the remnant must be a black hole and not a millisecond magnetar.

Another intriguing observational result from Fermi-LAT is the detection of GeV emission in nearly all GRBs, which lasts for about one hour after the trigger. Again, the nature of this emission is under debate, with inverse Compton being the prime suspect for the emission mechanism.

The afterglow emission of GRBs is now largely understood thanks to the unique capabilities of the Swift mission, providing the X-ray measurements but additionally enable ground-based follow-up observations through the rapid dissemination of accurate GRB positions. GROND, the 7-channel imager built at MPE and operated at the 2.2m MPI telescope at ESO/Chile since mid-2007, is one of the instruments that exploits the Swift positions. The

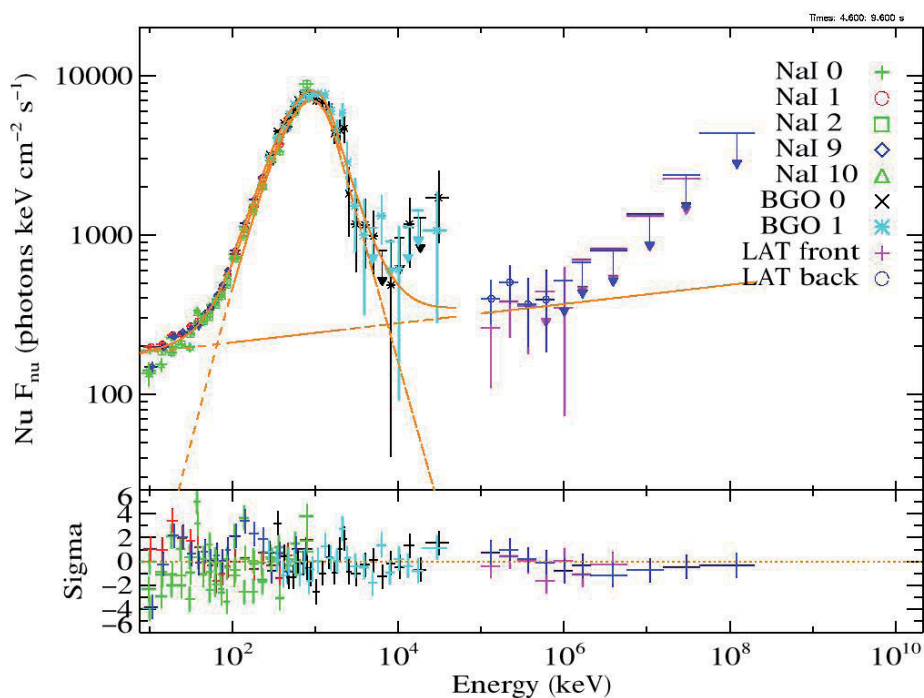


Fig. 1: The  $\nu F_\nu$ -spectrum of GRB 090902B between 10 keV and about 100 GeV. The underlying power-law component dominates the emission below  $\sim 50$  keV and 100 MeV. The Band component "sits" on top of this power-law spectrum.

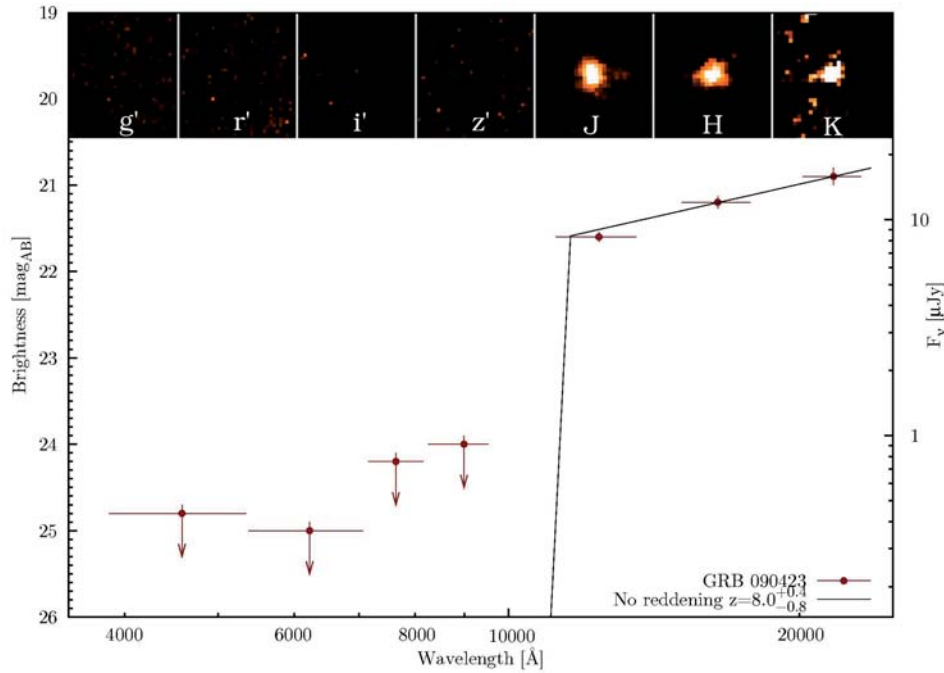


Fig. 2: GROND images and spectrum of GRB 090423. GROND detects the burst only in the three long-wavelength filters, which indicate a redshift of about  $z=8.0$ .

strategy of following each observable Swift burst for as long as possible has allowed us to discover surprising optical flaring activity on top of the canonical afterglow decay. One particularly rewarding case was the burst GRB 071031: The densely sampled early light curve (between 4 min and 7 hrs after the trigger) of the optical/near-infrared (NIR) afterglow consists of 547 individual data points and shows several flares which are superimposed onto the overall rise and decay of the afterglow. These flares have also been seen with the Swift X-ray telescope. We find evidence of spectral hardening in the optical/NIR bands contemporaneous with the emergence of the bumps from the underlying afterglow component. The extrapolation of these hard SEDs matches nicely the X-ray spectra (which actually soften during the flares), and can be consistently described as a continuous shift of the peak energy from the X-ray to the optical band. This and the timing properties suggest late central engine activity as the common origin of these flares.

Another example of the benefit of extended, simultaneous multi-band imaging is the possibility to constrain the jet geometry in the bursts GRBs 080413B and 080710: in both cases it was possible to develop a relatively simple model which fits both the GROND as well as the Swift X-ray data. The subtle changes in decay slope and correlated spectral changes lead pretty uniquely to a two-jet scenario (GRB 080413B) and an off-axis viewing angle (GRB 080710), respectively.

Star formation and chemical evolution in the Early Universe are the main areas where GRBs are particularly useful as tools. The gamma- and X-ray emission is used to pinpoint the locations of high-redshift objects, and the

bright optical/NIR afterglow emission is then used to study the physical conditions in the burst environment as well as along the line-of-sight. Since the launch of Swift in 2004, the GRB redshift frontier has been continuously pushed. A nice demonstration of the working principle of GROND to quickly identify high-redshift GRBs was the detection of the afterglow of GRB 080913 and the recognition of its high- $z$  nature via the detection of a spectral break between its  $i'$ - and  $z'$ -bands. Spectroscopic observations with the VLT were triggered by us within  $\sim 90$  min after the burst, confirmed the high redshift (6.69) and made GRB 080913 the highest redshift GRB at that time, and more distant than the highest-redshift QSO.

Only seven months later, after initial indications of a very high redshift by a British/American group, GROND provided the first reliable redshift-estimate  $8.0(+0.4, -0.8)$  for GRB 090423 (Fig. 2) which subsequently was confirmed by spectroscopic measurements with larger telescopes ( $z=8.2$ ). GRB 090423 is not only the highest-redshift object known to date (at the time of writing), but also demonstrates that massive stars were being produced and died as GRBs only 630 Myr after the Big Bang.



J. Greiner for the GRB team



In the past, just one ROSAT SSS was identified with an M 31 optical nova. This situation changed with the advent of Chandra and XMM-Newton and the improved optical nova catalogues triggered by pixel lensing surveys and more sensitive small telescopes and equipment that allowed effective nova searches in M 31, even by amateurs. Checking X-ray catalogues from archival observations, we identified more than 20 SSS correlations with optical novae. Many of them showed short SSS states, lasting less than half a year, some were still bright 10 years after outburst. We found that more than 30% of the optical novae showed SSS states (many more than previously estimated). From the duration of the SSS state we were able to estimate the mass of the ejecta and the burned mass. This sample could be extended by four SSS/nova correlations from the M 31 disk in the observations of our “deep XMM-Newton survey of M 31”.

Following the archival work on SSSs and optical novae in M 31, we systematically monitored the M 31 center area for a year with four XMM-Newton and four Chandra observations, separated by 1.5 months, starting June 2006. We detected eight X-ray counterparts of CNe, four of which were previously unknown. Two SSS were still visible more than 9 years after the nova outburst, whereas two other nova counterparts showed a short SSS phase of less than 150 days. One of them varied with a 1.6 hour periodicity which may indicate the orbit of the binary system. In the following years we changed the monitoring strategy to 10 observations with 10 day spacing, to be able to follow the very interesting very short SSS phases of novae involving massive WDs. We detected nine novae in X-rays, four within 4 months after the optical outburst. The SSS state of three novae lasted less than 3 months, with M31N 2007-11a holding the record of just 60 days. One SSS correlated with the first nova, detected in a M 31 globular cluster (the He/N nova M31N 2007-06b in Bol 111). We even detected a second SSS in a globular cluster, however unsuccessfully searched for a nova counterpart. This allowed us to estimate the nova rate in M 31 globular cluster systems. SSS and novae in globular clusters are extremely rare objects, just one SSS and two novae were known in globular clusters before the M 31 detections. Nova M31N 2007-12b started its bright SSS phase ~30 days after the optical outburst. In four XMM-Newton observations, in January 2008, it showed 1105 s pulsations (see Fig. 2) which can be explained as the WD rotation period. There are only two additional M 31 SSSs showing similar periodicities, one of which also may be an optical nova counterpart.

In an attempt to homogenize the information on all optical nova candidates in M 31, we created a regularly updated online catalogue (naming all the novae according to the IAU accepted scheme) which contains multi-wavelength information and references.

These first results show that the new monitoring strategy allows us to effectively select peculiar cases of SSSs and novae and to obtain a better understanding of the SSS nova population. This monitoring is also essential to improve the poor statistics of SSS and novae in globular clusters. An extension of the program is granted for 2009/2010.

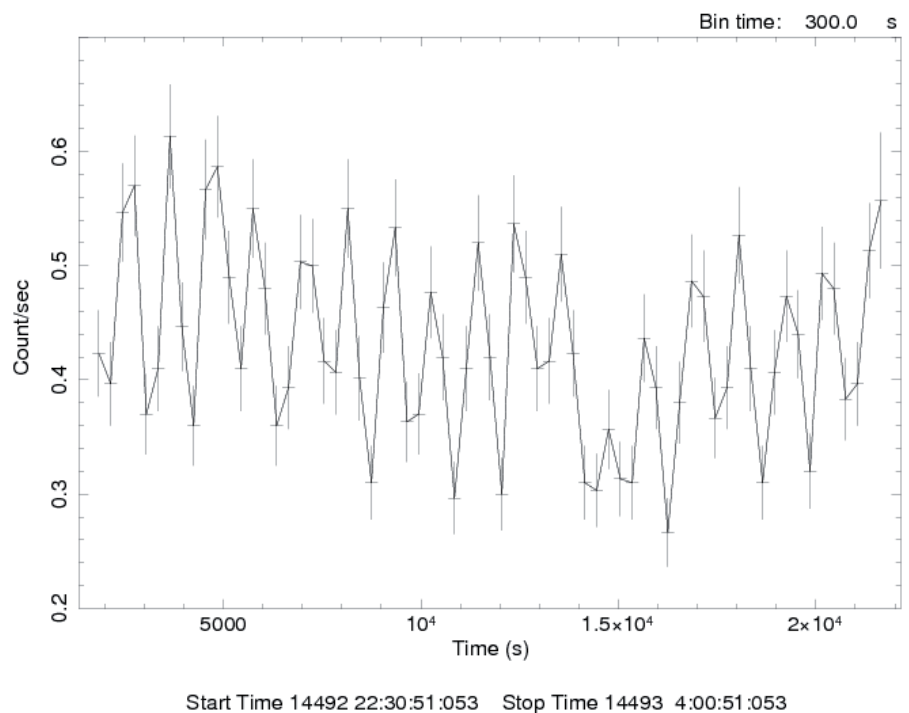


Fig. 2: XMM-Newton EPIC pn light curve of M31N 2007-12b, pulsating at a period of 1105 s.



W. Pietsch, V. Burwitz, F. Haberl, M. Henze and H. Stiele

## 2.5 PHYSICS OF THE SOLAR SYSTEM

In the early years of the Max-Planck-Institute for extraterrestrial Physics (MPE), founded in 1963, the scientific research concentrated on the investigation of near-Earth space with sounding rockets. Later on, this research was expanded, first to the exploration of the magnetosphere of the Earth, and subsequently to the Sun and solar system. At the same time, extraterrestrial astrophysical divisions were opened, covering X-ray, gamma-ray, and infrared astronomy and slowly shifting the focus of the institute from near Earth and solar system research to Astrophysics. In this section a short overview of the key developments in the solar system physics division of MPE is provided that came to an end in 2009.

shape the Earth's magnetosphere and determine dynamical processes as, for example, reconnection and convection (see article "The Magnetosphere", section "Magnetopause"). Furthermore, coronal mass ejections (CMEs) travelling with speeds up to  $\sim 2500$  km/s (the left part of Fig. 1 shows an image of a CME taken by SOHO) drive interplanetary shocks that in turn accelerate particles to high energies. A few days later, these CMEs impact on the magnetosphere of the Earth, causing magnetic storms, particle acceleration in the magnetosphere, and particle precipitation at high latitudes (middle part of Fig. 1), and aurorae, as observed on Earth (right part of Fig. 1).

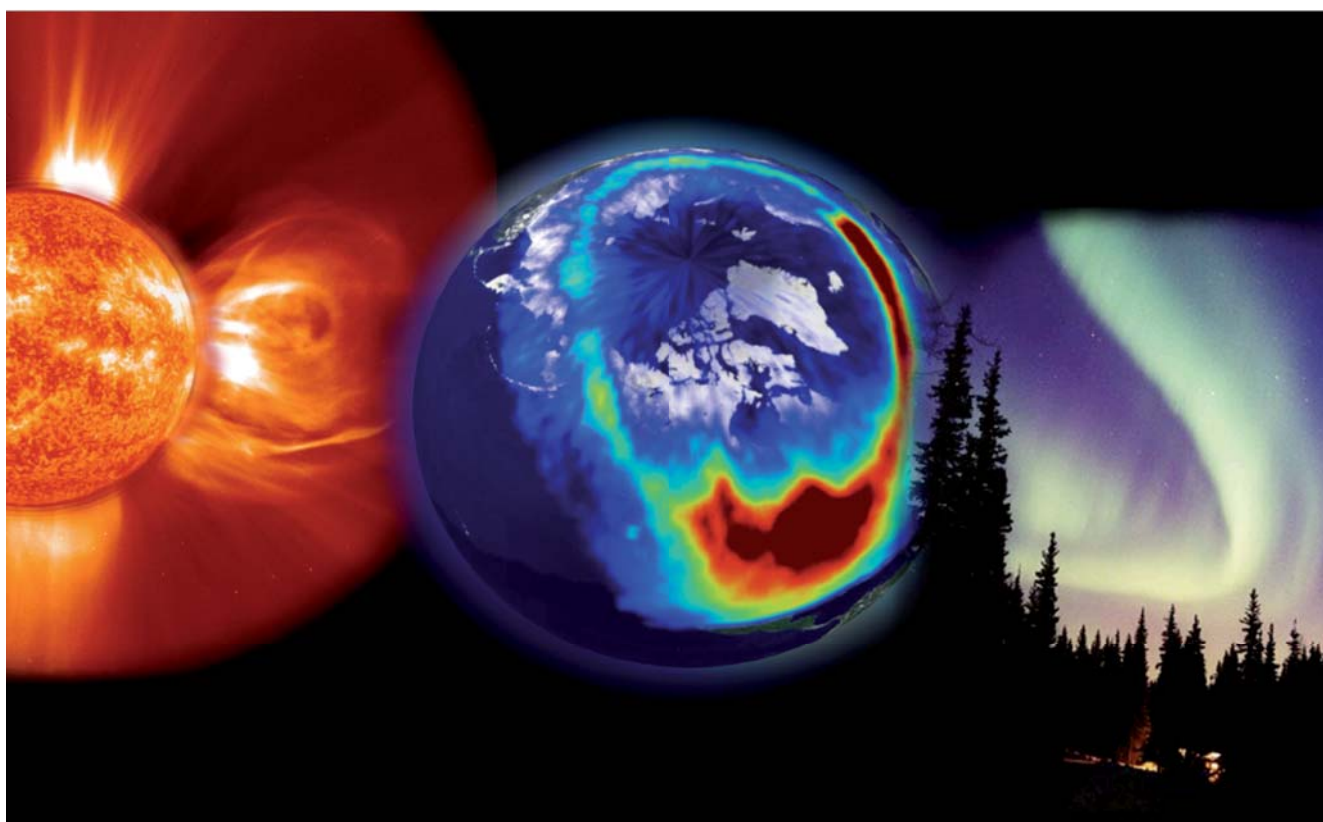


Fig. 1: The release of plasma from the Sun directly affects Earth and the rest of the solar system. This illustration shows a CME (left: EIT image, superposed on a LASCO C2 coronagraph image, both from SOHO) directed towards the Earth and its magnetosphere. (Objects and distances are not to scale, illustration courtesy to ESA).

The solar system is comprised of the Sun, the planets, their atmospheres and plasma environs, the small bodies, such as comets and down to dust particles, interstellar matter intruding from outside, and the cosmic radiation. At MPE we investigated the plasma physical phenomena in the solar atmosphere, in the Earth's magnetosphere and its boundaries, in interplanetary space and at other planets and comets.

We are, in particular, interested in the interaction of active phenomena of the Sun with the near-Earth environment as illustrated in Fig. 1: The continuous flow of the Solar Wind and its embedded interplanetary magnetic field

In order to explore the Earth's magnetosphere, its boundaries and interaction with the solar plasma as well as acceleration processes at the Sun, in interplanetary space, and in the magnetosphere of the Earth, a large number of space-born experiments have been developed at MPE over the last decades. They provide plasma and electric field diagnostics, and information on mass, energy, and the ionic charge of the accelerated particle populations in the near-Earth environment and in interplanetary space. In the next articles we provide a short overview of the most important accomplishments in the research of the aurora, the magnetosphere, and the particle environment in interplanetary space.

## Solar and Interplanetary Energetic Particles

The energetic particle populations in interplanetary space cover a large energy range from 1 keV/amu to 10 GeV/amu, as schematically shown for oxygen ions in Fig. 1. These populations are, from low to high energies, the slow and fast solar wind, particles accelerated at Corotating Interaction Regions (CIRs), particles accelerated at interplanetary shocks (ESP for energetic storm particles), driven by coronal mass ejections (CMEs), solar energetic particles accelerated at the Sun, Anomalous Cosmic Rays (ACRs), accelerated at the termination shock of the heliosphere or beyond, and galactic cosmic rays, accelerated at supernovae in our galaxy and penetrating into the heliosphere.

to study the distribution functions of solar wind ions and electrons between 0.3 and 1 AU in great detail. Based on its kinetic properties it was soon realized that the solar wind is a two-state phenomenon: quasi-stationary high speed streams (originating in coronal holes) and the slow solar wind. Helios provided also an ideal tool for the analysis of instabilities as derived from detailed distribution function measurements. The investigation of the solar wind was continued subsequently using new techniques with instruments onboard the ISEE-3 spacecraft, providing heavy ion elemental composition and ionic charge distributions. These measurements showed that ionic charge distributions, in particular of iron ions, are significantly different in the slow and the fast solar wind, and are much higher ( $Q_{Fe} \geq 15$ ) in the driver plasma (magnetic cloud) of coronal mass ejections. About 10 years later, with the development of more sophisticated and more sensitive instrumentation for SOHO, launched in 1995, high time resolution, elemental and charge composition measurements became available. These new instruments provided ionization temperature measurements on a 5 min time scale, showing the filamentary structure of the solar wind out to 1 AU. The now available detailed elemental and isotopic composition for many minor ions allowed the study of fractionation effects dependent on mass and on the first ionization potential.

### Solar Energetic Particles

High-energy particles originating at the Sun were first reported in 1946. At that time there was little doubt that these high energy particles were closely related to contemporary solar flares. Later it became clear that acceleration at interplanetary shocks, driven by coronal mass ejections is also an efficient mechanism for particle acceleration. Then, in the early seventies, a new type of event was discovered that showed enhanced  $^3\text{He}$  abundances with  $^3\text{He}/^4\text{He} \geq \sim 1$ , while the corresponding ratio in the solar corona and solar wind is  $\sim 5 \times 10^{-4}$ . From these early observations it was evident that the precise measurements of the elemental, isotopic, and ionic charge composition would be key observations for the investigation of acceleration and propagation processes in the inner heliosphere. Therefore members of the team at MPE decided to take a lead role in the development of instrumentation for compositional measurements in the MeV/nucleon energy range, and in the development of numerical models for the simu-

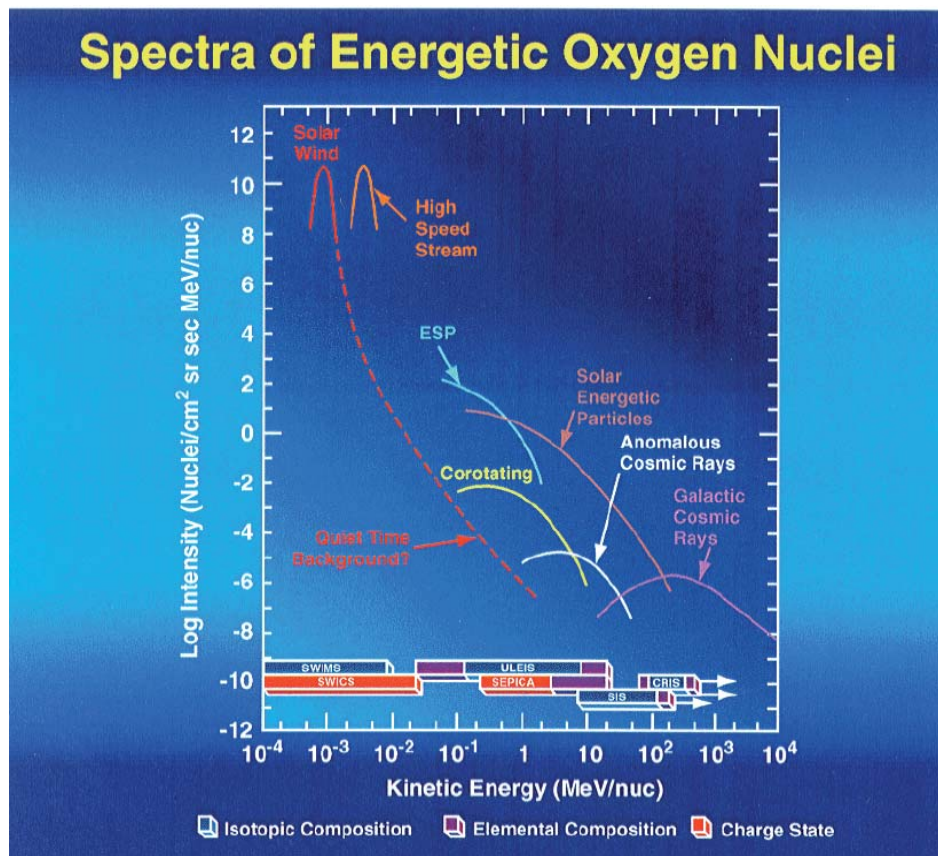


Fig. 1: Energy spectra of oxygen ions in interplanetary space.

### The Solar Wind

Already long before the beginning of the space age a continuous corpuscular radiation from the Sun was proposed, based on the observation of cometary plasma tails that always point almost radially away from the Sun. This radiation was named 'solar wind' in 1958 by E. Parker, who predicted a transition from a sub- to supersonic outflow of the expanding solar corona. Shortly afterwards, with the first space borne experiments in the early 1960s, the existence of a supersonic solar wind was confirmed and the detailed study of this plasma became one of the obvious targets of the MPE team. The two Helios missions, launched in 1974 and 1976 provided the ideal opportunity

lation of acceleration and propagation processes in the inner heliosphere. These instruments have then be flown on many NASA and ESA missions: IMP-7/8, ISEE-1/3, SAMPEX, SOHO, ACE. These measurements, obtained over the last ~40 years, contributed significantly to today's generally accepted view: The solar energetic particle events can basically be separated into two classes, gradual and impulsive events, following the classification of flares according to the length of soft X-ray emission. In this scenario impulsive events are related to flares and the gradual SEP events are related to coronal or interplanetary shocks, driven by coronal mass ejections, as is schematically shown in Fig. 2. In the following paragraph we summarize some key findings with significant contributions from the MPE team.

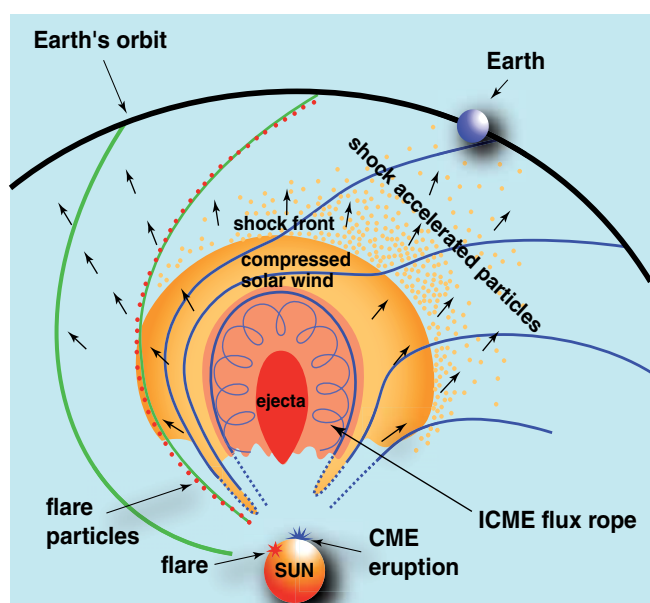


Fig. 2: Schematic view of the acceleration of solar energetic particles by an ICME driven interplanetary shock and by a flare at the Sun.

**Impulsive Events:** Soon after the discovery of  $^3\text{He}$ -rich events we found that for this type of events the elemental abundances of heavy ions increase systematically with mass (or nuclear charge), with enrichment factors of  $\sim 10$  for Fe at  $\sim 1$  MeV/nucleon. However, the enrichment factors of heavy ions and  $^3\text{He}$  are not correlated, suggesting different processes for the enrichment of  $^3\text{He}$  and heavy ions. The first ionic charge measurements of heavy ions at energies of  $\sim 1$  MeV/nucleon in Fe-rich events showed Si almost fully stripped and a mean charge of  $Q \sim 19$ -20 for Fe. Subsequent improvement in sensitivity and the extension of the energy range to lower energies of  $\sim 0.01$ -0.6 MeV/nucleon with instruments onboard SOHO and ACE revealed that all these events show a strong energy dependence of the mean ionic charge of heavy ions, most pronounced for iron. The new measurements yield an increase of the average ionic charge (for Fe) from  $\sim 10$ -12 at  $\leq 0.1$  MeV/nucleon to 18-20 at 0.5 MeV/nucleon, consistent (at high energies) with previous measurements, which were limited to high energies. This strong energy dependence can only be explained by charge stripping during acceleration in the dense environment of the low corona, at altitudes  $\leq 0.2$  solar radii.

The acceleration in impulsive events is best explained as a two-step process: preferential heating by (resonant) wave-particle interaction, followed by further acceleration to energies of 10s MeV/nucleon. The observed helium and heavy ion energy spectra are consistently explained by assuming stochastic Fermi acceleration as the second step. The recent ionic charge measurements, in combination with information on energy spectra and intensity-time profiles, have been used to infer acceleration and propagation parameters at the Sun and in interplanetary space. They imply particle acceleration in the low corona.

**Gradual Events:** Elemental composition measurements are now available from many missions over an extended energy range. Elements with low first ionization potential (FIP), e.g. Mg, Si, Fe, are overabundant (factor 3 to 5) with respect to local galactic or photospheric abundances, suggesting the importance of ion-neutral separation processes above the photosphere. The variation of elemental compositions (e.g. Fe/O) at the same energy per nucleon, often observed in the onset phase of SEP events, can be attributed to propagation effects with a rigidity dependent scattering mean free path. Intensity-time profiles, anisotropies, and compositional variations before the passage of interplanetary shocks are understood in terms of first-order Fermi acceleration models including scattering of heavy ions by proton-amplified waves and a rigidity dependent scattering mean free path. The first measurements of the mean ionic charge of heavy ions showed charge states consistent with coronal temperatures of  $1$ - $2 \times 10^6$  K. However, the subsequent extension of the observational range to lower and higher energies with SOHO, ACE and SAMPEX, showed that the ionic charge can be energy dependent. The SEP ionic charge states at  $\leq 0.5$  MeV/nucleon are usually consistent with solar wind charge states, whereas charge states at  $\geq 20$  MeV/nucleon can be as high as  $\sim 20$  (for Fe). This suggests the contribution of different particle populations to gradual events, i.e. a solar wind component at low energies and a flare component with high charge states at high energies. The present status of our knowledge about SEP events related to interplanetary shocks has been summarized in a recent review by members of our group.

### Anomalous Cosmic Rays

The anomalous component of low energy cosmic rays (ACR) was discovered in 1973 in the inner heliosphere. The anomalous feature was the flat energy spectrum of  $^4\text{He}$  between 10 and 80 MeV/nucleon, and a hump in the quiet-time cosmic ray energy spectrum of heavy ions (predominantly N, O, and Ne) at energies of  $\sim 3$ -20 MeV/nucleon, with unusual composition ( $\text{C/O} \leq \sim 0.1$ ). The early measurements showed He, O, N, and Ne in anomalous cosmic rays. Later, in the outer Solar System, also Ar, and H were identified in ACRs. The early measurements also showed a positive radial gradient, small latitudinal gradient and modulation similar to galactic cosmic rays, suggesting a source in the outer Solar System. All elements, initially identified as ACRs, had high first ionization potentials (He, N, O, Ne). Therefore interstellar neutral particles were suggested as a source, which are singly ionized in

the inner Solar System, picked up by the solar wind, convected with the solar wind into the outer heliosphere, and accelerated in the outer heliosphere, or at the termination shock. However, after the Voyager spacecraft passed the termination shock in 2004 and 2007, we now know that the acceleration is possibly even beyond the termination shock. The hypothesis of an interstellar source implied that ACRs should be singly ionized. Ionization states, indirectly inferred from modulation effects in the heliosphere, and propagation in the Earth's magnetic field provided upper limits, for example  $Q \leq 3$  for oxygen. Conclusive evidence for an interstellar origin came from the direct measurement of the ionic charge of N, O, and Ne for a large number of ions, using the cutoff of the Earth's magnetic field as a mass per charge spectrometer. The result was  $Q = 1$  for N, O, and Ne at 8 to 16 MeV/nucleon and that N, O, and Ne are multiply charged at higher energies. The higher charge states at higher energies are consistent with charge exchange during acceleration in the outer heliosphere.

### Pickup Ions in the Inner Heliosphere

The Solar System is moving relative to the Very Local Interstellar Medium (VLISM). While the plasma component of the VLISM is excluded from the Solar System by the interplanetary magnetic field, the neutral interstellar gas flows through the system. In the Solar System the neutral particles of the VLISM perform Keplerian trajectories under the influence of solar gravitation and radiation pressure. In the inner heliosphere the neutral gas is subject to ionization by solar ultraviolet radiation, charge exchange with solar wind ions and electron collisions. After ionization the particles are singly charged and picked up by the solar wind magnetic field, and convected with the solar wind into the outer heliosphere. These pickup ions (PUI) are also the source of ACRs (see article "Anomalous Cosmic Rays", above). Although predicted already in the

early 1970s, the discovery of this particle population was only possible with the improved instrumentation on MPES AMPTE/IRM spacecraft. It provided high resolution mass and mass per charge measurements in the energy range of pickup ions. Subsequently the systematic study of the distribution and energy spectra of helium PUIs in the inner heliosphere could be used for the determination of the density, speed, and temperature of interstellar helium and for the determination of the propagation characteristics of PUI in the inner heliosphere. We also found that, in addition to the solar wind, helium pickup ions are a major source of energetic ions in the inner heliosphere. They are accelerated by CIRs and interplanetary shocks.

Other sources of pickup ions in the inner solar system are the moon and comets. On 11 September 1985 ISEE-3 (renamed International Cometary Explorer - ICE) provided the first in-situ measurements of freshly ionized cometary particles and of their dynamics. The tail of comet Giacobini-Zinner was traversed downstream from the nucleus at a distance of 7800 km at closest approach. The existence of singly ionized water group ions in the cometary tail was established for the first time. The measured distribution functions and the observed density, probed through the tail, allowed the determination of the production rate of water-group cometary molecules.



B. Klecker

## The Magnetosphere

The Earth's magnetosphere, illustrated in Fig. 1, is created by the interaction between the Earth's magnetic field and the Sun's supersonically expanding corona, the solar wind. The boundary between the magnetosphere and solar wind is the magnetopause. Farther upstream from the magnetopause a collisionless bow shock is formed, at which the supersonic solar wind is slowed down and heated, creating a sheath of shocked solar wind around the magnetosphere. In the anti-solar direction, the magnetosphere is stretched out into a long tail. The magnetosphere and its environs contains long-lived plasmas with a large range of scales and exhibiting examples of key universal processes that are amenable to in-situ as well as remote-sensing, global observations. This makes it a unique plasma physics laboratory.

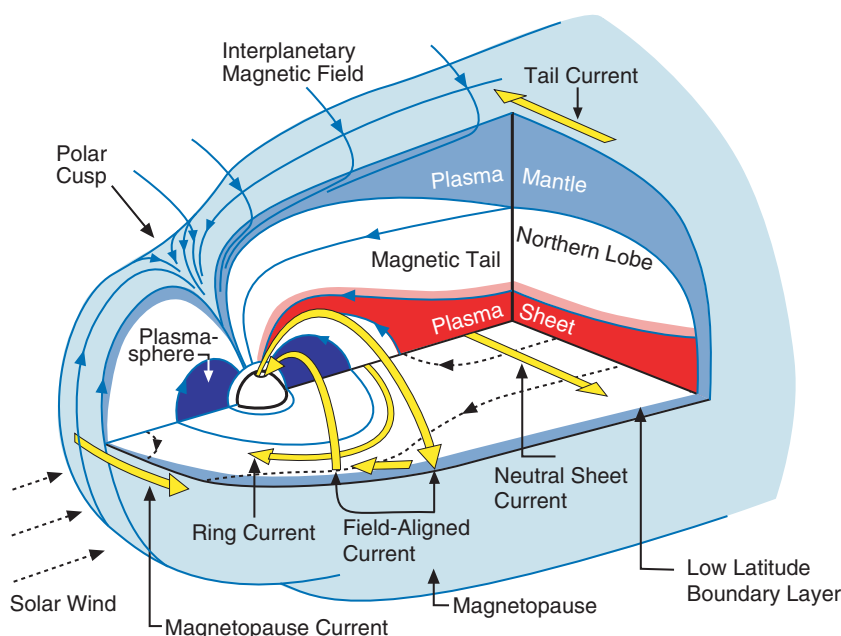


Fig. 1: Three-dimensional cutaway view of the magnetosphere. The light blue outer surface is the magnetopause, its boundary layers are shown in darker blue. Magnetic field lines are shown in blue, electric currents in yellow. The polar region where the magnetic field lines converge is the polar cusp. The bow shock has been omitted for clarity.

At MPE, we have been deeply involved in studying the physics of the magnetosphere, starting with measurements of the energetic particles in the Van Allen radiation belts with the first German research satellite AZUR. The AZUR instruments provided for the first time detailed distributions of trapped protons, alpha particles, and electrons in this region, and led to the discovery of energetic neutral atoms at low altitudes near the equator. Subsequently, energetic neutrals from charge exchange of radiation belt protons were also found in interplanetary space and were later extensively used by other missions to infer global maps of the magnetosphere.

In the following, we will focus on the observational findings pertaining to the outer reaches of the magnetosphere and its boundaries. These findings were obtained with plasma, energetic particle, and electric field instruments on numerous spacecraft (HEOS2; ISEE-1,-2, and-3; AMPTE-IRM and -CCE; Cluster), augmented by results from theory and numerical simulations. We also made important contributions to advanced data analysis techniques.

### Bow Shock

The purpose of the bow shock is to decelerate and heat the solar wind flow, so that in the region downstream of the shock the flow is subsonic, information about the obstacle can be transmitted, and ultimately the flow can be deflected around the obstacle. Since the solar wind is essentially collisionless, the creation of the bow shock requires the operation of collisionless mechanisms to provide the dissipation.

At the portion of the bow shock where the upstream magnetic field is nearly perpendicular to the shock normal direction, our measurements revealed that a fraction of the incident protons is reflected at the shock ramp. They gyrate around the upstream field and feel the motional electric field, so when they return to the ramp they are able to overcome the reflecting barrier and pass into the downstream region. Here they have very different velocity characteristics. They decrease the mean bulk flow and increase the mean velocity spread; that is, the downstream plasma is slower and hotter than the upstream one, which of course is exactly what the shock must, by definition, accomplish. The discovery of this shock reflection process is amongst the most striking highlights of space research. This discovery was only possible due to

the first high time-resolution plasma measurements with our instruments on the NASA/ESA ISEE spacecraft, and, subsequently with further improved instrumentation on MPE's AMPTE/IRM spacecraft, and finally with the spatially resolved measurements on Cluster. A second ion distribution backstreaming from the quasi-perpendicular bow shock are the field-aligned beams (FABs). During the reflection process solar wind ions can reach high energies, depending on the angle between the magnetic field and the shock normal. They are observed far upstream as beams propagating closely aligned with the magnetic field.

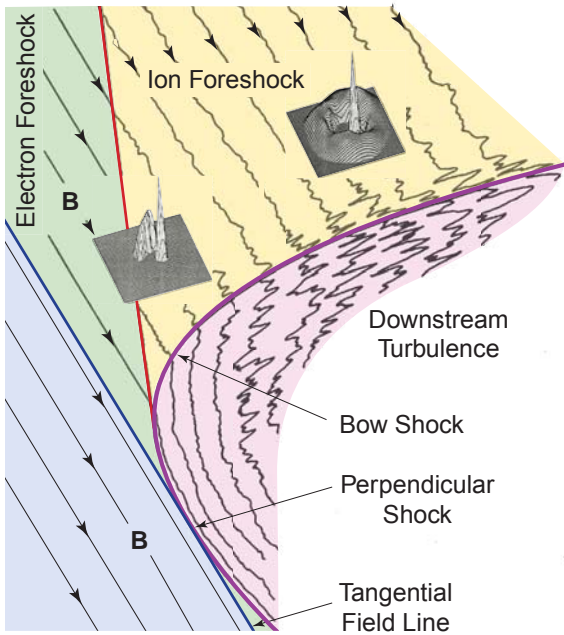


Fig. 2: Sketch of the Earth's bow shock ahead of the magnetopause (in red). The angle between the direction of the interplanetary magnetic field lines and the normal to the shock surface ranges (for the average direction of the IMF shown here) from quasi-parallel on the dawn side to quasi-perpendicular on the dusk side of the bow shock.

Under conditions where the unshocked magnetic field is more closely aligned to the shock propagation direction, ions can also be reflected. However, in these circumstances their guiding centre motion takes them further upstream rather than back to the shock. The result is an extended foreshock region, populated by such backstreaming ions (see Fig. 2). The counterstreaming particles drive plasma instabilities and create waves, which in turn scatter the particles in pitch angle. This small angle pitch angle scattering process results in spatial diffusion of the particles in the plasma upstream and downstream of the shock. This diffusion process is exactly what is required for particle acceleration via a first-order Fermi mechanism, which is considered responsible for the bulk of cosmic ray acceleration. Beginning with measurements on the ISEE spacecraft we contributed some of the key observations regarding the properties of these diffuse upstream ions, like near-isotropy in pitch angle space, energy spectra, upstream spatial extent, elemental composition, and time dependence of the acceleration process. These observations were continued with Cluster and allowed to determine the spatial diffusion coefficient from the underlying spatial scales in the upstream region. The field-aligned beams, backstreaming from the quasi-perpendicular bow shock, are eventually disrupted and, as the field lines are convected from the quasi-perpendicular regime into the quasi-parallel regime, contribute to a source population for acceleration and to wave excitation in the quasi-parallel regime.

The in-situ bow shock observations were accompanied by collisionless shock simulations. In the case of quasi-parallel shocks, where the relevant scales are large compared to the electron scales (electron Larmor-radius and electron inertial length) such simulations can be performed by the

hybrid simulation approach. Here, electrons are treated as a (massless) fluid and the ions are followed as individual (macro-) particles. These simulations showed how a part of the thermal solar wind ions are already accelerated in a first step at the shock, before they are subsequently injected into a diffusive acceleration mechanism. The observation of upstream diffuse ion spectra, being exponentials in energy rather than power laws, could be explained by the time dependent process of acceleration at the quasi-parallel bow shock as the point of connection of a field line with the shock changes. The one-dimensional hybrid simulations of quasi-parallel shocks also elucidated how upstream waves, produced by the diffuse ions, steepen up as they are convected into the shock, disrupt the shock, and lead to shock reformation. Two-dimensional hybrid shock simulations explained how these upstream waves develop into large amplitude magnetic pulsations as they convect into the region of increasing diffuse ion density near the shock.

At the quasi-perpendicular bow shock the specularly reflected ions lead to a foot in front of the shock ramp of the scale of the reflected ion Larmor-radius. In this foot the ions of the incident solar wind, the reflected ions, and the solar wind electrons stream relative to each other in the shock normal direction. This streaming can excite high frequency plasma waves which in turn may influence the shock structure. These high frequency waves can only be studied when resolving electron scales, i.e., the electron inertial length and the Debye length. This was done with full particle electromagnetic codes, where ions and electrons are treated as particles, and a Poisson equation for the electric field is solved. Since the growth rate of some of the instabilities depends on the ion to electron mass ratio the physical mass ratio should be used, which is rather challenging considering present computer resources. It has been found that in particular in the Mach number regime relevant for Earth's bow shock the modified-two-stream instability is excited, which can lead to shock non-stationarity. The theoretically predicted shock non-stationarity is currently studied intensively by analysing Cluster magnetic field and particle data. On larger scales instabilities can lead to ripples along the shock surface. Large-scale two-dimensional hybrid simulations have shown that the reflected ions generate an instability resulting in structures on the shock surface with scales of the order of the ion Larmor-radius travelling perpendicular to the upstream magnetic field.

A surprising phenomenon occurs when an interplanetary discontinuity that is almost aligned with the solar wind flow strikes the bow shock. This leads to the formation of a hot plasma bubble and a  $90^\circ$  deflection of the solar wind. We have contributed to the clarification of the nature of these so-called Hot Flow Anomalies.

## Magnetopause

The magnetopause is a thin current sheet that, to first order, separates the magnetosphere from the solar wind. It is one of the outstanding discoveries of the space age that this separation may be broken by a process called mag-

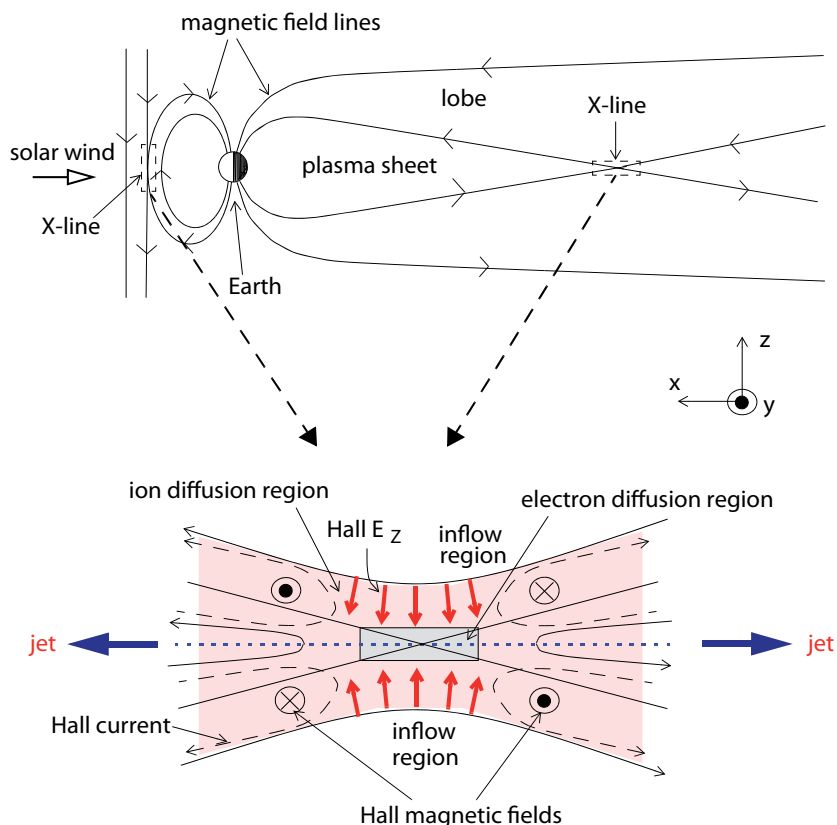


*Fig. 3: Magnetic reconnection in Earth's magnetosphere. Top: noon-midnight cut, showing magnetopause and magnetotail reconnection sites, the former for southward interplanetary magnetic field. Bottom: zoom-in on the region around the X-line, with the ion and electron diffusion regions indicated by the shading and the rectangular box, respectively. The quadrupolar Hall magnetic field is pointing in and out of the plane of the figure. The Hall electric field is shown by the red arrows, while the blue arrows mark the oppositely directed jets in the outflow regions.*

netic reconnection. While reconnection is a phenomenon of fundamental importance in many solar and astrophysical contexts, because it allows effective exchanges of mass, momentum and energy across thin current sheets, it is only in the Earth's magnetosphere that we can learn about the process from in-situ measurements and from observations of its more indirect, global consequences, such as boundary layer formation, plasma convection, and energy releases.

Reconnection is initiated on small scales, in a region referred to as the diffusion region, where the kinetic effects of the particle populations become important. Magnetic field lines are carried by the plasma into the diffusion region from both sides and become "cut" and "reconnected", forming an X-type configuration, as illustrated in Fig. 3. Once reconnected, the field lines form two oppositely directed wedges of field loops threading the current sheet. The magnetic tension of these loops accelerates the inflowing plasma away from the reconnection site on both sides. Our discovery of these outflow jets constituted the "smoking-gun" evidence for the occurrence of reconnection at the magnetopause, and we used this powerful tool to establish the detailed properties and occurrence frequency of magnetic reconnection at and near the magnetopause.

Reconnection occurs on a wide range of spatial and temporal scales. While the above observations imply large-scale and quasi-stationary conditions, at other times they can be patchy and transient. Our measurements have established the plasma properties of such transient events and probed their magnetic topology with energetic particles. Two-dimensional resistive magnetohydrodynamic (MHD) simulations of the sudden onset of reconnection resulted in a promising model for such transient events.

As a consequence of magnetic reconnection at the magnetopause, solar wind plasma can enter the magnetosphere and form boundary layers along the magnetopause (see Fig. 1). On average, about 1 kg of matter is entering the magnetosphere this way every second. We contributed many of the key observations, from the discovery of the "plasma mantle" that covers the polar magnetopause and dense plasma in the "polar cusps", via the low-latitude boundary layer on the front side and flanks of the magnetopause, to the spatially resolved measurements of their properties with Cluster. Another consequence of reconnection at the magnetopause is the setup of a global circulation of the plasma within the magnetosphere, which, with measurements of our Electron Drift Instrument on the Cluster spacecraft, we mapped comprehensively.

This is a continuation of the first reliable plasma convection measurements carried out by MPE's Barium ion cloud technique (see below).

### Magnetotail

As illustrated in Fig. 1, the Earth's magnetotail contains a hot dense plasma sheet at its center. Early measurements of energetic solar particles, carried out with the spacecraft AZUR and ESRO IV at low altitudes over the polar caps, deduced the length and the structure of the geomagnetic tail and its boundary. By our measurements with MPE's AMPTE-IRM satellite, we established the properties of the plasma sheet and its interface to the nearly empty lobe regions above and below.

The ISEE 3 Deep Tail Mission allowed a detailed in situ investigation of the distant geomagnetic tail for the first time. Also for the first time, the plasma flow velocity in the distant tail was derived from the measured anisotropy of suprathermal particles assuming that these particles are convected with the plasma flow. Statistically, there was equal earthward and tailward flow at about  $100 R_E$ . Beyond that point, the occurrence rate of the earthward flow decreases rapidly, which indicates the existence of a distant neutral line in this region. The predicted correlation between the polarity of the tail magnetic field (southward polarity on the tailward side of the neutral line and vice

versa) and the plasma flow direction was indeed established. Substorm models had proposed the formation of a neutral line at substorm onset. The new neutral line forms at  $\sim 15 - 20 R_E$ , as is illustrated in Fig. 4. Subsequent reconnection leads to a closed magnetic field structure, and finally to the pinching off of the plasma sheet. One of the important discoveries made by ISEE-3 during its passes through the distant tail was, that, consequent to substorms at Earth, plasmoids travel with high velocity in the tailward direction. In a statistical analysis the size of these plasmoids was determined to be between 50 and 100  $R_E$ . The statistical analysis of plasmoid velocities as a function of distance from the Earth indicated that plasmoids are further accelerated as they travel down the tail. ISEE-3 observations in the distant tail also revealed the existence of energetic ion and electron bursts in the lobes adjacent to the plasma sheet during substorms. These energetic particle bursts were interpreted to originate from the near-Earth neutral line.

The ISEE-3 Deep Tail observations triggered extensive numerical simulations for magnetic reconnection. Large scale two-dimensional resistive magnetohydrodynamic simulations, using a realistic magnetic field configuration for the tail, showed how plasmoids are accelerated and ejected tailward after severance due to near-Earth reconnection. Trajectory calculations of individual ions in such time-dependent MHD simulations of tail reconnection have contributed to the understanding of how the plasma sheet boundary layer with energetic ion beams develops. More local two-dimensional MHD simulations of undriven single X-line reconnection in a current sheet showed that, only when the resistivity is spatially localized in a small region near the reconnection X-line, fast Petschek-type reconnection with standing slow mode shocks is established. When the region of non-zero resistivity is increased, the diffusion region becomes larger and long current sheets develop. The reconnection rate decreases and reaches the slow Sweet-Parker rate, determined by the whole system size. Three-dimensional magnetohydrodynamic simulations of reconnection in a magnetotail configuration revealed how the cross-tail electrical current is diverted into a field-aligned current system which closes in the ionosphere.

Fast reconnection of the Petschek-type largely depends on standing slow mode shocks. In a collisionless plasma the occurrence of such shocks requires a collective mechanism. In order to investigate the possible occurrence of slow mode shocks, reconnection was studied by means of large-scale two-dimensional hybrid simulations. Slow mode shocks did not develop within about 50  $R_E$  from the neutral line. Instead, a reconnection layer in the outflow region develops which is characterized by highly anisotropic ion distribution functions in a boundary layer and a thin central current sheet with non-gyrotropic ion distributions. At distances larger than a few hundred ion inertial lengths the free energy in these distributions excites several instabilities, eventually resulting in a hot isotropic distribution. Heating is thus accomplished without the existence of slow mode shocks. Nevertheless, it is expected that eventually slow mode shocks appear. In order to study the

long-term development of the reconnection layer, a Riemann problem was studied by one- and two-dimensional hybrid simulations, where a current sheet with a normal magnetic field component was allowed to decay. The temporal development of such a configuration is a proxy for the spatial development along the reconnection layer. We were able to show that, due to counterstreaming ion beams in the boundary layer, the electromagnetic ion/ion cyclotron instability develops with obliquely propagating waves. This instability is at large distances responsible for the collective effect, needed for the development of slow mode shocks. Three-dimensional full particle simulations of reconnection yielded insights into the processes occurring in the reconnection diffusion region. Instabilities with k-vectors in the current direction in thin current sheets result in a collapse of the current sheet in localized areas and in a rapid onset of reconnection.

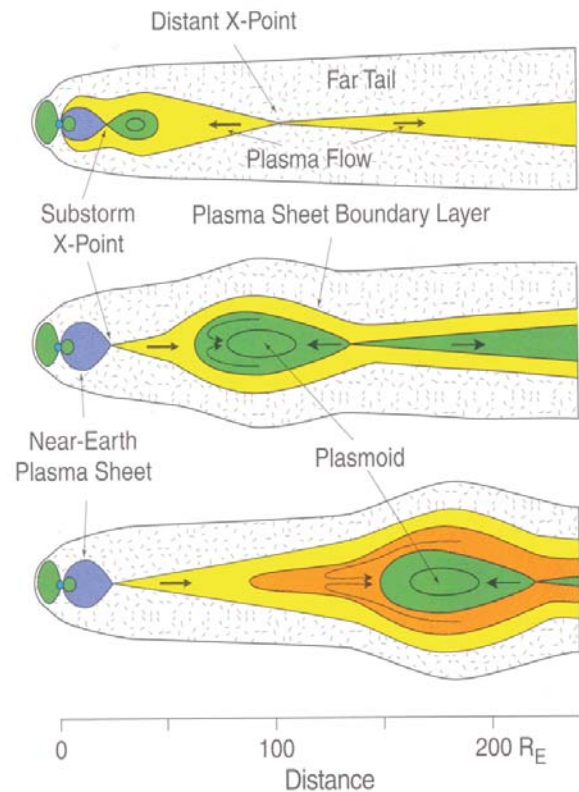


Fig. 4: Three stages of plasmoid formation in the geomagnetic tail by reconnection. Initially, there is a distant X-point at  $\sim 100 R_E$ . During substorm the added magnetic flux to the tail causes another X-point to form close to the Earth and a plasmoid (green) is formed traveling down the tail.



G. Paschmann and M. Scholer

## Active Experiments

25 years of experimentation with plasma clouds in near-Earth space are reviewed. The applications consisted of passive diagnostics of so far unobserved properties of the ionospheric/magnetospheric plasma and of various attempts to disturb the natural conditions and study the consequences. After two decades with sounding rocket experiments, mostly in the auroral and equatorial ionosphere and supported by extensive on-board diagnostics, these activities culminated in producing two artificial comets in the solar wind from the AMPTE satellite.

In 1961 the Max Planck Institute for Physics and Astrophysics began to engage itself experimentally in space research with establishing the Arbeitsgruppe Lüst, out of which the MPE grew in 1963. The first objective was to realize the idea of seeding visible plasmas in near-Earth space and to create thereby a means to study processes and transport phenomena, so far hidden from the eyes of the observer of the night sky. Mono-atomic barium gas appeared to be the most promising agent, because of its low photo-ionization potential and the existence of resonance lines from the ground state in the visible range. After two years of experimentation with sounding rockets, an efficient method of vaporization of the barium metal was found, and it turned out that the effective photo-ionization time in full sunlight was about 30 seconds.

The rather limited opportunities for seeding such observable plasmas in space rendered the technique less suitable as tracer of natural processes but made it an excellent tool for investigating the complex electromagnetic interaction processes with the plasma environment. However, also to the first aspect significant contributions were made. Tracking the plasma clouds in the ionosphere and magnetosphere and the related electric fields. But the presence of an artificially injected plasma alters to some extent the natural conditions by the generation of electric polarization fields. This manifests itself in two ways, by the formation of striations (Fig. 1) and occasionally by strong distortions transverse to the magnetic field, as shown in Fig. 2.

One of the central problems of magnetospheric physics is the coupling of the hot dilute plasma in the outer regions and the magnetotail to the dense, cool, and partially ionized plasma of the ionosphere. It ranges from complete frictional control of plasma motions at high altitudes to almost full decoupling through field-aligned electric potential drops. The barium cloud technique could shed some light on such processes. By filamentation of a cloud, generated at  $5 R_E$ , into narrow field-aligned striations a decoupling from the ionosphere was achieved, which completely removed any ionospheric control on the momentum exchange with its local environment. Another manifestation was the field-aligned acceleration of barium ions, injected to high altitudes with the help of a shaped charge release

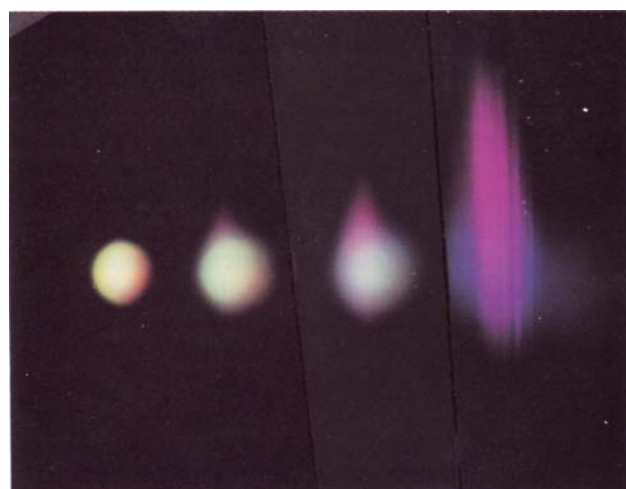


Fig. 1: Change of color and structure during the ionization of a cloud of barium atoms, created at a height of 260 km south of Lima/Peru after sunset in March 1979. The response of the barium ions to the magnetic field and the typical formation of field-aligned striations are well visible.

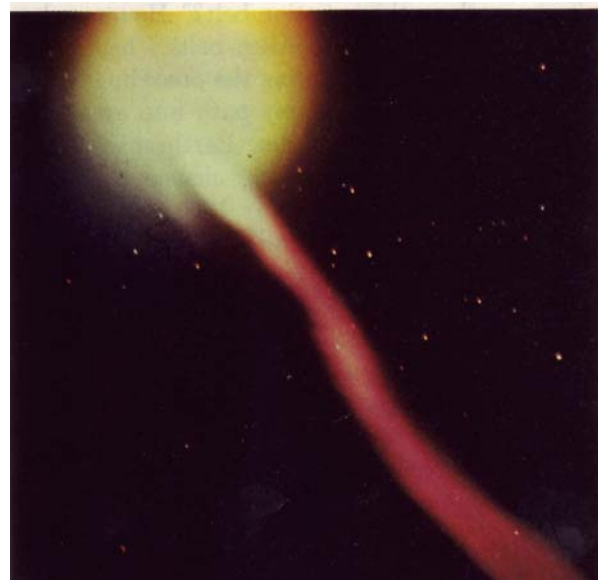


Fig. 2: A barium cloud above Ft. Churchill/Canada was horizontally distorted, i.e. perpendicular to the magnetic field direction, by more than 100 km within three minutes.

above an auroral arc, whereby 5 keV of kinetic energy were gained. Several times we observed the following effect related to auroral physics: electron precipitations were triggered by the electromagnetic impulse, generated by barium cloud injections in the auroral ionosphere and propagating upwards as an Alfvén wave.

The injection of barium atoms of high velocity (up to 14 km/s) by means of shaped charges provided the opportunity to test the Critical Ionization Velocity (CIV) hypothesis of Hannes Alfvén in space. A first attempt within the Porcupine sounding rocket program initiated many subsequent experiments.

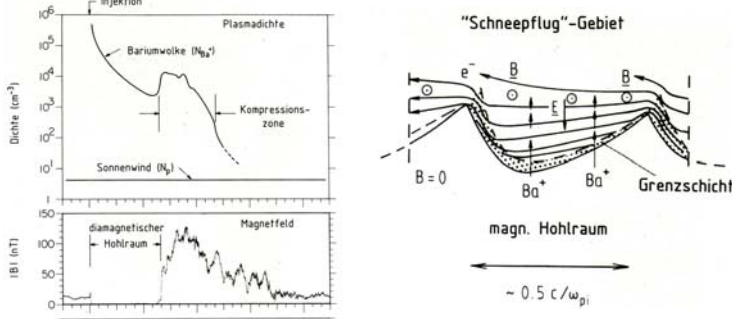
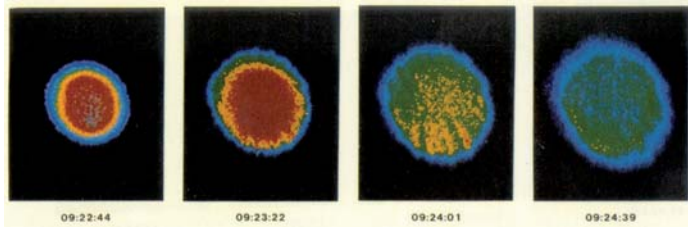


Fig. 3: Ripples on the surface of the plasma cloud enable the penetration of the external magnetic field into the field-free plasma cloud, whereby the plasma accumulates behind the front in a snowplow fashion.

A completely different objective was the attempt to massively perturb the natural plasma environment of the equatorial ionosphere by injecting dense plasma clouds and trigger the phenomena known as Equatorial Spread F (ESF). Several unsuccessful trials were finally honored with success in the Coloured Bubbles experiment in Brazil, although the instability evolved fully only after the barium clouds were overtaken by the Earth's shadow and were only observable by radio soundings.

The culmination of the barium plasma experiments was the releases from the AMPTE-IRM spacecraft in the solar wind and the magnetic tail, the artificial comet experiments. Two physical aspects were in the foreground, (1) the penetration of the ambient magnetic field into the initially created magnetic cavity, associated with the high kinetic pressure of the expanding plasma cloud, and (2) the coupling of momentum from the solar wind to the injected plasma with its five orders of magnitude higher mass density. (1) Optical observations from ground and in-situ magnetic field and plasma wave measurements led to the find-

ing that the magnetization of the plasma cloud was not a diffusive process, but the direct penetration of a magnetic front, loaded with the already magnetized plasma like a snowplow, aided by the large inertial length of the ions and the formation of ripples.

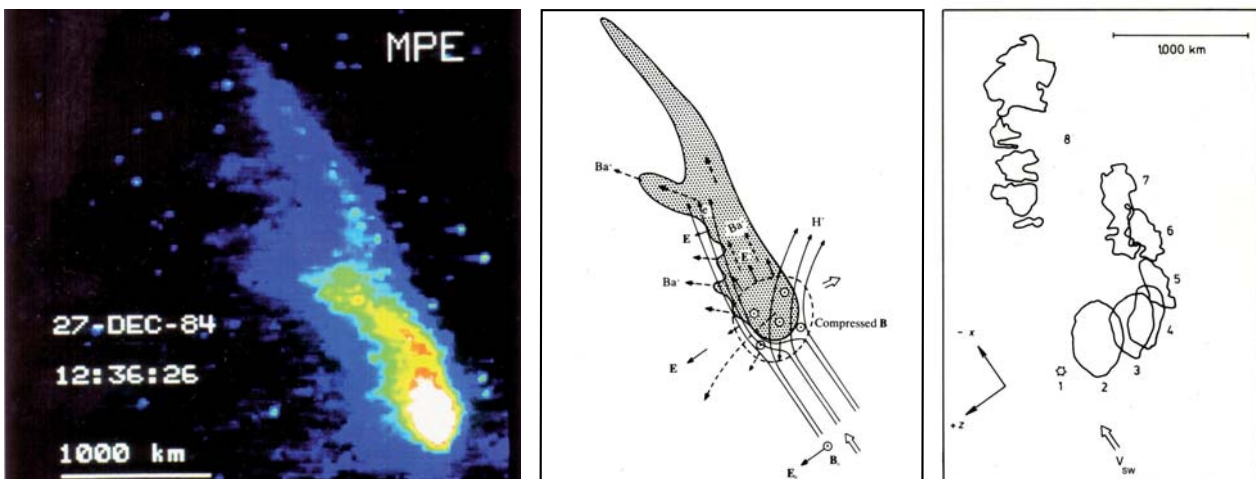
(2) The momentum of the solar wind was transferred to the plasma cloud by the external magnetic field, which was severely compressed owing to the high Alfvénic Mach number of the flow. The optical and in-situ observations revealed two most surprising facets of this process, which gave new insight into basic cometary physics. The main body of the plasma cloud did not move in the direction of the solar wind flow but in the perpendicular direction. This was caused by the extraction of ions in the opposite direction by the electric field ( $E = -V_{sw} \times B$ ), existing in the rest frame of the cloud, and the associated recoil effect. The force acting in the flow direction was transmitted through the eventually magnetized main cloud and imparted to the ions on the rear side thus creating a tail that was growing to a length of about 10,000 km within five minutes (see Fig. 4).

With this spectacular, but very demanding mission, AMPTE-IRM, MPE essentially terminated its 25 years long engagement in active plasma experiments in space.



G. Haerendel

Fig. 4 (below): An electric field exists in the frame of the plasma cloud. It extracts ions in the direction perpendicular to the magnetic field (out of plane) and solar wind flow. The related recoil shifts the main cloud (comet head) into the opposite direction. On the rear side, ions are injected at high speed into the flow direction and form a fast growing tail.



## Aurora Borealis

Auroral research has been in the focus of MPE ever since the barium plasma cloud technique allowed novel diagnostics of the convection electric field in the auroral ionosphere and of the particle acceleration process above auroral arcs. The experimental techniques were soon widened to include the Scandinavian incoherent scatter radar, EISCAT. In the 1990's MPE played a major role in the Swedish-German FREJA satellite mission. Theoretical research accompanied these activities all along and continues into the present.

The aurora borealis or northern lights has fascinated men and women probably ever since they were seen for the first time, because of their incredibly variable dynamics and multiplicity of forms, ranging from thin rayed arcs, long distinct rays, coronae, spirals, folds, curls, broad diffuse arcs and extended glows. All these are created at heights between 100 and about 250 km by the impact of electrons on the upper atmosphere, resulting in various collisional excitations with subsequent emission processes. Being engaged in experiments with plasma clouds in space, MPE naturally went into studies of the ionospheric plasma environment in which the auroral phenomena take place. The first objectives and results were on the electric fields or plasma flows in the neighborhood of, and inside,

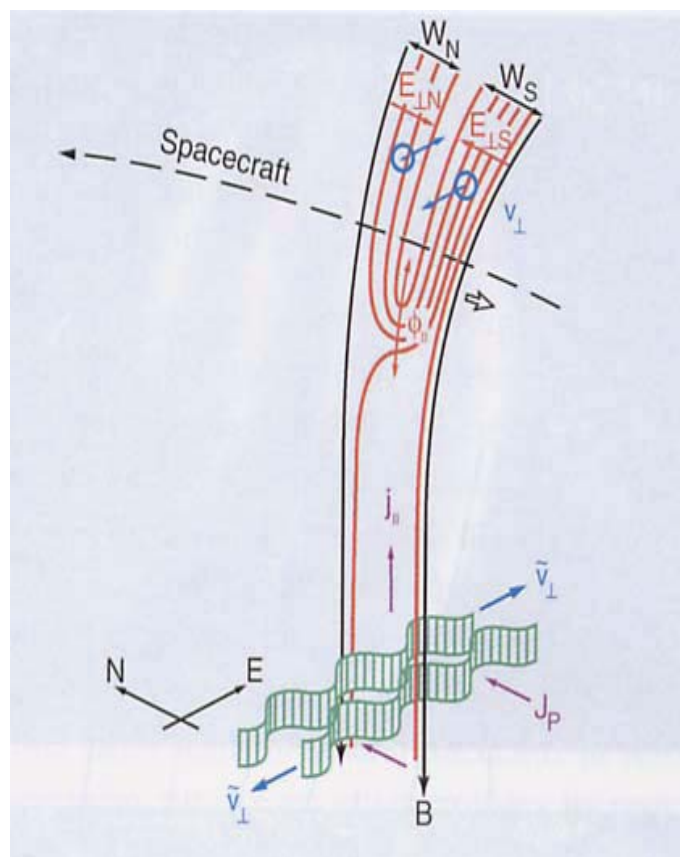


Fig. 2: Association of folds and rays moving in opposite directions along the arc with the electric field and flow structure in, and above the acceleration region.

auroral arcs. We found that in all cases the electric field was dominantly normal to the arcs, i.e., the plasma flow was mainly, but not fully, tangential to the arc. In a few cases even a crossing of arc and barium plasma, without its disintegration, was observed. The 'shaped-charge' technique was developed in order to inject fast ion beams into the magnetosphere from above the collisional atmosphere (~500 km), which is still accessible by sounding rockets. The goal was to probe the electric fields in the auroral acceleration region at heights of several 1000 km. Despite being very careful, such experiments need some luck for being successful. The ions have to be planted at the right time on the right location of the arcs, which are narrow and may move and fade within minutes. We were successful only once, above Greenland in January 1975. Fig. 1 shows the change in upward velocity along the magnetic field, after the arc contacted magnetically to the barium ions. The ions kinetic energy increased by about 5 keV. This proofed the existence of field-parallel electric voltages for the first time. Other aspects of auroral physics are noted in the section on active experiments. However, obviously this technique was not the proper tool to study auroral physics. Other approaches had to be found.

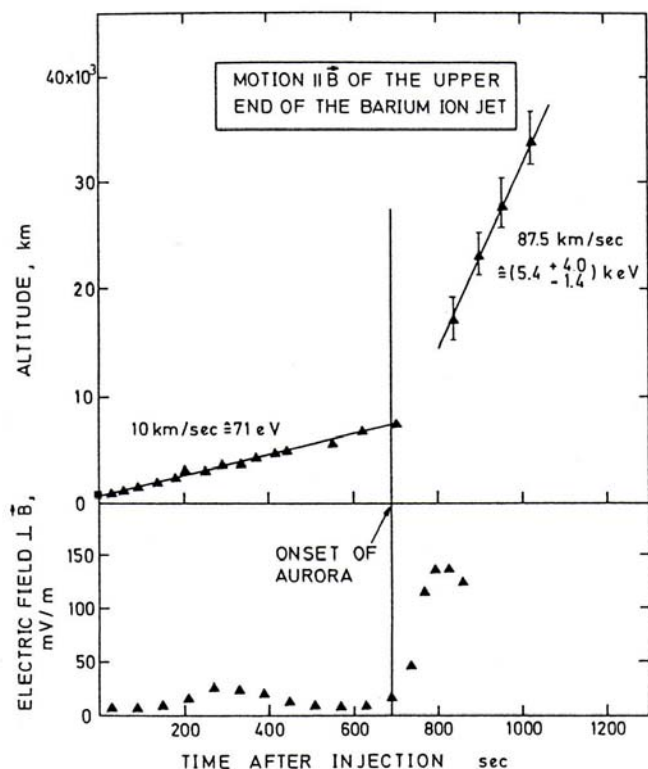


Fig. 1: Tracing the tip of a barium ion jet. It moves upward from an injection altitude of 615 km and reaches magnetic contact with a newly forming auroral arc after about 11 minutes. The change in velocity shows that the ions were accelerated along the magnetic field (B) at altitudes between 8000 and 15 000 km.

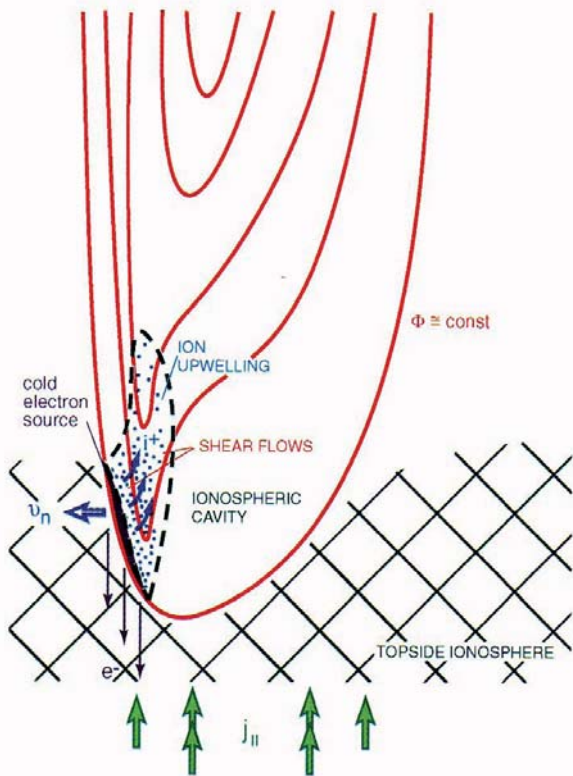


Fig. 3: The cavitation process is related to the progression of the auroral potential structure, which corresponds to the observed proper motion of auroral arcs. Electrons are accelerated parallel to the B-field, while the ions are being extracted transverse to the field.

Since the late 1980's the auroral research at MPE focused on two experimental techniques and on theory. One technique was the combination of plasma flow measurements in the ionosphere, using the EISCAT incoherent scatter facility, with auroral arc imaging by highly sensitive image-intensified CCD cameras, which were developed for the barium cloud observations. This allowed to determine the proper motion of the arcs, i.e., of the auroral acceleration region, with respect to the ambient plasma. A related aspect was the analysis of the auroral ray motions along the arcs. This was best observed by viewing along the magnetic field direction. Simultaneous measurements of the ionospheric plasma flow with EISCAT revealed a complete decoupling of these motions from the ionospheric plasma frame. They are the result of real motions in and

above the auroral acceleration region, and the release of magnetic shear stresses, set up by the field-aligned currents (Fig. 2). These findings suggested a new paradigm for the origin of auroral arcs as sites of magnetic stress release. By breaking the contact with the ionosphere, magnetic energy is liberated and is powering the auroral acceleration process. These new insights stimulated further observational and theoretical studies of this most intriguing aspect of magnetosphere-ionosphere interactions.

The second experimental line was to engage in a Swedish-German satellite project 'Freja'. We participated in the development of the spacecraft, as well as in the building of two scientific instruments: an electron detector and an electron beam experiment for electric field sensing. The 'Freja' satellite was launched in 1992. With an apogee height of 1750 km it could barely scratch the auroral acceleration region. Nevertheless, the mission revealed many new features of the aurora, in particular on the interaction of the electric fields of the acceleration region with the topside ionosphere. It transpired that much of the energy was expended by eroding the cool, dense ionospheric plasma and creating cavities, which in turn have an impact on the auroral dynamics and morphology. In this process, narrow field-aligned electron beams are injected downward, while the ions flow up and populate the magnetosphere (Fig. 3). Ground-based optical observations, coordinated with overflights of the Freja satellite, gave quantitative insights into the energy conversion process above the arcs.

The engagement in ground-based and satellite measurements of auroral parameters and the availability of data from the source regions in the tail and outer magnetosphere by the AMPTE-IRM and the Cluster mission, allowed us to make also contributions on the complex issue of substorms and auroral current generators. On the theory side this type of work is still ongoing.



G. Haerendel

## 2.6 COMPLEX PLASMAS

The three well-known forms of matter are solid, liquid and gas. Upon further heating, gases may become plasmas, decomposing into ions and electrons. This so-called fourth state of matter amounts to 99% of the visible matter in the Universe.

Complex plasmas have an additional component: charged supramolecular microparticles. Although these microparticles are small, they are comparatively heavy – many billions of times heavier than atoms – and carry thousands of electron charges. In fact, if their number is sufficiently large, they become the dominant dynamical component and determine the structure of the plasma. Because of this “huge” mass of the microparticles the physical processes taking place in complex plasmas can be viewed in super-slow motion. Complex plasmas become the unique model system to study numerous fundamental processes occurring in fluids and solids – where these studies can be performed at the level of individual “atoms”. Everyday examples of such processes – to name just a few – are: (1) liquid-solid phase transitions, (2) transitions from laminar to turbulent flow, and (3) phase separations in binary systems.

Earth’s gravity allows us to investigate complex plasmas in thin, horizontal layers of free-floating microparticles, or stressed 3-dimensional structures. Therefore Earth-bound experiments have naturally concentrated on flat or monolayer systems. These are of great interest in many areas including the study of surface physics, membranes and the stability principles of condensed matter. The physics of 2-dimensional liquids and crystallites is rich of interesting phenomena and can be studied in many different systems. Especially the transition between the phases is investigated. Complex plasmas help to understand such physics in greater detail due to their special observation possibilities, since the processes appear to be scale invariant and generic. Large 3-dimensional systems under stress that can also be created on Earth, provide insights into e.g. fluid dynamics or shear flow. Using simple scaling relations it is possible to compare the liquid plasma measurements with classical fluid flows. This suggests that liquid plasmas may provide a unique quantitative approach towards understanding nanofluidics and any nonlinear processes occurring at this level.

In the absence of gravity, however, the microparticles can occupy the whole plasma, and it is possible to obtain experimental conditions where the system is isotropic (uniform), homogeneous and not stressed by the pull of gravity and the compensating forces. For the precise measurements needed to study 3-dimensional systems and for stress-free processes, microgravity experiments are essential and complementary to research in the lab.

The idea that complex plasmas can form liquids and crystals (the latter being called plasma crystals) was the basis in 1992 for MPE to start laboratory work dedicated to this area. Initial theoretical calculations showed that microgravity would be necessary to produce plasma crystals and therefore an apparatus for space was developed and tested. In the course of this work, however, the first plasma crystal on the ground was discovered, which was the starting point for a new research field: The physics of complex plasmas has grown very strongly since then.

On ground, we built seven independent laboratories dedicated to different topics of research in complex plasmas, such as 2-dimensional or strongly magnetised systems, adaptive systems with application oriented topics or microgravity related systems. The space programme involves regular parabolic flights and reached optimum longterm conditions on the ISS, when in 2001 our experiment PKE-Nefedov, the first natural science project aboard the ISS, started to operate. PKE-Nefedov, a close collaboration between the Joint Institute for High Temperatures of the Russian Academy of Sciences in Moscow and MPE, was the most successful scientific experiment on the ISS. It was replaced by its direct successor PK-3 Plus in 2005. This lab is still in operation and delivers unique data. The future of microgravity research is in preparation with PK-4, which is in the design and development phase (Phase C/D) now, and with PlasmaLab, which is in a laboratory development phase. Laboratory and space programme are both complemented in our group by theory and numerical simulations.

Although this research is very successful and promising for the future and perfectly fits into the scope of the Institute by performing “extraterrestrial” physics, the field of complex plasmas will be closed down with the retirement of Prof. Gregor Morfill in 2013. Fortunately, DLR has recognised its potential and is very interested to bring this research to the Institute for Materials Physics in Space. The move of the group is currently planned for the second half of 2011, two years earlier than strictly necessary, to ensure a smooth transition.



Fig. 1: The Complex Plasma group celebrating.

## Bubbles and Droplets in Complex Plasmas

To investigate the dynamical evolution of a complex plasma, we used a vertical temperature gradient to compensate for gravity. We find that at low power microparticle bubbles, droplets, and spraying cusps form. This activity can be turned on and off by changing certain control parameters, such as discharge power, gas pressure, and particle number density. Several observational effects indicate the presence of surface tension, even at small “nanoscales” of a few hundreds of particles. We studied the detailed (atomistic) dynamics as well as the pressure dependence of the net force by tracing the individual microparticle motion. A possible mechanism that could drive the observed phenomena is analogous to the Rayleigh-Taylor instability.

Hydrodynamics describes fluid systems, for instance the flow of water in a tube or the airflow around the wing of an aircraft. An interesting question is on which scale this description breaks down and the effects of individual

particles start to dominate. Complex plasmas are ideally suited to study small fluid systems. In addition to neutral atoms, ions, and electrons, these plasmas contain micrometre-sized particles. The microparticles are highly charged by fluxes of plasma particles onto their surfaces and strongly interact with each other via a screened Coulomb potential.

Depending on the external conditions such as the buffer gas pressure and the discharge voltage, the subsystem formed by the microparticles exists in different phases. The particles can, for instance, form a crystal, or behave like a fluid. A major advantage of these systems is that every individual particle can be visualized with a CCD camera if illuminated by a laser.

In our experiments, the plasma is produced in a vacuum chamber by applying a radio-frequency voltage to two horizontal electrodes. We use argon or neon as buffer gas at typical pressures between 15 and 50 Pa. Monodisperse microspheres made of melamine-formaldehyde with sizes between 3 and 7  $\mu\text{m}$  are inserted into the gas and levitated above the lower electrode by the strong electric fields in the plasma sheath. A vertical laser sheet illuminates the particles.

In order to attain a homogeneous system, the microparticles should be levitated in the bulk of the plasma. This can be achieved either by conducting experiments under microgravity conditions or by compensating gravity with an equally strong force. In the work presented here, we used the latter approach: The lower electrode is heated and the upper one cooled. This induces a temperature gradient in the gas, which causes an additional, thermophoretic force on the microparticles.

When gravity is compensated by thermophoresis, the same phenomena which are typical for complex plasmas under microgravity conditions can be observed, the most pronounced being the particle free region in the centre of the system. This void is the result of a balance between the electrostatic force and the force exerted by the outward-streaming ions. Usually, it has very well defined, clear boundaries.

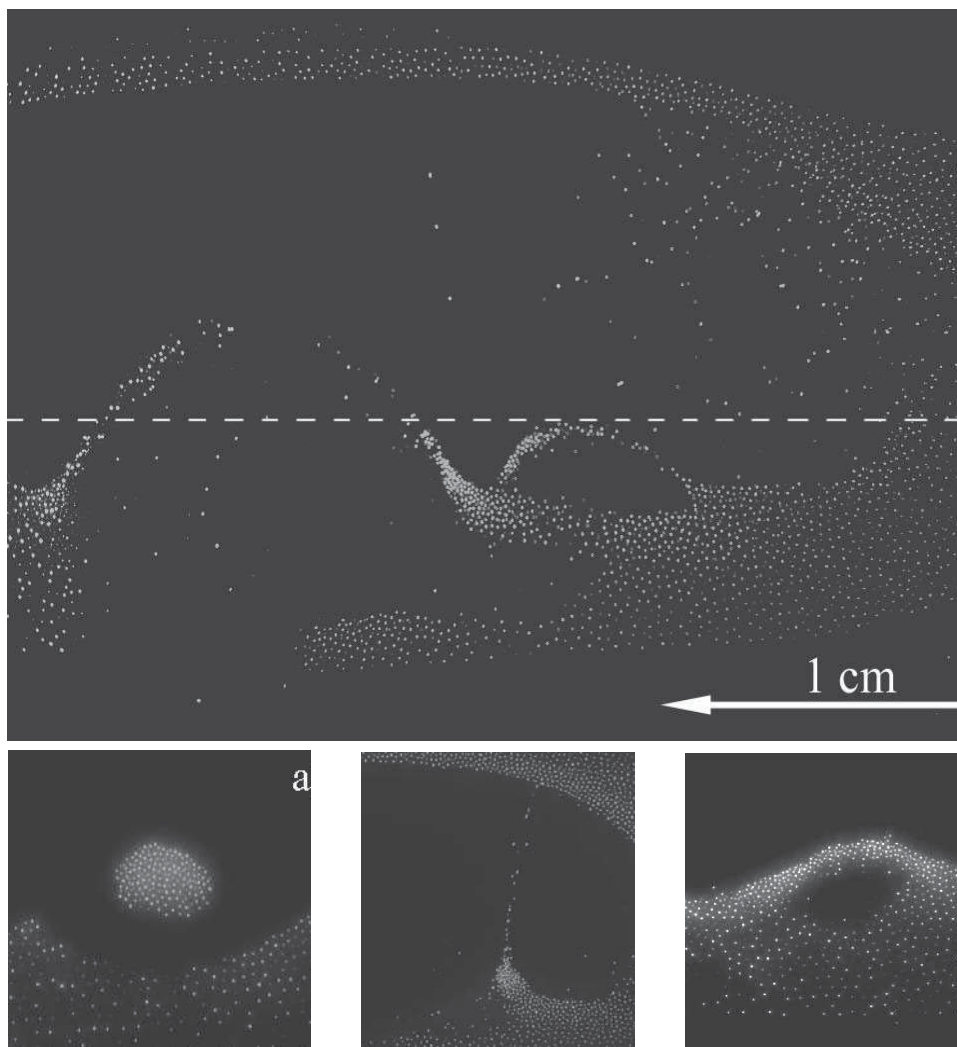


Fig. 1: Bubbles (top, c), droplet (a), and spraying cusp (b) in the microparticle fluid. The dashed line in the top panel corresponds to the position of the chamber horizontal midplane. Every white dot corresponds to an individual microparticle. The central particle-free region is the void.

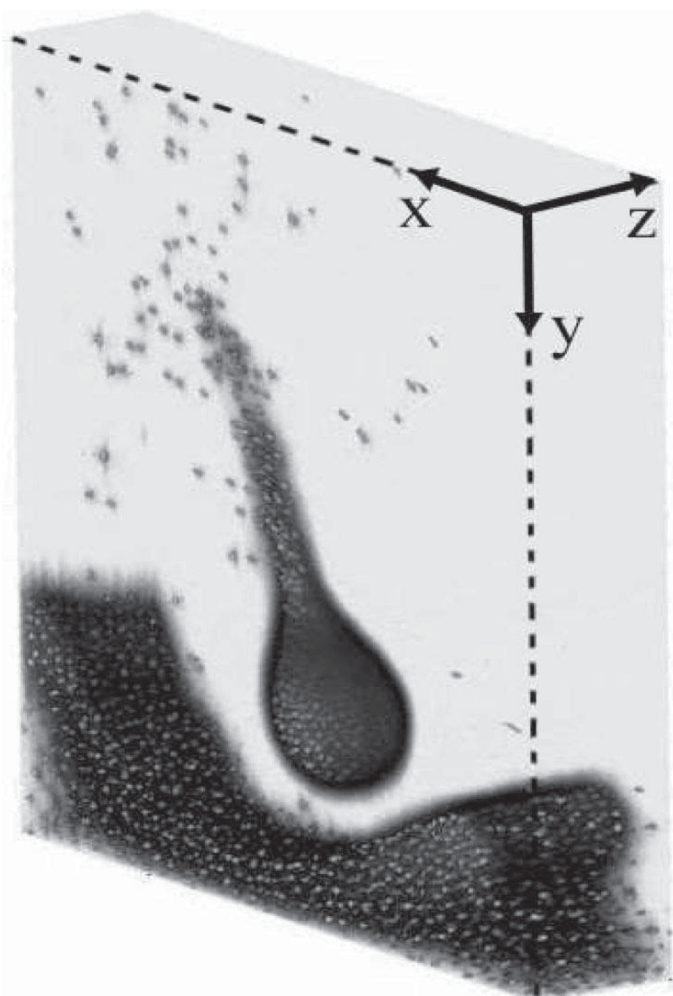


Fig. 2: Three-dimensional view of a microparticle droplet.

Under the conditions of our experiments, an instability develops in the microparticle fluid beneath the void. First, the void boundary displays indentations and ripples, and particles begin to move upwards through the void. Then, bubbles and droplets consisting of a few thousand particles form, which are then ejected into the particle-free region. Examples are shown in Fig. 1.

These phenomena occur in both neon and argon discharges and with microparticles of various sizes. They can be triggered by increasing the temperature gradient, the gas pressure or the particle number density or by decreasing the discharge voltage, and can be stopped by varying those settings in the opposite direction.

The camera and laser are mounted on a translation stage, which allows scanning horizontally through the system. Using this “tomographic” procedure, a three-dimensional structure can be reconstructed. This way, we can show that the drops are indeed self-contained and are not connected to the rest of the microparticle fluid in any direction. Fig. 2 illustrates a three-dimensional droplet structure. The region below the droplet corresponds to the lower void boundary.

By tracing the particles from frame to frame, we can study their movement. This allows for an analysis of the particle trajectories, velocities and forces acting on them. Fig. 3 shows the streamlines inside a droplet. The microparticles move in vortices, upwards on the sides and back downwards in the droplet centre. Some particles are also ejected upwards out of the droplet, forming a small spray.

The observed phenomena show remarkable similarities with those in conventional fluids. For instance, the movement of water molecules inside water drops in an airstream also occurs in vortices. Particles are ejected via tails as in our droplets. When these droplets break up, they can do so in forms that resemble the membranes formed by our bubbles (or between two droplets). Additionally, the surfaces of fluids under the influence of electric fields form so-called Taylor cones like those we observe at the void boundary (see Fig. 1).

In order to determine the cause for the observed instability, we measured the vertical velocity of particles moving upwards at the vertical centre of the chamber. In this position, the ion drag and electrostatic forces cancel. Fig. 4 shows the measured velocities as a function of gas pressure. It can be seen that the vertical particle velocity decreases with pressure, which excludes normal Rayleigh-Bénard convection of the buffer gas induced by the temperature gradient as the cause of the particle movement. In that case, the velocity should increase with pressure. On the other hand, this result allows for convection driven by a phenomenon called thermal creep. Thermal creep



Fig. 3: Streamlines of the microparticles moving inside a droplet.

occurs under low pressure conditions in systems where a temperature gradient is maintained along a wall. When gas particles coming from the hot side hit the wall, they transfer a higher momentum than those coming from the cold side. Since the reflection of the gas atoms from the wall is diffuse, net momentum is transferred to the gas directed towards the hot side. This effect can induce gas convection towards the warm electrode along the sides of the system, and a corresponding gas flux in the centre towards the cold electrode, in our case upwards.

With this mechanism, the particles localized beneath the void are accelerated upwards. This leads to the development of a Rayleigh-Taylor instability: the instability that occurs when a dense fluid is accelerated into a less dense one. This instability can be described by a dispersion relation depending on the strength of the surface tension and other parameters. Using the experimentally determined maximal growth rate and wave number, it is thus possible to estimate the surface tension.

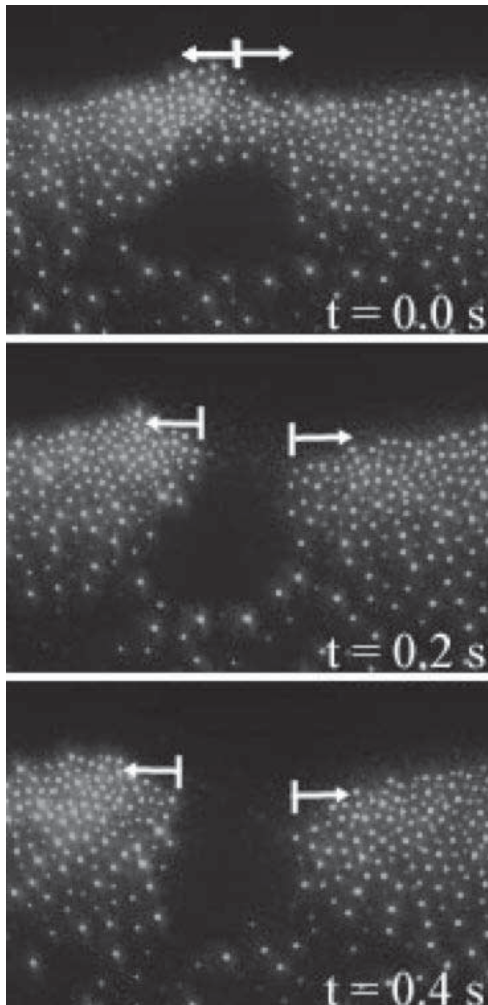


Fig. 5: Breakup of a bubble lid.

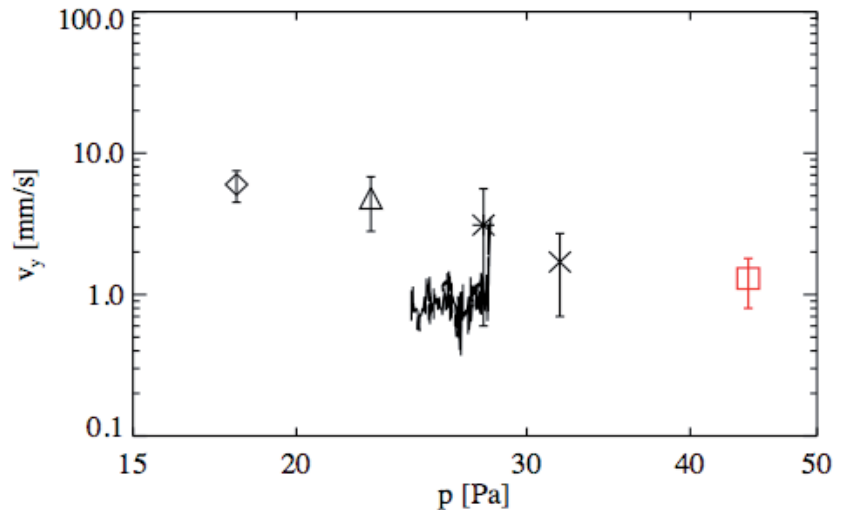


Fig. 4: Vertical velocity of the microparticles moving through the chamber centre as a function of pressure. The red square indicates measurements taken while the plasma was turned off. The bold line shows an experiment with a gradual pressure increase, in the other experiments the pressure was kept constant.

We can also directly estimate the magnitude of the surface tension by considering the breakup of bubble lids such as the one shown in Fig. 5. The surface tension is then given by the total transported mass divided by the square of the time needed for the breakup.

The directly measured value of the surface tension and the one obtained from the growth rate agree by the order of magnitude. Thus, the hydrodynamic description of the Rayleigh-Taylor instability can be applied even if only a comparatively small number of particles are involved in the movement.

In conclusion, we studied an instability that develops in complex plasmas under the influence of a temperature gradient. The observed phenomena, i.e., bubbles, droplets and cones, are similar to those observed in ordinary fluids. We showed that the onset of these phenomena can be explained in terms of a Rayleigh-Taylor instability. Complex plasmas thus allow the study of fluids at the level of individual particles, forming a link between the kinetic and hydrodynamic description.



M. Schwabe, M. Rubin-Zuzic, S. Zhdanov, A. Ivlev, H.M. Thomas and G.E. Morfill

## Optical phonons in 2D plasma crystals

Experiments with two-dimensional plasma crystals allow the study of phonon spectra with out-of-plane polarisation. We directly measured the dispersion relation for the first time using a novel method of particle imaging and could prove that the out-of-plane mode has a negative optical dispersion at small wave numbers. When we compare our results with theory, we find good agreement.

Two-dimensional (2D) complex plasmas are particularly convenient systems to study strongly coupled phenomena at the atomistic level in detail. These systems have the essential advantage that one can obtain complete information about the state of the entire particle ensemble in phase space. 2D complex plasmas usually are studied in ground-based experiments with radio frequency (RF) discharges. Microparticles injected in such a discharge levitate in the sheath region near the bottom electrode, where the electric field balances gravity. Under certain conditions the particles can form a monolayer, and if their electrostatic coupling is strong enough, the particles arrange themselves into ordered structures, i.e. 2D plasma crystals.

In 2D complex plasmas, as in any (strongly coupled) 2D system, two in-plane wave modes can be sustained. In crystals, both modes have an acoustic dispersion, one longitudinal, the other transverse. Since the strength of the vertical confinement in such systems is finite, there is a third fundamental wave mode associated with out-of-plane oscillations. So far, the systematic experimental

studies of the dust-lattice (DL) waves were limited to in-plane modes; the out-of-plane dispersion relation have never been directly measured. To a large extent, this is due to a lack of reliable diagnostics for the vertical dynamics of individual particles.

Here, we report on the first direct measurements of the out-of-plane DL wave mode in a 2D plasma crystal. The dispersion relation is obtained for a broad range of wave vectors. For the measurements we employed a new detection technique for the vertical (out-of-plane) particle displacement.

A sketch of the experimental setup is shown in Fig. 1. We used a capacitively coupled RF glow discharge in argon. The plasma parameters in the bulk discharge were deduced from Langmuir probe measurements. To form a 2D particle suspension, melamine formaldehyde microspheres levitated in the sheath above the RF electrode. The particles had a diameter of  $8.77\ \mu\text{m}$  and a mass of  $5.3 \cdot 10^{-13}\ \text{kg}$ . The diameter of the obtained crystalline structure was about 50–60 mm, depending on the number of injected particles. The interparticle distance was between 0.5 mm and 1 mm. The microparticles were illuminated by a horizontal laser sheet with a Gaussian profile in the vertical direction (with a standard deviation  $\sigma \sim 75\ \mu\text{m}$  which corresponds to a full width at half maximum of  $175\ \mu\text{m}$ ). The sheet thickness was approximately constant across the whole crystal. We imaged the particles through a window at the top of the chamber using a high speed camera that was able to obtain 250 frames per second.

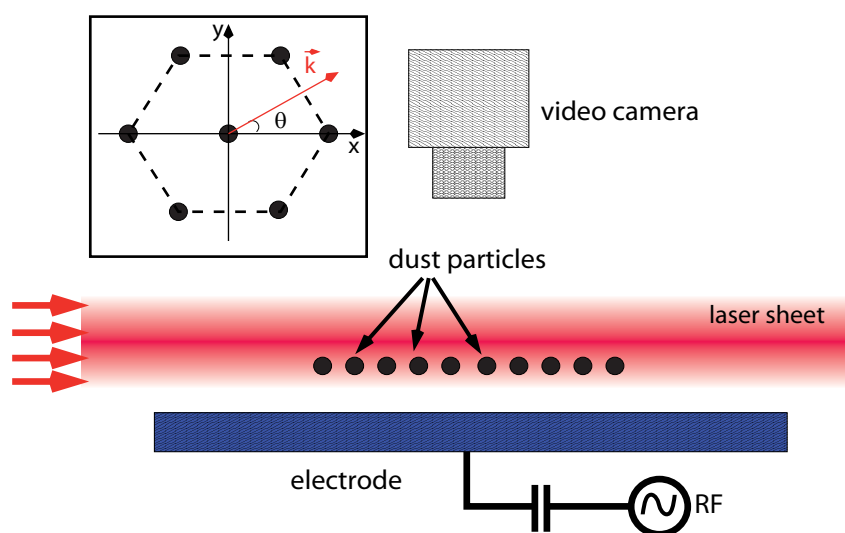


*Fig. 1: Sketch of the experimental setup. Microparticles are confined above the RF electrode and are illuminated with a horizontal laser sheet having a Gaussian profile in the vertical direction. The monolayer is levitated to well below the peak of the laser intensity, which results in strong intensity variations of the scattered light upon the vertical displacement of individual particles. The upward (downward) displacement corresponds to a positive (negative) intensity variation. The inset shows an elementary cell of the hexagonal lattice and the frame of reference, the orientation of the wave vector  $k$  is measured with respect to the  $x$  axis.*

Using a standard particle tracking technique, we could extract the horizontal coordinates as well as the velocity components in the horizontal plane for individual particles with sub-pixel resolution in each frame. With an additional side-view camera we were able to verify that our experiments were indeed carried out with a single layer of particles.

To extract the vertical position velocity of individual particles, we had to employ a very different technique. Unlike relatively compact Coulomb clusters, where these values can be directly measured by using the side view, the particles forming a large monolayer cannot be individually resolved from the side. Therefore, the out-of-plane tracking can be performed only by using the top view, where the vertical position  $z$  and velocity  $v_z$  have to be deduced from the relative variation of the scattered light intensity.

In the conventional method of particle visualisation, the intensity peak in the illuminating laser sheet practically coincides with the particle levitation height to facilitate the in-plane tracking, especially at higher frame

rates. This, however, is not appropriate to obtain  $z$  and  $v_z$  in our case for two reasons. The first problem of such a configuration is that the variation of the (particle image) intensity between consecutive frames gives us only the magnitude of the vertical displacement (and hence velocity), whereas the direction (up or down) remains undefined. The second problem of the conventional method is its sensitivity. We estimate the magnitude of the vertical displacement induced by thermal fluctuations as  $|\delta z| \leq 10 \mu\text{m}$ , which is much smaller than  $\sigma$ . The vertical gradient of the laser light intensity at the particle position is therefore very small. Consequently, the relative intensity variations  $\delta I/I$  are at a level of about 1%, which makes them very difficult to detect.

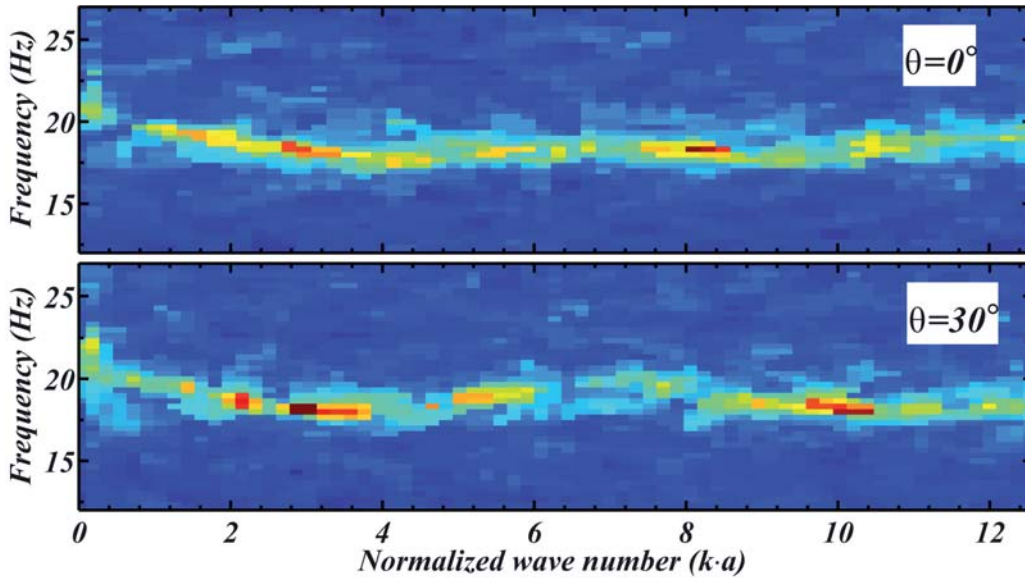


Fig. 2: Fluctuation spectra of naturally excited out-of-plane DL waves in a 2D crystal. The fluctuation amplitude is colour coded linearly, from dark blue to dark red, revealing the optical dispersion of the mode. The results shown are for a pressure of 0.8 Pa and an RF power of 15 W. The two panels depict the fluctuation spectra with the wave vector  $k$  pointed along the principal lattice axes,  $\theta=0^\circ$ , (top) and with an angle of  $\theta=30^\circ$  (bottom). For a visualisation see Fig. 1. The wave number is normalized by the inverse lattice constant  $a^{-1}$ .

In our experiments we employed an alternative method of particle visualisation. The position of the intensity maximum was set about  $100 \mu\text{m}$  above the levitation height. This allowed us to overcome both drawbacks mentioned above. Firstly, the particles now moved in the region where the vertical gradient of the illumination intensity remained positive, which allowed us to avoid ambiguity in determining the direction of the displacement. Secondly, the relative intensity variations thus scaled almost linearly with the displacement, so that the resulting magnitude of  $\delta I/I$  was about 15 times larger than in the conventional tracking configuration.

Experimental observation of the out-of-plane wave dispersion is the main result of our investigations. The resulting fluctuation spectra of the out-of-plane waves are shown in Fig. 2 for two principal orientations of the wave vector. The spectra represent the wave energy distribution in the  $(f, k)$  space, so that the “ridge” of this distribution yields the wave dispersion relation. The most conspicuous feature of the measurements is the optical character of the dis-

persion relation, i.e. the frequency of the long-wavelength waves is finite. Moreover, the dispersion at long wavelengths is negative; i.e., the wave frequency falls off as the wave number increases. At larger  $k$ , the wave dispersion is different for the different angles  $0^\circ$  and  $30^\circ$ . Fig. 2 shows that the wave frequency as a function of the wave vector  $k$  changes in a narrow interval of  $17 \text{ Hz} \leq f \leq 20 \text{ Hz}$ , which makes resolving the wave dispersion a challenging task. Our method, however, allowed us to clearly identify the wave dispersion. Indeed, the frequency resolution of  $\sim 1.5 \text{ Hz}$  is smaller than the measured wave frequency range  $\Delta f$  ( $\approx 3 \text{ Hz}$ ).

Our method allowed us to measure all three wave modes of a 2D plasma crystal in a single experimental run. In Fig. 3 we show the fluctuation spectra of the out-of-plane and the in-plane wave modes obtained from the same experiment as in Fig. 2, again for two principal lattice orientations,  $\theta=0^\circ$  and  $30^\circ$ . Only the first Brillouin zone, which is a uniquely defined primitive cell in reciprocal space, is shown here. The lines represent theoretical dispersion relations, which depend on the particle charge number  $Z_d$  and the lattice screening parameter  $\kappa=a/\lambda$ , where  $a$  is the interparticle distance (lattice constant) and  $\lambda$  the effective screening length. To calculate the theoretical dispersion relations we first

deduced the lattice parameters from the low- $|k|$  part of the in-plane fluctuation spectra. Secondly, we used these values in the theory of Zhdanov to calculate the whole dispersion curves.

As can be seen in Fig. 3, all three branches of the experimental wave spectra can be fitted with the same set of parameters for the theoretical curves. This provides a useful consistency check for our experimental method and also for theory. Good overall agreement of our measurements and theory serves as verification that our method correctly measures the out-of-plane motion of particles and also as indication that the theory correctly captures the essential physics of 2D plasma crystals.

The out-of-plane wave mode can also be useful for diagnostic purposes. The lattice parameter  $\kappa$  and dust particle charge  $Z_d$  are usually determined by fitting the in-plane dispersion relations. Another approach is to measure the propagation speed of externally excited pulses. This however it is not practical under certain conditions (e.g. near

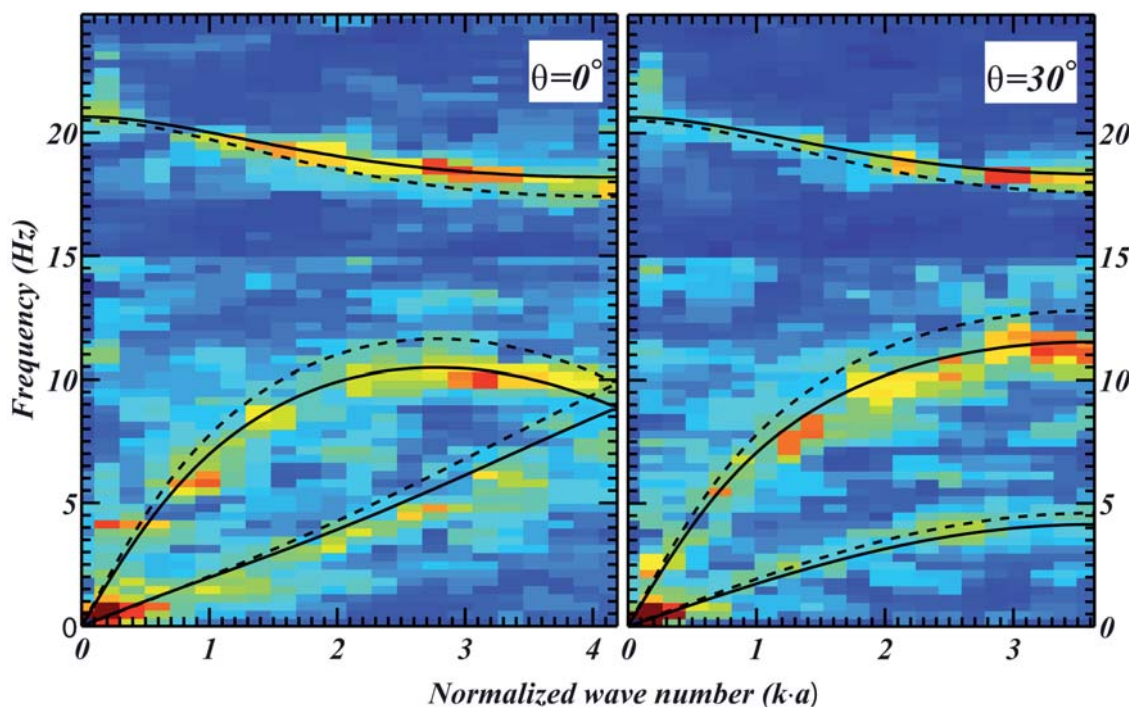
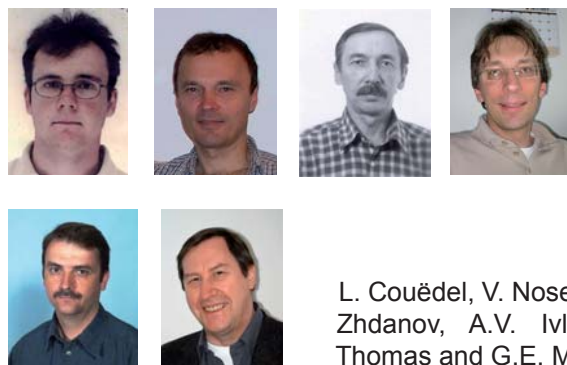


Fig. 3: Comparison of the experimentally measured DL dispersion relations with theory. Shown are the 2D in-plane and out-of-plane dispersion relations deduced from the experiments (with an RF power of 15 W and a pressure of 0.8 Pa) as well as theoretical curves. The results are presented for two directions of the wave vector  $k$  ( $\theta=0^\circ$  and  $\theta=30^\circ$ , see Fig. 1). The dashed lines are theoretical dispersion relations for pure Yukawa interaction between particles. For the solid lines the interaction with plasma wakes is taken into account. The range for  $|k|$  shown is limited to the first Brillouin zone and therefore depends on the direction:  $|k|a=4\pi/3$  for  $\theta=0^\circ$  and  $|k|a=2\pi/\sqrt{3}$  for  $\theta=30^\circ$ . The wave number is normalized by the inverse lattice constant  $a^{-1}$ .

the melting line) and one must rely on natural waves. In this case, the in-plane fluctuation spectra can be very noisy. Therefore, the additional fitting of the out-of-plane dispersion relation provides an important complementary tool to check the consistency of the measurements.

Direct observations of the atomistic dynamics in “regular” 2D or quasi-2D systems (such as carbon nanotubes and graphite) are inhibited, and therefore experimental measurements of phonon spectra in such systems rely on indirect methods. Natural model systems, such as complex plasma crystals, provide us with a unique opportunity to

study the generic properties of wave modes that are sustained in classical strongly coupled ensembles, to explore the limits of small “nano”-clusters, to investigate the peculiarities of the atomistic dynamics upon non-linear mode coupling, and so on. As compared to previously reported investigations of wave modes in 2D plasma crystals, the results presented here show a substantial improvement of the particle imaging technique. It allowed us for the first time to directly observe the optical phonon spectrum. In the future, this development will enable much better discrimination of the various subtle mechanisms affecting wave modes in 2D crystalline systems.



L. Couédel, V. Nosenko, S.K. Zhdanov, A.V. Ivlev, H.M. Thomas and G.E. Morfill

## Dissipative Dark Soliton in a Complex Plasma

We present the first observation of a dissipative dark soliton (DDS) in a three-dimensional complex plasma. The wave could be analyzed at the fully kinetic level of single particles. We performed our experiments in a capacitively coupled radio frequency (rf) gas discharge with a modified PK-3 Plus chamber. The complex plasma was prepared using spherical plastic beads of 3.4  $\mu\text{m}$  diameter levitated in the bulk of a neon plasma. The wave was impact excited by a short voltage pulse on the rf electrodes. In our experiment the DDS propagated with constant speed, the propagation time of the wave was at least 10 times longer than the damping time of single particle motion.

A soliton is a solitary wave packet that maintains its shape while it travels through a nonlinear and dispersive medium. Nonlinear effects transform the frequencies of the wave packet. Waves of different frequencies propagate with different velocities in a dispersive medium. The soliton is formed because of the dynamical equilibrium of these two counteracting processes. Historically the term soliton is used to designate pulse-like solitary waves in conservative (non dissipative) nonlinear systems.

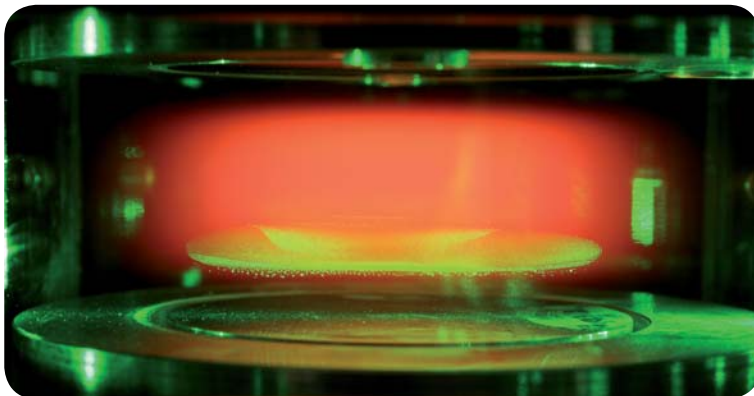


*Fig. 1: An example of the complex plasma formed in neon rf gas discharge used in the wave excitation experiments. The neon plasma (orange glow) is ignited between two rf electrodes, 3 cm apart. The micrometer sized particles levitated in the bulk plasma are illuminated by a green laser diode ( $\lambda = 532 \text{ nm}$ ).*

There are various types of dissipative systems which are capable of producing and stabilizing solitary structures. These waves form the new class of dissipative solitons. In contrast to solitons in conservative systems, dissipative solitons are dynamical objects that depend strongly on an energy supply from an external source.

The solitary wave structure we observed propagating in the complex plasma is of a rarefactive type. It resembles a so called dark soliton, observed in a many physical systems. For instance, the stable existence and propagation of compact rarefactive pulses is possible in multicomponent and non-isothermal plasmas. In addition, rarefactive ion acoustic solitary waves have been observed in auroral

plasmas, and in multicomponent plasmas with negative ions. Solitons and dark solitons have been predicted to exist in multicomponent self-gravitating molecular clouds consisting of, for example, a hydrogen gas and a dust component or a mixture of normal matter and dark matter. Since particle motion in our experiment is strongly damped, our system is highly dissipative. Therefore it is natural to call the waves “dissipative dark solitons” (DDS).

We use in our experiment a modified version of the PK-3 Plus design currently installed on board the International Space Station. Spherical monodisperse melamine-formaldehyde particles with a diameter of 3.42  $\mu\text{m}$  were injected into a neon plasma (Fig. 1). To situate the particle cloud in the bulk plasma, slightly below the center we used thermophoresis. For this purpose the lower chamber flange was heated to establish a temperature gradient of 500K/m. The resulting thermophoretic force was large enough to lift the particles out of the plasma sheath but still small enough to forestall the formation of a void that would appear if gravity is balanced completely. An approximately 100  $\mu\text{m}$  thick vertical slice through the center of the complex plasma was illuminated by a diode laser. The scattered light was recorded under 90° by a high-speed camera with a frame rate of 1000 Hz and a resolution of 1024x1024 pixels. We applied an optics to observe an area of 27.4x27.4 mm<sup>2</sup> resulting in a spatial resolution of 26.8  $\mu\text{m}/\text{px}$ . This camera and optics in combination with newly developed software allowed to track the full motion of 95% of all particles during the experiment (Fig. 2). The rf effective voltage was set to 13 V, a very low value, just high enough to sustain the discharge. Discharge pressures (20–35 Pa) were chosen in the under critical domain to avoid auto-wave excitations. This resulted in a stable single-wave regime without complications caused by the interaction of solitary and self-excited waves. Above 35 Pa the wave became unobservable due to strong damping.

To generate the solitary wave, the complex plasma was first compressed by a dc offset of 8.6 V externally applied to both electrodes. Switching off this dc offset triggers a solitary rarefaction wave. The dynamical scenario of the wave pattern formation is as follows: Immediately after switching off the negative voltage offset, the particles are at rest. Then the top layer accelerates into the empty region above the particle cloud, quickly followed by the second and further layers. These fast moving particles constitute the rarefaction zone. They are stopped suddenly, forming a sedimentation front. At low pressures (< 24 Pa) the fast particles can penetrate through the sedimentation front for up to five particle layers, resulting in a bidirectional flow. Independent of pressure the rarefaction zone was observed traveling at a speed of 2 cm/s. Inside the rarefaction zone the local particle number density was reduced by a factor of up to 7.8. At pressures below 2 Pa the DDS amplitude increased during propagation,

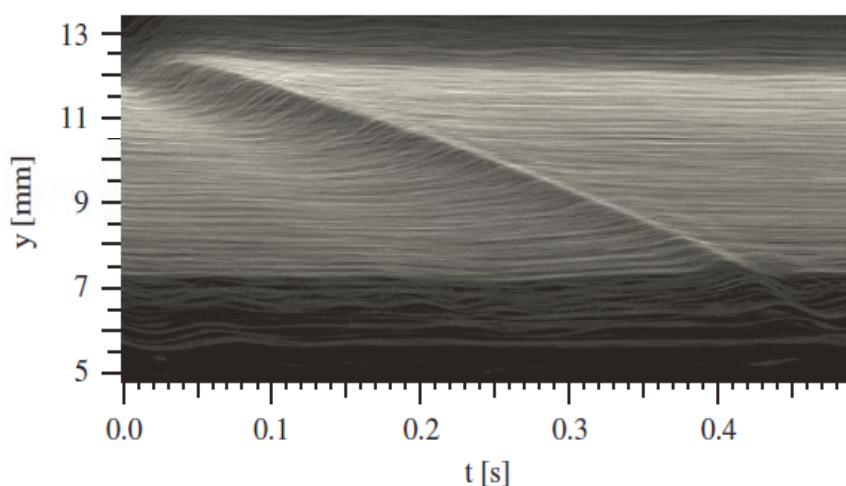


Fig. 2: Single-wave dynamics of the particle cloud. Upper row shows snapshots of the particle cloud. The field of view is  $13.7 \times 7.2$  mm<sup>2</sup>. The brighter, growing stripe on the top of each image is the sedimented part of the cloud. The bottom boundary of this stripe, expanding downwards, is the sedimentation front followed by the darker rarefaction zone. From left to right:  $t = 0.12$  s,  $0.20$  s,  $0.28$  s after the instant of shock excitation. Neon gas pressure is  $20.4$  Pa. Tracked particle positions for the same time instants are shown in the lower row ( $\sim 95\%$  of the particles were tracked). The dark soliton shifts rapidly downwards with respect to particle motion directed upwards. The maximal particle velocity is  $1.8$ – $2.0$  cm/s.

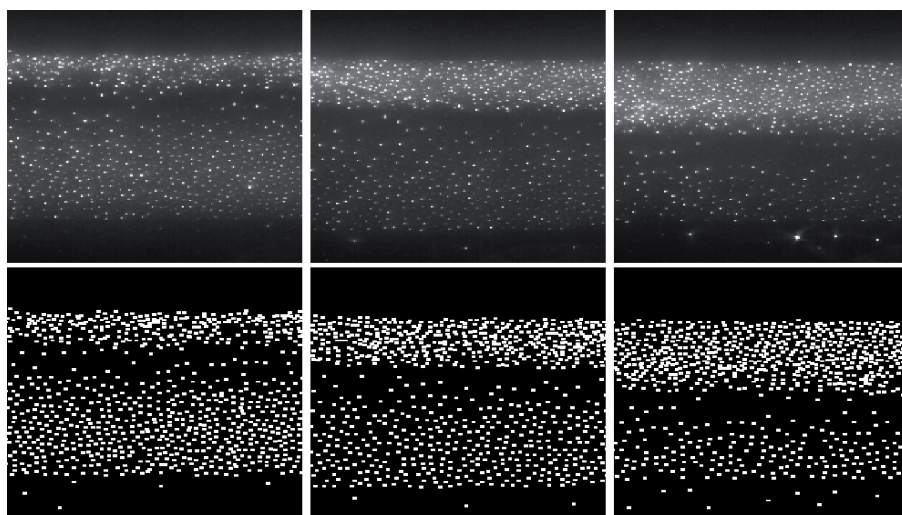


Fig. 3: Periodogram of the dark soliton in the complex plasma at  $24.1$  Pa. The wave is triggered by turning on or off a dc offset applied to both electrodes. The dark area corresponds to the rarefaction zone (see also Fig.2). The bright boundary on the right edge of the rarefaction zone is the narrow sedimentation front behind the wave. The periodogram is constructed from 490 images ( $0.49$  s). The vertical axis shows the distance from the lower electrode. The center of the plasma chamber is at  $15$  mm.

indicating a weak instability of the wave. Above  $22$  Pa the DDS amplitude decreased rapidly during the propagation time. The DDS amplitude decay rate was at least 10 times lower than the Epstein damping rate. Such anomalously low wave damping rates have already been observed in complex plasmas before. It is thought to be due to a collective effect but a final explanation is still missing.

Fig. 3 illustrates the propagation of the DDS through the particle system. In our experiment the DDS propagated vertically ( $y$  direction), and the particle distribution horizontally ( $x$  direction) was almost homogeneous (Fig. 2). The local particle density was proportional to the local visible brightness in the images. For each image the brightness

was averaged in  $x$  direction resulting in a line showing the vertical brightness distribution. The periodogram was constructed by stacking these lines together, representing the temporal evolution of the vertical brightness distribution in the recorded images, and thus the density of the particle cloud.

To conclude, a rarefactive strongly nonlinear solitary wave has been excited in a dense complex plasma, which is compensated for gravity by thermophoresis. We identify this wave as a dissipative dark soliton. We observed that the DDS could self-support its propagation for at least ten dissipation times. The excitation and free propagation of this nonlinear dissipative structure can be observed because the complex plasma is in an active under critical state for the pressure range used in the experiments. Dissipative dark solitons were observed in complex plasmas for the first time. The physical mechanism determining the behavior of rarefactive solitary waves is still under discussion. The complex plasma is a fully kinetic model system to study dissipative and dark solitons. This provides an excellent test for newly developed theories of such nonlinear structures. Furthermore dissipative dark solitons are signatures of peculiar features, allowing a deeper insight into the unique properties of the complex plasma itself.



R. Heidemann, S. Zhdanov, R. Sütterlin, H.M. Thomas, and G.E. Morfill

## Dynamics of Lane Formation in Driven Binary Complex Plasmas

We conducted a series of experiments to study non-equilibrium phase transitions in complex plasmas using the PK-3 Plus Laboratory on the International Space Station. In our experiments small (driven) micro-particles penetrate into a cloud of large (background) particles, revealing a strong tendency toward lane formation: When the driving force is strong enough, particles of both sorts form interpenetrating lines, which are characterized by a considerable anisotropic structural order and an enhanced unidirectional mobility of particles. We quantify the “laning” by using a universal „nematic“ order parameter for non-equilibrium phase transitions in driven systems. When we compare the time-resolved lane-formation process to a set of computer simulations of a binary Yukawa model with Langevin dynamics, this reveals a strong influence of the initial conditions on the dynamics of lane formation.

The formation of lanes is a ubiquitous non-equilibrium phase transition, occurring in nature when two species of particles are driven against each other. When the driving forces are strong enough, like-driven particles form “stream lines” and move collectively in lanes. This effect is most commonly known from pedestrian dynamics in highly populated pedestrian zones, and it occurs also in various systems of driven particles, such as colloidal dispersions, lattice gases, and molecular ions. Particle laning in complex plasmas occupies the important intermediate dynamical regime between undamped fluids and fully damped colloidal suspensions: The “atomistic” dynamics associated with the interparticle interactions is virtually undamped, whereas the large-scale (long-term) fluid patterns are determined by friction. While steady-state lanes have been studied in detail, the dynamical pathway toward the laning is still under debate.

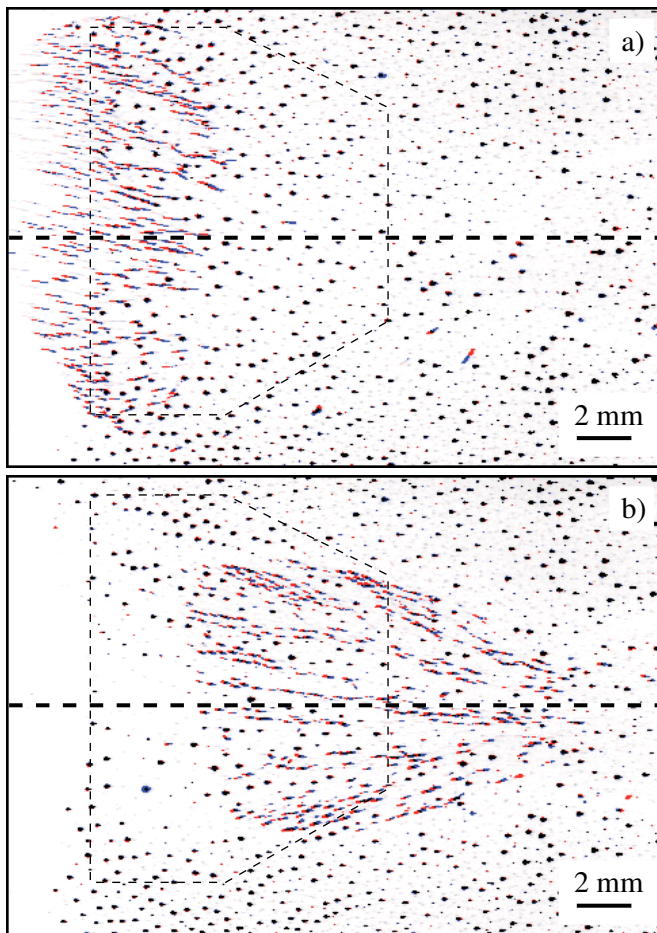


*Fig. 1: Lane formation in complex plasmas. A short burst of small ( $3.4 \mu\text{m}$ ) particles is injected into a cloud of large ( $9.2 \mu\text{m}$ ) background particles (close to the midplane of the chamber, indicated by the horizontal dashed line). Small particles are driven towards the centre. Panels (a) and (b) show stages of initial lane formation and lanes merging into streams, respectively. At stage (b) large particles also form well-defined lanes. The dashed box marks the measurement area for lane formation of large particles.*

The laning experiments are performed in the PK-3 Plus laboratory onboard the International Space Station (ISS). First, almost the whole plasma chamber is filled with large particles that form a stable and fairly homogeneous background. Then, small particles are injected from outside. The small particles are driven through the cloud of large particles toward the centre of the chamber. When the small particles enter the large-particle cloud, the subsequent penetration is accompanied by a remarkable self-organisation sequence (illustrated in Fig. 1): (a) Large particles are pushed collectively by the inflowing cloud of small particles, where the latter form “strings” drifting parallel to the driving force; (b) as the particles approach the centre of the chamber, the force decreases and the strings organise themselves into larger “streams”; (c) finally, when the force almost vanishes, the streams merge to form a spheroidal droplet with a well-defined surface, indicating the transition to the regime of phase separation (not shown here). During stage (b) large particles also form well-defined strings so that small and large particles create an “array” of inter-penetrating strings. After the flux of small particles is exhausted, the large-particle strings slowly dissolve.

The particles are illuminated by a thin laser sheet (about  $0.35 \text{ mm}$ ) from the side, and the scattered light is recorded by a 50 Hz progressive scan PAL camera under an angle of  $90^\circ$ . From these images full particle kinetics are reconstructed, allowing the analysis of the dynamics of lane formation. Some parameters cannot be deduced from the experiment and have been calculated from two independent numerical simulations. First, we performed simulations of the PK-3 Plus discharge chamber using a plasma fluid code (treating dust as a fluid species). This provided us with plasma density, electron temperature and electric fields, and suggested that the cloud of large particles is “self-confined” at its edges due to a self-consistent plasma field. Inside the cloud, the large particles are virtually free of external forces. For the small particles, however, there is a nonzero net force inside the background pushing

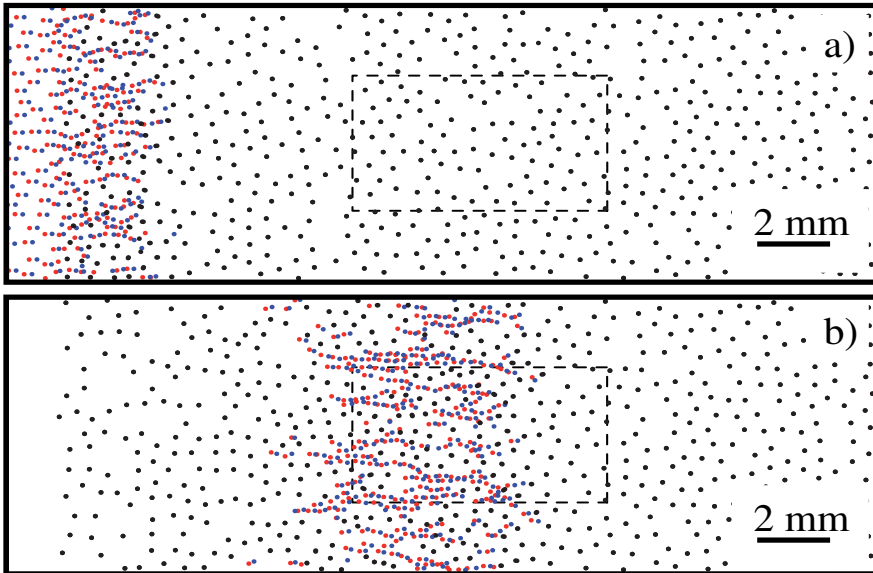


Fig. 2: Lane formation in a molecular-dynamics simulation corresponding to the experiment shown in Fig. 1. Two snapshots illustrate (a) the initial injection stage and (b) the steady state. The dashed box marks the measurement area for lane formation of large particles.

each small particle toward the centre. Second, we input these results in a particle-resolved molecular-dynamics (MD) simulation for a binary mixture of 5759 small and 12287 large particles (see Fig. 2). The 3-D MD simulation was used to calibrate our local anisotropic structure measures and the global “nematic” order parameter. Unlike in the experiment, we can directly and independently control any parameter defining particle interactions.

We globally measure lane formation using the order parameter  $S$ , whose definition is analogous to the nematic order parameter in liquid crystals. Using a locally adaptive anisotropic scaling index method, we obtain the direction of the largest anisotropy. This method allows us to define a unit vector associated with each single particle. The magnitude of  $S$  is a measure of how strongly these vectors are aligned:  $S=0$  corresponds to a random distribution and  $S=1$  indicates perfect alignment, i.e., perfect lane formation.

At first we compared the experimental data to the “best fit” parameter set of the 3-D MD simulation. We used all parameters measured in the experiment, substituted unavailable values from the 2-D fluid code, and then fine-tuned all remaining free parameters to reproduce single particle kinetics most accurately. For large particles, simulation and experiment agree almost perfectly (see Fig. 3). The important features are the initial nonzero value of the order parameter for the experimental data, the rise and fall times, and the non-vanishing “final” value of the order parameter. The slight initial anisotropy in the experimental data – due to a transverse density gradient – was not reproduced in the simulation because of periodic boundary conditions. The rise time is practically identical to the mixing time,

i.e. the time it takes for small particles to completely fill the measurement box. This means that – within the temporal resolution of the experiment – lanes in the background complex plasma are formed “immediately” by the small particles streaming through it. The fall time consists of three parts: (1) the demixing time needed by the small particles to leave the measurement box (lanes in the background cloud are kept for a while after the small particles are gone); (2) a period of fast relaxation, where these lanes decay at a characteristic timescale of  $\sim 1$ s, which is much slower than self-diffusion; and (3) a period where  $S_L(t)$  stays on some intermediate plateau, indicating that the structural relaxation might involve metastable states.

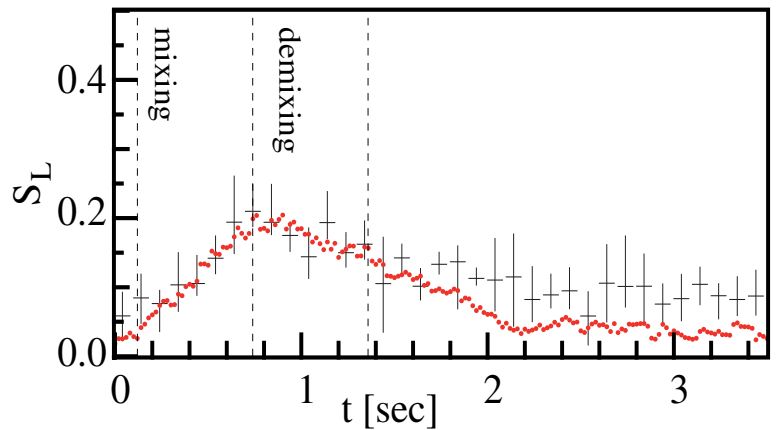


Fig. 3: Evolution of the order parameter for large particles  $S_L$ , as obtained from the anisotropic scaling index analysis of the experiment (crosses) and a molecular-dynamics simulation (dots). The dashed lines indicate the time it takes for small particles to fill (mixing) and then leave (demixing) the measurement area where  $S_L$  is determined (see Figs. 1 and 2).

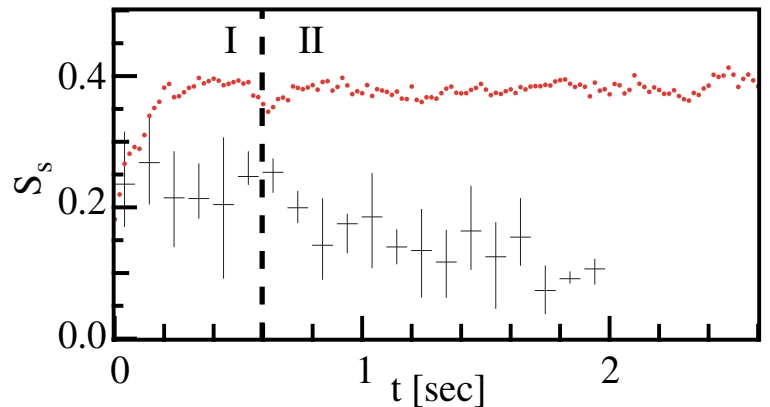


Fig. 4: Evolution of the “nematic” order parameter for small particles  $S_s$  in the experiment (crosses) and in a molecular-dynamics simulation (dots). The transition from the injection stage I to the steady-state stage II is indicated by the dashed line.

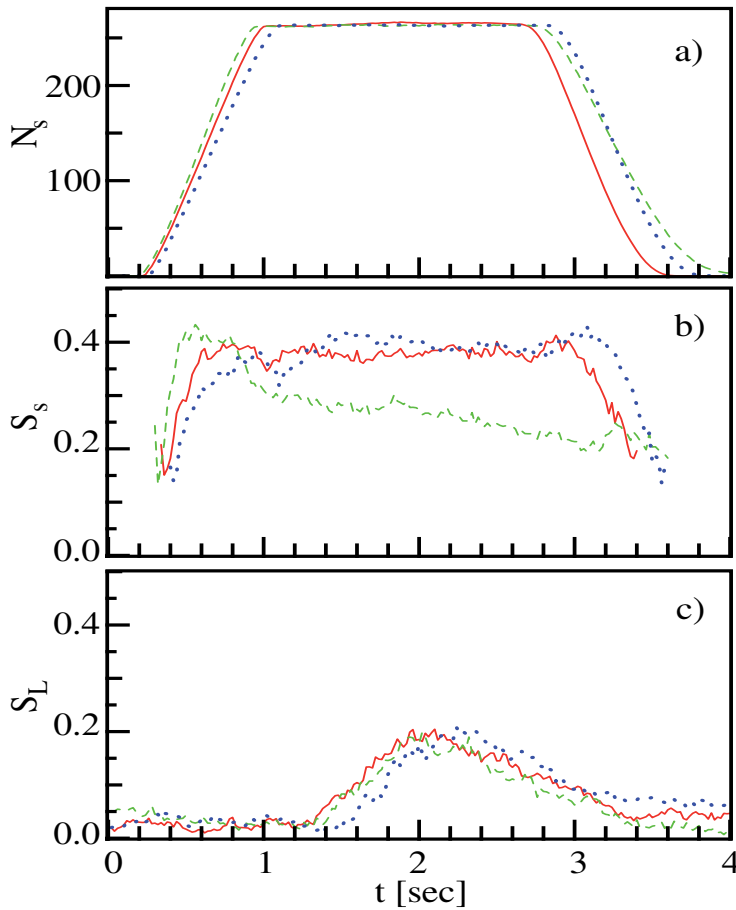


Fig. 5: Influence of particle charge  $Q$  and screening length  $\lambda$  on the dynamics of lane formation.  $Q$  and  $\lambda$  are varied in the molecular-dynamics simulations in a way that the coupling parameter  $\Gamma$  is kept constant: the different curves represent the “best fit” parameters (solid, red), shorter  $\lambda$  and enhanced  $Q$  (dashed, green), longer  $\lambda$  and reduced  $Q$  (dotted, blue). The panels show the number of small particles inside the background cloud of large particles (top), and the temporal evolution of the order parameter for small (middle) and large particles (bottom).

For small particles there are two distinct differences. First, the value of  $S_s$  determined in the experiment is artificially lowered by the uncertainty in identifying small particles in the experimental data. Second, unlike in the simulation, small-particle lanes in the experiment seem to decay after injection while the small particles travel through the background complex plasma.

The choice of “best fit” simulation parameters left us with one important free parameter to tune in the MD simulation: the decomposition of the coupling parameter  $\Gamma$  into particle charge  $Q$  and Debye screening length  $\lambda$ , which have larger uncertainties than  $\Gamma$ . We varied  $Q$  and  $\lambda$  in such a way that the resulting coupling parameter stayed constant; their influence on the dynamics of lane formation is shown in Fig. 5. The main result is that these variations strongly affect lane formation of the small particles. Simulations with shorter screening length and enhanced charge produce much better agreement with experiments. This investigation of lane formation thereby allowed us to indirectly estimate two otherwise inaccessible complex plasma parameters.



R. S utterlin, A.V. Ivlev,  
C. R ath, H.M. Thomas,  
M. Rubin-Zuzic and G.E.  
Morfill.

## 2D melting of plasma crystals

In different experiments we studied the melting of two-dimensional complex plasmas in steady and unsteady heating regimes. We demonstrate that the defect concentration exhibits an Arrhenius dependence with respect to the kinetic temperature in steady-state experiments. Unsteady experiments show evidence of metastable quenching, where the defect concentration follows a power-law temperature scaling. In all experiments, independent indicators suggest a grain-boundary-induced melting scenario.

Understanding the mechanisms governing the two-dimensional (2D) solid-liquid phase transition is a long-standing problem. Numerous models have been put forward to characterize melting and – most importantly – to reveal universality in the melting behaviour. Two competing models are of particular relevance: the theory of grain-boundary-induced melting and the dislocation theory of melting, the Kosterlitz-Thouless-Halperin-Nelson-Young (KTHNY) theory, which involves two phase transitions with an intermediate (so called “hexatic phase” in between).

The motivation for our comprehensive experimental studies of the 2D solid-liquid phase transition in complex plasmas is twofold: to identify the relevant melting scenario operating in systems with (exponentially) short-range interactions, and to find major similarities in characterizing the melting behaviour at various experimental conditions.

Four experimental series (each composed of several experiments) were performed at different pressures, employing qualitatively different heating methods and particles of different sizes. In each experiment, a monolayer of monodisperse melamine-formaldehyde microspheres was levitated in a sheath region above a horizontal electrode of a capacitively coupled RF argon plasma. The particles charged up to approximately  $-10^4e$  and interacted through a screened Coulomb, or Yukawa potential. Before heating was applied, the particles self-organized in an ordered triangular lattice, which, however, always contained defects, as revealed by the Voronoi diagrams (see Fig. 1a). A defect is defined as a lattice site where a particle has more or less than six nearest neighbours. Usually, defects cluster together to form edge dislocations (isolated pairs of 5- and 7-fold defects) or domain boundaries (chains of defects).

In three experimental series the particles were kept under steady heating conditions, while one series was used to study the evolution during a rapid recrystallization. Below we summarize the distinctive features of each series.

**Series I:** We used a laser-heating method, where two counter-propagating laser beams applied brief intense kicks to particles. The kinetic temperature of the particles  $T$  grew with the laser power applied; the concentration of defects  $c$  was on average uniform in the heated rectangular region. We refer to this series as the “*uniform heating*” experiment.

**Series II:** Here we used the same heating method to create a one dimensional temperature gradient in a particle monolayer and to study heat transport. Unlike in series I,  $T$  and hence  $c$  had a spatial gradient outside of the heated region. We therefore performed the analysis in narrow rectangular bins perpendicular to the gradient (where  $T$  and  $c$  were practically constant). We refer to this series as the “*temperature gradient*” experiment.

**Series III:** We created a shear flow in a 2D complex plasma to measure the shear viscosity. Two counter-propagating Ar<sup>+</sup> laser beams pushed the particles, causing a shear-induced melting of the monolayer and a shear flow in a planar (Couette) configuration. Similar to series II,  $T$  and  $c$  varied in the direction perpendicular to the flow and were calculated in narrow rectangular bins. Below, we call this the “*shear flow*” experiment.

**Series IV:** We melted a monolayer plasma crystal by applying a short electric pulse to two parallel wires located slightly above the particles, and then left the system to cool down naturally (due to a weak friction on the particles caused by the ambient neutral gas). We studied the evolution of  $T$  and  $c$  during the stage of recrystallization. We refer to this experiment as the “*recrystallization*” experiment.

In Fig. 1 we compare the results of the uniform heating (I, left column) and the recrystallization (IV, right column) experiments in different “temperature regimes”. This allows us to identify a qualitative difference between the *steady-state* experiments I-III and the *unsteady* experiment IV. The top panels (Fig. 1a) show the lattice before heating is applied. At high temperatures (Fig. 1b) monolayers contain a substantial fraction of 5/7-fold defects (dislocations) and even a few 4/8 defects. The number of defects in experiment I is somewhat larger than in experiment IV. The situation changes at lower temperatures (Fig. 1c), where the number of defects is smaller in experiment I than in experiment IV. At the same time, at lower temperatures the dislocations have a common tendency to cluster into strings separating domains with local hexagonal order.

The quantitative analysis of the experiments is summarized in Fig. 2. We measured the number of 5/7-fold defects,  $N_{5,7}$ , and plotted their concentration  $c_{5,7} = N_{5,7}/N$  as a function of temperature. (As  $c_7(T)$  is nearly identical to  $c_5(T)$  it is not shown here.) To compare the experiments, which were performed at somewhat different conditions, we introduced the inverse coupling parameter  $\Gamma^{-1} = T\Delta/Q^2$  as the natural “similarity number”, where  $T$  is the temperature,  $Q$  and  $\Delta$  the particle charge and interparticle distance, respectively).

A remarkable result is the principal difference in the behaviour of  $c(T)$  for steady-state experiments I-III and the recrystallization experiment IV. For this, the concentration exhibits a relatively slow power-law scaling over two

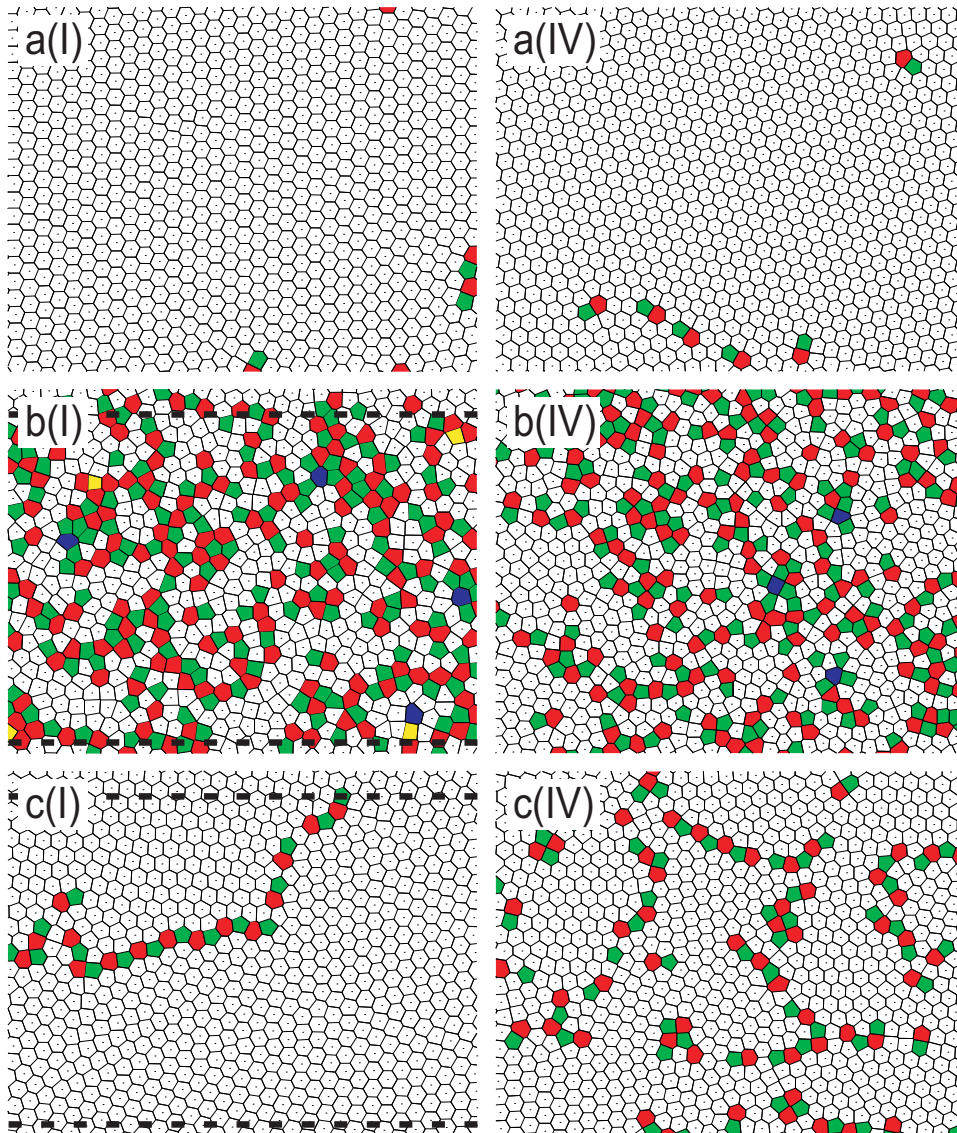


Fig. 1: Maps of defects in 2D complex plasmas. The left and right columns illustrate the difference between the uniform heating experiment I and the recrystallization experiment IV. Horizontal dashed lines indicate the heating region. The dots are individual particles located inside their Voronoi cell: green/red colours represent 5/7-fold defects, yellow/blue indicate 4/8-fold defects. The different temperature regimes a, b, and c are discussed in the text.

decades of temperature,  $c(T) \propto T^\alpha$ . Experiments I-III demonstrate a universal behaviour accompanied by a much stronger temperature dependence. The inset in Fig. 2 shows that the concentration of dislocations in the steady-state experiments obeys the Arrhenius law,  $c(T) \propto e^{-W/T}$ . A least-squares fit of  $c(T)$  yields values for the activation energy  $W$  of the 5/7-fold defects in the range of 0.9-2.6 eV for experiments I-III, as well as a value for the temperature exponent  $\alpha \approx 0.37$  for experiment IV.

It is generally believed that the value of the defect core energy  $E_c$  plays a critical role in the realization of the melting scenario. The KTHNY mechanism should operate when  $E \geq 2.8T_{hex}$ , where  $T_{hex}$  is the transition temperature to the hexatic phase, which in the KTHNY model is associated with the melting via unbinding of dislocation pairs. Otherwise, grain-boundary-induced melting should occur.

In the equilibrium case, the activation energy in the Arrhenius law is equal to twice the core energy. We therefore obtain  $E_c = W/2 = 0.5-1.3$  eV, whereas theoretical estimates for the hexatic transition temperature yield  $T_{hex} = 6-9$  eV. Hence,  $E_c$  is 10-20 times smaller than the critical value, which strongly suggests that in our experiments the grain-boundary-induced melting scenario is realized.

The conclusion that the KTHNY melting mechanism is “pre-empted” in our experiments by a first-order phase transition can also be drawn from empirical indicators of 2D melting. These can either be dynamical criteria (various forms of the Lindemann criterion) or static indicators. The latter are based on a drastic qualitative change occurring in the shape of the static structure factor within a narrow temperature range, which makes them particularly well suited for our experiments. Based on the height of the first peak of the pair correlation function, for example, we estimate the melting temperature to be 2.5-4.2 eV for experiment I, which is 2-3 times lower than  $T_{hex}$ .

Let us now focus on the principal difference revealed in the behaviour of  $c(T)$  for the experiments performed under steady and unsteady conditions. In all experiments the Epstein friction rate  $\gamma$  (which is due to the interaction of particles with neutral gas) was a factor of 10-30

smaller than the Einstein frequency  $\Omega_E$  (which characterizes the momentum/energy relaxation in mutual particle collisions). It is therefore not surprising that the measured velocity distributions of particles are well reproduced by the equilibrium Maxwellian form. The structural equilibration, however, might take much longer than the equilibration in velocity space. This is apparently the reason of the essential difference in the behaviour seen in Fig. 2 between series I-III and series IV: The former experiments were performed under steady conditions allowing structural relaxations during a few minutes, which is a factor of  $10^3-10^4$  longer than the “atomistic” timescale  $\Omega_E^{-1}$ . The Arrhenius law for  $c(T)$  observed in these cases naturally suggests a (quasi-)equilibrium regime of melting. In contrast, the exponential cooling of the system occurring at timescales  $\gamma^{-1}$  in the recrystallization experiment was just too rapid for the structural equilibration.

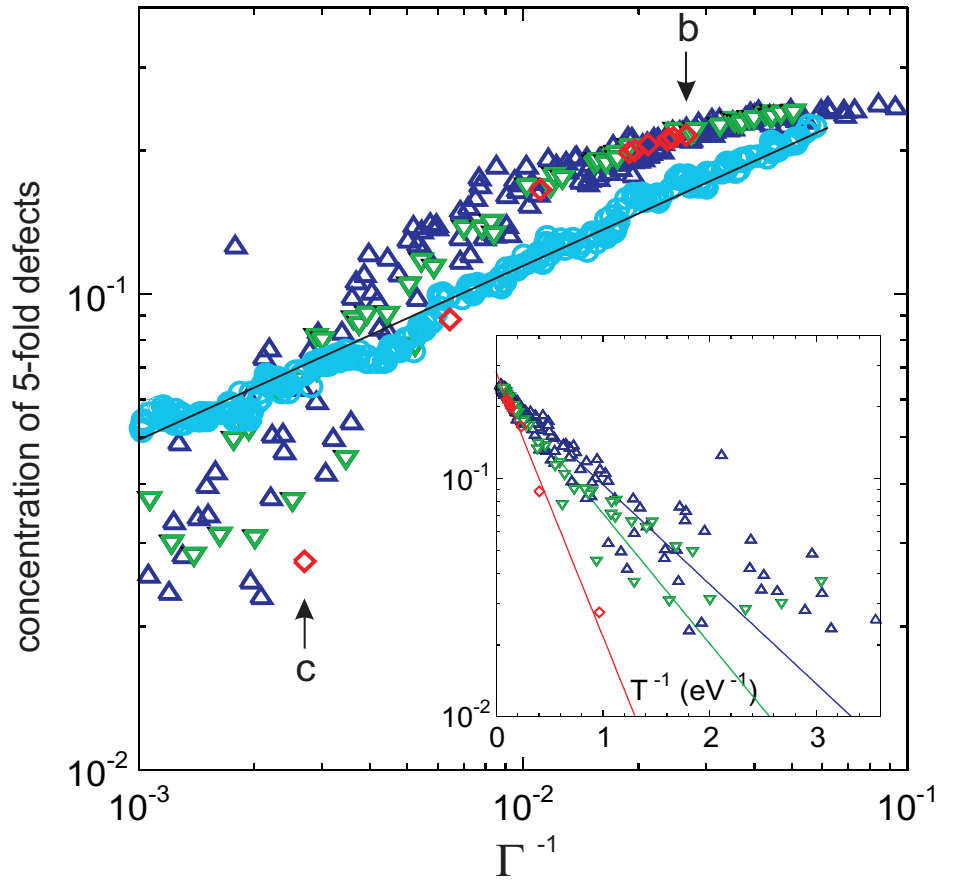


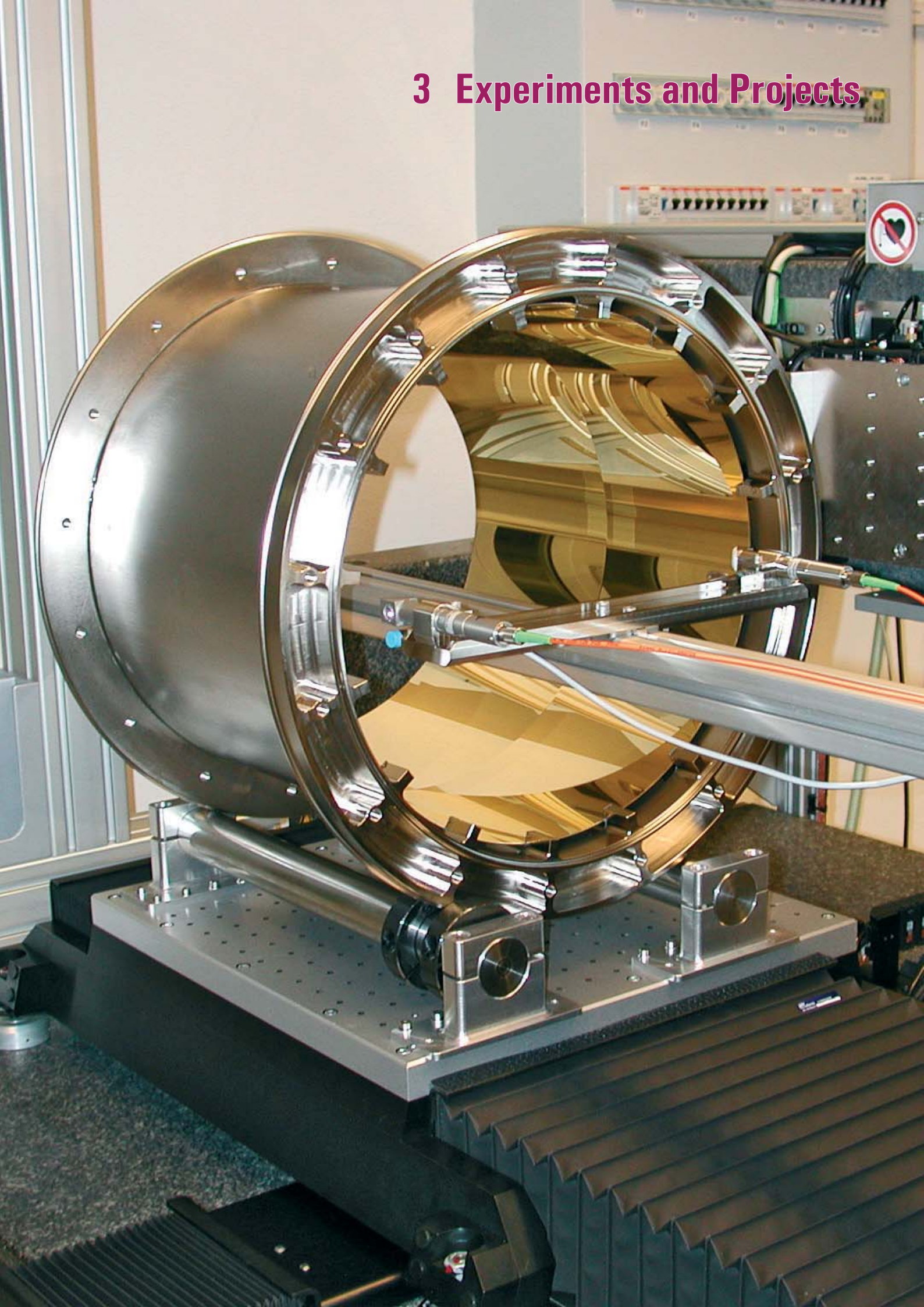
Fig. 2: Concentration of defects  $c_5$  versus temperature. The symbols correspond to the four experimental series: red diamonds for uniform heating (I), green down-triangles for temperature gradient (II), blue up-triangles for shear flow (III), and cyan circles for recrystallization (IV). Vertical arrows indicate the different temperature regimes illustrated in Fig. 1b,c. The normalized temperature is displayed as the inverse coupling parameter  $\Gamma^{-1}=T\Delta/Q^2$ .



V. Nosenko, S.K. Zhdanov, A.V. Ivlev, C.A. Knapek and G.E. Morfill



### 3 Experiments and Projects



### 3.1 INFRARED/SUBMILLIMETER ASTRONOMY

Our group is developing high resolution near-infrared instrumentation for large ground-based telescopes as well as space-based and airborne far-infrared instrumentation. Our intention is to tackle a few key scientific questions, simultaneously using a wide range of observing wavelengths and methods simultaneously.

Our suite of previously developed Very Large Telescope (VLT) instruments using adaptive optics continues to be scientifically extremely productive for the group and the community. These include the NACO near-infrared camera and spectrometer (commissioned 2002), the SINFONI near-infrared integral field spectrograph (commissioned 2004), and the PARSEC-Laser for the VLT Laser Guide Star Facility (commissioned 2006).

The MPE and other German institutes hold a 25% share in the dual 8m Large Binocular Telescope (LBT) on Mount Graham, Arizona. We have been receiving science data from the LBT prime focus optical imager since early 2007. Our first major instrument contribution to LBT is the multi-object spectroscopy unit that is part of the near-infrared imager/spectrograph LUCIFER, with the first unit commissioned in 2009 (see LUCIFER article). The ARGOS laser facility for ground-layer adaptive optics at the LBT will strongly enhance the LBT's capabilities for multi-object spectroscopy and imaging at high spatial resolution, by sharpening the point spread function over a wide field of view. After a 2007/08 Phase A study ARGOS was approved by the LBT Board and development is going ahead at full speed.

GRAVITY is a 2nd generation instrument for the VLT Interferometer, optimized for highest precision astrometry in the near-infrared K-band. Probing the physics and strong gravity next to the Galactic center black hole is one of the key goals of this instrument. Gravity was recommended by ESO's science and technical committee in 2007 to proceed into the preliminary design phase, which was completed in December 2009.

In collaboration with ESO, we set up a testbed in our MPE laboratories to jointly integrate and test the PRIMA astrometric facility for the VLT interferometer.

We are developing the analysis software for the near-infrared multi-integral field unit spectrograph KMOS being built for the VLT by an international consortium including MPE. KMOS has completed its final design review in April 2008 and is now in the manufacture, integration and test phase.

We are entering the era of extremely large optical/infrared telescopes with the MICADO study for a diffraction limited near-infrared imager/spectrometer for the 42m European Extremely Large Telescope (EELT) project. A consortium, led by the MPE, was awarded the contract for a Phase A study which was successfully completed in December

2009 (see also highlight article on the high resolution instruments GRAVITY, ARGOS, MICADO).

A decade of development of PACS for ESA's Herschel Space Observatory peaked by the Herschel launch on May 14, 2009 and the subsequent successful commissioning (see Herschel/PACS article). What has been MPE's biggest instrumentation project for some time is now entering a promising science phase.

The far-infrared integral field spectrometer FIFI-LS is awaiting its use on the US/German airborne observatory SOFIA, which has successfully performed its first open-door flight in late 2009. FIFI-LS will be transferred to the observatory in 2010.

We have studied hardware and science cases for a next generation far-infrared imager and spectrometer. This planned instrument, SAFARI, has been recommended by ESA's Cosmic Vision M-class down-selection process and may be contributed by a European consortium to the fully cryogenic 3m-class infrared space observatory SPICA, that is under study by the Japanese Space Agency.



Fig.1: The concept of the EUCLID satellite.

Together with the MPE OPINAS group and the international DUNE/EUCLID consortia, we have been designing the near-infrared imager for the DUNE satellite proposal to ESA's Cosmic Vision process, which successfully evolved into the EUCLID mission, to study dark energy, dark matter and galaxy evolution. EUCLID was recently recommended by ESA's M-class mission down-selection.

## Fly me to L2 – successful launch and commissioning of Herschel/PACS

Following extensive tests at MPE, the PACS Instrument for ESA's Herschel Space Observatory has been delivered for integration into the satellite. Herschel was successfully launched by an Ariane 5 rocket in May 2009. Within 6 months from launch, we have commissioned the instrument, optimized its operation, and already obtained a set of impressive results from this unique observatory.

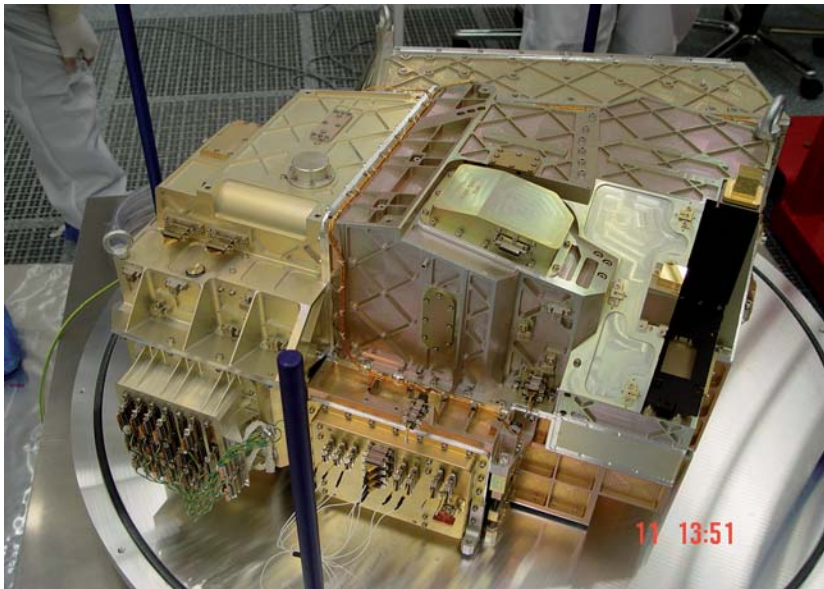


Fig. 1: The PACS Focal Plane Unit at the time of delivery to ESA/Industry.

This is about the successful conclusion of an instrument development program, which had kept us busy for more than a decade: the Photodetector Array Camera & Spectrometer (PACS), one of the three scientific instruments on board the Herschel Space Observatory for far-infrared/submillimeter astronomy. PACS comprises a “colour” camera system for photo-metric imaging in 3 bands in the 60 – 210  $\mu\text{m}$  range and an imaging grating spectrometer covering the same wavelength range with a spectral resolving power of around 1500. After the final, optical alignment and successful tests and calibration of the PACS instrument in our laboratory, PACS was declared ready for delivery in July 2007.

Its initial destination was Astrium (Friedrichshafen), where the Focal Plane Unit of the instrument was mounted on the optical bench of the Herschel cryostat and its warm electronics units were accommodated in the service module of the satellite. Functional tests and also some repair work on the satellite cable harness turned out to be necessary before – in the fall of 2007 – we could give green light, for the closure of the satellite cryostat. At that point, the operation moved to ESTEC (Noordwijk). The first important step, before the slow

cool-down process to a temperature of 4K could start, was the “bake-out” of the cryostat to remove water and other contaminants, which otherwise might have deposited on the optics of the instruments,

After each step of the integration and qualification process we performed tests designed to demonstrate that our instrument had survived the respective operation. The biggest potential risk for PACS in the qualification process was the acoustic noise test. Earlier tests with the empty satellite cryostat as well as our structural analysis had indicated that this particular test would apply forces to the delicate suspension strings of the PACS bolometric detectors close to their load limits. Much to our relief, no damage occurred, which also meant that no harm was to be expected during launch.

In August 2008, the first full tests started. We could confirm that PACS was still working as at MPE before, and that no performance degradation had occurred from the qualification tests. The final, comprehensive test campaign took place in the “Large Space Simulator” at ESTEC, where the satellite could be operated under nearly space-like conditions. The satellite was declared ready for launch and prepared for the transport to Kourou (French Guyana) shortly before Christmas of 2008 where it arrived on February 12, 2009 on board an Antonov cargo airplane. We performed our last test of PACS on the ground on March 5, 2009, and found everything ready for launch.

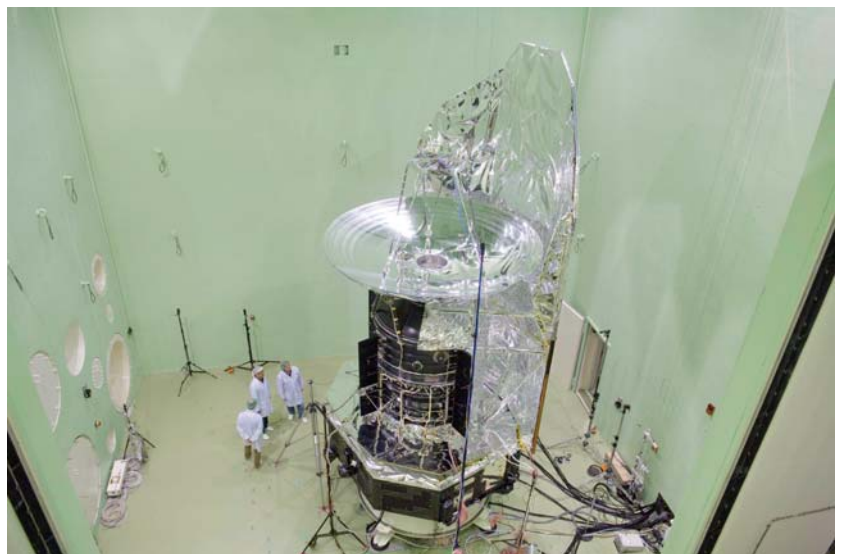


Fig. 2: The Herschel satellite in the Large European Acoustic Facility, where the acoustic noise during launch (up to 156 dB!) can be simulated.

Herschel – as well as Planck as the second pay-load on the launcher – were then mounted in the fairing of the Ariane 5 ECA rocket and finally rolled out to the launch pad on May 13, 2009. The liquid helium transfer lines, which cooled the heat shields of the Herschel cryostat in order to minimize boil-off from the cryostat tank, had to be disconnected about ten hours before the opening of the launch window. Any delay of the launch from that moment on would have meant a shortening of the mission life time!

The morning of May 14th started with a solid, tropical rainstorm. Fortunately, it stopped just in time before the launch window opened. Finally, our Ariane 5 took off exactly on time and delivered Herschel and Planck on their trajectories towards their respective orbits around the L2 Lagrangian point of the Sun-Earth system.

We could switch on PACS – still on its way to L2 – and check out the system already on May 24. Within hours we had confirmation that all subsystems were nominal and the PACS detectors were not experiencing any unexpected degradation from cosmic rays or solar protons.

The further commissioning of the instrument went so smoothly that ESA even asked us to attempt a first observation of an “impressive” object in the sky well before the official “first light” of the observatory, as soon as the lid on the cryostat would be opened. This seemed quite daring to us, without any knowledge of the exact pointing and the straylight/background level of the still relatively warm telescope. But we tried and – almost miraculously – got everything right at the first attempt. The result was a stunning image of the “Whirlpool Galaxy” M51 in three far-infrared colours, which immediately showed that the optical train of telescope and instrument combined (never tested end-to-end on ground!) delivered diffraction-limited resolution at all wavelengths.

The following months were dedicated to a systematic characterization, optimization and calibration of our complex instrument and its interaction with the satellite. By the fall of 2009, the effort was rewarded by an instrument that fulfilled all our expectations in terms of scientific performance.

Since then we have obtained a wealth of data, both, in photometry and in spectroscopy, from objects ranging from nearby, young stars to galaxies at cosmological distances. We are now looking forward to more than three years of routine operation with this new and unique observatory.

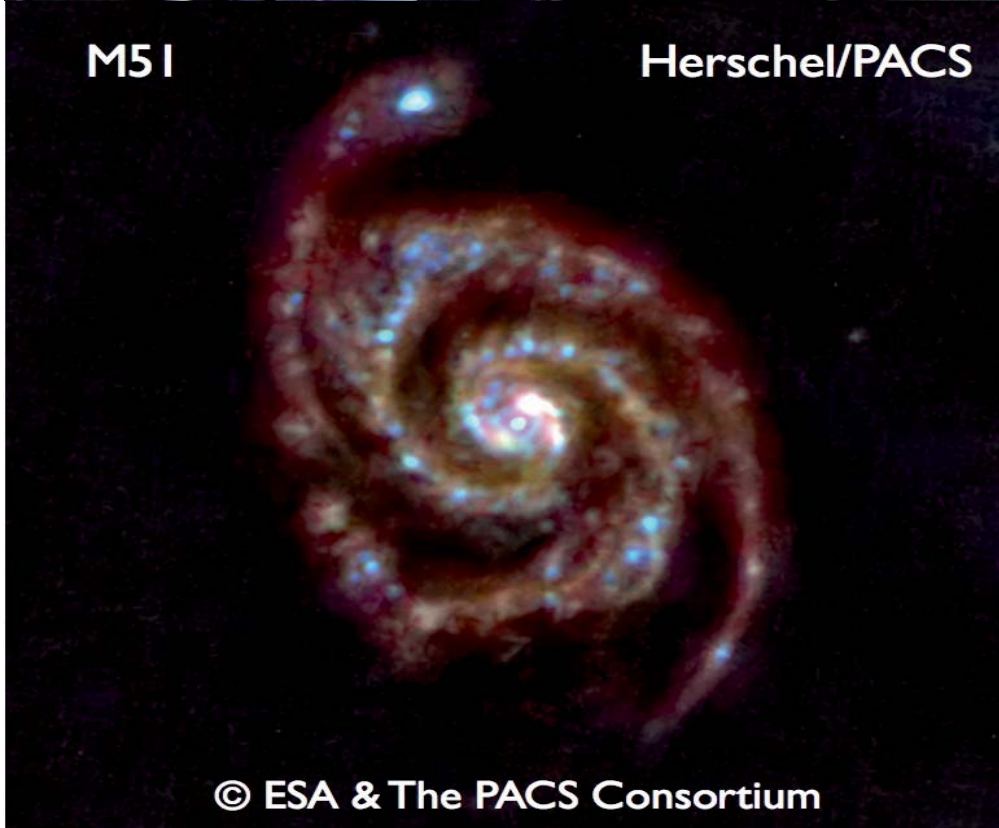


Fig. 3: The Launch of Ariane 5 ECA V188 with Herschel and Planck aboard.



M51

Herschel/PACS



© ESA & The PACS Consortium

Fig. 4: The PACS team after successful "first light" and the resulting image of the "Whirlpool Galaxy" M51 in three far-infrared colours.

## LUCIFER near-infrared multi-object spectrograph in operation at the LBT

LUCIFER 1 is the first of two identical near-infrared cameras-spectrographs installed at the LBT (Large Binocular Telescope) on Mount Graham in Arizona. Its commissioning took place between September 2008 and November 2009 and has been followed immediately by science operations in December 2009, when we started our spectroscopic survey of high redshift galaxies.

LUCIFER has a 4x4 arc minutes field of view. It is equipped with a 2048x2048 pixel HAWAII camera, suitable filters (broad-band z, J, H, K & Ks plus 12 medium and narrow band near-infrared filters) and three gratings for spectroscopy for a resolution of up to ~ 15000.

An innovative MPE designed mask unit allows to choose from a set of 33 masks to perform spectroscopic observations of multiple objects. 23 of those masks are inter-



*Fig. 1: PhD student Peter Buschkamp, being happy about the first successful cabinet exchange under full operational conditions between two consecutive scientific observing nights. The black cover behind the laptop hides the attachment point for the auxiliary cryostat used for the exchange of the mask's cabinet.*

LUCIFER is the result of ten years of design and development work, carried out by five German research institutes: Landessternwarte Heidelberg (LSW – PI institute), Max Planck Institute for Extraterrestrial Physics, Garching (MPE), Astronomisches Institut der Ruhr-Universität Bochum (AIRUB), Max Planck Institute for Astronomy, Heidelberg (MPIA) and Fachhochschule für Technik und Gestaltung, Mannheim. The MPE infrared group has been leading the multi-object spectrograph, part of the project which makes LUCIFER unique, compared to other “more” near-infrared imagers and spectrographs currently in use at 8m class telescopes.

changeable between two consecutive scientific observing nights in order to accommodate various scientific goals and to observe large samples of objects during a single observing run. The MPE major challenge was to design a system capable of exchanging the masks without warming up the instrument, which is operating at 77 Kelvin. Without this option, a week's observing time would be lost by warming up the instrument to room temperature, exchanging custom-built masks and then cooling down again to operating temperature.

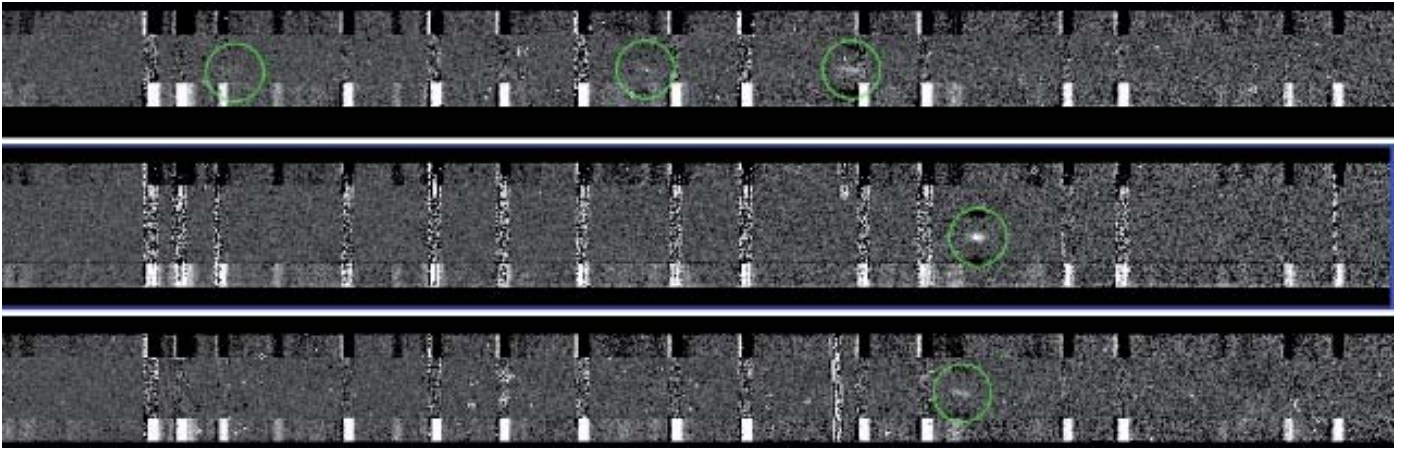


Fig. 2: Two-dimensional spectra of three slits of the first mask obtained for the MPE with LUCIFER. Image artifacts are still present due to the imperfect preliminary reduction. The emission lines that can be recognized are:  $H\beta$ ,  $[OIII]\lambda 4959$  and  $[OIII]\lambda 5007$  at redshift  $z=3.441$  (top),  $H\alpha$  at  $z=2.409$  (middle), and  $H\alpha$  at  $z=2.406$  (bottom).

In order to achieve this, two auxiliary cryostats are used. They are pumped and cooled down. The first one, empty, is attached to LUCIFER and receives the cabinet of masks that leaves the instrument. Once the sealing valve is closed again, the pressure between the two cryostats restored to ambient, this auxiliary cryostat is removed and replaced by the second one which contains the cabinet of new masks. The procedure is repeated then, with the difference that this time the new cabinet is inserted into LUCIFER. This is a unique feature of LUCIFER.

On December 17, 2009, between two consecutive scientific observing nights, for the first time we performed a cabinet exchange after the morning calibrations and before the next twilight (see Fig.1). Not only have masks been successfully exchanged but also new masks have spectacularly been used for excellent science results during that very night, as illustrated below.

The near-infrared is of special interest for extragalactic astronomy. Astronomers studying galaxies look for tell tale signs known as spectral lines. Well-studied lines at frequencies characteristic for atoms, such as hydrogen, nitrogen, oxygen and sulfur, provide a set of unique diagnostic tools for the study of galaxy properties, as e.g. the proportions of old and young stars, the presence and extent of regions of star formation, the activity of the galaxy's nucleus, and the amount of interstellar gas and dust. This work has traditionally been done for galaxies up to distances of redshift  $z\sim 1$ , because for more distant galaxies the characteristic lines shift into the infrared band, where the measurement of spectra is more difficult and therefore samples are small.

LUCIFER, incorporating unique technology to take infrared spectra of multiple objects at the same time, is ideal for survey work on galaxies at redshifts  $z>1$ . We have just embarked on a survey of  $z\sim 2.3$  and  $z\sim 1.4$  galaxies in the deep field GOODS-N, where ample ancillary data is available. Measuring the emission lines of hydrogen ( $H\alpha$ , and in some cases  $H\beta$ ), nitrogen ( $[NII]\lambda 6583$ ) and, in certain cases, oxygen ( $[OIII]\lambda\lambda 4959, 5007$ , see Fig.2), we will get an excellent handle on the galaxies' star formation rates, dynamics, presence of active nuclei, and abundances of heavy elements. The sample contains on the order of a hundred sources, which significantly increases the number of high redshift galaxies for which such measurements are available. Relating the observed metallicity to the galaxies' mass, we will be able to study the evolution of the mass-metallicity relation. This relation depends on key processes in galaxy evolution that regulate the metallicity of the intragalactic gas: enrichment by stellar winds and supernovae, loss of metals by outflows, and dilution by accretion of pristine gas. The mass-metallicity relation is still not well known at high redshift, and the LUCIFER project will provide an important next step in this science field.

## Sharpening the View

After the successful installation of the SINFONI adaptive optics integral field spectrometer and the PARSEC laser of the Laser Guide Star Facility at the European Southern Observatory (ESO) Very Large Telescopes (VLT), MPE is moving on with the development of the next generation instruments for ever sharper images. These are the GRAVITY interferometer for combining the light from the four 8m ESO VLTs, the ARGOS multi-laser guide star adaptive optics for the Large Binocular telescope (LBT), and the conceptual design study for MICADO, the adaptive optics imager for the planned European Extremely Large Telescope (E-ELT).

The main scientific goal of GRAVITY is to observe highly relativistic motions of matter close to the event horizon of the super-massive black hole at the centre of the Milky Way. This will be done by combining the light from the four 8m VLTs in Chile, which will then provide images as sharp as those from a 130 m telescope. Following the successful conceptual design study, the science and technical advisory committee and council of ESO recommended in 2007 to proceed with the preliminary design, which was finished in December 2009. GRAVITY is developed in an international consortium under the lead of MPE with major contributions from German and French partners. Much like in the case of long baseline radio interferometry (e.g. super-luminal motions in jets, maser disks around super-massive black holes in galaxies, supernova shell expansions, etc.), GRAVITY's position measurements with 10 micro-arcsecond accuracy and imaging with 4 milli-arcsecond resolution will make possible a number fundamental measurements over a wide range of astrophysics (Fig. 1).

The multi laser guide star adaptive optics ARGOS project was launched in 2008 to enhance the science return from the LBT by reducing the image degradation from the atmospheric turbulence and thereby providing several times sharper images compared to normal observations. This will boost in particular the spectroscopy with the LUCIFER instruments, whose multi-object spectroscopy units were also developed at MPE. Firing three green high power laser beams above each of the two eyes of LBT, and detecting the backscattered light with fast, low noise wavefront sensors, ARGOS will allow the correction of the atmospheric turbulence in the first kilometre above the telescope (Fig. 2). This Ground Layer Adaptive Optics is a novel and promising technique to "marry" adaptive optics correction with wide field observations - two properties that formerly could not be combined. Indeed, ARGOS can be considered as a 'seeing enhancer' to address most efficiently the key science projects with LBT and LUCIFER, in particular the exploration of galaxy formation in the early universe. ARGOS is a multi-national projects under the lead of MPE with major contributions from several German, Italian, and US research institutes. In 2009 ARGOS has passed its preliminary design review and is heading towards final design and components testing.

MICADO is the Multi-AO Imaging Camera for Deep Observations, which has been designed to work with adaptive optics on the 42-m E-ELT. Following a call for proposals by ESO, the MICADO consortium - led by MPE - was awarded the contract for the Phase A study in 2007. The study was successfully completed in December 2009. MICADO is optimised for the planned multi-conjugate



Fig. 1: GRAVITY and its key-experiments: GRAVITY will combine the light from the four 8m Very Large Telescopes to provide images with the sharpness of a 130 m telescope (image courtesy ESO). With a precision of 10 micro-arcsecond, GRAVITY will see objects moving throughout the Milky Way and even in distant galaxies: Clockwise from left centre are: jets/disk in nearby star forming region, planet/brown dwarf binary, dust disk with central gap, Arches star cluster, M31 star disks, NGC 1068 outflow/narrow line region, modelling of Galactic Centre flare, radial precessions of stellar orbit, S-star orbits, nuclear star cluster and radio emission in the Galactic Centre.

adaptive optics at the E-ELT, but it also comes with its own single conjugate adaptive optics using natural guide stars during the early operational phase. The instrument has two arms. The primary arm is a high throughput imaging camera with a 3 milli-arcsecond pixel scale covering about a field of one square arcminute. In the current design, the second arm provides (i) a high resolution narrow field camera, and (ii) a simple, medium resolution, long-slit spectrometer. The 10 milli-arcsecond resolution images from MICADO will be several times sharper than what is possible today, and will even outperform the sensitivity of the planned James-Webb-Space-Telescope (Fig. 3).

Fig. 2: Artist's view of the ARGOS multiple laser guide star adaptive optics for the LBT. Three laser beams are launched from the top of each eye to measure and correct the atmosphere turbulence in the first kilometre above the telescope. This Ground Layer Adaptive Optics is a novel technique providing 2-3 times sharper images over a large field of view. Small inset: the ARGOS high power lasers under test in the MPE laboratories.

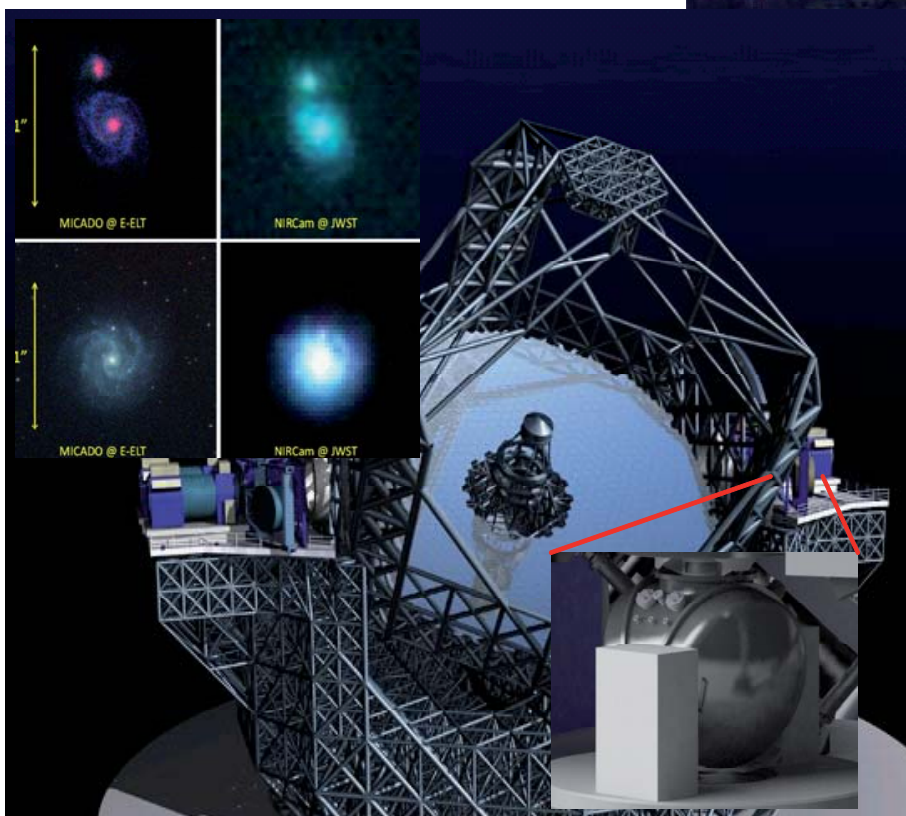
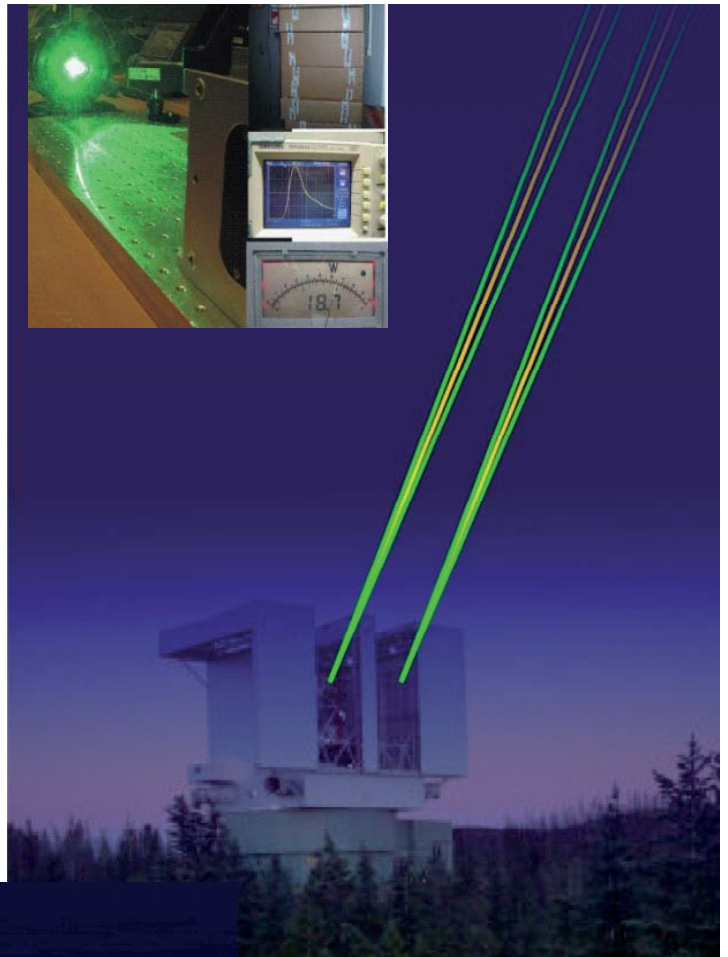


Fig. 3: The MICADO adaptive optics camera at the Nasmyth focus of the 42m E-ELT (image courtesy ESO). With its 10 milli-arcsecond resolution MICADO will outperform even the James Webb Space Telescope. The top left insert shows a comparison of simulated MICADO and JWST images of high-redshift galaxies.

## 3.2 OPTICAL AND INTERPRETATIVE ASTRONOMY (OPINAS)

The instrument building activities of the OPINAS group have focused on six main lines in the last three years: the designing and building of instruments for (1) the European Southern Observatory (KMOS and MICADO), (2) the McDonald Observatory with the Hobby-Eberly Telescope (HETDEX and VIRUS-W), (3) the Wendelstein Observatory (3KK Camera); the development of software for (4) the HETDEX experiment (the CURE pipeline), (5) the PanSTARRS1 project (the Photometric Classification Server); and, finally (6), the proposal for the ESA EUCLID satellite mission. As OpInAs is a joint group between the MPE and the Observatory (USM) of the Ludwig-Maximilians University Munich, in general all instrumentation projects are carried out with the support of both institutions. The USM-based part of the group also operates the Wendelstein Observatory for which it currently builds a 2m telescope. All instruments are built in international collaborations. Three of them, VIRUS-W, 3KK and CURE, are lead by us, in KMOS we are co-leaders.

KMOS is a multi-object integral-field near-infrared spectrograph for the Very Large Telescope of ESO. The project is now entering the final construction phase, which should bring the instrument to the telescope at the beginning of 2012. We will use our guaranteed time to pursue a number of science projects: a blind search for high redshift ( $z > 7$ ) Ly $\alpha$ -emitters along the critical lines of clusters of galaxies (which magnify the light of background objects), an investigation of the kinematics of a large sample of proto-disk galaxies at redshift 2, and, possibly, a study of the stellar populations of massive early-type galaxies between redshift 1 and 2 (see KMOS article).

MICADO is a first light diffraction-limited imager with simple long slit spectroscopic capabilities for the European Extremely Large Telescope (E-ELT). MICADO just concluded its initial design phase successfully under the leadership of MPE's Infrared group. We contributed to the science case and will be responsible for the MICADO electronics, and the instrument and operations software (for details on MICADO see article in section 3.1). The instrument will deliver K-band images with a angular resolution of 3 mas, and spectra of the nuclei of local galaxies, which allow dramatic improvements in black hole searches and mass determinations. It will also allow to astrometrically follow the motions of single resolved stars around the central supermassive black holes of M31 and other very close galaxies.

HETDEX is a project to study the properties of Dark Energy, by determining the redshift and the clustering properties of one million of Ly $\alpha$ -emitters at redshifts 2 to 4 and a few millions of [OII] emitters over 420 square degrees of the sky. It is based on VIRUS, a fiber-fed, massively replicated optical spectrograph. Its prototype, VIRUS-P, has been successfully tested at both, the HET and the 2.7m McDonald telescope in Texas. The production of the 200 copies, needed to accomplish VIRUS, has started

and should be completed by 2012. The OPINAS group has contributed to the construction and commissioning of VIRUS-P. It supplied 108 kms of fibers and is designing and implementing a pipeline (CURE) for the automatic reduction and analysis of the huge numbers of spectra HETDEX will produce. VIRUS-W is an optical integral field unit spectrograph, designed as a more sophisticated version of VIRUS-P, providing spectral resolutions up to 7000. The instrument is just undergoing tests in the lab and first light is foreseen for April 2010, at the 2.7m McDonald telescope. VIRUS-W is optimally suited to measure the kinematics of low-luminosity bulges and dwarf ellipticals (see the dedicated VIRUS article for details). The telescope interface of VIRUS-W is simple enough to be used easily at different telescopes. It may eventually be moved to the 2m Fraunhofer Telescope at Mt. Wendelstein at an altitude of 1836m, located 60 km south of Munich in the Bavarian Alps. This telescope is currently under construction and is expected to see first light in summer 2011.

The 3KK Camera is a further first-light instrument foreseen for the Fraunhofer Telescope. It is a 3-channel imager, able to take simultaneous blue, red and near infrared pictures of 8x8 arcmin of the sky, exploiting the best seeing nights of the mountain with a pixel size of 0.2 arc-sec. It is equipped with a Sloan filter set ('u'g'r'i'z') plus standard YJKs NIR filters. The construction phase has started and should be finished when the Fraunhofer telescope becomes operational. The camera will be used for the rapid follow-up of gamma ray bursts or supernovae, pixel-lensing events, extrasolar planet transits or to obtain photometric redshifts of galaxy clusters.

The Photometric Classification Server (PCS) for the PanSTARRS1 survey is a software package for the automatic star/galaxy/quasar classification of objects detected in the survey, and for the determination of stellar parameters or photometric redshifts, according to their typology. It interfaces the PanSTARRS1 photometric "grizy" database to the OPINAS photometric redshift code. Soon, when the survey will start regular operations, PCS will allow us to process millions of photometric entries per day, delivering photometric redshifts. Thus we can study the properties of Dark Energy at redshift  $\sim 0.7$ .

Finally, we proposed EUCLID to ESA, a satellite with a 1m class telescope for imaging a large fraction of the sky in the optical and the NIR, in order to obtain an optical weak-lensing map of the matter distribution of the Universe up to redshift 1. The NIR photometry is used to complement ground-based multi-band data (e.g. from PanSTARRS1) to yield photometric redshifts, reconstruct the growth of structure as a function of lookback time, and thus probe the nature of Dark Energy. Furthermore, a spectroscopic channel should provide spectra of many millions of galaxies.

## KMOS - a near-infrared spectrograph for the VLT

KMOS is a multi-object integral-field near-infrared spectrograph for ESO's VLT. The project is now entering the final construction phase, which should bring the instrument to the telescope at the beginning of 2012.

KMOS (K-band multi-object spectrograph) is a near-infrared multi-object integral-field spectrometer belonging to the second generation of VLT instruments. It will allow integral field spectroscopy of galaxies of medium and high redshift to study the processes of galaxy formation and evolution. The instrument is constructed by a consortium of UK (ATC-Edinburgh, Durham, Oxford) and German (MPE, USM) institutes, working as partners of ESO. It is currently in the manufacture, integration and test phase. The Opl-nAs group is responsible for the electronics, the instrument software and the observing preparation tools. Commissioning of KMOS on the VLT at Paranal is expected for 2011. KMOS will allow observations of up to 24 targets in parallel. The size of an integral field unit (IFU) is 2.8x2.8 arcsec. From the technical point of view the instrument consists of 3 nearly identical sectors. Each sector contains 8 pick-off arms with the slicing optics and two filter wheels (front segment) and one spectrograph (back segment). The actual status of the instrument is the following: The cryostat is complete. Its cryogenic performance is excellent. The first, almost fully filled front segment, with two

pickoff arms and IFUs, has been successfully integrated and tested in cryogenic environment. The first back segment also was successfully tested in the cold and then integrated in the cryostat. A test local control unit (LCU), a very mature prototype of one of the 3 KMOS electronics cabinets, is controlling the hardware in the integration lab. The manufacturing of the final cabinets is in progress. Furthermore there are smaller test LCUs in use at different locations. The control software allows operation of the hardware and is almost in final shape. Several releases were distributed within the Consortium to support the tests. The interaction of the instrument and telescope software was successfully tested at the ESO VLT Control Model. The first release of the observation preparation software, including the manual, were distributed within the Consortium. The first cold end-to-end tests with 2 arms and spectrograph are actually running. The manufacturing of a "corotator", necessary to supply the instrument with liquid Helium, cooling fluid, power, etc, and for synchronous rotation of the electronic cabinets with respect to the instrument, has been started. Its delivery is expected in April 2010. The data reduction is based on the SINFONI package.



Fig. 1: The cryogenic part of KMOS on the Nasmyth flange simulator.



Fig. 2: Four KMOS arms during tests in the USM laboratories.



Fig. 3: The cabinet, which is controlling one sector of KMOS.

## VIRUS-W - A High-Resolution Integral Field Spectrograph for Galaxy Dynamics

VIRUS-W is an optical integral field unit spectrograph providing spectral resolution up to 7000. The instrument is just undergoing tests in the lab and first light is foreseen for May 2010, at the 2.7m McDonald telescope. VIRUS-W is optimally suited to measure the kinematics of low-luminosity bulges and dwarf ellipticals.

instrument is connected to the focal plane through optical fibers, it does not need to be attached to the telescope: VIRUS-W is bench-mounted. This offers the advantages of a mechanically relatively simple interface to the focal plane - and thereby mobility, as well as a very stable set-up, since the instrument is not subject to a changing direction of gravity. The pseudo slit is located inside the folding mirror to the left of the figure (pointing out of the image plane). The fibers point perpendicularly to the surface of the collimating mirror. The collimated beam is reflected back onto the folding mirror and enters the dispersive element - in the R=7000 mode a 3300 l/mm, 220 mm x 170 mm large VPH grating, sandwiched between two large prisms (GRISM). Due to the large diffraction angle the prisms are needed to avoid internal reflections at the grating plate surfaces. A custom build 200 mm aperture f/1.4 camera finally images the spectra on a CCD. At the time of writing this report, VIRUS-W is fully integrated and being tested in the laboratory. We estimate that we will start observations at the end of May 2010.

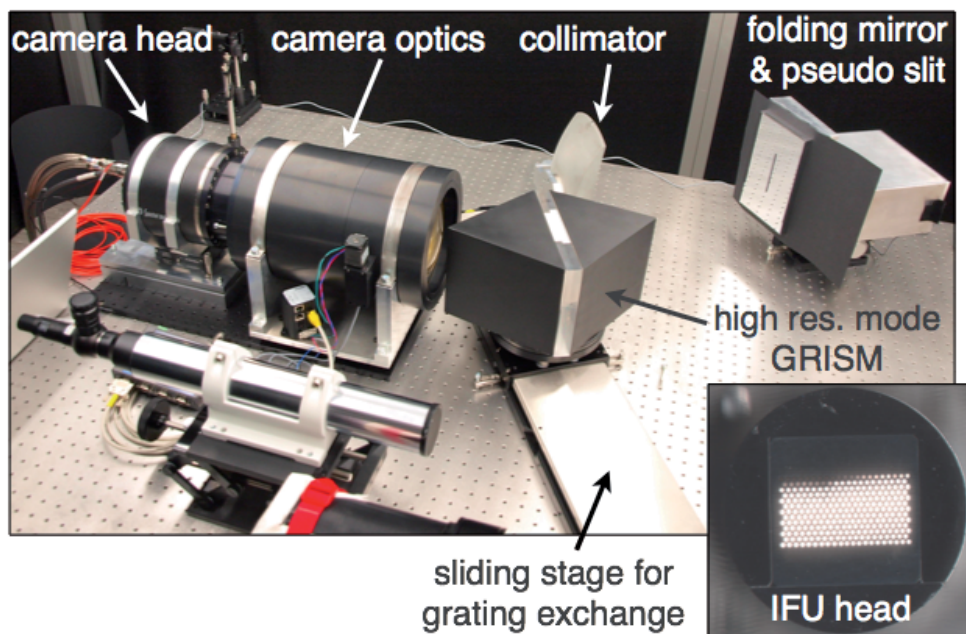


Fig. 1: Bench-mounted VIRUS-W.

Inspired by the VIRUS spectrograph design for the HETDEX experiment, VIRUS-W is a fiber based integral field spectrograph, which was specifically developed to conduct kinematic surveys of local spiral galaxies. In its high-resolution mode it will operate with a spectral resolution of  $R = 7000$  in the wavelength region from  $5070\text{\AA}$  to  $5450\text{\AA}$  and offer a field of view of about one by two arcminutes at two meter class telescopes. It will thereby allow to cover the full bulge region of most local spiral galaxies in one or two pointings. An additional lower resolution mode will address the underlying stellar populations. The instrument is developed for flexible use at different telescopes. We will conduct first observations at the 2.7m Harlan-J-Smith telescope at the McDonald Observatory in Texas. For the future we also plan to operate it at the 2m Fraunhofer Telescope, which is currently being built on Mt. Wendelstein in the Bavarian Alps by the University Observatory in Munich.

The Integral Field Unit is formed by a  $\sim 5.4\text{mm} \times 2.7\text{mm}$  large array of optical fibers. At the end of the spectrograph these fibers are rearranged into a one-dimensional configuration, forming the pseudo-slit of the spectrograph. Since the

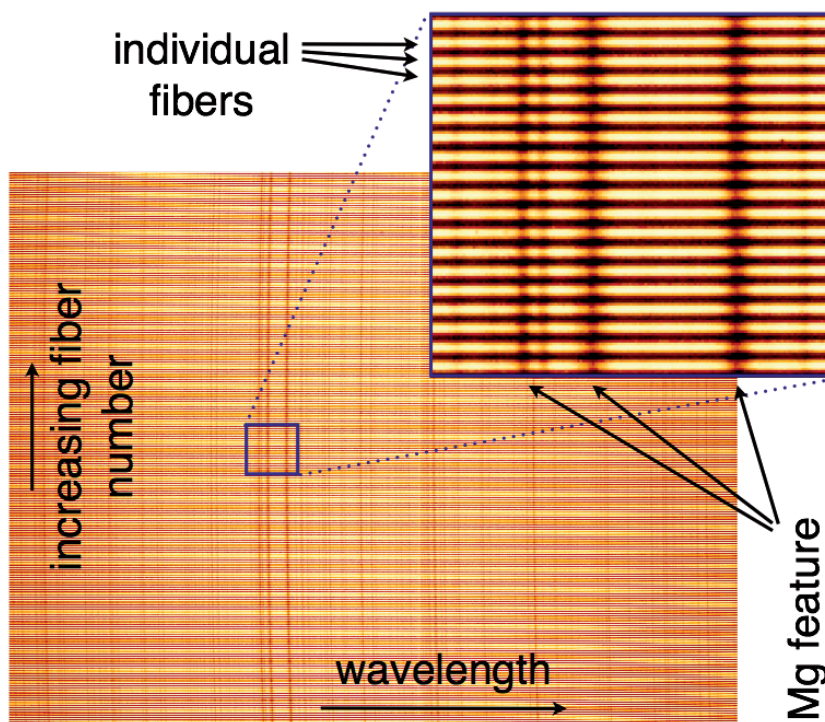


Fig. 2: A solar spectrum that was obtained in the laboratory. The upper right panel displays a magnified view of the Mg absorption region. One can easily identify the separate spectra that belong to different fibers.

### 3.3. HIGH-ENERGY ASTROPHYSICS

#### Projects in High-Energy Astronomy

The High-Energy group is developing X-ray and gamma-ray instrumentation for future astronomy projects. To be launched in 2012 on the Russian satellite Spectrum-Röntgen-Gamma, eROSITA is currently the main project of the group. In order to investigate key scientific topics like dark energy, eROSITA will perform an X-ray all-sky survey to measure the distribution of galaxy clusters in the universe. During the last three years the fabrication of mirror shells for the seven telescopes and the development of CCD detectors have proceeded significantly (see eROSITA article).

In 2009 the investigations for large X-ray observatories succeeding XMM-Newton and Chandra led to the decision to combine the efforts of the three agencies ESA (Europe), NASA (USA) and JAXA (Japan) in the studies for a new international X-ray observatory, IXO, to be launched in the time frame after 2020. A number of focal plane instruments with different strengths are planned with essential contributions from our group to the Wide Field Imager (WFI) and the High Time Resolution Spectrometer (HTRS). To build large lightweight segmented mirror systems for future missions like IXO, new technologies for the production of pore optics, based on silicon plates, and for glass slumping are developed. The group contributes to the studies of the glass slumping technique with own experimental work.

Such mirror systems can also be used for BepiColombo, a joint Cornerstone mission of ESA and JAXA to the planet Mercury. The mission is scheduled to be launched in 2014 and to arrive at Mercury in 2020. The payload will consist of two components: the Mercury Planetary Orbiter (MPO) and the Mercury Magnetospheric Orbiter (MMO). Our group is involved in one of the instruments onboard the MPO, the Mercury Imaging X-ray Spectrometer (MIXS). While the primary scientific aim of MIXS is to produce global elemental abundance maps of Mercury's surface, MIXS is likely to become the first instrument for investigating the X-ray emission resulting from charge exchange interactions between highly charged solar wind ions and Mercury's tenuous, surface-bounded exosphere. X-rays, due to this process, have already been observed on comets, Venus, Earth, and Mars, where our group has pioneered this novel field of research.

To characterise and measure new X-ray detectors and optics, our group operates the X-ray test facilities PUMA and PANTER. Using eROSITA prototype components like a framestore CCD with 75 micron pixels and graded shield for background reduction, the TRoPIC (Third Röntgen PANTER Imaging Camera) X-ray CCD-camera was specifically designed for measurements of X-ray optics in the energy range from 0.2-50 keV. Programs to demonstrate the overall feasibility of silicon pore optics from individual plates to a large petal were running at the PANTER facility. Most important, development and verification of mirror

shells for the eROSITA project have shown that the performance of the optics is within the requirements; the flight mirror production has been started recently.

The main observatories in orbit, XMM-Newton and INTEGRAL are continuing to work perfectly. On December 10, 2009 we celebrated the 10th anniversary of the launch of XMM-Newton. We are still strongly involved in the health monitoring and in-orbit calibration of the EPIC-pn camera and further work on methods to better utilise the data. Within the XMM-Newton Survey Science Center collaboration we maintain several scientific analysis tasks. Over the last years, our group was very successful with several large observing projects in the research areas of deep fields and nearby galaxies. INTEGRAL is now accumulating enough exposure to study also nuclear lines other than  $^{26}\text{Al}$ . After a decade of development, the GRB Burst Monitor started operation after a successful launch onboard the Fermi spacecraft in June 2008 (see Fermi-GBN article).

The optical high-time resolution photo-polarimeter OPTIMA was deployed on the Skinakas Observatory (Crete, Greece) 1.3m telescope in campaigns in 2007, 2008, and 2009. The primary goal was to promptly follow up the optical afterglow emission of gamma-ray bursts. Scheduled observations were also carried out on a wide range of targets, including cataclysmic variables, flare stars, pulsars, and AGN. Without doubt, the most spectacular result was the discovery of extremely bright and rapid optical flaring in the Galactic transient SWIFT J195509.6+261406, which was triggered by SWIFT as a potential gamma-ray burst (GRB070610).



Fig. 1: "First Light" of GROND.

GROND has started routine operations at the 2.2m MPI/ESO telescope in mid-2007, and beyond contributing to the race for the highest redshift objects also provides surprising constraints on the afterglow physics and gamma-ray burst late-engine activity.

## The X-ray Telescope „eROSITA”

In 2009 the official agreement was signed between the Russian and German space agencies Roskosmos and DLR, to launch eROSITA on the Russian satellite mission Spectrum-Roentgen-Gamma at the end of 2012. eROSITA is fully funded, and many flight components are already being manufactured. After launch, during the first four years of the mission, eROSITA will perform an all-sky survey, and will detect about 100.000 clusters of galaxies. From the study of their large-scale distribution we will learn more about the origin, geometry and dynamical evolution of our Universe.

A medium size Russian satellite, called Spectrum-Roentgen-Gamma“ (Spectrum-RG or SRG), is planned for launch in 2012 (Fig. 1a). A Soyuz-2 rocket will carry the satellite from Baikonur/Kazakhstan into an orbit around the Sun-Earth L2 point at approximately 1,500,000 km from earth. Besides eROSITA („extended Roentgen Survey with an Imaging Telescope Array“), the payload also includes the X-ray concentrator ART („Astronomical Roentgen Telescope“, IKI, Moscow) extending the hard X-ray sensitivity of SRG to about 30 keV.

eROSITA is now fully funded by the German Space Agency (DLR). An important milestone in 2009 was the signing of the official agreement between the Russian and German space agencies Roskosmos and DLR, to launch eROSITA on the Russian satellite mission Spectrum-Roentgen-Gamma at the end of 2012. Further technical milestones were passed and final detailing of parts as well as the production of flight hardware has begun. In

eROSITA will test cosmological models to assess the origin, geometry, dynamics, and the structure growth with time of our Universe via the study of the large-scale structure in the matter distribution. Galaxy clusters are ideal tracers of the large-scale structure. The amplitude and shape of the cluster density power spectrum, its growth with time, and the cluster mass function, depend sensitively on Dark Matter and Dark Energy. During the four years of the all-sky survey, eROSITA will detect about 100 thousand clusters of galaxies. This sample size is necessary for example to precisely characterize the cluster mass function and power spectrum in at least ten redshift bins, to follow the growth of structure with time. Baryonic wiggles due to the acoustic oscillations at the time of recombination are still imprinted on the large scale distribution of clusters and thus can give tight constraints on the curvature of space at different epochs. A statistics of at least 50,000 to 100,000 clusters is necessary to reveal the baryonic oscillations in the cluster distribution power spectrum. The eROSITA flux limit of the survey in the 0.5

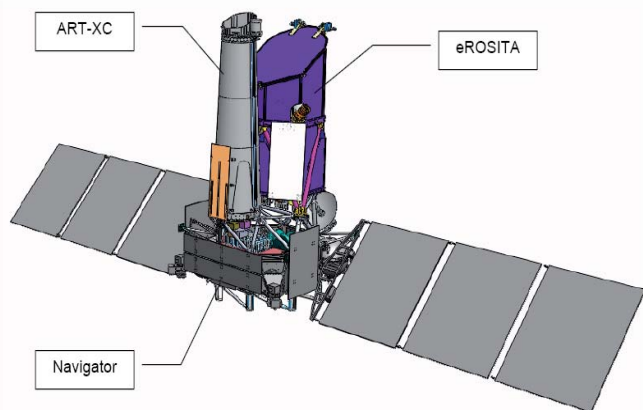
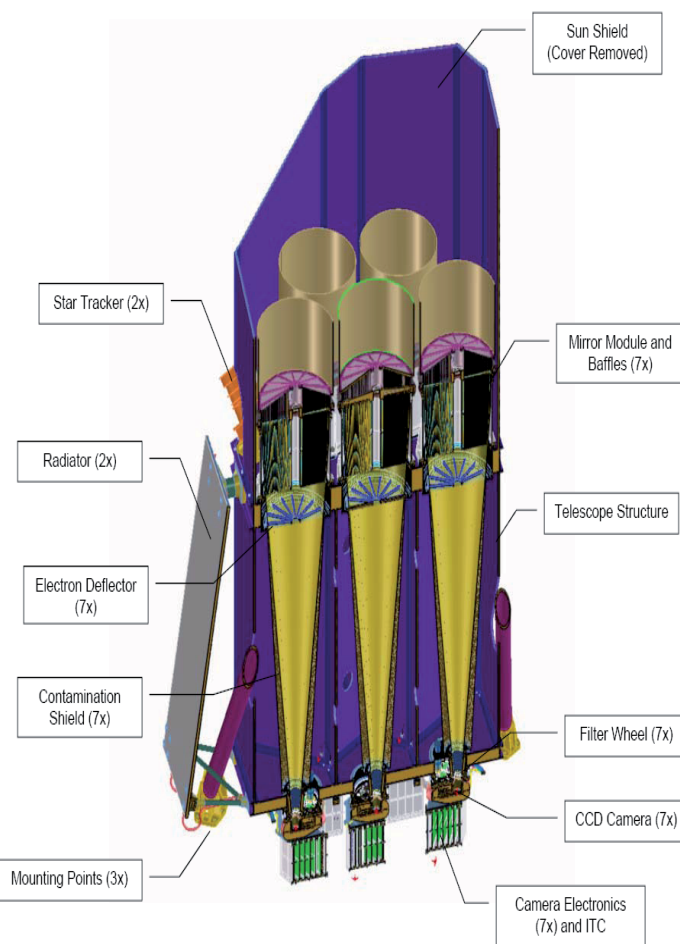


Fig. 1: (a) left: eROSITA and ART-XC on the Navigator satellite platform (b) right: A cut through a CAD model of eROSITA. The seven X-ray mirror modules with their baffles are located at the top and the CCD cameras and their electronic boxes at the bottom.

2009 a telescope support structure was manufactured and assembled and is now on its way to Russia where tests must prove that it fulfills the requirements regarding stiffness, stability and weight. Going to an L2 orbit means that the complex task of cooling the CCDs down to  $-80^{\circ}\text{C}$  by using passive components turns out to be slightly less challenging than in a low-earth orbit.



to 2 keV band will be  $\sim 4 \times 10^{-14} \text{ erg s}^{-1} \text{ cm}^{-2}$  (an order of magnitude deeper than the ROSAT survey) over most of the sky and about ten times deeper in the poles of the survey scan pattern. At this flux the X-ray sky is dominated by clusters and AGN, which can be separated with an angular resolution of 25 arcsec.

The detection of all including hidden AGN in the local Universe is another main goal of the new eROSITA instrument. Many hidden, but still very active black holes should be lurking in rather nearby galaxies, waiting to be detected by a hard X-ray survey. We expect to detect

with 54 mirror shells each. The diameter of the outermost shell is 360 mm (see Fig. 3 for a sense of scale). The inner 27 mirror shells are replicated from refurbished ABRIXAS mandrels, and therefore their focal length (1,600 mm) is kept the same. Unlike on ABRIXAS, the seven optical axes are co-aligned. Since the entire field of view (FoV,  $\sim 1^\circ$  diameter) is used for the surveys, the measure for sensitivity is the product of the FoV-averaged effective area and the solid angle of the FoV. Each of the seven mirror modules has its own CCD camera in its focus. These CCDs are advanced versions of the pn-CCD camera onboard of XMM-Newton: the pixel size is reduced to  $75 \mu\text{m}$  square, corresponding to  $\sim 10$  arc-sec. The sensitive area is  $\sim 3 \text{ cm}^2$  (or  $384 \times 384$  pixels). A frame-store area is add-

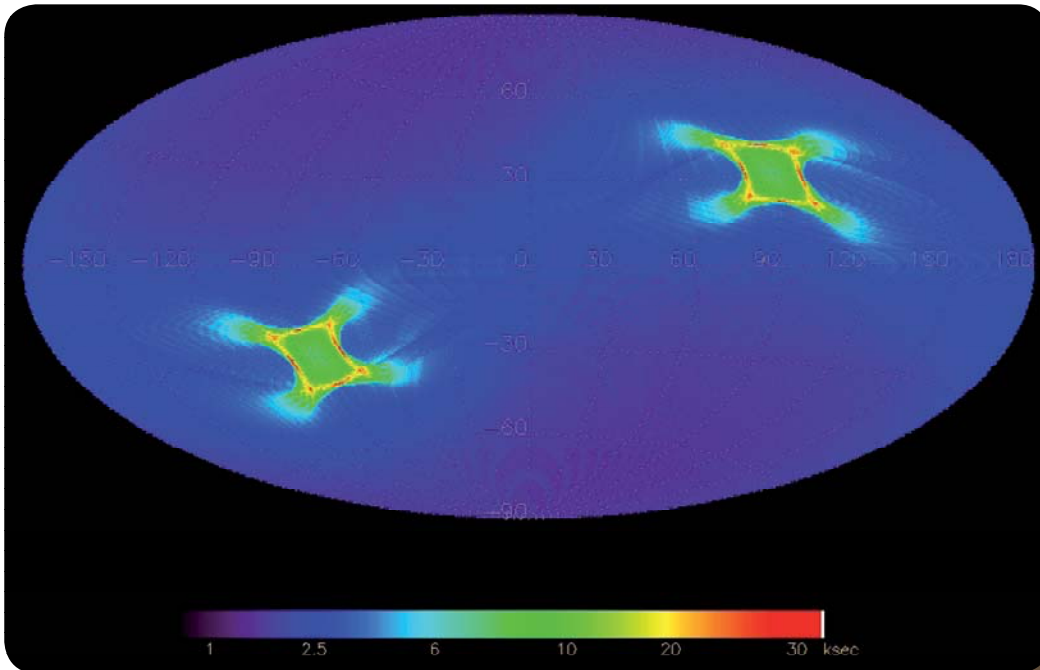


Fig. 2 (top): Exposure map of eROSITA for a four-year all-sky survey with the survey scan axis oriented towards the earth, note the two deep fields (scale 3 ksec purple to 30 ksec red) at the ecliptic poles.

Fig. 3 (right): eROSITA mirror module qualification model in MPE's X-ray test facility.



more than three million AGN with eROSITA. Many other science goals will be addressed with eROSITA as a result of the all-sky survey and the subsequent pointed observing phase.

The proposed all-sky survey scan strategy for eROSITA at L2 allows the scan rate (4-6 revolutions/day) to be optimized so that it can provide a close to homogenous exposure over most of the sky as well as two 100 square degree deep fields at the ecliptic poles (see exposure map in Fig. 2a). After the four-year all-sky survey phase a pointed observing phase of individual objects will be carried out. eROSITA's mirror system consists of 7 mirror modules

ed to the sensitive area which allows the fast shift from the image area in order to reduce so called out-of-time events, photons which are recorded during charge-transfer. The use of 6 inch silicon wafers with  $450 \mu\text{m}$  thickness provides higher quantum efficiency at the higher energies. We could also improve the low energy response and the energy resolution by modifying the fabrication process.

## The „Fermi“ Gamma-ray Burst Monitor (GBM)

The Fermi Gamma-ray Burst Monitor (GBM) is the result of our cooperation with NASA's Marshall Space Flight Center (MSFC) and the University of Alabama in Huntsville (UAH). It is designed to support Fermi's main instrument, the Large Area Telescope (LAT), in locating and investigating Gamma-Ray Bursts (GRB). GBM uses an array of 12 sodium iodide scintillators (NaI: 8 keV – 1 MeV) and two bismuth germanate scintillators (BGO: ~200 keV to ~40 MeV) to detect gamma rays over the full unocculted sky. As they cover more than seven decades in energy, GBM and LAT together are contributing a great deal towards a more detailed explanation of the GRB phenomenon. One of the foremost scientific goals of Fermi is to fully explore the behavior of GRBs in the  $>1$  MeV energy range.

Commissioned by MPE and co-financed by the German Space Agency DLR, the GBM detector hardware as well as their low and high-voltage power supply systems were built by Jena-Optronik GmbH and EADS Astrium in Friedrichshafen. The scientists of the GBM-team at MPE designed, built, tested and calibrated the GBM detectors. The American section of the team developed the central GBM computing system, and managed the project, including its harmonization with the manufacturer of the satellite and NASA's global project management.

The detector response of the GBM instrument was determined by Monte Carlo simulations, which were supported and verified by on-ground calibration measurements. All flight and spare detectors were extensively calibrated and characterized with radioactive sources at MPE. We measured energy/channel relations, the dependences of energy resolution and effective areas on energy and angular offsets. Calibration measurements in the energy range from 10 keV to 60 keV were performed at the BESSY synchrotron radiation facility in Berlin. These measurements were necessary for mapping the detector response, especially around of the Iodine K-edge at 33 keV.

The instrumental response of the BGO detectors at high energies, i.e. in the overlap region with the LAT from ~20 MeV to ~40 MeV, calibration measurements were carried out using a small Van-de-Graaff accelerator at the Stanford Linear Accelerator Center (SLAC).

The 12 NaI detectors of the GBM instrument are arranged around the outer parts of the satellite, each of them viewing the sky at a different angle. Thus the GBM can roughly determine the location of a GRB by comparing the differences between the event rates measured by the detectors. The result is communicated to the main instrument, the LAT, and transmitted to the ground station. As quickly



Fig. 1: Left: The Fermi Gamma-Ray Space Telescope. On top is the LAT with its reflective covering. Six of the GBM NaI detectors and one BGO detector (all white) can be seen on the front side of the spacecraft. Right: Lift-off of the Delta II Heavy rocket with Fermi from Cape Canaveral Air Force Station's launch pad 17-B on June 11, 2008 at 16:05 UT (images: NASA).



## The MPI Semiconductor Laboratory – High Speed Imaging from the Near-Infrared to X-rays

The MPI Halbleiterlabor (MPI-HLL) was founded in a joint effort of the MPE and the Max-Planck-Institut für Physik (MPP) in 1992 after a ramp-up phase which had started in 1987. The mission of the MPI-HLL is to develop high speed imagers and particle tracking detectors for the experiments of both Max-Planck Institutes and their associated collaborating partner institutions. MPI-HLL's main infrastructure is a class 1 cleanroom, 700 m<sup>2</sup> in size, equipped with high tech manufacturing tools to process double sided, very high purity silicon wafers with a diameter up to 150 mm.

The main project of the past and next years is eROSITA. The production of its first batch of flight devices is finished. The chips are currently under test. Various devices have already been assembled to laboratory cameras with the anticipated good imaging and spectroscopic properties. Seven focal plane arrays will be equipped with this improved version of the pnCCDs. The previous pnCCDs were in the focus of two international celebrations on the occasion of the launch and the First Light of XMM-Newton ten years ago.

The long range project is focussing on the International X-ray Observatory (IXO), currently under evaluation in the US Decadal Survey and the European Cosmic Vision Process. We proposed a new type of Active Pixel Sensor (DePFET) with 1024 x 1024 pixels being read out 1.000 times a second with spectroscopic performance. A wide field imager (WFI) consortium was under the leadership of MPE with partners from Japan, the US and Europe. In addition to the WFI, the MPE is supplying the X-ray spectrometers which are arrays of Silicon Drift Detectors (SDDs), to the High Time Resolution Spectrometer (HTRS) of IXO.

A first space experience with the DePFETs will be gained with the DePFET Macropixel arrays in the MIXS Experiment aboard ESA's BepiColombo Satellite, to be launched in 2014. A scan of Mercury's surface will reveal its chemical composition. The data analysis will be done by scientists from MPE and the MPI for Solar System Research in Lindau.

The initiative for the Center of Free Electron Laser Science (CFEL, founded by the MPG, DESY and the University of Hamburg) has led to a number of spectacular experiments at the FEL FLASH in Hamburg and the more energetic LCLS facility at SLAC, operated by the Stanford University, USA. In all of those experiments, pnCCDs as developed for XMM-Newton and eROSITA were the focal plane imagers. Because of this success, new collaborations were established between Stanford, RIKEN and DESY on one side and CFEL on the other. The recently founded European XFEL GmbH in Hamburg has asked for a long term collaboration with the MPI-HLL to equip the XFEL beamline with DePFET detectors from the MPI-HLL. A four year research contract for the development of a DePFET based camera was signed.

In addition to a large variety of applications for electron imaging, UV light imaging and X-ray microscopy, pnCCDs have recently been approved as wave front sensors in the adaptive optics system ARGOS for the LBT. 1.000 images/s will be recorded with low noise and processed in real time for the reshaping of the mirrors.

We have recently started X-ray measurements up to 30 keV in the ASDEX fusion reactor for the purpose of plasma diagnostics. Up to 500.000 X-rays per second were measured, with a heavy background of neutrons close to the plasma. In the future, those measurements will be extended up to 200 keV with the Anger camera DRAGO, based on LaBr scintillators coupled to our SDDs.

Because of our expertise in silicon based detector systems, we were invited to join the Japanese ASTRO-H mission for consultancy, test and analysis of the soft and hard X-ray detectors. This enables MPE researchers to equally participate in the science program of ASTRO-H.

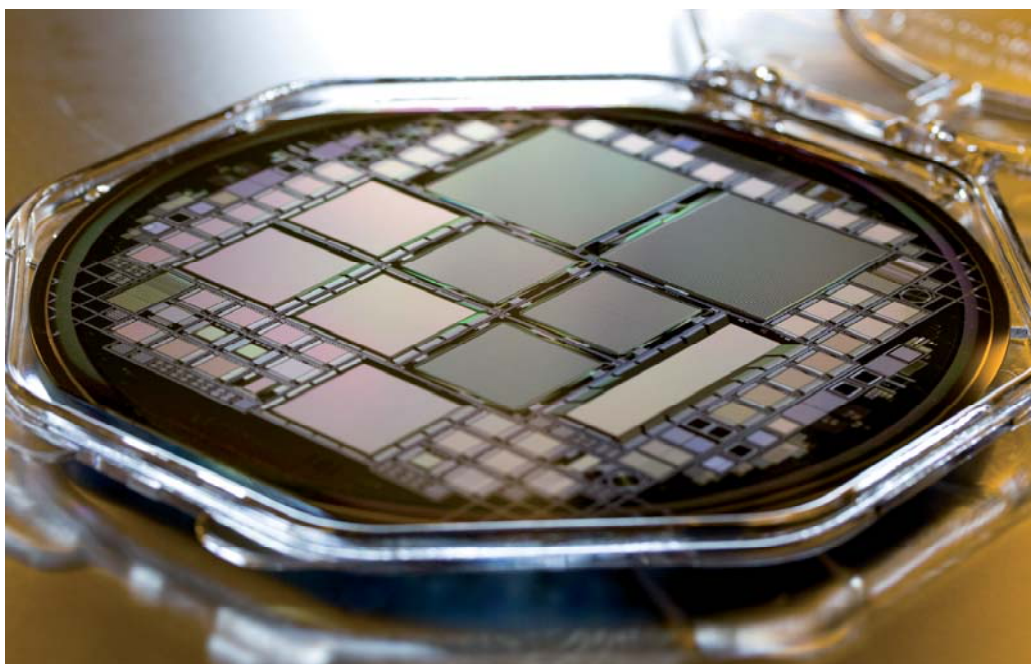


Fig. 1: Active Pixel Sensors, based on the DePFET concept for the space missions: BepiColombo and IXO.

## Development of space and ground-based CCD detectors for eROSITA and CFEL

The further development of pnCCDs in the MPI Halbleiterlabor after their use for the XMM-Newton project, led to optimized detector properties. The space telescope eROSITA as well as the ground-based CFEL project benefit from the optimizations.

A so-called pnCCD, a special type of CCD, was developed twenty years ago as focal plane detector for the XMM-Newton X-ray astronomy mission of the European Space Agency (ESA). Based on this detector concept and taking into account the experience of ten years of operation in space, a new X-ray CCD type was designed by the MPI Halbleiterlabor for the upcoming X-ray space telescope eROSITA. This space telescope will be equipped with seven X-ray mirror systems of Wolter-I type and seven CCD cameras, placed in their foci. The instrumentation permits the exploration of the X-ray universe in the energy band from 0.3 keV up to 10 keV by spectroscopic measurements with a time resolution of 50 ms for a full image comprising 384x384 pixels. A similar type of pnCCD type was tailored to the detector requirements of 'Free Electron Laser' experiments in the framework of CFEL.

pnCCDs of the eROSITA type were modified to X-ray imagers with 1024 x 1024 pixels and a frame rate of 120 Hz. They were used as a focal plane imager in the very first X-ray diffraction experiments at the world's most powerful high energy free electron laser at the Stanford Linear Accelerator Center (SLAC). Spectacular diffraction patterns from nano crystals and viruses were recorded as well as interference processes of atomic (e.g. Xe) clusters. The camera has proven all properties required for fast, spectroscopic X-ray imaging at FEL light sources. This work was performed within the initiative "Center for Free Electron Laser" (CFEL) science, founded by the MPG, DESY and the University of Hamburg.

The first eROSITA flight CCD wafers were finished in 2009 in the MPI Halbleiterlabor. The performance of the individual CCD chips was tested on a unique probe station. It allows for spectroscopic measurements without any mounting of the CCD chips to a board. By means of these measurements, the seven best pnCCD chips will be finally selected for the seven eROSITA cameras. By testing several CCDs in our standard lab set-up, we verified the full functionality and performance of the eROSITA CCD type. With a read noise of only 2 electrons rms, we measured an excellent energy resolution of about 50 eV FWHM for the C-K line @ 277 eV and 134 eV FWHM for Mn-K $\alpha$  line @ 5.9 keV.

Apart from the pnCCD, we redesigned in 2009 the CAMEX ASIC for readout of the eROSITA CCDs. Production of the ASIC was done in a JFET-CMOS process technology at the Fraunhofer Institute for Microelectronics in Duisburg, Germany.

The CCD detector chip and three CAMEX ASICs are mounted on a detector board with ceramic substrate. This eROSITA multi-layer board was designed in the MPI Halbleiterlabor, and our colleagues at the Max-Planck-Institut für Physik produced the board in hybrid circuit technology. With these components we assembled a prototype of the eROSITA flight detector. It also serves for first environmental qualification tests, in particular for thermal cycling and vibration tests.

We performed detector irradiation tests with protons at the TANDEM accelerator of the Maier-Leibnitz-Laboratory for analysis of the detector system's radiation hardness. An appropriate test chamber and electronic set-up was developed for this purpose. For measurement of the proton flux on the detector, we used the CCD detector itself in

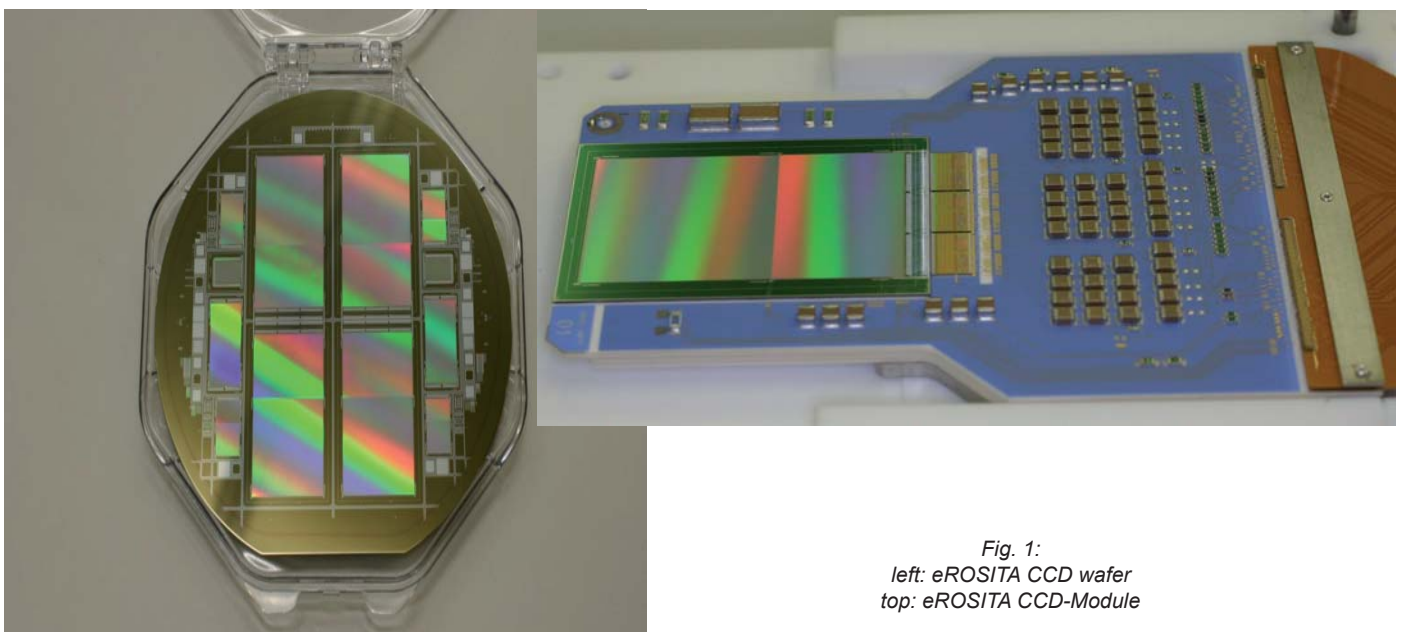


Fig. 1:  
left: eROSITA CCD wafer  
top: eROSITA CCD-Module

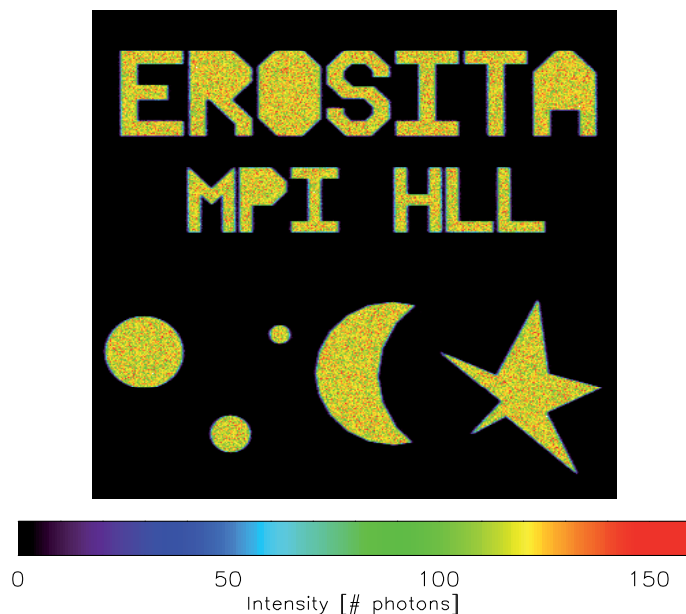


Fig. 2: X-ray illumination of the pnCCD through a mask. The image was taken in single photon counting mode, i.e. 10,000 single CCD images were compiled.

a special operation mode. This guaranteed a spatially resolved and accurate particle fluence determination. In the tests no irradiation induced failure occurred in the analog and digital parts of the detector system. This is due to the design of the devices and the appropriate fabrication technologies. Concerning the common degradation of energy resolution with increasing proton fluence, we investigate presently the possibilities to minimize this effect. Significant success was achieved with an optimized timing of detector operation.

We accomplished simulations about the instrument background of eROSITA. The model takes into account the graded-Z-shield geometry of the eROSITA camera, the radiation environment in space at L2 orbit as well as the interaction and event processing in the CCD detector. The simulations use a GEANT4-based simulation software package with a prototype version of an improved treatment of PIXE (particle induced X-ray emission), the SPENVIS (The Space Environment Infor-

mation System) software package and SRIM (The Stopping and Range of Ions in Matter) simulations. The results of our simulations proved the elimination of the fluorescence lines in the instrumental background spectrum and quantified furthermore the remaining background continuum to a level of  $3 \times 10^{-3} \text{ cm}^{-2} \text{ s}^{-1} \text{ keV}^{-1}$ .

We intensively studied the detector photon entrance window, which is equipped with the on-chip light filter. The theoretical models were compared with our experimental results which led to a deeper knowledge about production of filter layers and finally to optimized filters. We also measured the spectral response and quantum efficiency of the pnCCD detector at the BESSY synchrotron, in collaboration with the Physikalisch-Technische Bundesanstalt in Berlin. The quantum efficiency was determined in the wide energy range from 3 eV to 20 keV. In accordance with our simulations, we found high quantum efficiency in the X-ray region and strong suppression of visual light due to the light filter by more than 5 orders of magnitude. The spectral response was analyzed in the X-ray region of interest from 100 eV to 11 keV. The possibility to perform spectroscopy even at such a low energy of 100 eV, adds another interesting detector property to the portfolio of pnCCD features.

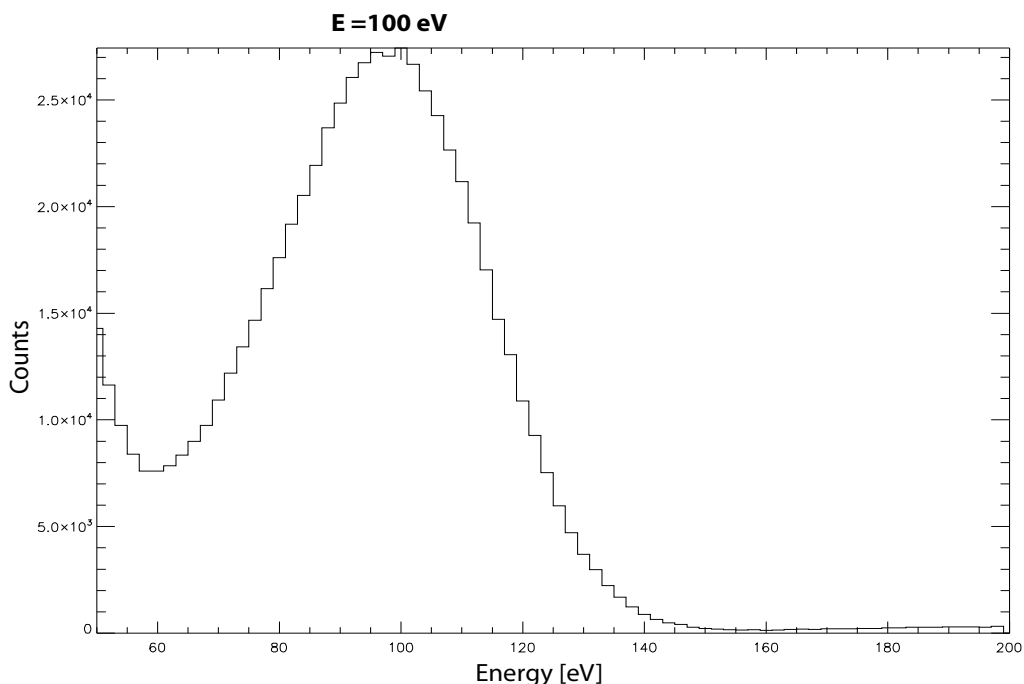


Fig. 3: The new pnCCD permits spectroscopy even at a very low X-ray energy of 100 eV, which is demonstrated by this spectrum, measured at the BESSY synchrotron.

### 3.4 SPACE PHYSICS OF THE NEAR-EARTH ENVIRONMENT

The Max-Planck-Institute für extraterrestrische Physik (MPE) was founded in 1963, in the early years of the space age/era. Therefore, the development of advanced instrumentation, needed for the in-situ investigation of plasma physical processes in near-Earth space and the solar system, was vital for the success, in particular with respect to the international competition.

The first 10 years, 1963-1973 approximately, were dominated by the development of instrumentation for the measurement of plasma and fields and by the development of active experiments in space, i.e. the release of artificial clouds (Ba) onboard sounding rockets. During that time the MPE team also proposed instruments for the investigation of electrons, protons and alpha particles for the first German spacecraft (AZUR). It was designed to investigate the radiation belts of the Earth in a near-Earth polar orbit and launched in 1969. With the instruments onboard AZUR a long history started of developing advanced space-borne instrumentation that was successfully proposed for many international missions, exploring the magnetosphere of the Earth, interplanetary space, and the solar system.

The success of the instrument development at MPE was largely due to the excellent support by the MPE engineering department which allowed in-house mechanical and electronic design, development, manufacturing and testing. Fig. 1 and Fig. 2 provide an overview of these missions.

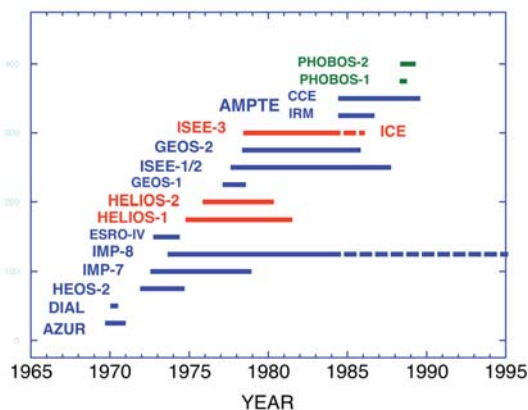


Fig. 1: Instruments onboard national and international missions between 1965 and 1985; red: Interplanetary missions; blue: missions in Earth orbit; green: planetary missions.

In addition to the development of advanced instrumentation, MPE took a leading role in the proposal, design, and management of several missions, with the support of the Max-Planck-Society and the German funding agency (DLR). These missions were not only the ill-fated Firewheel mission that was lost when the second Ariane-2 test launch from Kourou failed in May 1980, but also the very successful AMPTE (Active Magnetospheric Explorer) mission (launch 1984), the Freja mission (launch 1992), the Equator-S mission (launch 1997) and ESA's four-

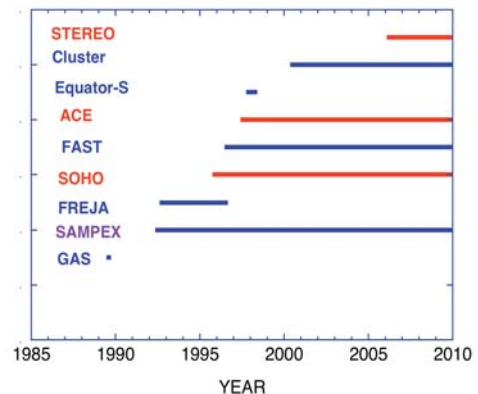


Fig. 2: Instruments onboard national and international missions between 1985 and 2010; red: Interplanetary missions; blue: missions in Earth orbit.

spacecraft Cluster mission (launch 2000), where MPE was heavily involved in the mission proposal.

To study the physical processes in-situ requires the measurement of electric and magnetic fields, and of ions and electrons over a large energy range, from space plasmas (eV to keV) to solar and interplanetary energetic particles (~0.1 MeV to ~100 MeV). The MPE team decided to concentrate in particular on the development of (1) a novel technique for the measurement of electric fields (Geos-2, Equator-S, Cluster), (2) instrumentation for the determination of the distribution function of space plasmas that finally led to a 3D analyzer with mass per charge resolution Helios-1/2, (Helios, ISEE-2, Equator-S, FAST, Cluster), and (3) particle telescopes, utilizing a stack of solid state detectors (AZUR), that were subsequently significantly improved by the combination with large-area gas proportional counters to combine high elemental resolution with high sensitivity (IMP-7/8, ISEE-1/3, SAMPEX, ACE). Combined with electrostatic deflection (SEE-1/3, ACE), or using the magnetic field of the Earth as a mass per charge spectrometer (SAMPEX), this technique also allowed the determination of the ionic charge of energetic particles over an extended energy range, (4) a technique using backscattering of alpha particles and X-rays for the determination of the surface composition of solid bodies in the solar system (Phobos), and (5) the development of time-of-flight technology that is able to provide elemental and ionic charge determination at low energies (AMPTE-IRM, SOHO, Equator-S, Cluster, STEREO).

Presently, several instruments for the determination of plasma parameters in the near-Earth environment and for the measurement of energy-, mass-, and ionic charge distributions of solar wind, suprathermal and energetic ions in interplanetary space are operational. These instruments are onboard the Earth orbiting satellites SAMPEX, FAST, and Cluster and onboard the interplanetary observatories SOHO and STEREO.

In the following articles, some of the measurement techniques developed over the last 40 years, are described more in detail.

## Plasma and Electric Field Instruments

The group had a long history already in the development of advanced instruments for the measurement of the velocity distributions of plasma electrons and ions, as well as for the measurement of the electric fields within the plasma.

In 1972, together with the Los Alamos National Laboratory, we proposed an instrument for the NASA/ESA International Sun-Earth Explorers ISEE-1 and-2, which were launched in 1977. The instrument employed quadrispherical electrostatic analyzers, with open electron multipliers as detectors. It had a time resolution for measuring the full electron and ion velocity distribution function of up to 3 s. This meant a progress of more than an order of magnitude over previous instruments, allowing for the first time to resolve the structure of the thin magnetospheric

### The Next Step: 3D Resolution in 1 Spin

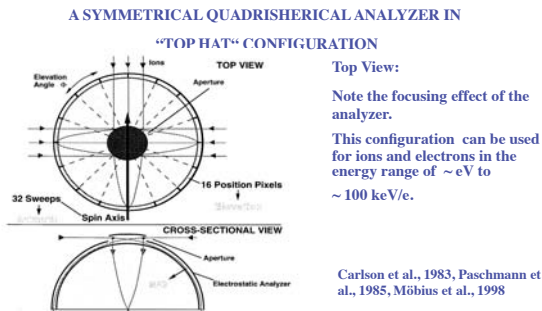


Fig. 1: Schematic of the top-hat electrostatic energy-per-charge analyzer used in the AMPTE-IRM and Cluster missions.

boundaries (bow shock, magnetopause). The discovery of gyrating reflected ions in the foot-region of the bow shock and the high-speed flows, caused by magnetic reconnection at the magnetopause, were the most prominent results. Flight-spares of this instrument were put on-board the sub-satellite that our group built for the ill-fated Firewheel mission.

The next step, together with the Space Science Laboratory at UC Berkeley, was the development, of hemispherical electrostatic analyzers of the top-hat design, which is the de-facto standard now for this type of space-plasma application. As illustrated in Fig. 1, it has an intrinsic field of view of  $360^\circ \times 10^\circ$  with uniform response, and, mounted on a spinning spacecraft, it can measure the full three-dimensional velocity distribution function in half a spin-revolution. Two detectors of this kind, one for electrons, the other for ions, were put

on MPE's own AMPTE-IRM spacecraft, launched in 1984, utilizing only a  $180^\circ$  field-of-view however. A set of eight Channel Electron Multipliers (CEMs) was used as detectors. In another first, the AMPTE instrument incorporated on-board computation of the moments of the electron and ion distributions, i.e., the density, bulk velocity, pressure and heatflux, at full time-resolution. This would otherwise not have been possible from the data sent to the ground, because of limited telemetry bandwidth. With this instrument, surveys of high-speed flows, generated by magnetic reconnection at the magnetopause and in the magnetotail, were possible for the first time, together with the evolution of the ion distribution function across the bow shock wave.

Top-hat electrostatic analyzers, similar to those on AMPTE-IRM, were used later on the Swedish-German Freja satellite, and subsequently proposed by a consortium under the leadership of CESR Toulouse for ESA's Cluster mission, together with ion-composition detectors, based on the time-of-flight technique (see below). The ion-composition analyzer is schematically shown in Fig. 2.

MPE had a strong role in Cluster, it was finally launched with Russian Soyuz rockets from Baikonur in 2000. A first attempt in 1996 had failed when the Ariane-5 had to be blown up on its second test flight from Kourou. At the moment, the Cluster mission is still active. Using the first opportunity for four-point measurements, Cluster measurements have established the spatial and temporal scales of fundamental plasma processes.

The institute's artificial Barium-ion clouds provided the first reliable measurement of the small electric fields in space plasmas, albeit at isolated points in space and time.

### M/Q Determination by E/Q and TOF Measurement

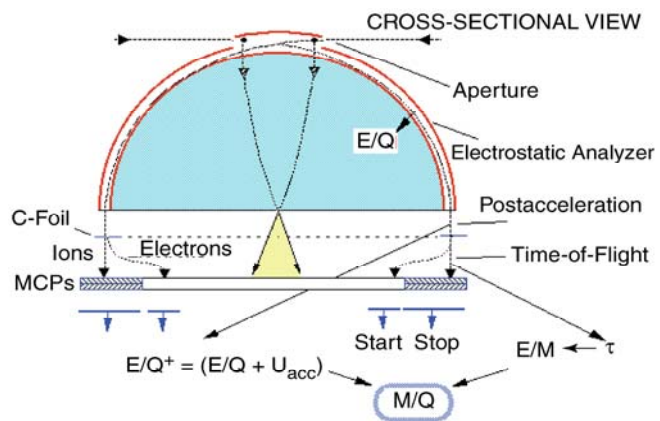


Fig. 2: Schematic of the ion-composition analyzer for Cluster, consisting of a top-hat energy/charge analyzer, followed by a time-of-flight segment between a carbon-foil and a micro channel plate (MCP) detector.

For continuous measurements from a spacecraft, MPE has developed a method, based on probing the electric-field-induced drift of artificial electron beams. Following a proof-of-principle application in 1977 on ESA's Geos-2 spacecraft, MPE led an international collaboration that proposed a highly advanced and ambitious concept for ESA's Cluster mission, launched in 2000. Early experience with this novel design had been gained by flying it on MPE's Equator-S spacecraft in 1997. The basis of the technique is the injection of weak beams of electrons and their detection after one or more gyrations in the ambient magnetic field. In the presence of a drift velocity, induced by an electric field, the otherwise circular electron orbits are distorted into cycloids, the shape of which depends on whether the beam is injected with a component, parallel or anti-parallel to the drift velocity, is illustrated in Fig. 3. Two electron guns and two detectors are needed (and had to be newly developed), both with electronically steerable pointing directions. For each gun there is only one orbit-solution that connects it with the detector on the opposite side of the spacecraft. Those solutions are determined by a beam, rapidly sweeping in the plane perpendicular to the ambient magnetic field (known from the on-board magnetometer), until a signal is detected and the sweep direction is reversed. The knowledge of the positions of the guns and of the firing directions that cause the beams to hit their detectors, allows to determine the drift velocity through triangulation. As is evident from the figure, the two orbits differ in length, and thus in the electron travel times. Measuring those travel time-differences also yields the drift velocity. For this purpose, and also in order to distinguish beam electrons from the high background of ambient electrons, the electron beams are amplitude-modulated with a pseudo-noise code and their time-of-flight is determined by a set of correlators. The characterization of the global plasma convection in the magnetosphere, as a function of the solar wind conditions, is one of the main results from these measurements.

Of quite a different nature, but also dedicated to the detection of electric fields, was the barium plasma cloud technique, which MPE began its experimental program with in 1961. Basically there were only two experimental issues involved: The development of an efficient barium vapor emission in space and a sensitive optical observation system. A broad engineering expertise enabled the development and production of many sounding rocket payloads, sometimes very complex, and loaded with a multitude of particle and field detectors that were provided by international colleagues from other countries. This know-how was subsequently exploited to build full orbiting space-

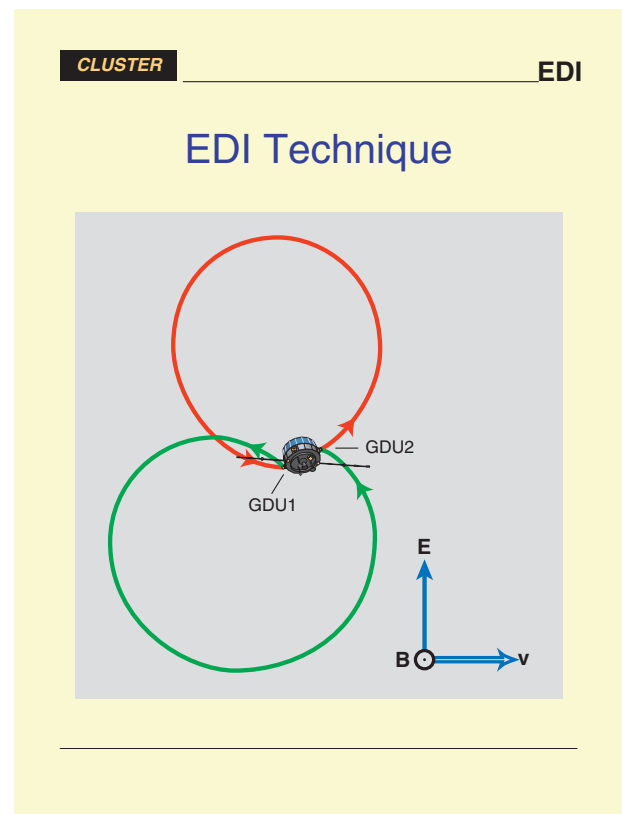


Fig. 3: Principle of operation of the electron drift instrument (EDI). Two gun-detector units (GDU) are mounted on opposite sides of the spacecraft. For any given combination of magnetic field  $B$  and drift velocity  $V_d$  (induced by an electric field  $E$ ), only a single electron-trajectory exists that connects each gun with the detector on the opposite side of the spacecraft. Note that the spacecraft size has been exaggerated for clarity. For realistic magnetic fields, the gyro radius is so large (e.g., 1 km for a 100 nT field) that the spacecraft would not be visible if it were on scale.

crafts, such as AMPTE-IRM and Equator-S. The barium release technique was fully developed by the end of 1964 and proven during various sounding rocket flights. The chemical reaction of fine Ba metal grains, with CuO as oxidizer and Ba in excess, turned out to be the most efficient reaction with a yield of about 10% of the excess Ba. The shaped-charge technique for creating fast barium jets for high-altitude injections became operational by 1969. The optical instruments underwent considerable evolution since the early sounding rocket campaigns. For the artificial comet experiments of the AMPTE mission, image-intensified CID and SEC cameras were attached to various optical systems, reaching sensitivities of a few tens of Rayleighs. For the auroral observations in the 1990's image-intensified CCD cameras were employed.

## Energetic Particle Instruments

The Space Plasma group developed sophisticated instruments for satellite missions to measure in-situ the distributions and properties, like energy, mass and ionic charge, of energetic particles in the near-Earth environment over a time span of forty years. Our instrumental activities ranged from the first German satellite Azur, launched in 1969, to NASA's STEREO mission, which started operations in 2006.

### Energetic Particle Instruments

The first instruments for the in-situ measurement of energetic electrons and ions was proposed for Germany's first mission in space, AZUR, dedicated to the detailed study of the newly discovered radiation belts of the Earth's magnetosphere. The measurement technique, a particle range and residual energy measurement with a stack of solid state detectors for the detection of proton energy spectra in the energy range of  $\sim 1.5 - 100$  MeV, was in principal known from instruments used in nuclear research. However, the high radiation background in the radiation belts and the stringent requirements on mass and power, required a novel compact design of solid state detector stack and electronics. The AZUR instruments for the first time provided detailed distributions of trapped protons, alpha particles, and electrons in the radiation belt of the Earth, and led to the discovery of energetic neutral atoms at low altitudes near the equator. The low-altitude polar orbit of AZUR also allowed the first systematic study of the entry of solar energetic particles over the polar cap into the magnetosphere of the Earth.

In the early 1970s a series of NASA's interplanetary missions (IMP, for Interplanetary Measuring Platform) provided an opportunity to apply the newly developed solid-state detector technology to the measurement of solar energetic particles (SEP). The requirement to measure ionic charge states and elemental composition in the mass range of hydrogen to iron from suprathermal to  $\sim$ MeV/nucleon energies, led the teams of the University of Maryland (UMd) and of MPE to propose a package of two sensors, the Electrostatic Energy versus Charge Analyzer (EECA), and the Ultra Low Energy Particle Telescope (ULET). ULET was developed at MPE. In order to cover elemental composition at sub-MeV/nucleon energies, the sensor used an energy-loss and residual energy measurement in a particle telescope. Because the energy loss  $\Delta E$  in a (thin) detector is proportional to the differential energy loss,  $E/dx$ , and  $dE/dx$  depend on the mean ionic charge of the ion, the energy loss for p, He and heavy ions, at the same residual energy, is different and can therefore be used to determine elemental abundances.

However, in order to extend the measurements to the then unexplored sub-MeV energy range without loosing high sensitivity, a large area  $dE/dx$  sensor element was needed. This was not possible with silicon solid state detectors (SSD) (because of their limited size and homogeneity) and therefore a very thin ( $\sim 150 \mu\text{g}/\text{cm}^2$ ) gas proportional counter system (PC) was developed. In order to guarantee constant response of the PC, the gas density inside was controlled in a flow-through system, using the current of a radioactive source in a control volume for a feedback circuitry. This sensor system was first used in the UMD/MPE experiments, onboard IMP-7 (launch 1972) and IMP-8 (launch 1973) and led to the discovery of heavy ions (O, N, Ne) in the anomalous component of cosmic rays (see section 2.5), the first systematic study of compositional variations during large SEP events and to the discovery of heavy ion enrichment in  $^3\text{He}$ -rich events.

Subsequently, these PC-SSD systems were further improved by using stacks, consisting of several large-area PCs with a position sensing hodoscope, and several SSDs, improving sensitivity and elemental resolution, and extending the energy range to higher energies (ISEE-1, launch 1977; ISEE-3, launch 1978; SAMPEX, launch 1992).

### Ionic Charge Measurement of Energetic Particles

In order to fully characterize energetic ions by their energy, mass and ionic charge, an unambiguous determination of energy, mass and charge is necessary. In the MeV/nucleon energy range this is possible by combining the "dE/dx versus E" technique, described above, with electrostatic deflection. Fig. 2 of the previous article shows the

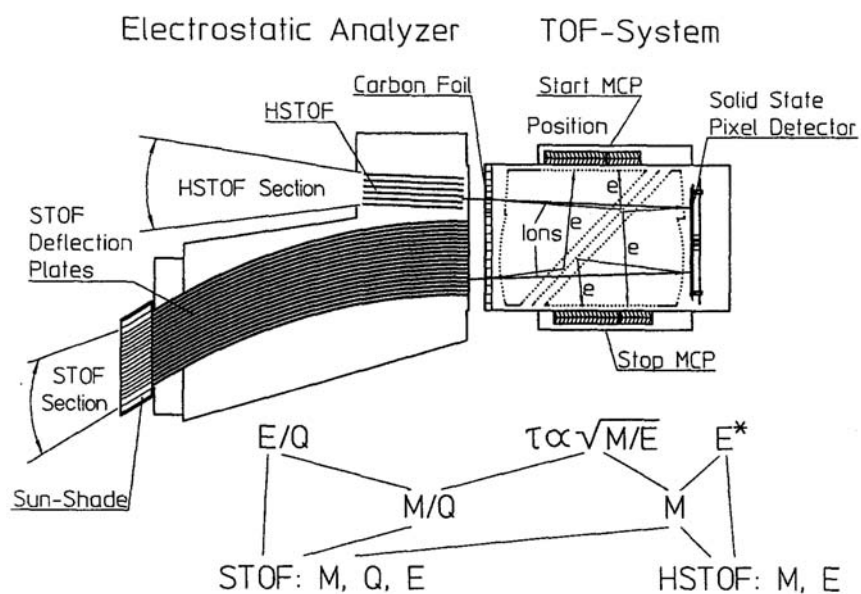


Fig. 1: Functional cross section of the STOF sensor onboard SOHO.

cross section of such a sensor developed for the ULEZEQ sensor of the MPE/UMd experiment package, proposed for ISEE-1 and ISEE-3. This technique was first used for the ULEZEQ sensor of the MPE/UMd experiment package, proposed for ISEE-1 and ISEE-3. The measurement of the deflection of ions with a position sensitive detector provides energy per charge ( $E/Q$ ). This, together with the determination of energy ( $E$ ) and nuclear charge ( $Z$ ) or mass ( $A$ ), allows the unambiguous determination of  $E$ ,  $Z$  (or  $M$ ), and  $Q$ . This sensor allowed the first systematic study of the charge states of solar energetic particles and led to the discovery of characteristic differences of heavy ion charge states in SEPs, accelerated at the Sun and in interplanetary space, as described in section 2.5.

A much improved version of this sensor design, with a higher resolution and sensitivity, covering lower energies between  $\sim 0.1$  and  $0.6$  MeV/nucleon, was later proposed for the SEPICA (Solar Energetic Particle Ionic Charge Analyzer) experiment onboard ACE (Advanced Composition Explorer, launch 1997). SEPICA was developed under the lead of the University of New Hampshire, in collaboration with the MPE team. Observations with this sensor between 1997 and 2000 led to the discovery of a systematic energy dependence of the ionic charge of heavy ions in Fe-rich solar energetic particle events that allowed to locate the acceleration site in the lower corona (see section 2.5).

Because of practical limitations for the deflection high voltage, an obvious limitation of the electrostatic deflection technique for ionic charge determination is its limited energy range. In order to extend the energy range to higher energies, the Solar Anomalous Magnetospheric Particle Explorer (SAMPEX) was proposed for NASA's first Small Explorer mission (launch 1992) which used the magnetic field of the Earth as a mass per charge spectrometer. We developed the HILT (Heavy Ion Large Telescope) experiment for this mission, a multiple PC - SSD system of unprecedented sensitivity with a geometric factor of  $\sim 50$  cm<sup>2</sup>sr. The determination of energy and mass with the  $dE/dx$ -E technique, combined with the rigidity cutoff measurement in the low-altitude, polar orbit of SAMPEX, provided for the first time ionic charge measurements up to 70 MeV/nucleon (for Fe). The measurements with SAMPEX allowed the first unambiguous determination of the ionic charge of ACRs and led to the discovery of multiply charged ACRs at energies  $> 20$  MeV/nucleon (see also section 2.5).

## Time-of-Flight Instruments

In order to close the gap between solar wind energies and several 100 keV/nucleon for the measurement of ionic charge and elemental composition, the time-of-flight technique was developed for space applications in the early 1980s. At MPE, the first time-of-flight system was proposed for SULEICA (Suprathermal Energy Ionic Charge Analyzer) onboard AMPTE/IRM. With this technique the flight time of ions,  $\tau$ , is measured over a distance  $L$  of typically  $\sim 3 - 50$  cm. Knowing  $\tau$  and  $L$ , the velocity (or energy per mass  $E/M$ ) can be determined. This, together with the measurement of energy per charge ( $E/Q$ ) by an electrostatic analyzer system, provides the mass per charge ( $M/Q$ ) of the ions. Combined with the energy determination in a solid-state detector, such systems unambiguously provide energy, mass, and ionic charge of the ions. A schematic cross section of a later version of this type of sensor (Suprathermal Time-of-Flight Sensor STOF, developed under the lead of MPE for the CELIAS experiment onboard SOHO (launch 1995) is shown in Fig. 1. The HSTOF section of the sensor, using planar analyzer plates (see Fig. 1) allows the determination of mass and energy of incoming particles, and, at energies below the cutoff energy of the electrostatic analyzer, the measurement of energetic neutral atoms.

In the near-Earth environment it is often sufficient to resolve the major ion species of solar wind and ionospheric origin, contributing significantly to the mass density of the plasma (usually  $H^+$ ,  $He^+$ ,  $He^{2+}$ ,  $O^+$ ). In this case, limited mass per charge resolution is sufficient and can be obtained by  $E/Q$  and mass determination. A sensor design, using a top-hat electrostatic analyzer, post acceleration (to extend the energy range to  $\sim 40$  eV) and time-of-flight, was the 3-D CODIF sensor (Composition and Distribution Function Analyzer) onboard the FAST, Equator-S, and the four Cluster spacecraft, schematically shown in Fig. 1 of the previous article. A similar design as CODIF, extended by the determination of energy for heavy ion composition and ionic charge determination in the solar wind, is now used onboard the two STEREO spacecrafts.

Measurements with the SULEICA sensor onboard AMPTE/IRM led to the discovery of helium pickup ions ( $He^+$ ) of interstellar origin in the inner heliosphere. The STOF sensor onboard SOHO allowed the systematic study of the ionic charge of solar energetic particles at suprathermal energies. With HSTOF, energetic neutral atoms (H, and He) from the outer heliosphere were discovered in the inner heliosphere.

### 3.5 COMPLEX PLASMAS

Experiments as well as theoretical investigations with complex plasmas at the MPE during the last years revealed the great value of this kind of research in particular for interdisciplinary topics (see section 2.6). As in other fields of soft matter, e.g. colloids, complex plasmas are very well suited for studying interesting questions, like phase transitions and separations in statistical physics, or in electrorheological liquids and bubble formation in fluid physics. The significance of complex plasmas as model systems for other many-body systems in physics is that complex plasmas can be investigated on the microscopic and kinetic level and that it is possible to tune the interaction potential between the microparticles by adjusting the external parameters (pressure, particle size, electric

plex plasmas in the absence of gravity. This can be done on board of the International Space Station (ISS) or in parabolic flights.

The experiments PKE-Nefedov (performed on the ISS from 2001 until 2005) and PK-3 Plus (in operation on the ISS since 2006) successfully demonstrated the use of microgravity experiments with complex plasmas in space. Further experiments on board the ISS are planned and already in preparation: PK-4 is under construction and shall replace PK-3 Plus in 2012. PlasmaLab is currently in the laboratory development phase. Both experiments have already been run and tested in parabolic flight campaigns. After all, laboratory experiments on earth are cru-

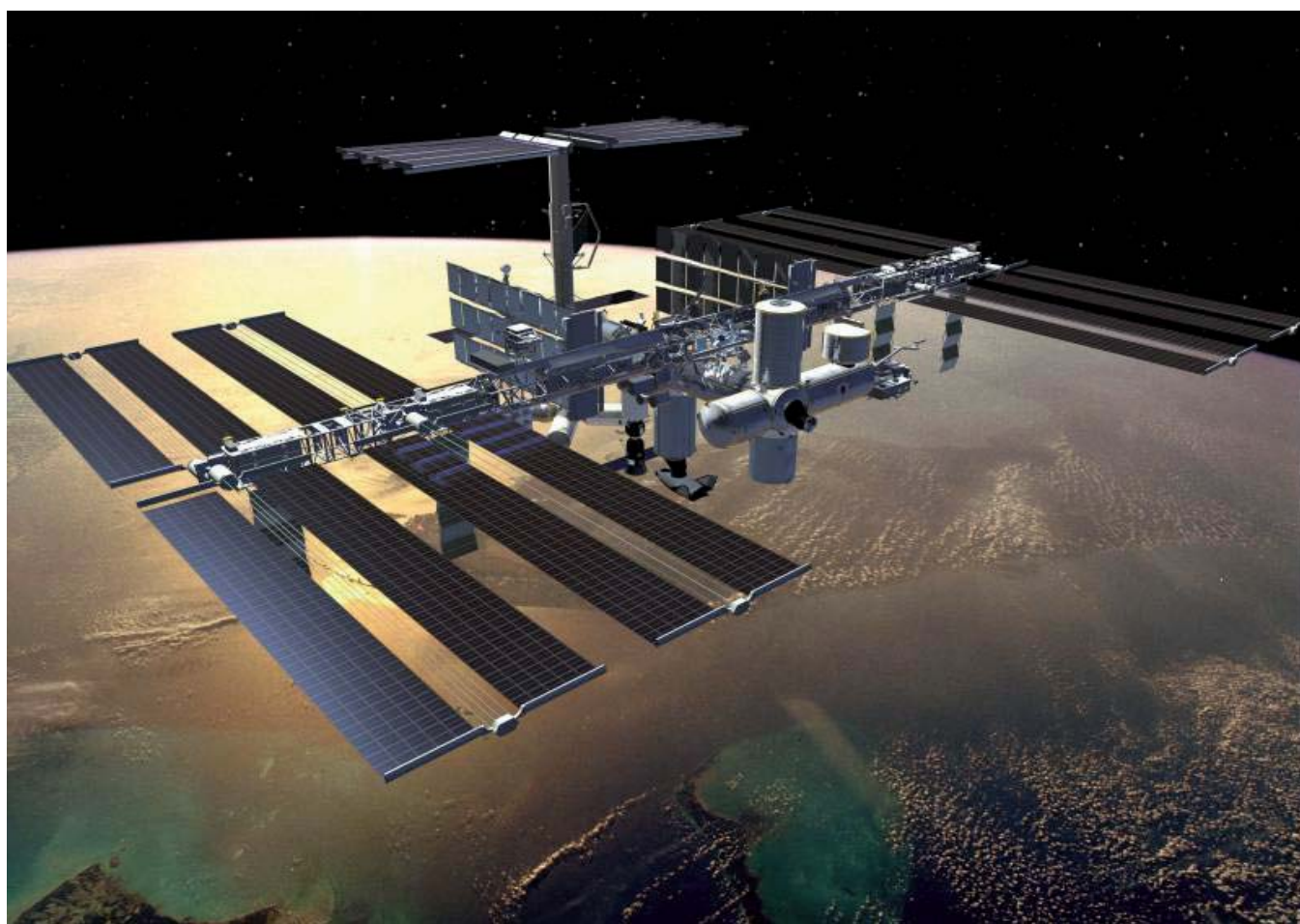


*Fig. 1: The International Space Station ISS (Image: NASA).*

power) in the experiments. These experiments can be performed in the laboratory where the charged microparticles are suspended against gravity by electric fields or temperature gradients inside the plasma chamber. However, the levitation of the microparticles in most cases is restricted to a limited region (plasma sheath) and the system is subject to stress by external forces. Hence, to answer many questions it is highly desirable to study com-

cial since they are much easier to prepare and to conduct. Also some equipment necessary for certain investigations, e.g. strong magnets, can only be utilized in ground based laboratories. Therefore both, microgravity and laboratory experiments, are important and complimentary to each other. In the following we will concentrate on the microgravity projects, PK-3 Plus, PK-4, and PlasmaLab. Scientific results obtained in our laboratories are discussed in section 2.6.

## PK-3 Plus – Microgravity Research on the ISS

PK-3 Plus is our current laboratory for microgravity research on complex plasmas on the International Space Station ISS and delivers interesting new and unique data frequently. It was launched end of 2005 and has been continuously operated over the last three years. PK-3 Plus is a cooperation between MPE and the Joint Institute for High Temperatures of the Russian Academy of Sciences in Moscow. This partnership provides free access of accommodation and resources on the ISS. The German contribution is financed by the German Space Agency DLR.

The most successful research on the ISS up to now, the complex plasma research with MPE's PKE-Nefedov laboratory, is continued by its successor PK-3 Plus. We performed seven independent experimental missions on the ISS with several Russian cosmonauts in the years 2007 – 2009. Each mission typically contains



Fig. 1: Cosmonaut Yuri Malenchenko aboard the ISS with our control and data storage computer, running a complex plasma experiment.

three experimental runs of 90 minutes and delivers unique data, which are analysed and published by the Russian-German team. Recent discoveries from this microgravity laboratory are, for example, the first observation of electrorheological plasmas, non-equilibrium phase transitions, phase separation in binary complex plasmas (see Figures 2-4). These investigations open up a new direction of research in complex plasmas, being a model system for solids and fluids to investigate scale invariant and generic processes on the most fundamental – the kinetic level.

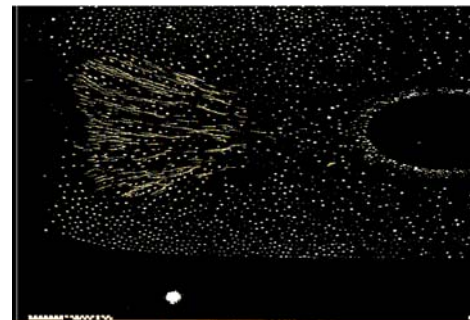


Fig. 3: Non-equilibrium phase transition in a binary complex plasma: one particle component penetrates the other and forms lanes.

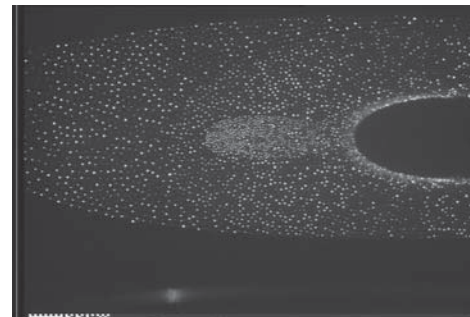


Fig. 4: Phase separation (droplet formation) in a binary complex plasma, observed by experiments on the ISS.

In 2008 we celebrated 10 years of our cooperation with Russia with a joint scientific symposium at MPE together with a large Russian delegation consisting of scientists from our partner institute, engineers and officials from RKK-Energia and the Yuri Gagarin Cosmonaut Training center, as well as the cosmonauts - the experimenters in Space. The Russian-German team was invited by the Bavarian Minister for economics, Martin Zeil, to honour the successful cooperation during a reception at the ministry. This offered an opportunity to talk to politicians, industry and to our German Astronaut Thomas Reiter.

In January 2009 we performed the already 10th mission with PK-3 Plus on the ISS with cosmonaut Yury Lonchakov. The cosmonauts are well trained to perform part of the experiments in a manual mode – guided by the scientists and engineers from ground, at the control centre in Korolev. During the experimental sessions, live video downlink from the experiment for a maximum of 20 minutes and audio contact to the cosmonaut for the full period are available. The control of the experiment is discussed with the ISS crew before the cosmonaut reacts. This needs a well-rehearsed team on ground and in space on the ISS.



Fig. 2: First observation of the transition of an isotropic fluid into a string fluid in an electrorheological plasma. The control parameter is the voltage applied to the electrodes.

## PK-4 – Complex DC Plasmas on the ISS

PK-4 is a European-Russian project onboard the ISS to investigate complex plasmas in a DC discharge under microgravity conditions. The launch of the PK-4 facility is scheduled for 2012.

Complex plasmas, i.e. plasmas containing micron size particles, can be produced in an RF or DC low-temperature discharge plasma by injecting microparticles into this plasma. The successful ISS experiments PKE-Nefedov and PK-3 Plus use an RF discharge plasma chamber. Our Russian partners, the Joint Institute for High Temperatures in Moscow (JIHT, formerly IHED) also investigated complex plasmas in a DC discharge on ground as well as under microgravity. The Russian experiment PK-2 on the orbital station MIR was based on a first simple DC discharge chamber containing microparticles. After the realization of PKE-Nefedov the first ideas arose for an advanced complex DC plasma experiment within a collaboration of MPE and JIHT. In 2002 a laboratory pre-development phase, supported by DLR, started and resulted in two laboratory set-ups at MPE and JIHT, and a parabolic flight set-up. The DC discharge takes place in an elongated glass tube (see Fig. 1) with DC electrodes at the end of the U-shaped chamber.

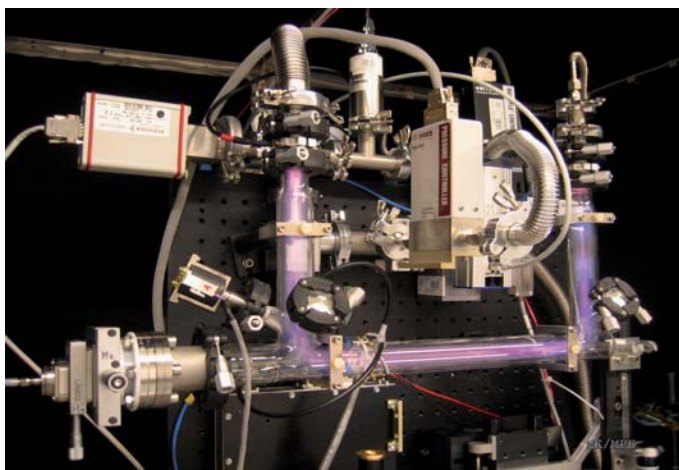


Fig. 1: The PK-4 laboratory set-up at MPE.

Applying a voltage of the order of 1 kV to these electrodes, the neon or argon gas, filled into the chamber with a pressure between 10 and 200 Pa, is converted into the plasma state. Particle dispensers mounted on the glass chamber allow the injection of the microparticles. Entering the plasma these particles become negatively charged and drift, with velocities of a few cm/s, to the anode due to a longitudinal electric field in the plasma of the order of 2 V/cm. Due to its particular geometry this system is suited to investigate flow phenomena, like as the transition from laminar to turbulent flow, in the liquid phase of complex plasmas. Therefore PK-4 allows complimentary experiments compared to PKE-Nefedov and PK-3 Plus, focusing is on the crystalline state. As in previous experiments the microparticles are illuminated by a laser sheet and recorded by CCD cameras. Using various manipula-

tion devices – gas flow, polarity switching between the DC electrodes with a frequency of about 1 kHz, external RF coils, an additional electrode inside the chamber, a powerful manipulation laser (up to 20 W), or a heating wire around the glass tube – the microparticles can be confined or accelerated, allowing to study stable extended clouds of microparticles or shear flow.



Fig. 2: The PK-4 experiment container for the ISS.

In 2006 the project for implementing PK-4 on the ISS started with the Phase A/B (feasibility study, preliminary design). The project is supported by ESA. The construction phase (Phase C/D) started in 2008. The critical design review is planned for the end of 2010 and the launch from Baikonur with a Progress Transporter in the beginning of 2012. PK-4 will be accommodated in the European Physiology Rack (EPM) in the European Laboratory Module Columbus. The heart of the experiment, the integrated base plate containing the plasma chamber, the observation system, and the manipulation devices, will be installed in a container as shown in Fig. 2.

Up to now we participated with PK-4 in seven DLR and ESA parabolic flight campaigns for scientific experiments as well as for apparatus tests (see Fig. 3). Laboratory and parabolic flight experiments already led to several scientifically interesting results with subsequent publications.



Fig. 3: Parabolic flight test with PK-4.

## PlasmaLab – The Future of Complex Plasmas on the ISS

PlasmaLab is planned to be the next generation experiment for complex plasmas research on the ISS. One of actually two investigated plasma chambers will be used, allowing a wide range of plasma parameters and microparticle manipulation. Presently PlasmaLab is in a laboratory development phase supported by DLR.

The “PlasmaLab” is a possible follow-up experimental set-up for PK-3 Plus and PK-4 to perform complex plasma research aboard the International Space Station (ISS). The idea of PlasmaLab is to set up a complex plasma facility that is flexible in its configuration, allows to access a parameter space several orders of magnitude larger than in earlier experiments, and supports user controlled plasma manipulations that result in an active modification of the particle interaction in a complex plasma. First studies on possible configurations were performed under the working titles IMPF (International Microgravity Plasma Facility) and IMPACT (International Multiuser Plasma, Atmospheric, and Cosmic Dust Facility). They began in 1999 and were supported by ESA and DLR.

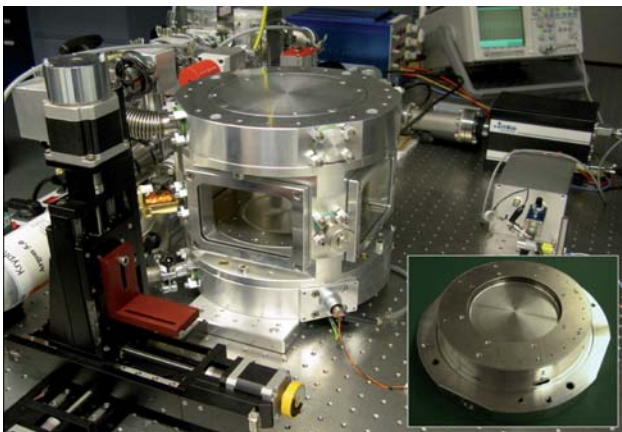


Fig. 1: Experimental setup of the new PlasmaLab “Zyflex” chamber with its movable electrode and guard ring combinations (inset). The setup also includes a gas support system (left) and translation stages (in front) for the optical access to the complex plasma by illuminating lasers and observing cameras.

Since the end of 2007 we started to design and investigate two possible plasma chambers and a novel plasma generator that can fulfil the requirements for a future PlasmaLab on the ISS in close collaboration with the Joint Institute for High Temperatures in Moscow (JIHT, formerly IHED). In the course of this DLR financed study we designed the first plasma chamber in 2008 which is based, as former experiments, on a cylindrical geometry. Despite the other experimental setups however, the inner geometry of the plasma chamber can be modified by an electronically controlled positioning system. Electrodes and guard shields are movable over a significant range, even during an experiment run. An exchange of the electrode system in the laboratory is effortless, and so different types of plasma generation methods can therefore easily be tested, for example combinations of driven parallel plate electrodes or

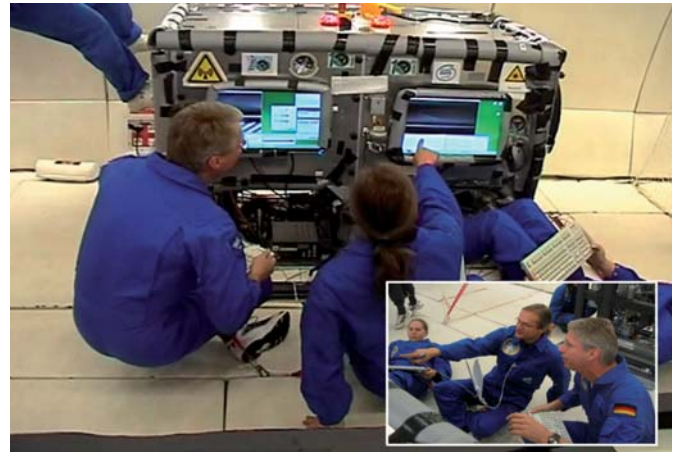


Fig. 2: Experiment setup with Zyflex chamber operated by Thomas Reiter, Uwe Konopka and Lisa Wörner (inset from right to left) during DLR's parabolic flight campaign in September 2009.

other secondary plasma sources embedded into the movable electrode bodies. A laboratory setup with such a cylindrical, “flexible” plasma chamber (Zyflex-chamber) as built in 2008/2009, is shown in Fig. 1. To test this chamber under microgravity conditions, a parabolic flight setup was built in 2009, and successfully operated during the DLR parabolic flight campaign in September 2009 (Fig. 2).

A plasma chamber having an approximately spherical geometry was proposed for study. We started the design in 2009. It consists of twelve independently controllable electrodes, ordered geometrically as a dodecahedron, a regular polyeder that represents a close approximation to a sphere (see Fig. 3). The manufacturing of a first prototype of this novel kind of plasma chamber (“Dodecahedron” chamber) is foreseen for 2010. Its electrodes will be driven by a twelve channel radio frequency (rf) generator that also allows each electrode to be biased by an arbitrary static (or low frequency) voltage. This newly designed rf-generator will allow the experimenter to extend the accessible plasma parameter space as well as the required interparticle force manipulation. The latter is the basis to extend our study of complex plasmas towards multi-particle systems that are defined by attractive forces which are inaccessible by the present setups.

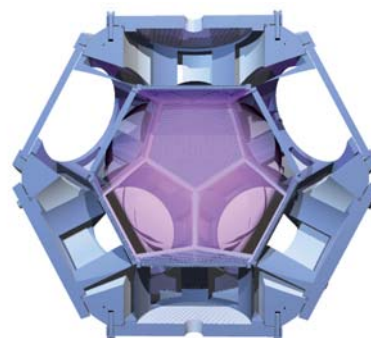


Fig. 3: Design sketch of the novel “Dodecahedron” plasma device. This device should allow the experimenter to actively change the interparticle forces between the particles of a complex plasma in a nearly spherical symmetric environment.

### 3.6 KNOW-HOW TRANSFER

Developments in the context of our research hold a large potential for applications in other scientific fields or for industrial utilization. For that reason, the institute is actively involved in different interdisciplinary research projects and is initiating new developments. The theory department transfers its know-how arising from the study of complex systems and complex plasmas to applications in e.g. engineering, biology and medicine.

In the framework of our recent theoretical studies we focus on new approaches to characterize synchronization and correlation phenomena in complex systems. Synchronization occurs not only in physical but also in many technical or biological systems. Our novel approach to characterize similarities in data sets is based on the concept of symbolic representations. Since these symbols represent permutations and the set of permutations defines a group, we can make use of the general properties of groups to define transcription symbols. This proves to be a very useful way to describe synchronization and to quantify the complexity of the spatio/temporal interdependence among the system components.

In neuroscience synchronization processes have gained a great deal of attention, as they are responsible for a variety of the brain's essential functional properties. Aim of a project, carried out with our partners from the Department of Anesthesiology (TUM, Munich), is a characterization of the anesthetized state in terms of synchronization properties. In a study anesthetic drugs are administered to yield controlled states of consciousness. Our results show significantly enhanced synchronization patterns during anesthesia, which give some hints on the underlying physiological processes in the brain. The purpose of our activities is to gain deeper insights in physiological mechanisms and may result in an anesthetic depth monitor.

A cooperation with the Department of Neuropathology (TUM) and the Department of Crystallography (LMU, Munich) deals with methods for a label-free imaging of human cells. Confocal Raman spectroscopy is a non-destructive technique and therefore allows for further use and investigation of living cells after imaging. To gain knowledge about the spectral interpretation, we combined Raman imaging with Immunofluorescence (IF) microscopy for the identification of different subcellular compartments. A variant of information redundancy is applied for accurate registration between the different data modalities. Subsequently, we are able to compare Raman and IF data with the help of information theoretical concepts to assign spectral fingerprints to specific cell compartments (see Fig. 1). At the same time our approach overcomes the practical restriction of IF-images to three types of fluorescence anti-bodies and renders pre-treatment (fixation) dispensable. The development of these techniques is a prerequisite to study the molecular chemistry of living cells. This is of particular interest for future studies of glioblastoma cells in the context of brain tumor research.

A proper description of the structure of the trabecular bone network helps to evaluate the deterioration of bone tissue caused by osteoporosis and to predict spine and hip fractures. To elucidate the morphological and mechanical factors for bone strength we model the stress/strain distribution in the trabecular network using the Finite Element Method (FEM). As a morphological measure we calculate scaling indices (SIM) to locally quantify the bone structure and to discriminate between different structural elements (e.g. 1D-like rods and 2D-like plates). Our results prove that plates are the main load-bearing substructures of the trabecular network. Thus the relative amount of plates to rods plays the main role for bone strength and stability.

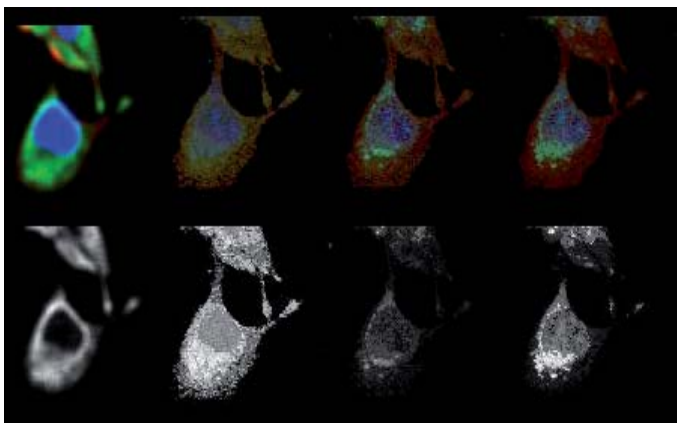


Fig. 1: Original IF-image (leftmost column with endoplasmic reticulum) and three (re)constructions based on Raman spectra. Upper row: RGB representations, red channel: cytoskeleton, blue: nucleus, green channels indicate from left to right: endoplasmic reticulum, mitochondrion, and Golgi apparatus. Lower row: Associated green channel intensities.

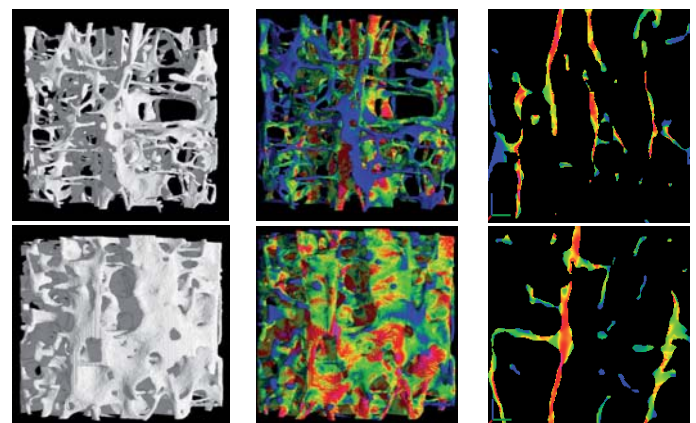


Fig. 2: Left column: 3D  $\mu$ CT images of bone specimens with different bone fraction. Middle and right columns: 3D visualization and cross section of the effective strain redistribution in the trabecular network calculated by FEM.

## Plasma Medicine and Healthcare

An interdisciplinary plasma medicine project, initiated by the MPE, triggered the development of new low-temperature atmospheric plasma technologies that open a wide field of applications ranging from clinical and industrial to even personal use.

Atmospheric plasma sources have attracted a great deal of attention since they combine many advantages such as simple design, easy handling and low cost. Various medical applications have been investigated with growing interest, as it became possible now to treat material or tissue which must not be exposed to vacuum or heat. The bactericidal effect is mainly due to reactive species produced by the plasma and UV light. Especially for the treatment of living tissue, plasma devices were designed that avoid surface contact, heat damage and other painful sensation.

In cooperation with Adtec Plasma Technology Co. Ltd (Japan) we have developed an atmospheric plasma device using microwave technology for the treatment of chronic wounds in clinical practice. This device has a plasma torch and is operated with microwaves at 2.45 GHz and Argon gas. In parallel, we developed plasma devices following different plasma production techniques intended for non-clinical purposes, e.g., the “VenturiPlaSter”, “HandPlaSter” and “PersonalPlaSter” (see Fig. 1). The “VenturiPlaSter” is a “plasma-jet” device based on the Venturi principle, which allows atmospheric plasma production in a local low-pressure environment. It facilitates a more efficient plasma production and control of the plasma chemistry. Since the plasma is produced in a confined space, ambient air can be used, which makes this device easy to handle. The “HandPlaSter” and “PersonalPlaSter” are both based on the “Barrier Corona Discharge (BCD)” technology. A plasma electrode consists of an insulator plate sandwiched by a metal plate and a wire mesh. By applying high AC voltage (typically a few kV in kHz range,  $\sim 0.5 \text{ W/cm}^2$ ) between the metal plate and wire mesh, plasma is produced on the wire mesh side of the insulator plate via numerous micro-discharges. This electrode can be produced in any desired shape and is scalable to different sizes. Therefore, these devices are in particular designated for personal use.

The development of a large area plasma torch made it possible to carry out the first clinical phase II study in plasma medicine worldwide. Our medical partners at the Clinic for Dermatology, Allergology and Environmental Medicine (München Schwabing) and at the Department of Dermatology, University Hospital of Regensburg conduct the clinical part of the study. The objective of the clinical trial is the plasma treatment of chronic wounds such as venous or arterial ulcers. These wounds are very painful, cause considerable reduction of life quality and are difficult to heal. About 1% of the German population suffers from these diseases, with a cost of around 1-2% of the annual health budget. Standard treatments by administering antibiotics have the problem of developing multiresistance, allergic reactions and other side effects. Low temperature plasmas promise a complementary, contact free approach for treatment of wounds that overcomes these problems. Whereas the primary goal of the treatment is to speed up wound closure, from a pathophysiological point of view it is important to reduce bacterial colonization. Infections of the wound with germs are associated with inflammations and cause further complications. The evolution of wounds during plasma therapy is documented with the help of digital imaging before and after each treatment (Fig. 2). Thus, in addition to the clinical evaluation, we use image processing techniques for a comprehensive, close-meshed documentation and detailed characterization of the wound healing process and re-epithelization that allows for quantitative diagnostic findings.

In addition to the clinical and computer assisted assessment of the healing progress microbiological examinations (e.g. smears and wound imprints) are employed. Imprints of the wound surface fluid taken by means of nitrocellulose filters (impregnated with a culture medium) are used not only to monitor the evolution of the bacterial load during the healing process but also to determine its spatial distribution on the wound surface. A recent clinical study performed on a sample of 291 cases showed that plasma therapy leads to an additional bacterial reduction larger than 30% with respect to the control group, which received only a standard anti-bacterial therapy.

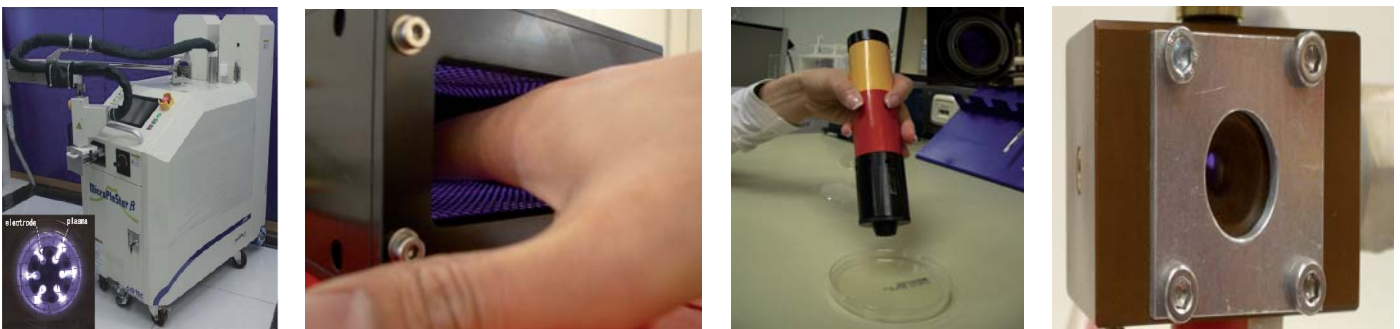


Fig. 1: Development of plasma devices using different plasma generating technologies. From left to right: The MicroPlaSter (torch type), HandPlaSter, PersonalPlaSter (BCD type) and VenturiPlaSter.



Fig. 2: Sequence of digital images showing the wound closure progress within several weeks of plasma treatment and example of computer-assisted segmentation for a quantitative assessment.

In parallel to this phase II study, the newly developed plasma devices (Fig. 1) were characterized with regard to the emission of UV, gas temperature, electric field, charged particles and reactive species. These plasma diagnostic results allow to identify new applications in medicine (treatment of skin irritations and diseases; equipment sterilization), cosmetics (corrective surgery; dental, scars and nail cosmetics) and hygiene. In professional hygiene the most important plasma contribution is sterilization, decontamination and disinfection. One aim is the prevention of diseases or their containment and therefore the prophylaxis of nosocomial infections (which lead to estimated 2 Million hospital induced infections each year in the US alone, and about 100,000 resulting deaths). At the personal level, plasma disinfection can play a role in household appliances, for periodontitis and tetanus prophylaxis, for the prevention and treatment of fungal diseases or for the reduction of perspiration-corrosive bacteria (plasma deodorant).

To some extent plasma can be “designed” with respect to the aforementioned physical properties and especially - in cooperation with the University of California (Berkeley) - to the plasma chemistry by adding, e.g., different gases or catalysts or/and by changing the electron energy distribution function. Plasmas can include different active species that can have an effect on the cellular level. The medical use of ionized atoms and molecules acting on a cellular level needs to be evaluated. First steps towards pharmacological utilization are currently being taken in various biological studies. In cooperation with the Russian Academy of Sciences (Moscow), the Medizet Department of Microbiology (Clinic München Schwabing), the Institute of Experimental Oncology and Therapy Research (TUM), and the Department of Neuropathology (TUM) the effect of plasma on eukaryotic and prokaryotic cells, viruses and fungi was thoroughly studied. The results showed that our plasma devices can efficiently kill all kinds of Gram-positive and Gram-negative bacteria as well as viruses and fungi in seconds to minutes. The “HandPlaSter”, e.g., reduces multi-resistant bacteria (MRSA) by a factor larger than  $10^5$  in less than 10 seconds. Further experiments detected no resistance build-up against the plasma treatment so far.

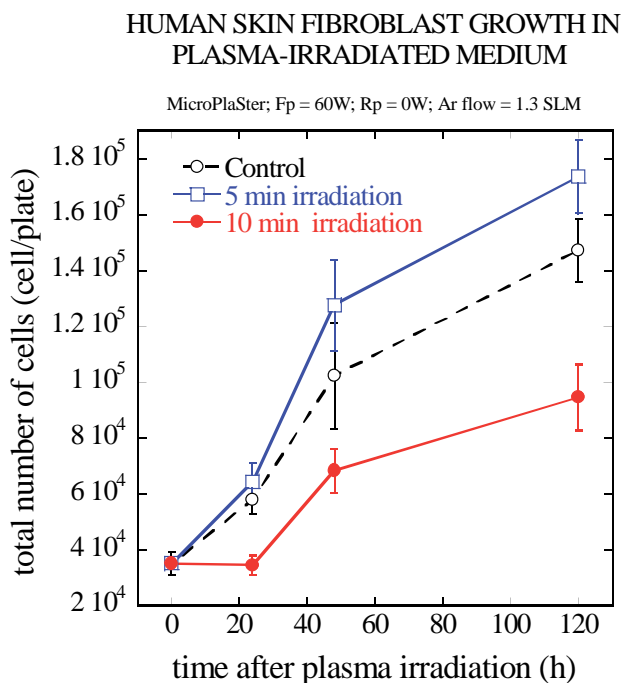


Fig. 3: Effect of reactive species produced by the plasma in the liquid medium on human skin fibroblast proliferation. Human skin fibroblasts have been maintained in the liquid medium irradiated with argon plasma for 0 (dashed black line), 5 (solid blue line) and 10 (solid red line) min. The number of the viable cells have been assayed after 24, 48 and 120 h of incubation.

To identify the optimal dose and composition of the plasma for chronic wound disinfection the effects of plasma irradiation on human skin cell viability, migration and proliferation were analyzed. The results of the in vitro experiments show that the reactive species, produced by the plasma, cause no significant changes in the human skin cell viability and migration and have a dosage-specific effect on their proliferation. Proliferation of human skin fibroblasts was induced by low doses and inhibited by high doses of plasma-generated reactive species (Fig. 3). A bactericidal effect was observed for both doses.

# 4 The Institute



## 4.1 TECHNICAL SERVICES

It would be impossible to realise our scientific visions and ideas from the exploration of the Universe with satellites and earthbound instruments to fundamental research experiments during manned and unmanned spaceflights without the support of MPE's "central technical services". This division mainly consists of three different groups of specialists: the department of electrical engineering, the department of mechanical engineering, with their mechanical workshops each and the data processing group. They all work closely together with each other and the responsible project scientists.

### Electrical Engineering

At the moment 33 staff members (at the MPE and the Semiconductor Laboratory in Neuperlach) are working in the department of electrical engineering altogether. Their tasks vary widely from the planning phase (drafting concepts), designing and manufacturing to commissioning of instrumentation for terrestrial and extraterrestrial observations and scientific experiment design for the International Space Station (ISS). The group technically supports ongoing missions and observations. The staff is expected to demonstrate substantial knowledge of electrical engineering, the confident and reliable handling of modern design and simulation tools and also to be well informed about electronic components. Experience in the field of vacuum-, cryo-, laser technique as well as other areas is required until our scientific visions finally take shape in an experiment. In order to keep their high standards these people cooperate internationally and interdisciplinary, continue professional training regularly, keep pace with the newest state-of-the-art techniques and are prepared to be away on business for several weeks at home and abroad.

Between 2007 and 2009 the department has contributed to the following instrumental projects of MPE: the X-ray mission eROSITA, the far-infrared instrument PACS on the Herschel satellite, the forthcoming instruments for complex plasma research PK-4 and PlasmaLaB, the

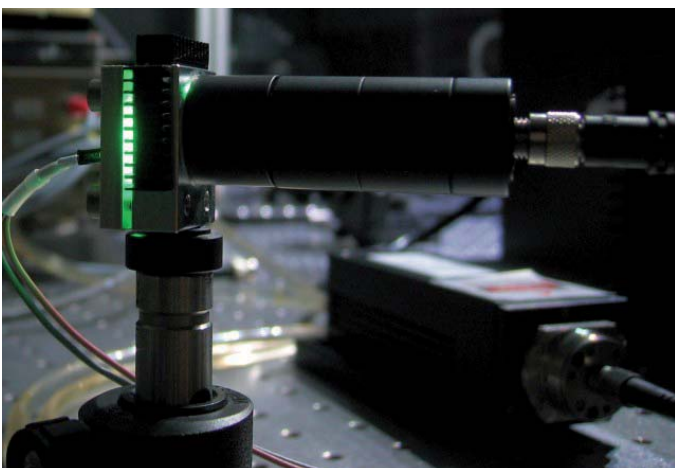


Fig. 1: A 532 nm LED light source for calibration of the wave front sensor for ARGOS.

ground-based astronomy cameras FIFL-LS, GROND and LUCIFER, the laser guide star for the LBT ARGOS, and the interferometer for the VLT GRAVITY.



Fig. 2: The laser test setup for ARGOS.

### Mechanical Engineering

The department of mechanical engineering has 36 staff members altogether and 8 apprentices, working in the design office, the test facility for environmental tests, the plastic laboratory, mechanical workshops and the education workshop. It develops and partly manufactures instruments for the experimental astrophysics mainly. For some of the projects the people of the mechanical engineering department also work closely with industry.

The department deals with a wide spectrum of tasks reaching from precision instrument engineering over special purpose machines to extreme lightweight construction. Also included are product assurance and verification. Particular development problems result from mostly extreme requirements such as cleanliness, stress due to vibration loads during rocket launch or the operation of the instruments in vacuum and at deepest temperatures near absolute zero. For design and development, 2D/3D-CAD as well as FE-software are standard tools. For environmental tests e.g. a shaker and two thermal vacuum chambers can be utilized in the test facility.

In the years 2007 until 2009 the mechanical engineering group supported the following main MPE projects: the far-infrared instrument PACS on Herschel, the forthcoming X-ray mission eROSITA, the complex plasma research instrument PK-4, the multiobject spectrograph LUCIFER, and GRAVITY, the interferometry instrument for the ESO-VLT.

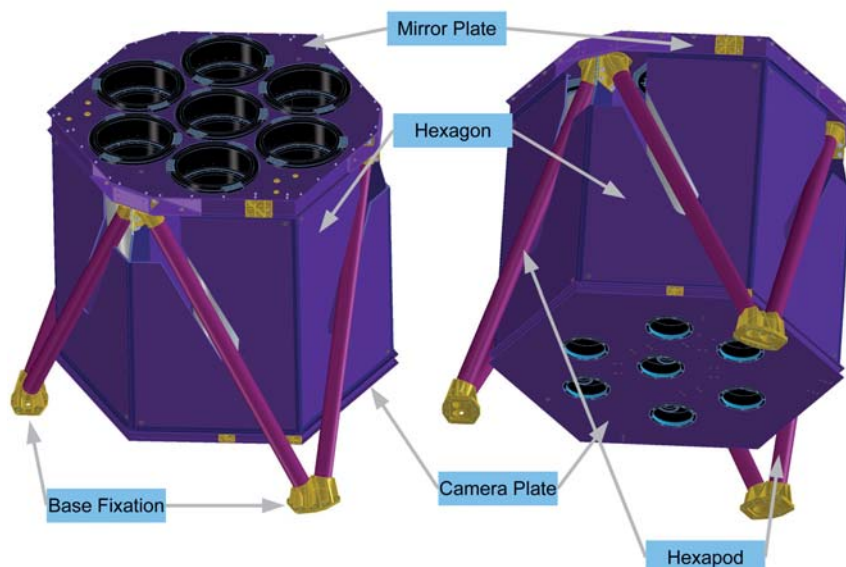


Fig. 3: Main components of the eROSITA telescope structure, designed by the Mechanical Engineering Group. The main materials are CFRP (carbon-fibre reinforced plastic) and aluminum.



Fig. 4: Manufacturing the Base Fixations.

## Data Management and Processing

Data management and processing is generally a collaborative task of the MPE computing support group and the individual research groups. The support people cover the central tasks and, in addition, support the science groups in their specific work with their IT-knowledge and manpower.

Computing and data processing activities are coordinated and handled by a committee with representatives from all working groups of the institute. A central group for system support and programming is assisting this committee whose main tasks are coordination and evaluation of new hardware as well as the software procurement, concep-

tion and control of central installations such as the local-area network, access to external networks and the public printers. In addition, the committee is co-ordinating the collaboration with the Garching Computer Centre (RZG) and takes care of the computer-related training of MPE members.

The members of the central computing support group maintain the central installations i.e. network, server workstations, printers, and the official www pages, with up-to-date information about the institute. They are also part-time involved in the data processing of and software development for our main science projects like XMM-Newton, Herschel/PACS, PanSTARRS. This guarantees the horizontal flow of information and experience.

## 4.2 GENERAL SERVICES

The institute's **administration** plays a very distinct but equally essential role as the technical services mentioned above. It supports the managing directors of the Max Planck Institute für Astrophysik and the Max Planck Institute für extraterrestrische Physik in carrying out their executive duties. These activities also extend to the branches of the MPI for Extraterrestrial Physics in Neuried (test facilities) and in München-Neuperlach (semiconductor laboratory).

The administration's main areas of work involve the handling of personnel matters relating to its own staff as well as to junior researchers and foreign guest scientists, the procurement of scientific and other equipment, and the organization and maintenance of the institute's infrastructure.

Additional core tasks include the planning and administration of institutional and external funds, along with the due processing of receipts and expenditures, supplying proof of the correct usage of appropriated funds. The administration is required to comply with the laws, statutory instruments, legal provisions and guidelines applicable to the Max Planck Society and its institutes. In addition, the Administration can advise and assist the directors on the implementation of these rules and guidelines.

Our **publication services**, are also indispensable for the effectiveness of the institute's work flow. They are in the position to prepare all kinds of graphics and images for publications, brochures, and posters. We also have our own graphic group.

The **print shop** owns all the digital machinery necessary for the production of reports, brochures and preprints for both the MPE and the MPA. In addition, it produces business products such as stationary and envelopes and reproduces colour copies for both institutes.

The Astrobibliothek is the joint **library** for both the Max-Planck-Institute for Astrophysics and the Max-Planck-Institute for Extraterrestrial Physics. We also work together with related institutes and their scientists. With a stock of 280 current journals and about 15,000 monographs (increase of about 400 a year) and 20,000 journal volumes (increase of about 600 a year) we are a rather small and specialized library for the use of our colleagues and guests.

Our stock of monographs and journals is electronically registered. Among our special collections one can find observatory publications, reports, and preprints as well as slides, films, and videos. New incoming preprints and reports are shown on the MPA website. We also manage and send out reprints, reports, and preprints from both our related institutes.



Fig. 1: The joint MPE/MPA Library.

### 4.3 VOCATIONAL TRAINING AND EDUCATION

Besides our education workshop for apprentices in the mechanical area of MPE, there is another new field, where we, together with 5 other renowned scientific institutions, all located in the Munich-Garching area, support young people to promote their knowledge and careers:

#### **The International Max-Planck Research School on Astrophysics (IMPRS)**

IMPRS is a graduate School offering a three year Ph.D. program in astrophysics and cosmology. Open for students from all countries world wide, the school intends to attract highly qualified and motivated young scientists heading for a graduate degree in Physics and Astronomy. Outstanding research facilities and training programs as well as Ph.D. fellowships available for all students provide a unique environment for participants. The school can lay the foundation for long-term international cooperation and thus play a significant role for future science and research.

IMPRS was founded on the initiative of the Max-Planck Society in 2000. The five local institutes, all internationally renowned in astrophysics research, MPE, the Max-Planck Institute for Astrophysics (MPA), the European Southern Observatory (ESO), the Astroparticle Physics groups at the Technical University of Munich (TUM) and the Max-Planck-Institute for Physics (MPP, also known as Werner-Heisenberg-Institute), form the school together. Access to their facilities

will provide graduate students with a very wide range of possibilities for research. There are fewer than a handful of places world wide which can compete in breadth and level of research with the participating institutes. The large number of teaching scientists and advisors actively involved in research guarantee that the know-how available in the participating institutes is presented to the students by the experts themselves.

About 130 students applied for the IMPRS programme in 2009. Approximately 20% of them are accepted, based on their excellence as proven by their university record and by letters of recommendation. A committee composed of members from all participating institutes will review the applications and advise the potential supervisors about the candidates and their qualifications. Successful applicants with a degree equivalent to the Diploma can receive fellowships for a maximum period of three years if required.



*Fig. 1: Excursion during the IMPRS Introductory Workshop 2009.*

## 4.4 PUBLIC OUTREACH

Fundamental research is a condition for the long-term survival of a modern, technological society. In a democracy however, this kind of research cannot exist without its acceptance in the public. Therefore it is absolutely necessary to communicate its activities and results to a broad public, which will then support it as an integrated and basic part of a vital and developing society.

In principle MPE's scientific secretary had, amongst others, the function of building a link between the institute and the public. In order to meet the increasing amount of work in this area and the very specific requirements of modern media, the institute's public outreach however was strengthened by the provision of dedicated press officer position in 2008.

The public outreach team has organized a number of quite different activities in and outside MPE during the last 3 years. In 2007 MPE opened its doors for the public to contribute to the campus-wide Science Night, where the institute's latest technological developments could be watched, and scientists offered public talks on interesting astrophysical topics, like Black Holes and the evolution of the Universe. In 2009 the MPE took part in the normally bi-annual "Open House" event on the Garching science campus. Many MPE volunteers prepare special children's programmes for these events, called „Astronomy for Kids“. With attractions like rocket workshops, puzzle rallies etc. they have become equally popular with teachers, parents and children of all ages and attract a growing number of visitors and participants every year. The next „Open House“ is planned for 2011.

Since 2008 we also take part in the nationwide "Girls' Day". Sponsored by the European Union, the Federal Ministry of Education and Research (BMBF) and the Federal Ministry for Families, Senior Citizen, Women und Young People (BMFSFJ) the yearly initiative "Girls' Day" has been established in Germany in 2001. Not only here but also in many other European countries it aims to give girls and young women aged between 10 and 15 years a wider perspective concerning the choice of their future occupational field. Although on average they do reach a higher level of education at school than their male peers, girls still tend to choose traditional female fields of occupation. By providing them with contact to professionals and an insight

to modern working places in the area of technology, IT and natural sciences it is often possible to catch their interest and to encourage them to change their attitude. 40 girls visited MPE during that day in 2008 and 2009.

The International Year of Astronomy 2009 marked the 400th anniversary of the first astronomical observation through a telescope by Galileo Galilei. It was a global celebration of astronomy and its contributions to society and culture, with a strong emphasis on education, public engagement and the involvement of young people, with events at national, regional and global levels throughout the year. MPE has initiated some own projects in the context of this special year, like a series of vodcasts (see below), and took part in many common events, for example with contributions to the opening ceremony in Berlin in January 2009, a cosmology Exhibition „Evolution of the Universe“ in the 'Deutsche Museum', and a series of arti-



Fig. 1: Impressions from the Open House 2009.

cles in a special edition of „Sterne und Weltraum“, a popular German journal for astronomy.

Besides the organisation of these special events there are also the more traditional tasks of the public outreach team. To groups the MPE offers guided tours through the institute on request. The tours are available in German and English. After a general introduction, scientists of the various groups of the institute will guide the visitors through their departments. This service has always been requested quite frequently (about 25 groups per year) and it can be really challenging to meet the requirements of the different visitors as the groups can be as diverse as sport club members, pupils and students, interested hobby astronomers or even colleagues from other scientific institutions.

The MPE regularly issues press releases, either on its own or in cooperation with other scientific institutions, to communicate its research results also to a wider public. Our first video podcast ("vodcast") was produced at MPE in January 2009, number one of a series of short films about our institute. The topics are our main scientific results, but also the institute itself with its particular corporate identity, its unique research atmosphere and, most importantly, the people meeting and working here.

The MPE brochure describes the institute's research topics, current and new projects and recent results. The first one was issued for the "Open House 2005". It is available in German only and can be downloaded from the Internet. A new version of the MPE brochure in English and German will be available in 2010.



Fig. 2: Girl's Day 2009.



Fig. 3: View from the entrance into the exhibition hall of "The Evolution of the Universe" in the Deutsches Museum Munich. The picture was taken just before the opening of the exhibition in December 2009.

## 4.5 SOCIAL EVENTS

Knowing colleagues not only from a common working place but also from spending some time together in joint social activities can help to form a positive atmosphere in the institute. These activities help to link people from normally quite separated areas and to integrate new MPE-members. Our social activities range from small group-internal celebrations (e.g. the success of a certain scientific project or a PhD defence, special birthdays) to MPE-wide celebrations, such as the Christmas party and the other three well established annual trips: the skiing excursion, the summer works outing, and the visit to the Munich Oktoberfest in autumn.



*Fig.1: Visit to the Oktoberfest.*



*Fig. 2: MPE outing to Salzburg in 2009.*

Another popular and well accepted tradition for many MPE members is the joint visit of the famous Munich Oktoberfest. In 2009, as every year, a large MPE crowd spent a pleasant afternoon (and most of the evening) together, enjoying the special atmosphere, beer or non-alcoholic drinks and traditional, hearty food. Some colleagues even dressed up for the occasion in traditional Bavarian costumes. These circumstances are especially conducive for developing new connections among MPE staff members, students and guests even across "group boundaries".

For the summer outing in 2009, we visited the famous Austrian "Mozart city" Salzburg. After a guided tour through the city during the morning hours there was plenty of leisure time available in the afternoon. Depending on their interests, different groups of people spent these hours either discovering some famous locations in Salzburg by themselves or balancing office work with sports activities, such as a bike tour along the river Salzach.

# Max-Planck-Institut für extraterrestrische Physik

Giessenbachstraße  
85748 Garching, Germany  
Phone: (0 89) 30000-0  
Telefax: (0 89) 30000-3569  
email: [mpe@mpe.mpg.de](mailto:mpe@mpe.mpg.de)  
<http://www.mpe.mpg.de>

All rights reserved:  
Dokumentationsstelle of the MPE  
ISSN 0947-8787  
June 2010

